MONTAN
UNIVERSITÄT
LEOBEN

Chair of Nonferrous Metallurgy

Doctoral Thesis

Optimization and investigations along the industrial establishment of 5/7 crossover alloys

Dipl.-Ing. Sebastian Samberger, BSc

August 2024

MONTANUNIVERSITÄT LEOBEN
www.unileoben.ac.at

AFFIDAVIT

I declare on oath that I wrote this thesis independently, did not use any sources and aids other than those specified, have fully and truthfully reported the use of generative methods and models of artificial intelligence, and did not otherwise use any other unauthorized aids.

I declare that I have read, understood and complied with the "Good Scientific Practice" of the Montanuniversität Leoben.

Furthermore, I declare that the electronic and printed versions of the submitted thesis are identical in form and content.

Date 15.08.2024

Signature Author
Sebastian Samberger

ACKNOWLEDGEMENTS

First of all, I want to thank Univ.-Prof. Dipl.-Ing. Dr.mont. Stefan Pogatscher for the great opportunity to conduct my doctoral thesis in the framework of his Christian Doppler Laboratory for Advanced Aluminum Alloys. I'm very grateful for all the inspiring discussions and numerous chances to grow beyond myself over the last years and the constant support to develop myself in all directions.

Moreover, I deeply appreciate the extensive support by Univ.-Prof. Dipl.-Ing. Dr.mont. Helmut Antrekowitsch and Univ.-Prof. Dipl.-Ing. Dr.mont. Peter Uggowitzer, who always provided scientific and personal assistance and help when needed. In addition, many thanks to my industrial advisors at AMAG rolling GmbH, Dipl.-Ing. Dr.mont. Ramona Tosone, Dipl.-Ing. Dr.mont. Lukas Stemper, and Dipl.-Ing. Dr.mont. Florian Schmid, for expanding my knowledge horizon in best-practice industrial processing and the great cooperation to drive this project forward.

I also want to express my gratitude to all my co-workers at the chair of non-ferrous metallurgy for both their friendship and enormous support in all possible matters. In this regard a special thank needs to be given to Dipl.-Ing. Andreas Weidinger, Dipl.-Ing. Stefan Tichy for their friendship and open ears and good advice. Also, a special thank you to Dr. Eva Gerold for her invaluable advice and encouragement. Her dedication and passion in her work have been a constant source of inspiration, pushing me to strive for more.

Lastly, I would like to express my heartfelt gratitude to my family for their unwavering support throughout the highs and lows of my academic journey. Their belief in me has been a constant source of strength. I also wish to extend my deepest thanks to my beloved wife, Felicitas. Without your guidance and steadfast support, I sincerely believe I would not made it here.

Success cannot be achieved in single player mode. So, thank you all for being there for me.

ABSTRACT

This thesis addresses the critical strength/ductility trade-off in aluminum alloys, particularly in the context of automotive applications. Traditional 5xxx series alloys offer good formability but lack sufficient strength, while 7xxx series alloys offer high strength but poor formability. To overcome these limitations, 5/7 crossover alloys have been developed that combine the best of both series. The resulting alloys achieve high elongation and significant hardenability, with yield strengths exceeding 400 MPa after industrially feasible thermo-mechanical treatments, making them ideal for advanced automotive and aerospace applications.

This thesis includes a detailed study of the effects of heating and cooling rates, the simulation of industrial heat treatment processes and the unique properties of 5/7 crossover alloys. It also examines the acceleration of quality control measurements.

The sustainability aspects of the aluminum industry are examined, highlighting the potential of the crossover alloying concept to accommodate higher recycled content and support a circular economy. Increased use of recycled materials in the production of these alloys introduces higher levels of impurities, particularly iron and silicon, which can adversely affect mechanical properties. Studies are therefore being undertaken to investigate the phase formation, nature and modifiability in the system of 5/7 crossover alloys. The goal is to develop advanced alloy design and processing techniques to counteract and mitigate their detrimental effects.

The development of 5/7 crossover alloys represents a significant advance in aluminum metallurgy, providing a sustainable solution to the strength/ductility trade-off with unique possibilities in the area of rapid plastic and superplastic forming. This innovation paves the way for a shift from multi-material to single-material car bodies, enabling closed-loop recycling of vehicles in the future.

KURZFASSUNG

Diese Arbeit befasst sich mit dem kritischen Kompromiss zwischen Festigkeit und Verformbarkeit von Aluminiumlegierungen, insbesondere im Zusammenhang mit Automobilanwendungen. Herkömmliche Legierungen der Serie 5xxx bieten eine gute Umformbarkeit, aber keine ausreichende Festigkeit, während Legierungen der Serie 7xxx eine hohe Festigkeit, aber eine schlechte Umformbarkeit aufweisen. Um diese Einschränkungen zu überwinden, wurden 5/7 Crossover Legierungen entwickelt, die das Beste aus beiden Serien vereinen. Die daraus resultierenden Legierungen erreichen eine hohe Dehnung und eine signifikante Härtbarkeit mit Streckgrenzen von über 400 MPa nach industriell durchführbaren thermomechanischen Behandlungen, was sie ideal für fortschrittliche Anwendungen in der Automobil-, Luft- und Raumfahrtindustrie macht. Diese Arbeit umfasst eine detaillierte Untersuchung der Auswirkungen von Erwärmungs- und Abkühlungsraten, der Simulation industrieller Wärmebehandlungsprozesse und der einzigartigen Eigenschaften von 5/7 Crossover Legierungen. Zudem werden die Nachhaltigkeitsaspekte der Aluminumindustrie untersucht, wobei das Potenzial des Crossover Legierungskonzepts für einen höheren Recyclinganteil und die Unterstützung einer Kreislaufwirtschaft hervorgehoben wird. Der verstärkte Einsatz von Recyclingmaterial bei der Herstellung dieser Legierungen führt zu einem höheren Anteil an Verunreinigungen, insbesondere Eisen und Silizium, was sich negativ auf die mechanischen Eigenschaften auswirken kann. Daher werden Studien durchgeführt, um die Phasenbildung, die Beschaffenheit und die Modifizierbarkeit dieser Phasen im System der 5/7 Crossover Legierungen zu untersuchen. Die Entwicklung von 5/7 Crossover Legierungen stellt einen bedeutenden Fortschritt in der Aluminummetallurgie dar, da sie eine nachhaltige Lösung für den Kompromiss zwischen Festigkeit und Verformbarkeit mit einzigartigen Möglichkeiten im Bereich der schnellen plastischen sowie superplastischen Umformung bietet. Diese Innovation ebnet den Weg für eine Umstellung von Mehrstoff- auf Einstoffkarosserien und ermöglicht so das Recycling von Fahrzeugen in einem geschlossenen Kreislauf.

TABLE OF CONTENT

1 INTRODUCTION

The pursuit of carbon neutrality has become a global imperative, driving industries to adopt more sustainable practices and materials. Aluminum, known for its lightweight potential, is a crucial material in various applications, especially in the transportation sector. However, its primary production is highly energy-intensive, contributing significantly to CO_2 emissions. Recycling of aluminum offers a more sustainable alternative, as it requires substantially less energy. Despite the benefits, due to the current use of a multi material car body, recycling introduces higher levels of impurities, presenting significant challenges in maintaining the materials quality and performance.

One of the main obstacles in reducing the multi material car body for transportation applications is the strength-ductility trade-off present in the state-of-the-art aluminum alloys system. Aluminum alloys, particularly those used for lightweighting in the automotive industry, must possess both high strength and good ductility. Traditionally, achieving this balance has been difficult. For example, 5xxx-series aluminum alloys are known for their good formability but lack the high strength needed for demanding applications. On the other hand, 7xxx-series alloys offer excellent strength but suffer from poor formability.

To address this trade-off, 5/7 crossover alloys are introduced, which combine the beneficial properties of both 5xxx and 7xxx series. These crossover alloys leverage the high magnesium content from 5xxx-series for good formability and the precipitation hardening characteristics of 7xxx-series for enhanced strength. The resulting material achieves high elongations and significant hardening responses, with yield strengths exceeding 400 MPa after industrially feasible thermo-mechanical treatments. This makes them promising candidates for advanced automotive and aerospace applications where both high strength and good formability are required.

However, an increased use of recycled materials in the production of these alloys introduces higher levels of impurities, particularly iron and silicon, which can adversely affect the mechanical properties. In order to effectively manage these impurities, it is essential to have a comprehensive understanding of their phase formation, nature and modifiability. With that knowledge, advanced alloy design and processing techniques, determinantal impacts of increased impurity concentrations can be countered and mitigated or even turned into an advantage.

The development of 5/7 crossover alloys represent a significant advancement in aluminum metallurgy, providing a sustainable solution to the strength-ductility trade-off while accommodating higher levels of recycled content. This not only reduces the environmental impact associated with aluminum production but also supports the circular economy by maximizing the use of end-of-life scrap. This might allow a shift from a multi material car body to a single material car body allowing a closed-loop recycling of vehicles in the future.

1.1 Aim of this work

The primary aim of this research is to achieve a deeper understanding of 5/7 crossover alloys and to support as well as accelerate their industrial implementation. This advanced material present unique challenges and opportunities. The aim is to identify both their potential and their inherent weaknesses, by investigating its fundamentals. Recognizing the potential is important to optimize these alloys and find suitable industrial applications, ensuring peak performance. Identifying weaknesses enables the development of strategies to mitigate or eliminate these drawbacks, which can go as far as to reengineer the alloys composition.

This research combines fundamental scientific investigation with practical feedback from customers and industry stakeholders. Integrating basic research with customer requirements, allows to create a responsive framework for heat treatment development with near industrial parameters. This dual focus ensures accelerated adaptability to changing situations and evolving industry needs.

The major goal is to bridge the gap between theoretical research and practical application. Understanding the fundamental properties of crossover alloys such as phase formation, their dependence on heating/cooling rates as well as the interplay of different elements in the matrix, allows the development of a more effective, versatile and sustainable material.

1.2 Document structure

To effectively establish and utilize a close laboratory/industrial framework for the development of new alloys as discussed in section 1.1, it is first necessary to understand the current trade-offs involved in the application of aluminum. Consequently, Section 2 concentrates on the investigation of market requirements, thereby facilitating a more profound understanding of the leverages given by material physics for the tailoring of alloys to a particular use case. Furthermore, a summary of the work done in the field of crossover alloying, with a particular focus on 5/7 crossover alloys, is provided to illustrate the outstanding performance of this innovative alloying approach. Section 4 assesses the environmental and economic aspects of aluminum primary production and recycling and highlights the necessity for the development of new alloys from a sustainability perspective. Sections 5 to 8 present a summary of the major findings acquired during this research, which have been published in peer-reviewed journals or peer-reviewed conference proceedings. Section 9 gives a summary of the work and provides an outlook on further research to be conducted in the field.

2 STATE OF THE ART

In order to support the industrial implementation of novel alloys, it is essential to understand and specify the market gap which is driving such a development, as well as the fundamentals of materials technology associated with the targeted material properties. The following chapter summarizes knowledge essential for this understanding and provides valuable insight into the work published in the field of crossover alloying.

2.1 Aluminum alloys and the transport sector

Aluminum has been replacing wood for lightweight construction since 1920 [1]. By 1987, it had become widely acknowledged as an important material in the automotive industry [2]. Although the primary production remained at around 20 million tons annually from 1980 to 2000, it has almost quadrupled over the past twenty years and is expected to reach 70 Mt by the year 2025. This tremendous increase is further underlining its success and acceptance in society [3]. It is no surprise that nowadays aluminum continues to be recognized as a significant winner in the transportation sector, accounting for 24% of the total aluminum consumption [4], as it is utilized for lightweighting, resulting in weight reductions of more than 30% [5–7]. Since 2010, the aluminum usage in vehicles has grown from 130–160 kg to around 208 kg per vehicle in 2020 with a forecast weight of around 260 kg in 2030 [8–10]. The ongoing transition from internal combustion engine (ICE) vehicles to battery electric vehicles (BEV) is changing the requirements for the materials used, creating additional new challenges and opportunities for aluminum. [11]

The addition of alloying elements to aluminum results in a wide range of alloys with tailored properties for different purposes. These alloys can be divided into two groups: wrought and cast alloys. Wrought alloys are further divided into age hardenable and non-age hardenable (or natural hard) alloys, depending on whether the alloy can form re-dissolvable precipitates that contribute to the alloys strength. A list of the classification system of aluminum alloys is given in Table 2-1. [12,13]

Each class comprises several alloys that exhibit unique properties suitable for specific applications. In the automotive industry, alloys from the 1xxx to 7xxx series (mainly 5xxx and 6xxx) are prevalent, along with cast alloys from the 2xx.x and 3xx.x group. While the alloying content of cast alloys can reach up to 30 wt.-%, it is limited to approximately 5 wt.-% in wrought alloys. [6,9,14–16]

However, aluminum in the transportation sector is not limited to the automotive industry. It has been the primary structural material for aircraft applications for almost 90 years, accounting for 60–80% of the total material used (nowadays highly challenged by composite materials). All types of Al wrought alloys are used in aerospace applications, with the highest proportion of 2xxx series alloys, followed by 7xxx series alloys. [17–19]

Table 2-1: Classification systems of aluminum wrought alloys and cast alloys (after American standard) [12,13,20]

Wrought alloys

Group	Main alloying elements	Hardenability
1xxx	Pure Al	Natural hard
2xxx	Al-Cu	Hardenable by Θ-Al_2Cu or S-Al_2CuMg
3xxx	Al-Mn	Natural hard
4xxx	Al-Si	Natural hard
5xxx	Al-Mg(Mn)	Natural hard
6xxx	Al-MgSi	Hardenable by β-Mg_2Si
7xxx	Al-ZnMg	Hardenable by η-$MgZn_2$ or T-$Mg_{32}(Al,Zn)_{49}$
8xxx	Al-FeSi	Natural hard

Cast alloys

Group	Main alloying elements
2xx.x	Cu
3xx.x	Si+Cu, Si+Mg, Si+Cu+Mg
4xx.x	Si
5xx.x	Mg
7xx.x	Zn
8xx.x	Sn

The cast aluminum alloys most utilized in the aerospace industry are typically of the types of Al-Si, Al-Cu and Al-Mg. These are employed for the manufacture of baggage compartments, cabin castings, engine parts and non-structural components of mechanical and hydraulic systems. [19]. In the automotive industry, cast alloys such as 319.0 (AlSi6Cu3.5Zn) and A380.0 (AlSi9Cu3.5FeZn) are employed as engine blocks and cylindrical heads. With a usage volume of > 80% of all casting alloys, these are the most commonly used alloys and additionally represent the highest scrap sink due to their high impurity tolerance [21]. The distribution of cast and wrought aluminum alloys in the automotive industry is approximately 44% and 56%, respectively [22].

Wrought alloys are constrained by specific composition boundaries in order to guarantee the desired properties. In particular, elements such as Fe, Si and, depending on the alloy class, Cu are regarded as detrimental, as they result in the formation of coarse primary particles with a deleterious impact on the mechanical and chemical properties. [23]

The single alloys used in a car body are often welded together or joined in a way, that separation during recycling is nearly impossible. Furthermore, joining methods still used today are itself a source for Fe impurities [24]. As a result, the alloys used, in combination with the current possibilities for separation and recycling, are leading to an increase in the impurity content of end-of-life (EOL) material. The expected elemental composition of scrap derived from the automotive industry between the years 2030–2050 is expected to be 4–5 wt.-% Si, 0.6–0.7 wt.-% Fe and 0.2–0.3 wt.-% Cu [25]. Table 2-2, displays the maximum allowed content of Fe, Si and Cu in the individual wrought alloy classes as well as the average permitted content of each class. This demonstrates, that the chemical composition limits are too tightly bound to allow an exclusive use of End-of-life material in the production of wrought alloys [12]. The highest scrap sink currently known are engine blocks made from aluminum cast alloys [21]. However, the availability of this scrap sink is diminishing as the transition from ICE vehicles to BEVs continues.

Yet, the utilization of recycled materials in the production of aluminum alloys, especially wrought alloys is a crucial factor for a sustainable development of our society. There is an urgent need for recycling of aluminum which is closely related to the CO_2 emissions associated with its production.

This topic, as well as potential methods for the removal of impurities and other mitigation techniques designed to counter the detrimental effects of elevated Fe and Si levels, is addressed by Samberger et. al [26] which is presented in chapter 4.

Table 2-2: Maximum content of the elements Fe, Si and Cu per wrought alloy class, as well as the mean value for all alloys in each class in weight percent [wt.-%]; created with data from [12]

Alloy class	Max. (mean) content Fe [wt.-%]	Max. (mean) content Si [wt.-%]	Max. (mean) content Cu [wt.-%]
2xxx	1.4 (0.5)	1.2 (0.5)	6.8 (4.3)
3xxx	0.8 (0.7)	0.6 (0.5)	0.3 (0.2)
4xxx	0.8 (0.7)	13 (7)	0.5 (0.3)
5xxx	0.7 (0.4)	0.45 (0.3)	0.5 (0.2)
6xxx	0.8 (0.4)	1.5 (0.7)	1.1 (0.3)
7xxx	0.5 (0.2)	0.5 (0.2)	2.6 (1.4)
8xxx	1.3 (0.9)	0.8 (0.4)	0.1 (0.075)

The existence and utilization of the wide range of aluminum alloys is a consequence of the drastically changing properties resulting from the addition of different elements. Each element imparts a unique set of characteristics to the alloy, making it suitable for specific applications within a vehicle. This effect is not solely limited to the addition of an element, but also on the amount and ratio with other elements. Therefore, each alloy class consists of multiple subclass alloys, which have been designed to serve a specific purpose. A comparison of the mechanical properties of selected age hardenable alloys of the 2xxx, 6xxx and 7xxx series, as well as non-age hardenable alloys such as the 1xxx and 5xxx series, is presented in the following section see Figure 2-1. The strain and strength of the alloy varies according to the heat treatment conditions and the ability to harden. While age-hardenable alloys are categorized according to their ageing process (T4, T6, T7...), non-age-hardenable alloys are categorized according to their work-hardening condition, with "O" being soft-annealed and "H" being work-hardened. [12]

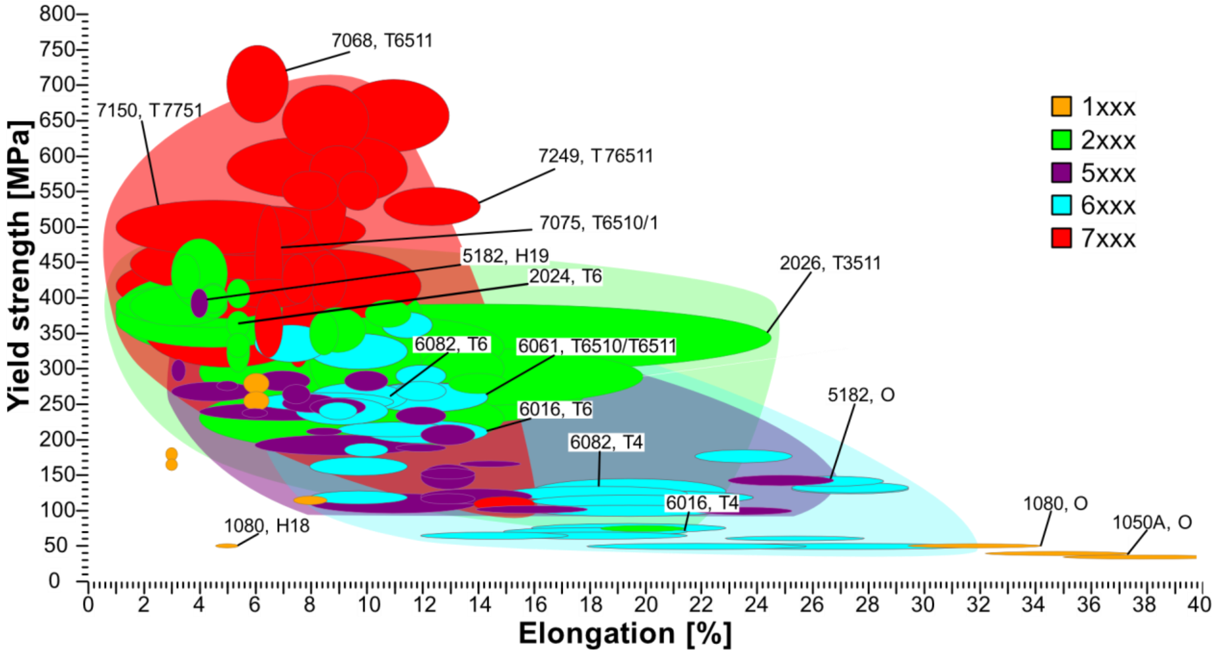

Figure 2-1: Mechanical properties of selected classes of natural-hard and age-hardenable commercial alloys under different heat treatment conditions [27]

6xxx series alloys are widely used for exterior body panels and extrusions [5,15] as they offer a high ductility and a reasonable softness during the forming process. They also offer the possibility for hardening [28].

5xxx series alloys are the second most commonly used wrought aluminum alloy in automotive applications. These alloys achieve the highest strength of all non-heat treatable alloys while retaining good formability, and they have a good corrosion resistance and weldability [29]. They are used for parts that require deep drawing, such as door inner panels, and can be used for structural components [28]. However, the alloys are only usable for non-visible parts as the occurrence of Lüders elongation [30] and the Portvein-Le Chatelier (PLC) [31] effect leads to undesired surface quality. In terms of surface quality, 6xxx series alloys are superior. Therefore, doors are usually a combination of a 5xxx series inner panel with 6xxx series outer surface. [28]

As an alternative to 6xxx series alloys, 2xxx series alloys could be considered as they achieve higher strength. With a reduced Cu content, they even achieve the formability requirements and still retain the peak strength to allow replacement of heavier steel plates [32,33]. However, as Cu is a slow diffusing element, it is difficult to achieve peak hardness during automotive manufacture. Therefore, 6xxx series alloys are chosen over 2xxx series alloys as they are more formable and achieve a better hardening behaviour during standard manufacturing processes [34]. In addition, Cu segregations in 2xxx series alloys lead to susceptibility to filiform corrosion and minimal weldability, properties that are better in 6xxx series alloys. [29,35]

7xxx series alloys offer highest strength and could replace steel even in crash management applications. However, the alloy is highly unstable in the solution annealed (soft) condition, meaning the hardness increases immediately after heat treatment resulting in a loss of cold formability. [29]

Although they can achieve yield strength values > 600 MPa, they are prone to stress corrosion cracking and show minimal weldability, which limits their use in the automotive industry to special circumstances. There are, several techniques to mitigate the negative effects. However, these increase the complexity of the manufacturing process and reduce the strength of the alloy. [28]

Due to the complexity of manufacturing, 2xxx and 7xxx series alloys are used sparsely in automotive applications but are used extensively in aerospace applications. The 2xxx series alloys are primary aluminum alloys used in airframe structural applications and the 7xxx series alloys with the highest strength are used in upper wing skins, stringers and stabilisers. The development of alloys in this sector is driven by the trade-off between high strength and low fatigue resistance, as 2xxx series alloys have good resistance to damage and fatigue cracking, but their low yield strength limits their use in components subjected to high stress, where 7xxx series alloys are applied. A step forward in aerospace applications has been the introduction of Al-Li alloys as they offer lower density, high strength and high fatigue resistance [17,19,36,37].

All these manufacturing implications and alloy properties lead to the conclusion that the automotive industry suffers from a strength-ductility trade-off present in aluminum alloys, necessitating the use of a multi-material car body. Also in aerospace applications, there is a trade-off between ductility and strength, even though the limiting design parameter here is the fracture toughness [38] and corrosion resistance of the alloys.

To overcome this strength/ductility trade-off, and in the long term to enable better recycling of vehicles, future development of alloys will need to increase strength and formability to allow greater design freedom and the manufacture of more complex parts [28].

2.2 Strengthening mechanisms

Among the various requirements for materials, strength and ductility have been identified as two of the most important. As there is a known trade-off between strength and ductility in aluminum alloys, particularly for those used in the automotive sector, it is important to understand the mechanisms that increase the strength of materials and how they affect ductility. There are four main strengthening effects used in commercial aluminum alloys, namely solid solution strengthening, second phase particle strengthening, grain size effects and work hardening. The strengthening mechanisms, except work hardening are described in the following. As most commercial alloys are annealed during automotive processing, dislocations are removed from the system and thus the contribution of work hardening is negligible [39]

- **Solid solution strengthening**

Solid solution strengthening is the main strengthening mechanism in non-heat treatable alloys such as 3xxx Al-Mn and 5xxx Al-Mg alloys. In the Al-Mg alloy system, both yield stress and ductility increase with increasing Mg content. As Mg has a decreasing solubility in Al, β-Al_3Mg_2 precipitates are formed during ageing at Mg levels > 10 wt%, which subsequently reduce the ductility of the material. [40,41]

The main mechanism responsible for the increase in strength due to solid solution strengthening arises from the elastic interaction between the solute and the solvent atom due to the difference in size of the two atoms creating a strain field around the atom and a difference in elastic modulus leading to a 'hard' or 'soft' spot in the matrix [42]. Early work on the effect of solute elements on the strength of aluminum alloys was carried out by Dorn et. al. [43]. They found, that an increasing amount of solutes not only increase the flow stress ($Rp_{0.2}$) but also lead to an increase in the work hardening rate. This is caused by the effect of solutes on the thermal component of the flow stress, the athermal storage rate of dislocations and their dynamic recovery effect [44]. There are several models to predict the work hardening rate such as the model by Nes and Marthinsen [45,46] or Kocks and Mecking [47].

The strengthening effect on the flow stress caused by atoms in solid solutes can be described as shown by equation (2-1) [42]:

$$\sigma=\sigma_{\mathrm{pure}}+Hc^{n} \tag{2-1}$$

Here, σ_{pure} is the flow stress of the pure metal and c is the concentration of the solute. H and n are constants with n in the range of 0.5–0.75 for pure fcc solid solutions.

- **Strengthening by second phase particles**

In general, strengthening by second phase particles is described as the interaction of dislocations with an array of point obstacles [39]. The second phase particles referred to in this section are in the range of 0.1–1 μm [48] and can be further divided into two categories: dispersoids and hardening precipitates.

In aluminum alloys, dispersoids refer to a second phase precipitated during a thermal treatment like homogenization. Those particles are thermally stable and cannot be dissolved back into the matrix. These dispersoids are intermetallic phases like $Al_6(Fe,Mn)$ or $Al_x(Fe,Mn)_3Si_x$, which are formed through the addition of Mn [49]. In the case of Mn, the addition is made to suppress, to some extent, the detrimental impact of Fe and Si-bearing intermetallics and to increase the strength of the alloy at the same time [50]. Other elements such as Zr, Cr and Sc are added to form thermal stable trialuminides (Al_3X) [51,52] which act as obstacles for dislocation movement.

Thermally unstable intermetallic particles can be dissolved into the matrix and re-precipitated in a desired form during heat treatment at the end of the processing cycle, which is also known as age-hardening [53]. This allows for a tailored hardening process, whereby alloys are initially soft and malleable during the manufacturing process, but achieve a high hardness during the use phase.

The commercial aging process involves the following steps: (i) solutionizing and quenching, resulting in a supersaturated solid solution (SSSS); (ii) forming of small accumulations of atoms, known as Giunier-preston zones (GP-Zones) [54] or phase precursors, either by natural ageing (NA) or a pre-aging (PA) treatment; (iii) formation of the hardening phase during a commercial paint-bake (PB) treatment. [12]

For example the precipitation sequence in 7xxx series alloys is usually given as: [55,56]

$$\mathrm{SSSS}\rightarrow\mathrm{GP\ zones}\rightarrow\mathrm{metastable}\ \eta'\rightarrow\mathrm{stable}\ \eta\ (MgZn_2)$$

The strengthening mechanism of secondary particles is dependent on the hardness of the particle in comparison to the matrix, as well as its fit with it. Depending on the particle composition and structure, it can be coherent, partly coherent, or incoherent with the matrix. At the start of the strengthening process, the movement of dislocation is hindered by the particle. As the stress increases, the dislocation has two options to interact with the obstacles, which are schematically displayed in Figure 2-2. In the case of relatively soft, small, and coherent or semi-coherent particles, the dislocation can cut the particle, leading to a shear deformation. This deformation strains the surrounding matrix, and the new surfaces created by the steps increase the amount of work required to generate the corresponding surface energy. In contrast, in the case of incoherent, hard particles, the dislocation is unable to "cut" the particle. The dislocation line bows around it until it collapses, forming dislocation rings around the particle. This process is also known as the Orowan mechanism. [57–59]

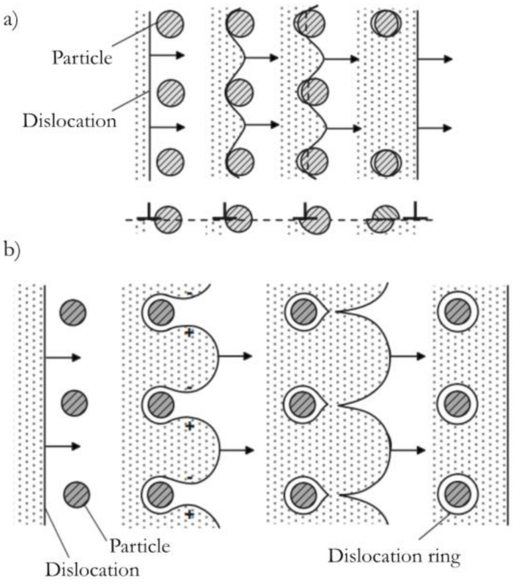

Figure 2-2: Interaction of dislocations with particles in the matrix. Particles can either be sharable (a) creating new surfaces or non shearable (b) leading to Orowan-dislocations rings or loops around the particles [60]

The strengthening that occurs as a result of cutting particles involves a number of different effects, including the stress required for the deformation of the particle, the work needed for surface generation and the increase in internal energy due to the alteration of the dislocation line. A consideration of all of the factors involved leads to the strengthening effect given in equation 2 (2-2): [57,61]

$$\sigma \approx \sigma_{pure} + const \cdot f_v^{\frac{1}{2}} \cdot r_p^{\frac{1}{2}} \tag{2-2}$$

Where f_v is the volume fraction of small particles and r_p is their radius given as perfect sphere. It should be noted that equation (2-2) is only valid for particles approx. ≤ 10 nm. Coarser particles lead to an increase in particle spacing and at this size coherent particles behave like incoherent once leading to Orowan-strengthening [61]. The stress increased caused by the Orowan strenghening mechanism is given by equation (2-3): [59]

$$\sigma \approx \sigma_{pure} + \frac{K_{Orowan}}{\left(\frac{L}{D_p}\right)\sqrt{D_p}} \tag{2-3}$$

K_{Orowan} combines multiple empirical factors into a single value, D_p is the particle diameter and L the mean interparticle free path. Even though particle strengthening is the most pronounced strengthening mechanism in aluminum alloys, it is important to note, that secondary particles, even when they are <1 µm, lead to a decrease in possible elongation of the material resulting decrease in ductility. This is due to the particles acting as sites for cavity formation, leading to cavity growth and cavity coalescence, ultimately resulting in tough fracture of the material. [62]

- **Strengthening by grain size**

As the slip plane is interrupted at a grain boundaries they behave like obstacles for the dislocation movement. Consequently, dislocations can accumulate at grain boundaries leading to a increase in stress. More grain boundaries, meaning more thus smaller grains, leading to a greater number of obstacles, thus necessitating a greater amount of work for the successful movement of dislocations through the matrix. The strengthening mechanism by grain size is described by the Hall-Petch relationship, which is shown in equation (2-4): [63]

$$\sigma=\sigma_{pure}+kd^{-\frac{1}{2}} \tag{2-4}$$

The factor k is a material specific constant known as the Hall-Patch constant. For example, k has a value of 68 MPa·m$^{-1/2}$ [13] for Al99.99, 161 MPa·m$^{-1/2}$ for AlMg1 and 236 MPa·m$^{-1/2}$ for AlMg5 [12]. The factor d refers to the grain size. It is to note, that the positive slope of the Hall-Petch relationship has a limit at a grain size of about 10–40 nm, where the slope of the curve changes from positive to negative. [64]

Strengthening by grain size is the only known strengthening mechanism that not only has no detrimental impact on the ductility of the material but is also able to increase it. The enhancement of ductility is a well-documented phenomenon in commercial alloys, such as the peak-aged 7xxx series alloys [65,66], as illustrated in Figure 2-3.

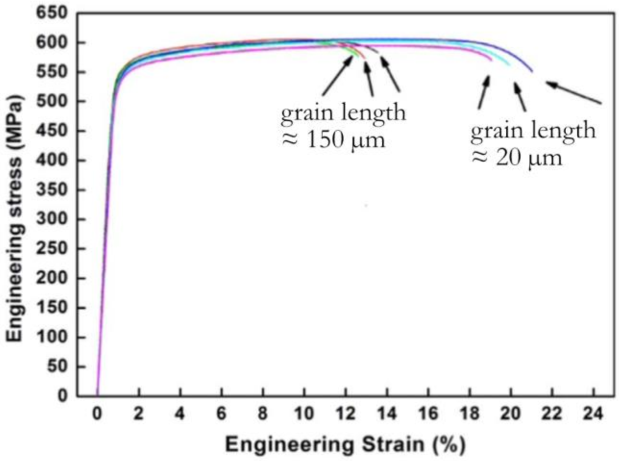

Figure 2-3: Engineering stress-strain curves of an industrial peak aged (T6) 7055 alloy showing the effect of grain reduction on the ductility of the material; redone after [66]

A small and stable grain size does not only allow strengthening and enhancement of ductility at room temperature. A grain size < 10 µm is a key requirement for commercial aluminum alloys to show superplastic properties [67–71]. Superplastic forming is a process in which a polycrystalline material can undergo elongations of several hundred percent without failure. Commercially, such processes are conducted at low strain rates of 10^{-4}–10^{-2} s^{-1} at temperatures in the range of ≥ 0.5T_m (solidus temperature)

[68]. Industrial, superplastic forming is applied for 5xxx series alloys via superplastic forming (SPF) and quickplastic forming (QPF) at elevated temperatures and varying strain rates. [72–74]

In commercial alloys, a combination of the previously mentioned hardening mechanisms occurs in dependence on the alloy type (age-hardenable, non-age-hardenable). The yield strength of an alloy can be calculated with good agreement with experimental values through the addition of all contribution mechanisms. Figure 2-4 demonstrates this for an Al-4Cu alloy with varying Zn and Mg content. [75]

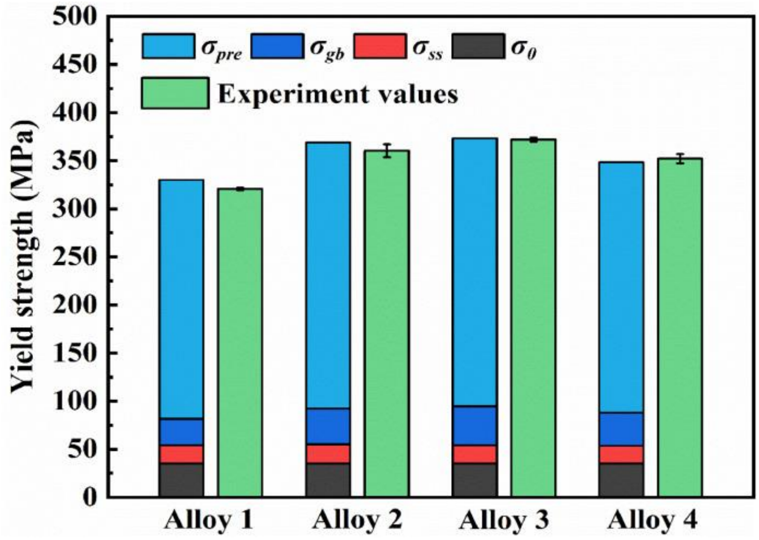

Figure 2-4: Theoretical contributions to the yield strengh of an Al-4Cu-xZn-yMg alloy compared to experimental values; Contributors to the yield strength are: σ_0(pure Al = 35 MPa), σ_{pre} (precipitates), σ_{gb}(grain boundaries), σ_{ss}(solid solution) [75]

2.3 Grain refinement techniques

In order to enhance the universal applicability of alloys, it is necessary to strive for an increase in both ductility and strength. As shown in chapter 2.2, a simultaneous increase in strength and ductility can be achieved by reducing the grain size. Therefore, the following section considers the various options for grain refinement and their industrial applicability.

Guan and Tie [76] describe four grain refinement techniques that can be carried out during or after the solidification process. During solidification the grain size is influenced by the solidification speed, addition of grain refiners or vibration and steering.

Vibration and steering technique aim for the destruction of the dendritic arm structure during solidification and thus decreasing the grain size [76]. The addition of grain refiners is done to increase the number of nucleation particles. As more particles nucleate, they are constrained to a maximum achievable size within a given volume. Commonly employed grain refiners in the aluminum industry include those derived from the systems Al-Ti-B [77] and Al-Ti-C [78]. Another possible path for grain refinement is through dendrite disintegration. This phenomenon is caused by the combination of high undercooling and subsequent remelting due to constitutional superheating effects, which results in the refinement of the solidified structure [79,80]. Rapid solidification methods include twin-roll casting [81], high-pressure die casting [82] and melt spinning [83] However, rapid solidification techniques are not yet on an industrial mature level or are designed to produce cast alloys rather than wrought alloys. An interesting approach for accelerated solidification is the Nexcast technique which utilizes a horizontal block caster with a plant currently planned in the US. [84,85]

Following solidification severe plastic deformation (SPD) operations can further refine the grain structure. These include techniques such as high-pressure torsion (HPT) [86,87], friction stir processing (FSP) [88], equal-channel angular pressing (ECAP) [89] and accumulative roll-bonding (ARB) [90]. A comprehensive overview of SPD techniques can be found elsewhere [91]. However, it is important to note that SPD techniques are not yet suitable for the large scale production of aluminum sheet alloys.

Yet, there is a fifth option for grain refinement, which can be utilized in wrought alloys via deformation introduced by cold rolling. It is essential to view this as a fifth option, as cold rolling on an industrial scale is not often severe enough to be considered a severe plastic deformation process. During deformation, the free energy of the material is raised by the presence of dislocations and interfaces, which makes the microstructure thermodynamically unstable. Two processes are known to restore the material to a stable condition: recovery and recrystallisation. These processes are significantly influenced by particles present in the matrix, which interact with dislocations and interfaces, thereby affecting the stability and size of the subgrain structures. This interaction can be exploited to tailor the microstructure to a fine-grained condition. [92]

During **recovery**, two processes can occur. Either dislocations with opposite burgers vector annihilate or the dislocations rearrange into stable structures. The stable structures, also known as subgrains have a cell structure usually in the range of about 0.5–1 μm. Subgrains tend to coalesce and grow, thereby reducing the overall energy of the system. However, if small particles < 1 μm are present in a uniformly distributed manner in the matrix they exert a pinning effect on the subgrain structure limiting its size. Furthermore, small particles stabilizing the subgrain structure also hinder the initiation of recrystallization. The schematic process of annealing involving recovery and recrystallization as well as the effect of different small particles on the grain structure is displayed in Figure 2-5. The pinning pressure (P_{sz}) on the grain boundaries is described by the Smith-Zener drag as given in equation (2-5): [92,93]

$$P_{SZ} = \frac{3F_V\gamma_s}{2r} \tag{2-5}$$

Where F_v is the volume fraction and of the particles, r is their radius and γ_s the grain boundary energy per unit area. One must note that several assumptions are made for equation (2-5). Consequently, there exist multiple modifications of this equation to account for differing circumstances, such as particle shape, coherence with the matrix, grain shape, and particle size distributions. [94]

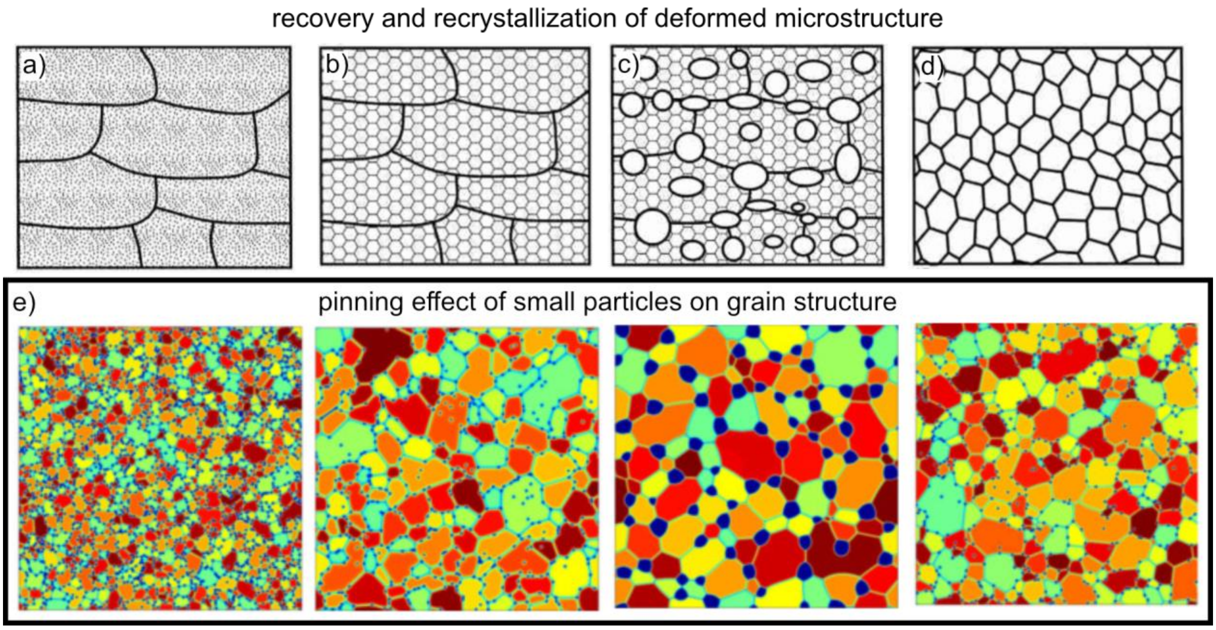

Figure 2-5: Schematic of an annealing process. The deformed structure (a) recovers with the formation of a subgrain structure (b); The microstructure further partially recrystalizes to new dislocation-free grains (c) that grow and consume the whole structure (d); Small particles in the matrix can hinder recrystallization and subgrain growth; the effect varies with different particle size and distribution (e) redone after [92,95]

Recovery is followed by **recrystallization** which involves the formation of new strain-free grains in certain parts of the microstructure. The strain-free grains subsequently consume the deformed or recovered microstructure. This process can involve normal or abnormal grain growth, resulting in an undesired coarse microstructure. Commercial alloys typically comprise secondary particles with both closed-packed dispersoids and coarse particles (> 1 µm). While closed-packed dispersoids impede recrystallisation, coarse particles facilitate recrystallisation, as they can act as nuclei for new grains via a particle-stimulated nucleation (PSN) process. In commercial alloys, the size at which a particle is able to act as a nucleus (d_g) is given by equation (2-6): [92]

$$d_g = \frac{4\gamma_b}{P_D - P_{SZ}} = \frac{4\gamma_b}{\frac{\rho G b^2}{2} - \frac{3F_v\gamma_s}{2r}} \qquad (2\text{-}6)$$

Where γ_b is the interfacial energy of the matrix, ϱ is the dislocation density, G is the shear modulus and b the burgers vector. For a bimodal particle distribution, the driving pressure for recrystallization P_D is offset by the pinning effect of small particles.

The PSN effect offers the possibility for grain size reduction in commercially available alloys by solely cold working and heat treatment. When thermal non-stable phases are employed for the effect, they can be dissolved into the matrix after grain refinement, thereby avoiding detrimental effects on the mechanical properties, as demonstrated by Wert et al. [96] for the 7xxx series alloys. This effect is also applicable to novel 5/7 crossover alloys. [97]

2.4 Crossover alloying concept

State-of-the-art aluminum alloys are designed to fulfill a specific purpose requiring narrow composition limits. Furthermore, in accordance with the classification standard for alloys, it is not possible for an alloy that contains magnesium as the main alloying element to be age hardenable. This is because alloys with Mg as the main alloying element belong to the 5xxx class, which by definition are non-age hardenable. A similar argument can be made with regard to a 6xxx alloy, which would exhibit increased Fe and Si contents. By definition, the maximum permitted content of Fe is limited to 0.8 wt.-%, thereby precluding any further increase (see Table 2-2). [12]

The crossover alloying concept challenges the conventional classification system, as it introduces an innovative fit-the-need system by combining advantageous properties from different alloy classes. This approach offers greater design freedom and flexibility, while representing an innovative approach to metallurgical design. It aims to overcome the limitations inherent in traditional aluminum alloys by integrating beneficial properties from distinct alloy classes [98]. The strategic combination of the advantageous formability of AlMg(Mn) alloys with the superior strengthening capabilities of AlZnMg(Cu,Ag) alloys, known as **5/7 crossover alloys**, has the potential to overcome the strength-ductility trade-off present in the automotive industry. [99]

A further implementation of the crossover concept was conducted by Trink et. al. [100,101], who combined the ductility of 6xxx series alloys with the high Fe content of 8xxx series alloys. This **6/8 crossover alloy** concept has the potential to mitigate the effects of increasing Fe and Si content in future automotive scrap as predicted by [25]. The higher fraction of Fe is leading to an increase in the formation of primary intermetallic compounds (IMCs). By deploying advanced thermomechanical processing, the Fe- and Si-bearing IMCs can be fragmented into a fine dispersed particle. These particles no longer exert a detrimental effect on the mechanical properties and can be utilized to form a fine-grained structure trough a PSN effect. This results in a number of beneficial effects, including increased strain hardening, high achievable elongation, and an increase in yield and tensile strength in the alloy in comparison to the base 6061 alloy. The 6/8 crossover approach allows for an increase in Fe levels of up to 1.5 wt.-% and Si levels for 2.3 wt.-%, leading to a yield strength level of 254 MPa in the T6 condition. This represents an increase of approximately 40 MPa compared to the base alloys with an Fe and Si content of 0.19 and 1.09 wt.-%, respectively. Furthermore, the elongation to break is not negatively influenced [101]. Despite the alloys impressive ability to withstand the predicted increase in Fe and Si levels in automotive scrap, making it an interesting option for a future scrap sink, it is important to note that its strength is significantly lower than that of 2xxx or 7xxx alloys in their fully age-hardened condition. This makes a potential implementation of the alloy for structural applications questionable.

Another type of crossover alloys are AlCuZnMg **2/7 crossover alloys**, which combine the effects of 2xxx and 7xxx series alloys. In these alloys hardening is achieved by multi-phase strengthening through the interplay of Cu, Zn an Mg, with the goal of reducing the lengthy and complicated deformation process of 2xxx series alloys [75,102]. Nevertheless, an increase in the Zn content in 2xxx series alloys has been found to give rise to new problems concerning the corrosion resistance of the alloys. The addition of 0.67 wt.-% Zn to 2024 series alloys has been demonstrated to result in a widening of the precipitation-free zone (PFZ) at the grain boundaries, thereby increasing the alloys sensitivity to intergranular corrosion [103]. Tan et. al. [104] demonstrated that a suitable addition of Zn to the alloy increases the resistance to intergranular corrosion (IGC). They found that the addition of Zn promotes the formation of S-phase (Al_2CuMg), as Zn can replace Cu in Cu–Mg clusters. The accelerated grain boundary precipitation of S-phase by Zn addition leads to a widening of the precipitation-free zones (PFZs) as solutes are consumed from the surrounding matrix, which then decreases the resistance to IGC. However, if the Zn content is increased beyond 2 wt.-% the precipitation of a η-phase ($MgZn_2$) is favoured over S-phase due to the higher diffusion rate of Zn. The η-phase is limited in amount due to the limited Zn content and the precipitates consume Mg, leading to a decrease in nucleation sites for S-phase. This interplay of precipitation sequences is resulting into a discontinuous distribution of grain boundary precipitates and a decrease in PFZ width. Consequently, the IGC resistance in 2xxx series alloys with Zn addition of > 2 wt.-% is elevated as the grain boundary precipitates are tailored to a non-continuous form. However, the susceptibility to pitting corrosion is concomitantly augmented. [104]

The utilization of the hardening potential given by the addition of Zn to a 6xxx series alloy could be considered as a **6/7 crossover alloy**. The effect of Zn additions to an Al-0.48Mg-1.03Si alloy was studied by Jiao et al. [105] by the addition of 2.98 wt.-% Zn to the base alloys. Solution annealing at 565°C for 30 min with quenching in cold water is followed by aging at 180 °C. The hardness evolution of the alloy with Zn addition compared to that observed in the base alloy, was with 120 HV about 10 HV higher. Zn was also found to modify the precipitation morphology and interface between the precipitates and the matrix. This is because Zn can enter the structure of all phases, without altering the precipitation sequence, yet it does result in precipitate disorders. [105,106]. When the Zn level in an Al-1Mg-0.5Si alloy is raised to approximately 3 wt.-%, the coexistence of β-Mg_2Si and η-$MgZn_2$ is observed following aging at 170 °C for 120 h. It has been demonstrated that the addition of Zn is found to accelerate the age hardening response, resulting in the precipitation of the η-phase and a peak Vickers hardness of approximately 125 HV. [107]

The impact of Zn addition on the corrosion resistance of Al-Mg-Si alloys was examined by Gou and colleagues [108] who observed an increase in intergranular corrosion (IGC) susceptibility up to an Zn level of 1 wt.-%, which then decreased when the Zn level exceeded this value. The IGC resistance can be attributed to the evolution of the microstructure during the ageing process as schematically illustrated in Figure 2-6. When the Zn content is low (<1 wt.-%), a continuous film of Zn is present on the grain boundary. During further ageing treatment this film slowly transforms into discontinuous coarse grain boundary precipitates. This results in a wide PFZ, as the Zn film is able to consume a high fraction of solid solution elements from the surrounding matrix, thus implying a high susceptibility to IGC. If the Zn content is increased, the driving force for the formation of Mg-Zn precipitates sufficiently high to suppress the formation of a Zn-rich grain boundary layer. Further heat treatment also leads to the formation of coarser grain boundary precipitates, yet they cannot grow to the same size as in the case with a Zn film, leading to a more narrow PFZ and better resistance to IGC. [108]

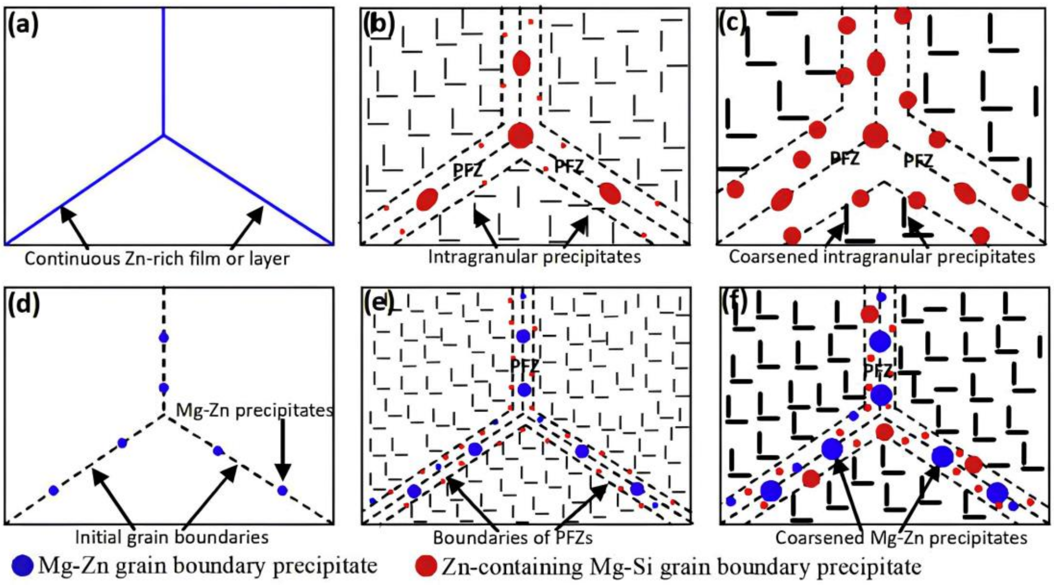

Figure 2-6: Schematic diagram of the grain boundary precipitation behaviour in Al-Mg-Si-Cu alloys with different Zn additions: **low Zn** content (a-c) in under aged condition (a) peak aged condition (b), and over aged condition (c); **high Zn** content (d-f) in under aged condition (d) peak aged condition (e), and over aged condition (f). Reprinted from [108]

Another potential approach for crossover alloying is the **5/2 crossover alloy** combination. This involves merging the high formability of the 5xxx base material with the age-hardening response of 2xxx series alloys. When Cu is added to 5xxx series alloy hardening is allowed by precipitation of S-phase (Al_2MgCu) with a similar precipitation sequence as found in 2xxx series alloys which is as follows: [109,110]

$$\text{SSSS} \rightarrow \text{Cu/Mg clusters (GPB zones)} \rightarrow \text{S}''\text{-phase} \rightarrow \text{S}'\text{(S)}$$

Although the Cu/Mg ratio is considerably lower than that observed in 2xxx series alloys, 5/2 crossover alloys still exhibit an accelerated hardening response. Medrano et al. [111] demonstrated that the addition of 0.12 wt.-% Cu is sufficient to form stable Mg-Cu clusters after 20 minutes of aging. The clusters are of a similar size and geometry to those found in 2xxx series alloys, although incorporating a smaller amount of Cu. [111]

Ratchev et al. [112,113] investigated the effect of the Cu/Mg ratio on the hardening response. The alloys utilized in this study exhibit Cu/Mg ratios that span a range from 0.14 (alloy X) to 0.29 (alloy Z). The expected phases as well as the hardening response during ageing are displayed in Figure 2-7. During the aging process at 180 °C, all alloys demonstrated an initial increase in yield strength of 20–40 MPa, followed by a linear progression towards the peak hardness value. The highest yield strength is observed for alloy Z, which reaches approximately 205 MPa, representing a hardening response of approximately 120 MPa. The hardening is attributed to the precipitation of the S-phase (Al_2MgCu). Despite the fact that the T-phase ($Mg_{32}(Al,Cu)_{49}$) was predicted by thermodynamic calculations, it was not observed. Furthermore, in addition to the high age-hardening response, the detrimental effects of natural aging, such as the deterioration of hardenability or limitations to formability, which are known from the AlMgSi system, were not observed for 5/2 crossover alloys. [99,112,113]

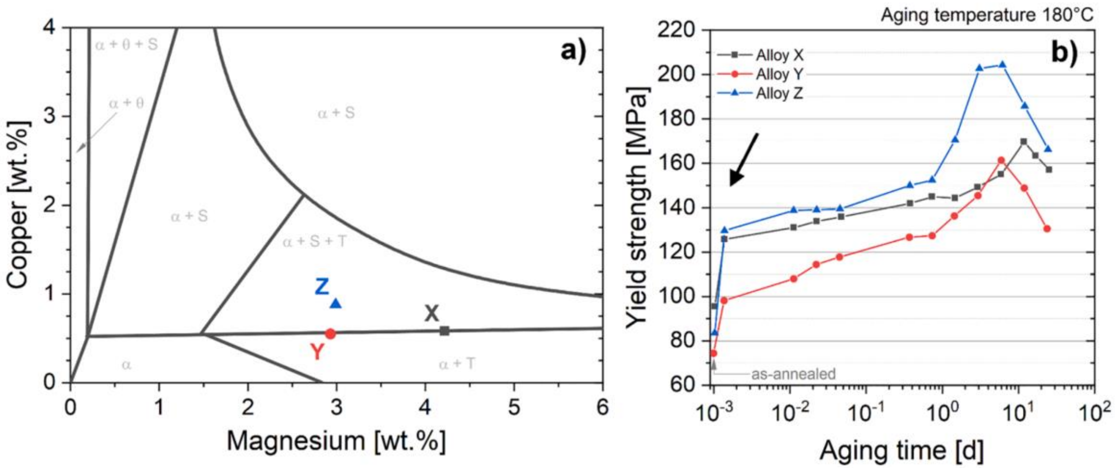

Figure 2-7: Equilibrium phase diagram Al-Cu-Mg at 190°C (a). Evolution of yield strength in dependence of the Cu/Mg ratio during aging at 180 °C (b). Reprinted from [99] after [113]

The addition of copper to 5xxx series alloys has been shown to inhibit magnesium diffusion towards grain boundaries, thereby reducing the formation of Al_3Mg_2 at these boundaries. This is due to the consumption of magnesium into Mg-Cu clusters, which then form the hardening phase. This results in 5/2 crossover alloys exhibiting enhanced resistance to intergranular corrosion (IGC) when subjected to an appropriate solutionizing treatment [114]. While the susceptibility to pitting corrosion remains unaltered when compared to a Cu-free alloy, the addition of Cu has been observed to decrease the resistance to filiform corrosion [115].

2.4.1 AlMgZn(Cu,Ag) 5/7 crossover alloys

These alloys represent the most advanced crossover alloys available today, having been scaled up to industrial size and made commercially available under the brand name Crossalloy.57 by AMAG [116]. Its composition allows for excellent adhesive bonding, resistance spot welding, and self-pierce riveting, outperforming traditional alloys such as 5182 and 6016 in these areas. Additionally, Crossalloy displays remarkable surface properties, maintaining a high-quality appearance after clear anodizing, which is essential for consumer electronics and specialty products. The alloys uniform grain distribution is leading to consistent performance across different thicknesses. Furthermore, industrial prototyping trails of 2 mm material via superplastic forming (SPF) [117] and hot form quenching (HFQ) [118] demonstrate the high forming and hardening potential given by this alloy, even under non ideal laboratory conditions. [119]

By keeping the Zn/Mg ratio < 1, hardening takes place by precipitation of the T-phase instead of the η-phase, which is known as the hardening phase in the 7xxx system [120,121]. The T-phase ($Mg_{32}(Al,Zn)_{49}$) [122] has a bcc-like structure with 162 atoms per unit cell and a wide range of compositions depending on alloy composition and heat treatment [123–125]. Compared to other hardening phases such as Mg_2Si, Mg_2Zn or Al_2Cu, T-phase has the highest negative value of formation enthalpy, which means that the driving force for T-phase precipitation is high [126]. Xue et al. [127] calculated and simulated the structural properties of T-phase. They found that the formation enthalpy is further decreased by increasing the Zn content in the phase. The addition of Cu and Ag are also decreasing the formation energy, leading to an increased number density of GP-zones during the precipitation process and thus higher achievable hardening response. Due to deeper orbital hybridization, this effect is expected to be more pronounced for Ag than for Cu [127]. These simulation results are affirmed by various researches which find an enhanced hardening potential by the addition of Ag [128,129] or Cu [99,129,130] due to the increased number density of Guinier-Preston(GP)-zone formation during early-stage clustering. The addition of Cu also prevents or supresses Lüders elongation and the Portevin-Le-Chatelier (PLC)-effect [131,132]. It should be noted that the kinetics of T-phase precipitation is also influenced by the grain size of the alloy, as precipitation has been found to be accelerated in ultra-fine grained alloys. [133]

The high formation enthalpy and stability of the T-phase allows applications in extreme environments. The T-phase and thus the hardening potential, is retained even when exposed to high doses of irradiation. This irradiation is present in space weather and destroys other hardening phases, making space applications of aluminum alloys currently challenging. [126,134]

The hardening potential of novel A-Mg-Zn-(Cu) crossover alloys is strongly influenced by the heat treatment. Cao et al. [135] investigated the effect of a pre-aging treatment on the ageing behaviour of novel 5/7 Crossover alloys. They found that without pre-aging treatment, the T-phase formed during aging is of a coarse lath like structure. With pre-aging treatment (in this case 80 °C for 12h) the microstructure has a higher density of finer equiaxed T-phase particles. This results in a better age hardening response during subsequent aging at 180 °C with a peak hardness value of about 125 HV, which corresponds to a hardening potential of about 30 HV. Without the pre-aging treatment, the hardening potential is in the range of 15 HV with the peak hardness shifted to longer aging times. The phase formation with and without pre-aging treatment is shown schematically in Figure 2-8. [135]

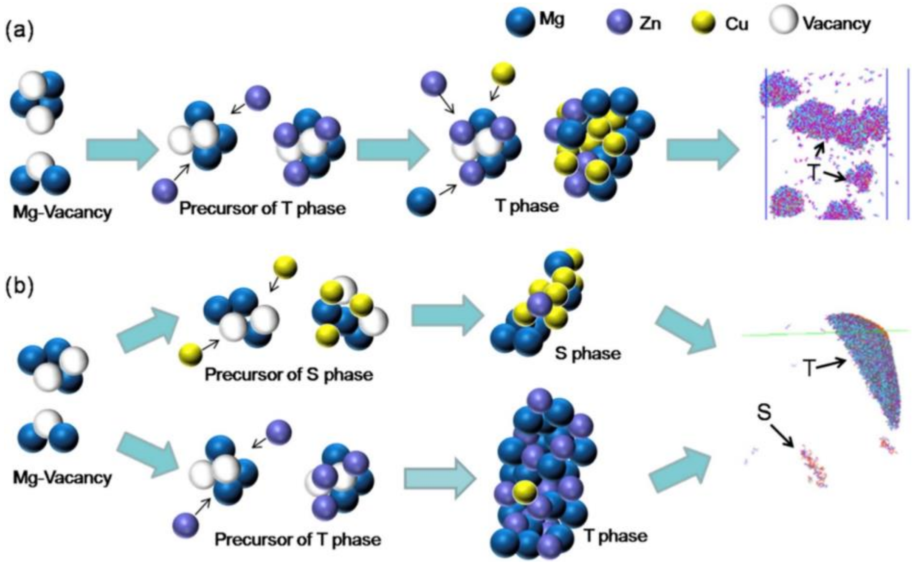

Figure 2-8: Schematic of the precipiation behaviour of 5/7 crossover alloys without (a) and with pre-ageing treatment (b) reprinted from [135]

The exact sequence of precipitation is still under investigation. Several authors propose different paths for T-phase precipitation, which are often closely related to the precipitation of Mg_2Zn-η-phase precipitation. Some proposed precipitation sequences are summarized in Table 2-3.

Table 2-3: Proposed precipitation sequences for T-phase in the Al-Mg-Cu system, reprinted from [98]

SSSS → GP (Guinier-Preston) zone → intermediate η' →equilibrium η → equilibrium T	[136]
SSSS → solute–vacancy-complex → GP zone → intermediate η' or T' →equilibrium η or T	[137]
SSSS → GP zone → intermediate η' or T' →equilibrium η or T	[138]
SSSS → GP zone → intermediate T' →equilibrium T	[139]
SSSS → GPI zone → GPII zone (T'') → intermediate T' →equilibrium T	[140]
SSSS → GPI zone →(transient η' →) intermediate T' →equilibrium T	[99]

Stemper et. al [99] applied a pre-ageing treatment to achieve yield strength values above 400 MPa in an Al-4.5Mg-3.5Zn-0.5Cu alloy. They combined a pre-ageing treatment at 100 °C for 3 h (PA) with a 2 % pre-strain prior to bake-hardening at 180 °C/20 min (TMT2). The tensile testing data in Figure 2-9 show the effect of thermomechanical treatment on the aging response of the alloy, where the blue line (TMT1) represent a hardening process without the application of 2% pre-strain for comparison. In addition, the hardening potential due to the alloying of Zn (Figure 2-9b) and the enhanced precipitation by Cu addition (Figure 2-9c) are visible.

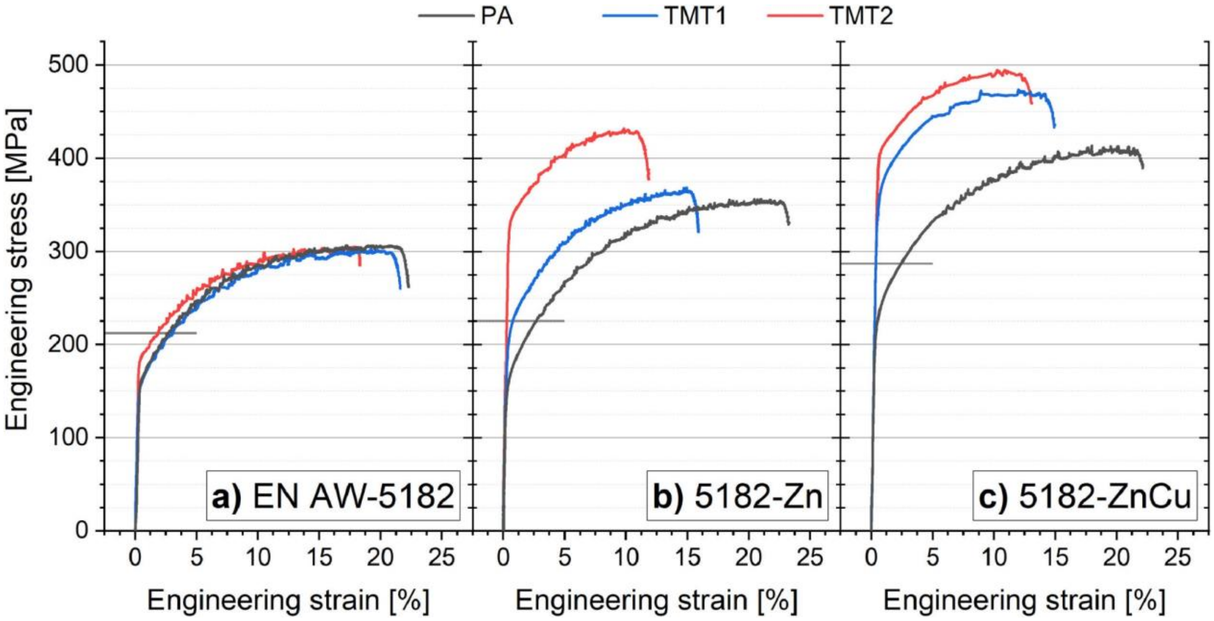

Figure 2-9: Age hardening response with different aging treatments and alloying elements [99]

The increased hardening potential after applying pre-strain prior to bake hardening could be due to an effect known as "strain induced clustering". It describes the increased diffusivity of elements during forming due to strain-induced formation of excess vacancies. Due to this effect, the volume fraction of clusters in 5/7 crossover alloys increases by about 20% at 5% strain compared to the undeformed state. [141]

In addition to the enhanced hardening kinetics allowing highest strengths, good formability and irradiation resistance of these alloys, they also exhibit outstanding corrosion properties. The intergranular corrosion resistance (IGC) is enhanced by the formation of narrow precipitation free zones (PFZ) [142,143]. Furthermore, 5/7 crossover alloys are also reported to have improved stress corrosion cracking (ICC) and exfoliation resistance properties [144,145].

3 REFERENCES

[1] M. Ashby, Materials and the Environment: Eco-Informed Material Choice, Butterworth-Heinemann, 2021.

[2] R. Knoll, Aluminums growing role in montor vehicles, in: F. Jeglitsch (Ed.), 8. Internationale Leichtmetalltagung/Leoben-Wien 1987: 8th [eight] International Light Metals Congress Leoben-Vienna 1987, Aluminum-Verlag, Düsseldorf, 1988, pp. 200–205.

[3] International Aluminum Institute, Global Aluminum Cycle 2020:. alucycle.international-aluminum.org/public-access/public-global-cycle/.

[4] CRU International Ltd, Opportunities for aluminum in a post-Covid economy (2022).

[5] J. Hirsch, Aluminum in Innovative Light-Weight Car Design, Materials Transactions 52 (2011) 818–824.

[6] J. Hirsch, Recent development in aluminum for automotive applications, Transactions of Nonferrous Metals Society of China 24 (2014) 1995–2002.

[7] J. Hirsch, J. Søreide, T. Payer, Environmental Advantages of Sustainable Aluminum Structures, Journal of Light Metal Welding, Vol. 58 (2020).

[8] A. Svendsen, Aluminum Continues Unprecedented Growth in Automotive Applications: DuckerFrontier Report Shows Increased Demand for Body Closures and Electric Vehicles. www.lightmetalage.com/news/industry-news/automotive/aluminum-continues-unprecedented-growth-in-automotive-applications/.

[9] P.K. Mallick, Materials, design and manufacturing for lightweight vehicles, CRC Press, Boca Raton, Fla, Oxford, 2011.

[10] H. Wagnies, J. Hansen, I. Kraft, A. Abraham, L. Ling, T. Castel, Rakoto et al., Aluminum Content in Passenger Vehicles (Europe), 2023.

[11] W. Zhou, C.J. Cleaver, C.F. Dunant, J.M. Allwood, J. Lin, Cost, range anxiety and future electricity supply: A review of how today's technology trends may influence the future uptake of BEVs, Renewable and Sustainable Energy Reviews 173 (2023) 113074.

[12] F. Ostermann, Anwendungstechnologie Aluminum, 2nd ed., Springer, Berlin Heidelberg, 2007.

[13] C. Kammer, Grundlagen und Werkstoffe, 16th ed., Aluminum-Verl., Düsseldorf, 2002.

[14] F. Czerwinski, Current Trends in Automotive Lightweighting Strategies and Materials, Materials (Basel, Switzerland) 14 (2021).

[15] W. Miller, L. Zhuang, J. Bottema, A. Wittebrood, P. de Smet, A. Haszler, A. Vieregge, Recent development in aluminum alloys for the automotive industry, Materials Science and Engineering: A 280 (2000) 37–49.

[16] P. Jagadeesh, M. Puttegowda, Y.G.T. Girijappa, K. Sathyanarayana, S.M. Rangappa, S. Siengchin, S.A. Hassan, Lightweight and sustainable materials for structural applications, in: Lightweight and Sustainable Composite Materials, Elsevier, 2023, pp. 197–217.

[17] T. Dursun, C. Soutis, Recent developments in advanced aircraft aluminum alloys, Materials & Design (1980-2015) 56 (2014) 862–871.

[18] X. Zhang, Y. Chen, J. Hu, Recent advances in the development of aerospace materials, Progress in Aerospace Sciences 97 (2018) 22–34.

[19] S.-S. Li, X. Yue, Q.-Y. Li, H.-L. Peng, B.-X. Dong, T.-S. Liu, H.-Y. Yang et al., Development and applications of aluminum alloys for aerospace industry, Journal of Materials Research and Technology 27 (2023) 944–983.

[20] European Aluminum Association, Materials - Designation system, The Aluminum Automotive Manual (2002).

[21] D. Raabe, D. Ponge, P.J. Uggowitzer, M. Roscher, M. Paolantonio, C. Liu, H. Antrekowitsch et al., Making sustainable aluminum by recycling scrap: The science of “dirty” alloys, Progress in Materials Science 128 (2022) 100947.

[22] P. Krall, I. Weißensteiner, S. Pogatscher, Recycling aluminum alloys for the automotive industry: Breaking the source-sink paradigm, Resources, Conservation and Recycling 202 (2024) 107370.

[23] Z. Que, Y. Wang, C.L. Mendis, C. Fang, J. Xia, X. Zhou, Z. Fan, Understanding Fe-Containing Intermetallic Compounds in Al Alloys: An Overview of Recent Advances from the LiME Research Hub, Metals 12 (2022) 1677.

[24] V.K. Soo, J. Peeters, D. Paraskevas, P. Compston, M. Doolan, J.R. Duflou, Sustainable aluminum recycling of end-of-life products: A joining techniques perspective, Journal of Cleaner Production 178 (2018) 119–132.

[25] A.N. Løvik, R. Modaresi, D.B. Müller, Long-term strategies for increased recycling of automotive aluminum and its alloying elements, Environmental science & technology 48 (2014) 4257–4265.

[26] S. Samberger, P. von Czarnowski, S. Pogatscher, J. Hirsch, New strategies to improve Recycling and reduce CO_2-emission of Aluminum production and processing, Journal of Light Metal Welding 62 (2024) 119–132.

[27] CES EduPack2023, Granta Design Limited, Cambridge, 2023.

[28] A. Poznak, D. Freiberg, P. Sanders, Automotive Wrought Aluminum Alloys, in: Fundamentals of Aluminum Metallurgy, Elsevier, 2018, pp. 333–386.

[29] F.C. Campbell, Elements of Metallurgy and Engineering Alloys, ASM International, 2008.

[30] D.J. Lloyd, S.A. Court, K.M. Gatenby, Lüders elongation in AI-Mg alloy AA5182, Materials Science and Technology 13 (1997) 660–666.

[31] H. Halim, D. Wilkinson, M. Niewczas, The Portevin–Le Chatelier (PLC) effect and shear band formation in an AA5754 alloy, Acta Materialia 55 (2007) 4151–4160.

[32] J.E. Hatch, Aluminum: Properties and physical metallurgy, American Society For Metals, Metals Park, Ohio, 1984.

[33] R.B. Erickson, S.J. Murtha, Highly formable aluminum alloy rolled sheet, 1996. patents.google.com/patent/us5582660a/en.

[34] S.J. Murtha, New 6XXX Aluminum Alloy for Automotive Body Sheet Applications, in: D. Williams, J. Allen, R. Hukkeri (Eds.), Electronic control module network and data link development and validation using hardware in the loop systems, SAE International, Warrendale, PA, 2009.

[35] F.S. Bovard, K.A. Smith, G.J. Courval, D. McCune, T. Jafolla, J.L. Tardiff, S. Ramamurthy et al., Cosmetic Corrosion Test for Aluminum Autobody Panels: Final Report, SAE Int. J. Passeng. Cars – Mech. Syst. 3 (2010) 544–553.

[36] A. Gloria, R. Montanari, M. Richetta, A. Varone, Alloys for Aeronautic Applications: State of the Art and Perspectives, Metals 9 (2019) 662.

[37] A.A. Luo, Recent advances in light metals and manufacturing for automotive applications, CIM Journal 12 (2021) 79–87.

[38] J.C. Williams, E.A. Starke, Progress in structural materials for aerospace systems, The Golden Jubilee Issue—Selected topics in Materials Science and Engineering: Past, Present and Future, edited by S. Suresh, Acta Materialia 51 (2003) 5775–5799.

[39] J.D. Embury, D.J. Lloyd, T.R. Ramachandran, Strengthening Mechanisms in Aluminum Alloys, in: Aluminum Alloys—Contemporary Research and Applications, Elsevier, 1989, pp. 579–601.

[40] M. Jobba, R.K. Mishra, M. Niewczas, Flow stress and work-hardening behaviour of Al–Mg binary alloys, International Journal of Plasticity 65 (2015) 43–60.

[41] H.T. Jeong, W.J. Kim, Strain hardening behavior and strengthening mechanism in Mg-rich Al–Mg binary alloys subjected to aging treatment, Materials Science and Engineering: A 794 (2020) 139862.

[42] Ø. Ryen, B. Holmedal, O. Nijs, E. Nes, E. Sjölander, H.-E. Ekström, Strengthening mechanisms in solid solution aluminum alloys, Metall and Mat Trans A 37 (2006) 1999–2006.

[43] J.E. Dorn, P. Pietrokowsky, T.E. Tietz, The effect of alloying elements on the plastic properties of aluminum alloys, JOM 2 (1950) 933–943.

[44] Ø. Ryen, H.I. Laukli, B. Holmedal, E. Nes, Large strain work hardening of aluminum alloys and the effect of Mg in solid solution, Metall and Mat Trans A 37 (2006) 2007–2013.

[45] E. Nes, Modelling of work hardening and stress saturation in FCC metals, Progress in Materials Science 41 (1997) 129–193.

[46] K. Marthinsen, E. Nes, A general model for metal plasticity, Materials Science and Engineering: A 234-236 (1997) 1095–1098.

[47] U.F. Kocks, H. Mecking, Physics and phenomenology of strain hardening: the FCC case, Progress in Materials Science 48 (2003) 171–273.

[48] T.S. Srivatsan, M.A. Imam, R. Srinivasan (Eds.), Fatigue of Materials III, Springer International Publishing, Cham, 2016.

[49] S.L. George, L. Magidi-Chicuba, Intermetallic and dispersoid structures in AA3104 aluminum alloy during two-step homogenisation, Scientific Reports 14 (2024) 2958.

[50] X. Qian, N. Parson, X.-G. Chen, Effects of Mn addition and related Mn-containing dispersoids on the hot deformation behavior of 6082 aluminum alloys, Materials Science and Engineering: A 764 (2019) 138253.

[51] F. Schmid, D. Gehringer, T. Kremmer, L. Cattini, P.J. Uggowitzer, D. Holec, S. Pogatscher, Stabilization of Al_3Zr allotropes in dilute aluminum alloys via the addition of ternary elements, Materialia 21 (2022) 101321.

[52] C.Q. Chen, J.F. Knott, Effects of dispersoid particles on toughness of high-strength aluminum alloys, Metal Science 15 (1981) 357–364.

[53] Aluminum-Zentrale, Merkblatt W7: Wärmebehandlung von Aluminumlegierungen, 1st ed., 2007.

[54] T. Konno, K. Hiraga, M. Kawasaki, Guinier-preston (GP) zone revisited: atomic level observation by HAADF-TEM technique, Scripta Materialia 44 (2001) 2303–2307.

[55] G. Sha, A. Cerezo, Early-stage precipitation in Al–Zn–Mg–Cu alloy (7050), Acta Materialia 52 (2004) 4503–4516.

[56] C.D. Marioara, W. Lefebvre, S.J. Andersen, J. Friis, Atomic structure of hardening precipitates in an Al–Mg–Zn–Cu alloy determined by HAADF-STEM and first-principles calculations: relation to η-$MgZn_2$, J Mater Sci 48 (2013) 3638–3651.

[57] J.L. González-Velázquez, Mechanical Behavior and Fracture of Engineering Materials, Springer International Publishing AG, Cham, 2020.

[58] E. Orowan, Zur Kristallplastizität. III, Z. Physik 89 (1934) 634–659.

[59] J.B. Ferguson, H. Lopez, D. Kongshaug, B. Schultz, P. Rohatgi, Revised Orowan Strengthening: Effective Interparticle Spacing and Strain Field Considerations, Metall and Mat Trans A 43 (2012) 2110–2115.

[60] W. Bergmann, Werkstofftechnik 1: Struktureller Aufbau von Werkstoffen - Metallische Werkstoffe - Polymerwerkstoffe - Nichtmetallisch-anorganische Werkstoffe, 7th ed., Hanser, Carl, München, 2013.

[61] B. Ilschner, R.F. Singer, R.F. Singer, Werkstoffwissenschaften und Fertigungstechnik: Eigenschaften, Vorgänge, Technologien, 4th ed., Springer, Berlin, 2005.

[62] E. Roos, K. Maile, Werkstoffkunde für Ingenieure: Grundlagen, Anwendung, Prüfung, 2nd ed., Springer, Berlin [u.a.], 2005.

[63] R.B. Figueiredo, M. Kawasaki, T.G. Langdon, Seventy years of Hall-Petch, ninety years of superplasticity and a generalized approach to the effect of grain size on flow stress, Progress in Materials Science 137 (2023) 101131.

[64] W. Xu, L.P. Dávila, Tensile nanomechanics and the Hall-Petch effect in nanocrystalline aluminum, Materials Science and Engineering: A 710 (2018) 413–418.

[65] W.T. Huo, J.T. Shi, L.G. Hou, J.S. Zhang, An improved thermo-mechanical treatment of high-strength Al–Zn–Mg–Cu alloy for effective grain refinement and ductility modification, Journal of Materials Processing Technology 239 (2017) 303–314.

[66] J. Zuo, L. Hou, J. Shi, H. Cui, L. Zhuang, J. Zhang, The mechanism of grain refinement and plasticity enhancement by an improved thermomechanical treatment of 7055 Al alloy, Materials Science and Engineering: A 702 (2017) 42–52.

[67] O. D. Sherby, J. Wadsworth, O.D. Sherby, J. Wadsworth, Superplasticity and superplastic forming processes, Materials Science and Technology 1 (1985) 925–936.

[68] N. Ridley, Metals for superplastic forming, in: Superplastic Forming of Advanced Metallic Materials, Elsevier, 2011, pp. 3–33.

[69] L. Bhatta, A. Pesin, A.P. Zhilyaev, P. Tandon, C. Kong, H. Yu, Recent Development of Superplasticity in Aluminum Alloys: A Review, Metals 10 (2020) 77.

[70] R.B. Figueiredo, T.G. Langdon, Effect of grain size on strength and strain rate sensitivity in metals, J Mater Sci 57 (2022) 5210–5229.

[71] J.W. Edington, K.N. Melton, C.P. Cutler, Superplasticity, Progress in Materials Science 21 (1976) 61–170.

[72] J.S. Vetrano, C.A. Lavender, C.H. Hamilton, M.T. Smith, S.M. Bruemmer, Superplastic behavior in a commercial 5083 aluminum alloy, Scripta Metallurgica et Materialia 30 (1994) 565–570.

[73] I. Vysotskiy, K. Kim, S. Malopheyev, S. Mironov, R. Kaibyshev, Superplastic behavior of friction-stir welded Al–Mg–Sc–Zr alloy in ultrafine-grained condition, Transactions of Nonferrous Metals Society of China 32 (2022) 1083–1095.

[74] R. Verma, A.K. Ghosh, S. Kim, C. Kim, Grain refinement and superplasticity in 5083 Al, Material Science and Engineering A191 (1995) 143–150.

[75] P. Tan, J. Qin, X. Quan, D. Yi, B. Wang, Co-strengthening of the multi-phase precipitation in high-strength and toughness cast Al–Cu–Zn–Mg alloy via changing Zn/Mg ratios, Materials Science and Engineering: A 873 (2023) 145024.

[76] R.-G. Guan, Di Tie, A Review on Grain Refinement of Aluminum Alloys: Progresses, Challenges and Prospects, Acta Metall. Sin. (Engl. Lett.) 30 (2017) 409–432.

[77] Z. Fan, Y. Wang, Y. Zhang, T. Qin, X.R. Zhou, G.E. Thompson, T. Pennycook et al., Grain refining mechanism in the Al/Al–Ti–B system, Acta Materialia 84 (2015) 292–304.

[78] A. Banerji, W. Reif, Grain refinement of aluminum by TiC, MTA 16 (1985) 2065–2068.

[79] A.L. Greer, Grain refinement in rapidly solidified alloys, Materials Science and Engineering: A 133 (1991) 16–21.

[80] D.M. Herlach, K. Eckler, A. Karma, M. Schwarz, Grain refinement through fragmentation of dendrites in undercooled melts, Materials Science and Engineering: A 304-306 (2001) 20–25.

[81] N.S. Barekar, B.K. Dhindaw, Twin-Roll Casting of Aluminum Alloys – An Overview, Materials and Manufacturing Processes 29 (2014) 651–661.

[82] F. Casarotto, A.J. Franke, R. Franke, High-pressure die-cast (HPDC) aluminum alloys for automotive applications, in: Advanced Materials in Automotive Engineering, Elsevier, 2012, pp. 109–149.

[83] L. Katgerman, F. Dom, Rapidly solidified aluminum alloys by meltspinning, Materials Science and Engineering: A 375-377 (2004) 1212–1216.

[84] G. Fick, O. Jepsen, The next generation aluminum minimill. www.sms-group.com/insights/all-insights/the-next-generation-aluminum-minimill, (2024).

[85] K. Stanford, US grants for the metal industry, in: International Aluminum Journal, 5, (2024)16–21.

[86] S.V. Dobatkin, E.N. Bastarache, G. Sakai, T. Fujita, Z. Horita, T.G. Langdon, Grain refinement and superplastic flow in an aluminum alloy processed by high-pressure torsion, Materials Science and Engineering: A 408 (2005) 141–146.

[87] A.P. Zhilyaev, T.G. Langdon, Using high-pressure torsion for metal processing: Fundamentals and applications, Progress in Materials Science 53 (2008) 893–979.

[88] R.S. Mishra, Z.Y. Ma, Friction stir welding and processing, Materials Science and Engineering: R: Reports 50 (2005) 1–78.

[89] C. Xu, M. Furukawa, Z. Horita, T.G. Langdon, Developing High Strain Rate Superplasticity in Aluminum Alloys, MSF 475-479 (2005) 2949–2954.

[90] Y. Saito, N. Tsuji, H. Utsunomiya, T. Sakai, R.G. Hong, Ultra-fine grained bulk aluminum produced by accumulative roll-bonding (ARB) process, Scripta Materialia 39 (1998) 1221–1227.

[91] E. Bagherpour, N. Pardis, M. Reihanian, R. Ebrahimi, An overview on severe plastic deformation: research status, techniques classification, microstructure evolution, and applications, Int J Adv Manuf Technol 100 (2019) 1647–1694.

[92] J. Humphreys, Rohrer, S., Gregory, A. Rollett, Recrystallization: and related annealing phenomena, Elsevier, 2017.

[93] P.R. Rios, G.S. Da Fonseca, Grain Boundary Pinning by Particles, MSF 638-642 (2010) 3907–3912.

[94] P.A. Manohar, M. Ferry, T. Chandra, Five Decades of the Zener Equation, ISIJ International 38 (1998) 913–924.

[95] S. Manna, H. Chan, A. Ghosh, T. Chakrabarti, S.K. Sankaranarayanan, Understanding and control of Zener pinning via phase field and ensemble learning, Computational Materials Science 229 (2023) 112384.

[96] J.A. Wert, N.E. Paton, C.H. Hamilton, M.W. Mahoney, Grain refinement in 7075 aluminum by thermomechanical processing, MTA 12 (1981) 1267–1276.

[97] S. Samberger, I. Weißensteiner, L. Stemper, C. Kainz, P.J. Uggowitzer, S. Pogatscher, Fine-grained aluminum crossover alloy for high-temperature sheet forming, Acta Materialia 253 (2023) 118952.

[98] L. Stemper, M.A. Tunes, R. Tosone, P.J. Uggowitzer, S. Pogatscher, On the potential of aluminum crossover alloys, Progress in Materials Science (2021).

[99] L. Stemper, M.A. Tunes, P. Dumitraschkewitz, F. Mendez-Martin, R. Tosone, D. Marchand, W.A. Curtin et al., Giant hardening response in AlMgZn(Cu) alloys, Acta Materialia 206 (2021) 116617.

[100] B. Trink, I. Weißensteiner, P.J. Uggowitzer, K. Strobel, S. Pogatscher, High Fe content in Al-Mg-Si wrought alloys facilitates excellent mechanical properties, Scripta Materialia 215 (2022) 114701.

[101] B. Trink, I. Weißensteiner, P.J. Uggowitzer, K. Strobel, A. Hofer-Roblyek, S. Pogatscher, Processing and microstructure–property relations of Al-Mg-Si-Fe crossover alloys, Acta Materialia 257 (2023) 119160.

[102] S. Wenner, J. Friis, C.D. Marioara, R. Holmestad, Precipitation in a mixed Al–Cu–Mg/Al–Zn–Mg alloy system, Journal of Alloys and Compounds 684 (2016) 195–200.

[103] W. Mo, C. Tang, P. Deng, Z. Ouyang, B. Luo, Z. Bai, Effect of trace Zn addition on microstructure and corrosion behavior of AA2024 under different aging treatments, Materials Characterization 195 (2023) 112440.

[104] P. Tan, Z. Liu, J. Qin, Q. Wei, B. Wang, D. Yi, Enhanced corrosion performance by controlling grain boundary precipitates in a novel crossover Al-Cu-Zn-Mg alloy by optimizing Zn content, Materials Characterization 208 (2024) 113615.

[105] N.N. Jiao, Y.X. Lai, S.L. Chen, P. Gao, J.H. Chen, Atomic-scale roles of Zn element in age-hardened AlMgSiZn alloys, Journal of Materials Science & Technology 70 (2021) 105–112.

[106] T. Saito, S. Wenner, E. Osmundsen, C.D. Marioara, S.J. Andersen, J. Røyset, W. Lefebvre et al., The effect of Zn on precipitation in Al–Mg–Si alloys, Philosophical Magazine 94 (2014) 2410–2425.

[107] X.P. Ding, H. Cui, J.X. Zhang, H.X. Li, M.X. Guo, Z. Lin, L.Z. Zhuang et al., The effect of Zn on the age hardening response in an Al–Mg–Si alloy, Materials & Design (1980-2015) 65 (2015) 1229–1235.

[108] M.X. Guo, J.Q. Du, C.H. Zheng, J.S. Zhang, L.Z. Zhuang, Influence of Zn contents on precipitation and corrosion of Al-Mg-Si-Cu-Zn alloys for automotive applications, Journal of Alloys and Compounds 778 (2019) 256–270.

[109] R. Marceau, G. Sha, R. Ferragut, A. Dupasquier, S.P. Ringer, Solute clustering in Al–Cu–Mg alloys during the early stages of elevated temperature ageing, Acta Materialia 58 (2010) 4923–4939.

[110] S.P. Ringer, K. Hono, T. Sakurai, I.J. Polmear, Cluster hardening in an aged Al-Cu-Mg alloy, Scripta Materialia 36 (1997) 517–521.

[111] S. Medrano, H. Zhao, F. de Geuser, B. Gault, L.T. Stephenson, A. Deschamps, D. Ponge et al., Cluster hardening in Al-3Mg triggered by small Cu additions, Acta Materialia 161 (2018) 12–20.

[112] P. Ratchev, B. Verlinden, P. de Smet, P. van Houtte, Precipitation hardening of an Al–4.2wt% Mg–0.6wt% Cu alloy, Acta Materialia 46 (1998) 3523–3533.

[113] P. Ratchev, B. Verlinden, P. de Smet, P. van Houtte, Artificial Ageing of Al–Mg–Cu Alloys, Mater. Trans., JIM 40 (1999) 34–41.

[114] A. Alil, M. Popović, T. Radetić, M. Zrilić, E. Romhanji, Influence of annealing temperature on the baking response and corrosion properties of an Al–4.6 wt% Mg alloy with 0.54 wt% Cu, Journal of Alloys and Compounds 625 (2015) 76–84.

[115] O. Engler, C.D. Marioara, T. Hentschel, H.-J. Brinkman, Influence of copper additions on materials properties and corrosion behaviour of Al–Mg alloy sheet, Journal of Alloys and Compounds 710 (2017) 650–662.

[116] AMAG Austria Metall AG, AluReport 02 2022.

[117] A.J. Barnes, Superplastic Forming 40 Years and Still Growing, J. of Materi Eng and Perform 16 (2007) 440–454.

[118] K. Zheng, Y. Dong, J.-H. Zheng, A. Foster, J. Lin, H. Dong, T.A. Dean, The effect of hot form quench (HFQ®) conditions on precipitation and mechanical properties of aluminum alloys, Materials Science and Engineering: A 761 (2019) 138017.

[119] L. Stemper, F. Schmid, R. Tosone, AMAG CrossAlloy®—Lightweighting the Future by Unconstraint Alloy Design: A Case Study, in: S. Wagstaff (Ed.), Light Metals 2024, Springer Nature Switzerland, Cham, 2024, pp. 241–247.

[120] A. Bigot, P. Auger, S. Chambreland, D. Blavette, A. Reeves, Atomic Scale Imaging and Analysis of T' Precipitates in Al-Mg-Zn Alloys, Microsc. Microanal. Microstruct. 8 (1997) 103–113.

[121] Y. Zou, X. Wu, S. Tang, Q. Zhu, H. Song, M. Guo, L. Cao, Investigation on microstructure and mechanical properties of Al-Zn-Mg-Cu alloys with various Zn/Mg ratios, Journal of Materials Science & Technology 85 (2021) 106–117.

[122] G. Bergman, J. Waugh, L. Pauling, The crystal structure of the metallic phase $Mg_{32}(Al,Zn)_{49}$, Acta Cryst. 10 (1957) 254–259.

[123] J.H. Auld, B.E. Williams, X-ray powder data of T phases composed of aluminum and magnesium with silver, copper or zinc, Acta Cryst. 21 (1966) 830–831.

[124] Y. Song, S. Zhan, B. Nie, H. Qi, F. Liu, T. Fan, D. Chen, First-Principles Investigations on Structural Stability, Elastic Properties and Electronic Structure of $Mg_{32}(Al,Zn)_{49}$ Phase and $MgZn_2$ Phase, Crystals 12 (2022) 683.

[125] Y. Zou, X. Wu, S. Tang, Q. Zhu, H. Song, M. Guo, L. Cao, Correlation between bulk and precipitate composition in Al-Zn-Mg-Cu alloys, Philosophical Magazine Letters (2021) 1–12.

[126] P.D. Willenshofer, M.A. Tunes, H.T. Vo, L. Stemper, O. Renk, G. Greaves, P.J. Uggowitzer et al., Radiation-resistant aluminum alloy for space missions in the extreme environment of the solar system, arXiv, 2022.

[127] B. Xue, W. Xiao, X. Li, G. Gao, X. Li, Y. Zhang, L. Wang et al., Comprehensive investigation on the structural, electronic and mechanical properties of T-$Mg_{32}(Al, Zn)_{49}$ phases in Al-Mg-Zn alloys, Journal of Materials Science & Technology 173 (2024) 237–246.

[128] H. Liu, Z. Zhang, Di Zhang, J. Zhang, The effect of Ag on the tensile strength and fracture toughness of novel Al-Mg-Zn alloys, Journal of Alloys and Compounds 908 (2022) 164640.

[129] L. Stemper, M.A. Tunes, P. Oberhauser, P.J. Uggowitzer, S. Pogatscher, Age-hardening response of AlMgZn alloys with Cu and Ag additions, Acta Materialia 195 (2020) 541–554.

[130] Y. Geng, Q. Song, Z. Zhang, Y. Pan, H. Li, Y. Wu, H. Zhu et al., Quantifying early-stage precipitation strengthening of Al–Mg–Zn(-Cu) alloy by using particle size distribution, Materials Science and Engineering: A 839 (2022) 142851.

[131] Y. Geng, Di Zhang, J. Zhang, L. Zhuang, On the suppression of Lüders elongation in high-strength Cu/Zn modified 5xxx series aluminum alloy, Journal of Alloys and Compounds 834 (2020) 155138.

[132] Y. Geng, Di Zhang, J. Zhang, L. Zhuang, Zn/Cu regulated critical strain and serrated flow behavior in Al–Mg alloys, Materials Science and Engineering: A 795 (2020) 139991.

[133] P.D. Willenshofer, M.A. Tunes, C. Kainz, O. Renk, T.M. Kremmer, S. Gneiger, P.J. Uggowitzer et al., Precipitation behaviour in AlMgZnCuAg crossover alloy with coarse and ultrafine grains, Materials Research Letters 11 (2023) 1063–1072.

[134] M.A. Tunes, L. Stemper, G. Greaves, P.J. Uggowitzer, S. Pogatscher, Prototypic Lightweight Alloy Design for Stellar-Radiation Environments, Advanced Science (Weinheim, Baden-Wurttemberg, Germany) 7 (2020) 2002397.

[135] C. Cao, Di Zhang, L. Zhuang, J. Zhang, Improved age-hardening response and altered precipitation behavior of Al-5.2Mg-0.45Cu-2.0Zn (wt%) alloy with pre-aging treatment, Journal of Alloys and Compounds 691 (2017) 40–43.

[136] H. Inoue, T. Sato, Y. Kojima, T. Takahashi, The Temperature Limit for GP Zone Formation in an Al-Zn-Mg Alloy, Metall Trans A 12 (1981) 1429–1434.

[137] N. Afify, A.-F. Gaber, G. Abbady, Fine Scale Precipitates in Al-Mg-Zn Alloys after Various Aging Temperatures, Materials Sciences and Applications 02 (2011) 427–434.

[138] I. Polmear, D. St. John, J. Ne, M. Qian, Light Alloys: From Traditional Alloys to Nanocrystals, 5th ed., Elsevier Science & Technology, Oxford, 2017.

[139] Z.W. Huang, M.H. Loretto, R.E. Smallman, J. White, The mechanism of nucleation and precipitation in 7075-0.7 Li alloy, Acta Metallurgica et Materialia 42 (1994) 549–559.

[140] S. Hou, P. Liu, Di Zhang, J. Zhang, L. Zhuang, Precipitation hardening behavior and microstructure evolution of Al–5.1 Mg–0.15Cu alloy with 3.0Zn (wt%) addition, J Mater Sci 53 (2018) 3846–3861.

[141] P. Aster, P. Dumitraschkewitz, P.J. Uggowitzer, F. Schmid, G. Falkinger, K. Strobel, P. Kutlesa et al., Strain-induced clustering in Al alloys, Materialia 32 (2023) 101964.

[142] Y. Pan, Di Zhang, H. Liu, L. Zhuang, J. Zhang, Precipitation hardening and intergranular corrosion behavior of novel Al–Mg–Zn(-Cu) alloys, Journal of Alloys and Compounds 853 (2021) 157199.

[143] C. Cao, Di Zhang, X. Wang, Q. Ma, L. Zhuang, J. Zhang, Effects of Cu addition on the precipitation hardening response and intergranular corrosion of Al-5.2Mg-2.0Zn (wt.%) alloy, Materials Characterization 122 (2016) 177–182.

[144] M.C. Caroll, M.J. Mills, G.S. Daehn, B.R. Dunbar, Effects of Zn additions on the grain boundary precipitation and corrosion of Al-5083, Scripta Materialia 42 (2000) 335–340.

[145] C. Meng, Di Zhang, L. Zhuang, J. Zhang, Correlations between stress corrosion cracking, grain boundary precipitates and Zn content of Al–Mg–Zn alloys, Journal of Alloys and Compounds 655 (2016) 178–187.

4 UPCOMING CHALLENGES FOR ALUMINUM ALLOYS

The success story of aluminum, with its potential for lightweighting and fuel savings, is overshadowed by the high energy consumption of primary production and the associated high CO_2 emissions. The high energy consumption in primary aluminum production is largely due to the electrolytic reduction process, which is energy-intensive and results in substantial CO_2 emissions, making aluminum production a significant contributor to industrial greenhouse gas emissions. Recycling, on the other hand, requires only a fraction of the energy used in primary production and reduces greenhouse gas emissions. Despite these benefits, the recycling of aluminum presents some challenges due to the high affinity of aluminum for oxygen and its low standard electrode potential.

Therefore, the potentials and limitations of primary aluminum production in terms of energy requirements and CO_2 emissions have been investigated. The study explores the energy requirements and CO_2 emissions associated with primary aluminum production, evaluates current recycling practices, and presents strategies to mitigate impurity content in recycled aluminum. As the removal of elements from aluminum is challenging, the crossover alloying concept is also reviewed as a possibility for a future scrap sink.

The findings offer valuable insights into improving the sustainability of aluminum production and recycling. Understanding these challenges and potential solutions is crucial for developing more sustainable aluminum production practices, which can significantly contribute to global efforts to reduce industrial carbon footprints.

The main part of this review has been published in the Japanese Journal of Light Metal Welding.

New strategies to improve recycling and reduce CO_2-emission of aluminum production and processing[1]

Authors contributions

Sebastian Samberger:	Conceptualization, Methodology, Investigation, Visualization, Writing – Original Draft.
Peter von Czarnowski:	Investigation, Conceptualization Validation, Writing – Review & Editing.
Stefan Pogatscher:	Supervision, Review & Editing.
Jürgen Hirsch:	Project Administration, Conceptualization, Supervision, Writing – Review & Editing.

Abstract

The aluminum industry is witnessing a transformation towards sustainable practices and reduced CO_2 emissions, primarily in the primary sector. However, achieving this goal necessitates a significant shift in the electricity mix, and even then, the emissions remain higher than those in secondary production. To embrace a greener future, there is a growing drive towards secondary aluminum, supported by horizontal and upcycling processes. Despite these promising developments, certain challenges, such as the readiness of some technologies, need to be addressed through focused research in the areas of sorting, pre-casting, and post-casting. The successful recycling of aluminum for applications, such as in electric vehicles (EVs), demands an expansion of the state-of-the-art alloy classification scheme. Embracing this fit-the-need approach is crucial for integrating higher levels of recycled material, promoting circular economy principles, and driving innovation in the use of aluminum alloys across diverse industries.

---

[1] S. Samberger, P. von Czarnowski, S. Pogatscher, J. Hirsch, New strategies to improve Recycling and reduce CO2-emission of Aluminum production and processing, Journal of Light Metal Welding, 2024, Volume 62, Issue 3, Pages 119-132, Released on J-STAGE March 29, 2024, Online ISSN 2186-618X, Print ISSN 0368-5306, https://doi.org/10.11283/jlwa.62.119, https://www.jstage.jst.go.jp/article/jlwa/62/3/62_62.119/_article/-char/en

4.1 Introduction

Aluminum is one of the most important metals due to its specific versatile properties, suitable for various applications. However, the success story of Aluminum is overshadowed by its high energy consumption and critical CO_2 emission rate in its primary production process when the electricity needed for electrolysis comes from non-regenerative sources like coal or gas. This be reduced by implementing recycling strategies, which shifts the balance towards higher sustainability, also since much less (< 10 %) energy is needed to melt Aluminum from scrap. The amount of primary Aluminum produced is illustrated in Figure 4-1 and is expected to reach 70 million tons (Mt) in 2025 after the IAI 2022 reference scenario. About the same slope can be observed for recycled Aluminum about 20 to 30 years shifted. Due to its high metal value, the global recycling efficiency rate (RER) is high (76 %) [1] and the amount of recycled Aluminum available for recycling is estimated to double by 2050. High scrap utilization (pre- and postconsumer scrap) will partially substitute the use of primary produced Aluminum. It is predicted that in the year 2030 the final product shipment increases by 26 %. It is estimated that the global annual scrap usage will increase by about 20 Mt (+54 % according IAI) while the production of prime aluminum continues to rise, exceeding 100 Mt by 2050, as can be seen in Figure 4-1.

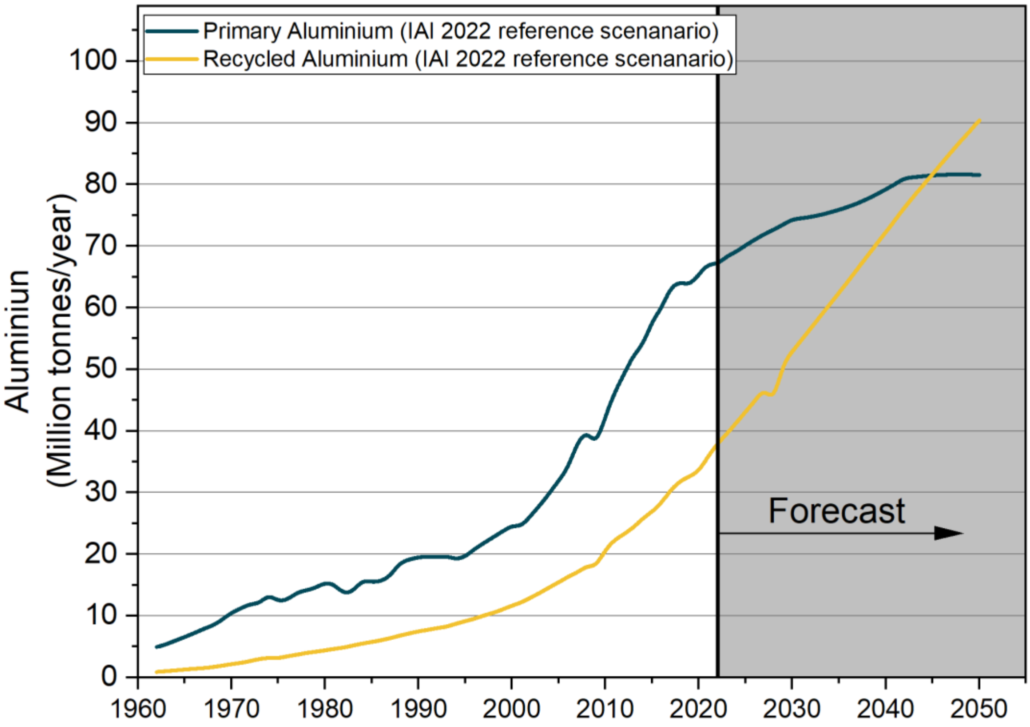

Figure 4-1: World-wide production of primary and recycled Aluminum according to the 2022 IAI estimation [2]

Figure 4-2 illustrates the life-cycle of Aluminum. The increased usage of recycled material creates the problem of high levels of elemental contamination which can be divided into 3 categories:

1. Downcycling: resulting alloys are used in “secondary” (lower quality) alloys than the original one.

2. Horizontal Recycling: (about) the same quality is achieved and can be applied in the same product range: e.g., can recycling or production scrap recycling, so called alloy-to-alloy recycling.
3. Upcycling: Run suitable processes to reduce contaminations and provide alloys of higher quality than the original source.

A “green Aluminum” trend has already triggered new grades for low-carbon Aluminum alloy variants at most of the Aluminum producers, traded also at the London Metal Exchange. The shift from primary synthesis (alumina reduction) to secondary synthesis (scrap melting) requires R&D investigations to better understand how multiple scrap-related undesired elements act on Aluminum alloys and how future alloys can be designed upfront to become scrap-compatible and composition-tolerant.

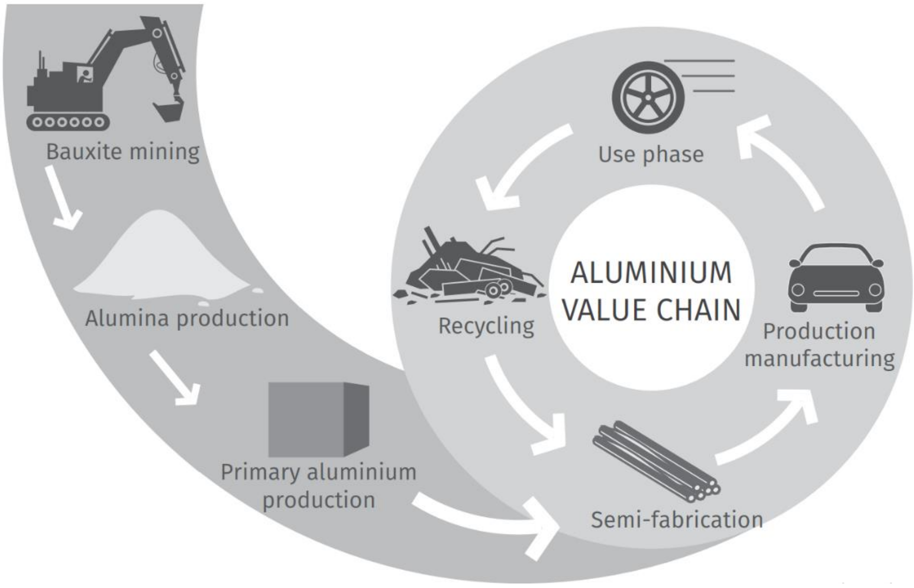

Figure 4-2: Life cycle of Aluminum reprinted from [3]

In the “Progress in Materials Science” overview paper: “Making sustainable Aluminum by recycling scrap: The science of “dirty” alloys” Raabe and colleagues [4] describe and discuss in some detail the main metallurgical effects involved:

1. The influence of scrap-related impurities on the thermodynamics and kinetics of precipitation reactions and their mechanical and electrochemical effects.
2. Impurity effects on precipitation-free zones around grain boundaries.
3. Effects on casting microstructures; and the possibilities presented by adjusting processing parameters and the associated mechanical, functional and chemical properties.

The objective is to foster the design and production of Aluminum alloys with the highest possible scrap fractions, using even low-quality scrap and scrap types which match only a few target alloys when recycled. The global Aluminum flow (2022) with application according to sectors is displayed in Figure 4-3. It shows the scrap origins and states construction and transport sectors as the most important industries for Aluminum usage.

There are several facets of Aluminum when it comes to sustainability. While it helps to save fuel due to its low density, producing it from ores is very energy intensive. Despite major technological evolution, todays primary production consumes 190 MJ/kg ±17 % from mining to ingot (coming from 300 MJ/kg in 1970) [5]. The most energy consuming production step during primary production is smelting. With a maximum of green energy and best practice, it can be as low as 51.12 MJ/kg [6]. The theoretical minimum for Al smelting is 22.43 MJ/kg [7]. The energy needed for smelting is composed of 85 % electrical energy [8]. It is hence of great interest to determine the source of energy from which the electricity is obtained. Data from the International Aluminum Institute (IAI) [9] show, that in 2021, coal was used for 53 % of primary aluminum smelting worldwide, with hydro sources accounting for 31.2 % and natural gas for 9.7 %. Excluding China from the perspective (which is the biggest producer of primary aluminum [10]), hydro sources are the dominant energy source, accounting for 55.8 % of primary Aluminum smelting, with natural gas at 25.3 % and coal at 16.4 % [9]. Besides the energy intensive primary production, Aluminum is highly recyclable, and the energy needed for production of 1 t of Al via recycling is drastically lower. [11]

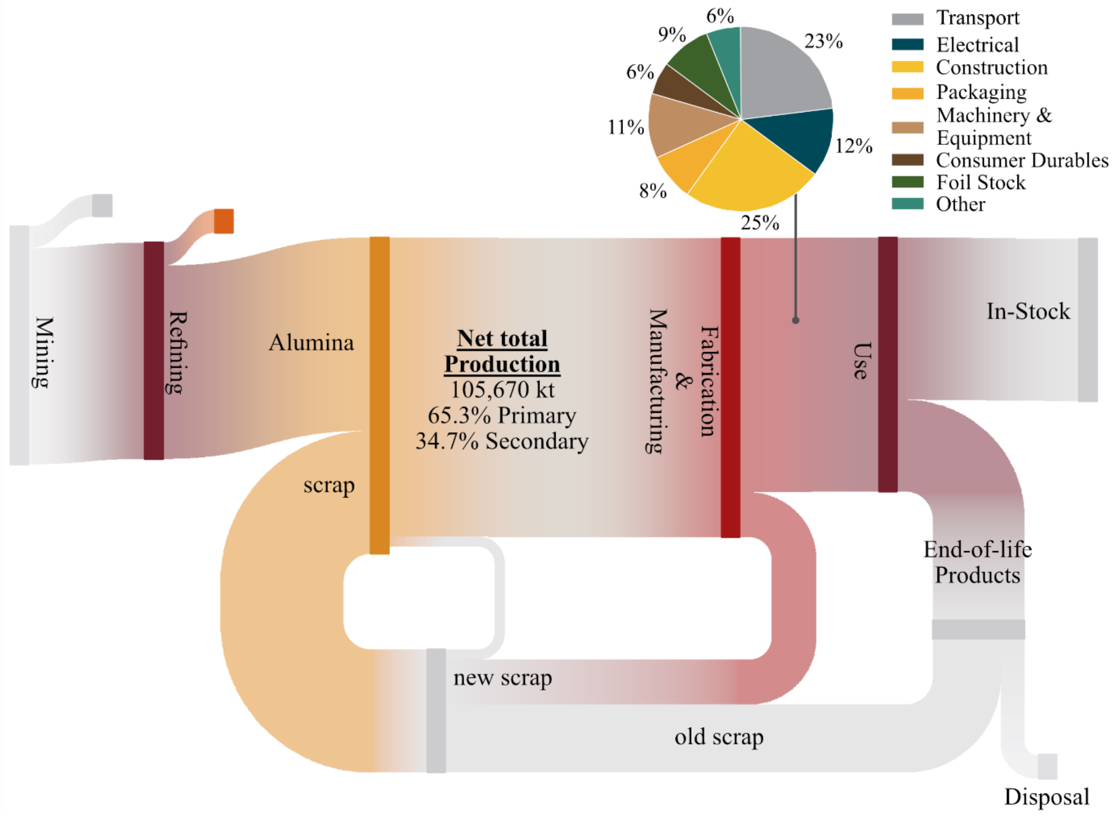

Figure 4-3: Global aluminum flow for the year 2022 (2022 IAI reference scenario) with usage of semi-finished Aluminum products made with data from [2,12]

4.2 Greenhouse Gas Emissions associated with Primary Metal Production

The corresponding life cycle impact assessments (LCIA) [13] helps to identify, quantify and control emissions along manufacturing value chains taking into account material and metallurgical sustainability.

The model is using the tool for reduction and assessment of chemicals and other environmental impacts (TRACI). The global warming potential (GWP), ozone depletion (OD), carcinogenic effects (CE) and acidification potential (AP) shown in Table 4-1 are an excerpt of the whole LCIA.

Table 4-1: LCIA after TRACI method for each production step redone after [13]; values represent the production of 1 Kg Al

Impact category	Bauxite	Alumina	Smelting	Refining
GWP (kg CO_2 eq.)	0.08	1.23	10.91	0.28
OD (kg CFC^{-11} eq.)	3.02·10-12	1.21·10-08	1.48·10-10	4.32·10-12
CE (CTUh)	1.01·10-09	9.23·10-09	1.53·10-08	1.61·10-09
AP (kg SO_2 eq.)	1.3·10-03	9.3·10-03	75·10-03	2.16·10-03

The global warming potential depends to a major extent on the type of energy sources used. The different energy mix scenarios shown in Table 4-2, reveal possible reduction leverages. The German (GER) scenario represents a grid mix consisting of lignite (24 %), hard coal (18 %), nuclear (14 %), wind power (12 %) and natural gas (10 %). The China (CN) scenario is a mix of hard coal (69 %) and hydropower (19 %). In the Norway/Canada (NO) scenario hydropower is used for 96 % of electrical grid mix. [14]

Table 4-2: LCIA for different energy mix, redone after [14]; Values for 1 kg of produced Aluminum.

Impact category	GER	CN	NO
GWP (kg CO_2 eq.)	11.53	18.12	4.07
AP (kg SO_2 eq.)	$2.29 \cdot 10^{-03}$	$7.97 \cdot 10^{-03}$	$2.62 \cdot 10^{-03}$

Depending on the source of energy, the GWP of primary Aluminum production fluctuates strongly. By the usage of 96 % of the power from hydro sources, the GWP potential of electricity is close to zero, while it is accountable for over 12 kg CO_2 emissions in the CN and 8 kg CO_2 emissions in the GER mix scenario. The rest of the GWP is split into transport, processes, thermal energy, and raw materials. [14]

The various forms of greenhouse gases (GHG) are relevant for global warming, including the gas's long atmospheric lifespan. Over the next century, at least 68.4 Mio tones CO_2 equivalent/per year (taking the todays average of 18.3 kg CO_2 eq./kg Al [15] and a production of 68.4 Mt Al (2021) [2]) of GHG (CO, CO_2, SO_2, fluorocarbon and polycyclic aromatic hydrocarbon) are associated with primary Al production. This number is highly volatile depending on the production rate, electricity mix and technological adaptions. As an example: the market for Aluminum is growing so the accompanying environmental problems will grow as well. To reduce greenhouse gas emissions, one needs to develop more environmentally friendly industrial processes with qualified metallurgy, with very high potential leverage to combat global warming. In the production of aluminum, electrolysis accounts for 70 % of the cradle-to-gate GHG [15]. Replacing carbon anode with an inert anode would eradicate, or at least significantly reduce, the direct emissions of greenhouse gases from Aluminum electrolysis. By doing so a reduction of the carbon footprint of aluminum production by up to 10 % is feasible, which is small proportion compared to the savings potential through decarbonization of electricity generation. Because the direct emissions are not the main driver for the high GHG of aluminum production, changes in smelting technology are not enough to decrease the GHG to a satisfactory level. [15,16]

The dataset [17] for alumina refining has been revised retrospectively to reflect a change in modelling assumptions for the process. Under the 1.5 °C Paris agreement scenario of IAI [18], thermal energy emissions from alumina, aluminum casting and mining would need to reduce by 94 % – vs 59 % for “Beyond 2 Degrees’ Scenario (B2DS) – from 2018 levels. Under both the 1.5 °C and B2DS, the carbon intensity from electricity would need to be reduced by at least 98 % compared to 2018. [18]

The International aluminum Institute has launched a new scenario, with supporting data, that is consistent with limiting global warming to 1.5 °C [18]. The data of this scenario is shown for the whole aluminum sector in Figure 4-4 and compared to a business-as-usual case. The data complements the existing work which includes:

- Detailed historical emissions
- A ‘Business as Usual’ scenario (BAU) to 2050
- A ‘Beyond 2 Degrees’ Scenario (B2DS).

Both the 1.5 °C and B2DS are consistent with the Paris agreement. Under the 1.5 °C, carbon intensity of direct emissions would need to reduce by 93 % – vs 58 % for B2DS – compared with 2018 levels. These scenarios will guide the industry’s efforts and need to be considered. [18]

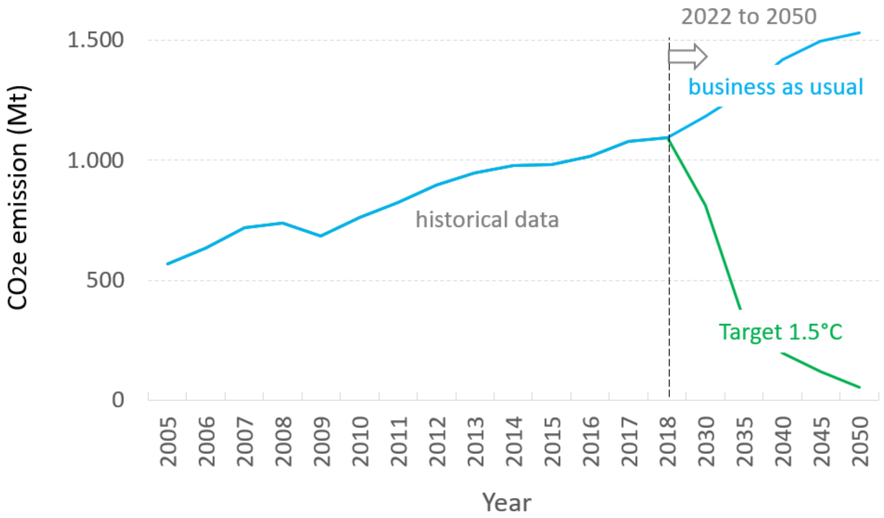

Figure 4-4: Global Carbon emission forecast for the aluminum sector after a business as usual and the target 1.5 °C scenario [18]

When the aluminum industry continues business-as-usual the CO_2 emissions will continue to increase from about 1.000 Mt to 1.500 Mt in 2050, as indicated in Figure 4-4 (blue curve). To meet the targeted reduction of CO_2 and reach the 1.5 °C limit, aggressive actions across the entire value chain are required, i.e., in its upstream and downstream processes. Their contribution to the targeted CO_2 reduction accumulates to roughly 70 % upstream and 30 % downstream (see Table 4-3).

Table 4-3: Contribution of Upstream and Downstream processes to CO_2 emissions

Upstream		Downstream	
Low CO2 Power (nuclear & CCS)	≈55%	Higher design efficiency (process & production)	≈10%
Low CO2 smelters (anodes &CCS)	≈10%	Improved recycling rates and recovery	≈10%
Low CO2 refiners (boilers & calcination)	≈5%	Low CO2 electricity or H_2 across value chain	≈10%

In 2018, the production of 82 million tons of aluminum products relied heavily on primary aluminum, accounting for approximately 80 % of the total global shipment volume. To achieve the CO_2 emission goal associated with the 1.5 °C target, it is necessary to decrease the high proportion of primary aluminum to around 50 %. Therefore, forecasts for scrap utilization given by the IAI reveal an extraordinary increased utilization of accumulated End-of-Life (EoL) scrap. Moreover, the data show that the industry is actively striving to minimize new scrap generation, takes place especially in two critical areas: In the production of aluminum components, specifically customer fabrication scrap, and the aluminum manufacturing process, particularly mill runaround scrap. [2]

To achieve a scrap content of 50 % in aluminum, it is essential to address every step in the value chain. This includes collecting products, sorting components, separating alloys, and implementing processes that can tolerate higher levels of impurities commonly found in scrap materials, and last but not least a compatible alloy concept to promote material efficiency.

Block casting technology concepts like "Nexcast" [19] may support more aggressive targets in the field of improved scrap recovery technologies. It has the capability to make significant contributions to both targets, namely increased scrap utilization and reduced energy consumption in the recovery of both old and new scrap materials. Additionally, the compact MiniMill concept in Flat rolled products (FRP) production promotes environmental consciousness by minimizing resource usage, concrete, buildings, and soil sealing, thus reducing the ecological footprint. The block cast process is not bound to casting limitations from alloy families and lead to improved alloy properties through enhanced cooling conditions. In terms of sustainability an innovative MiniMill can have energy savings of more than 25 % in comparison to an conventional DC Hot rolling mill [20]. Therefore, such technologies could also contribute to a reduction in CO_2 emissions associated with the production of aluminum sheet.

MiniMill concept, one of which is shown in Figure 4-5, brings molten Metal directly to the Hot Coil in a continuous process with significantly less equipment to install, operate, and maintain.

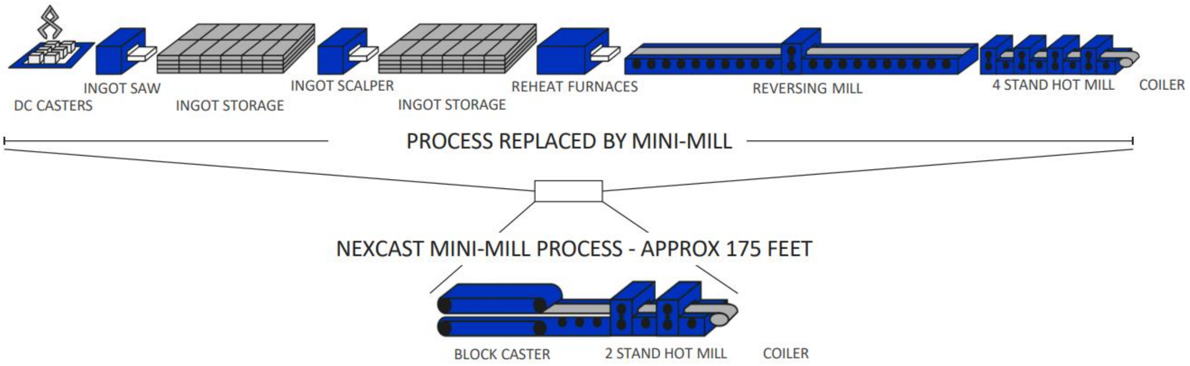

Figure 4-5: Dimension of Nexcast-Technology compared to a conventional sheet-production route leading to a lower carbon Footprint also by more efficient plant design [19]

In the long term, the most significant factor in reducing CO_2 emissions is the substitution of prime materials with scrap. However, at present, the most substantial potential for CO_2 emissions reduction lies within the smelter industry.

Pedneault et. al [15] indicate the role of three key factors in the mitigation of CO_2 emissions associated with primary Al production:

- the change of electricity mix,
- the improvement of energy intensity of the smelting process,
- the progressive deployment of inert anode.

The Figure 4-6 shows a forecast for the Greenhouse gas emission with focus on those key factors. With an primary production forecast for 2050 of 83 Mt Al (IAI 2022 ref. scen.) [2], the CO_2 emissions could sink from about 1518 Mt to 1328 Mt CO_2 eq. per year in a baseline scenario. With an assumption of stagnant primary demand from 2050 to 2100 and best practice, the CO_2 emission could sink further to a value of 996 Mt CO_2 eq. per year. The sooner a change in the electricity mix is achieved, the faster a reduction in GHG is feasible. Looking at a 1.5 °C scenario a reduction of CO_2 emissions down to a value of 498 Mt CO_2 equivalent per year seems feasible. Nevertheless, one has to note that even in a best case scenario the CO_2 emissions from primary production will exceed those of recycling which are as low as 0.6 kg/kg Al [21].

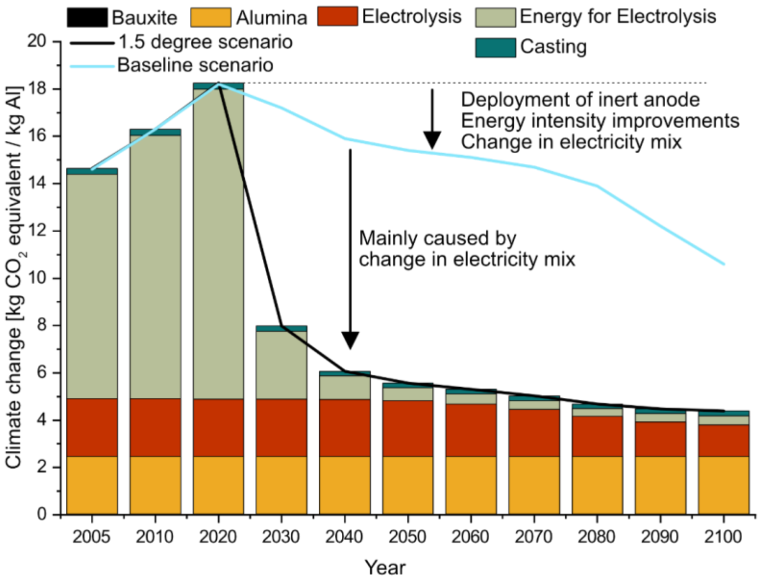

Figure 4-6: GHG emissions and avoidable potential with focus on smelting of primary Aluminum for a 1.5-degree scenario and a baseline scenario. Redone with data from [15]

4.3 Challenges and Opportunities for sustainable Aluminum

3 % of all industrial greenhouse gas emissions and 8 % of the global industrial electricity consumption [15,22] are related to the production of Aluminum. Additionally every year 380 million tons of minerals are mined [23], and several million tons of by-products are exploited. Therefore, Aluminum and its production and processing must become more sustainable.

The influence of metal production and processing on global warming needs to be considered with respect to mitigation strategies and socio-economic factors and the fundamental aspects to make Aluminum more sustainable. These aspects are being addressed by almost all Aluminum producers and their customers worldwide. The huge challenge and its environmental effects, caused by almost 70 million tons of Aluminum being produced every year, make its sustainability an essential research topic from a technological point of view and also from a basic materials research perspective. This is exemplified by the challenges and opportunities of Al for automotive applications in Figure 4-7.

The critical aspects are the energy-intensive upstream and downstream processing. It is a key mechanism to help to reduce CO_2 emissions and finally render metallurgy environmentally safe and fossil-free, addressing – and even exceeding - the current discussion. The potential role of Aluminum alloys is mainly focused on their low specific weight and special properties. Figure 4-7 shows the challenges and requirements for Aluminum alloys in the automotive industry as well as the possible direct and indirect sustainable influence light-weighting inflicts. Utilizing improved aluminum alloys, such as formable non-heat treatable 5xxx series or high-strength 6xxx or 7xxx series alloys, can provide car body structures with a weight advantage of over 30 % and cost savings of up to 7.8 €/kg when employing suitable technologies for high-volume assembly cycles. [24]. Ever since aluminum suffers from a high strength-good formability trade-off, limiting the applications of single alloys. Recent approaches are addressing this issue by combing the beneficial formability of AlMg(Mn) alloys with the high hardening potential of AlZnMg(Cu) alloys in so called crossover alloys. [25]

The traditional automotive structure, known as the Body-in-White (BIW), has been in use for decades as a monocoque body design. However, in the case of Battery electric vehicles (BEV) using skateboard structures, a different approach is taken. The subcomponents in these structures serves multiple purposes, including containing the battery safely, absorbing crash energy and protect the battery from thermal runaways, rightsizing vehicle stiffness, and accommodating the other vehicle components [26]. Moreover, Aluminum components play a critical role in acoustic, electrical, and thermal management [27]. To accommodate various demands in battery structure and cell design, Aluminum alloys from the 1xxx to 8xxx families are employed, encompassing thicknesses ranging from 10 microns to a few millimeters.

Ensuring sustainability in product design necessitates the alignment of material innovations and engineering considerations. This holds true for various components in the battery skateboard design, including lightweight wheels designed for Electric Vehicles (EVs). With the increasing prevalence of EVs, there is a growing importance placed on EV-battery protection and aerodynamic lightweight wheels [26,28]. This highlights the need to prioritize both safety and sustainability in their development. High-strength alloys, e.g., a Cu-free 7020 based alloy or potentially a tailored 5/7 crossover alloy, applied in wheels may offer advantages in terms of radial and corner fatigue strength, as well as crash performance. However, it is important to note that high-strength aluminum alloys are also susceptible to crack propagation. To enable the utilization of high-strength alloys, it is beneficial to engineer a product in the way that it primarily bears tension and compression forces rather than bending forces.

EVs are about 20 % heavier than internal combustion engine (ICE) vehicles due to heavy battery weight, requiring weight reduction to improve the driving range on a single battery charge [29]. Lightweighting goals are similar for both ICE and EV, but the unique product architecture of EVs necessitates a specific lightweighting approach. BEVs have a distinct architecture, primarily focused on securely accommodating large and heavy battery packs at the vehicle's bottom and enabling platform versatility for multiple vehicles. This prompts the automotive industry to reconsider frame design for BEVs. A 10 % weight reduction in an EV typically leads to about a 14 % increase in range [30]. But not only weight reduction, also aerodynamic and rolling resistance play a crucial role in the range of BEVs. With enhanced wheel design and grip, range increases of over 20 % are feasible [30,31].

Besides driving performance and comfort, car buyers and OEMs (original equipment manufacturers) now pick the sustainability trends, demanding more sustainable and transparent production methods and lower CO_2 footprint of the metals delivered. However, proper sustainable approaches for material development and processing must take into consideration both the indirect benefit of advanced materials, e.g. through weight reduction, and the direct ones, by producing the same or better materials as before, but with lower energy consumption and reduced CO_2 emissions. The first step of the approach is referred to as "indirect sustainability” (sustainability gain through material properties) and the second one as “direct sustainability” (sustainability gain through less harmful material production). [32]

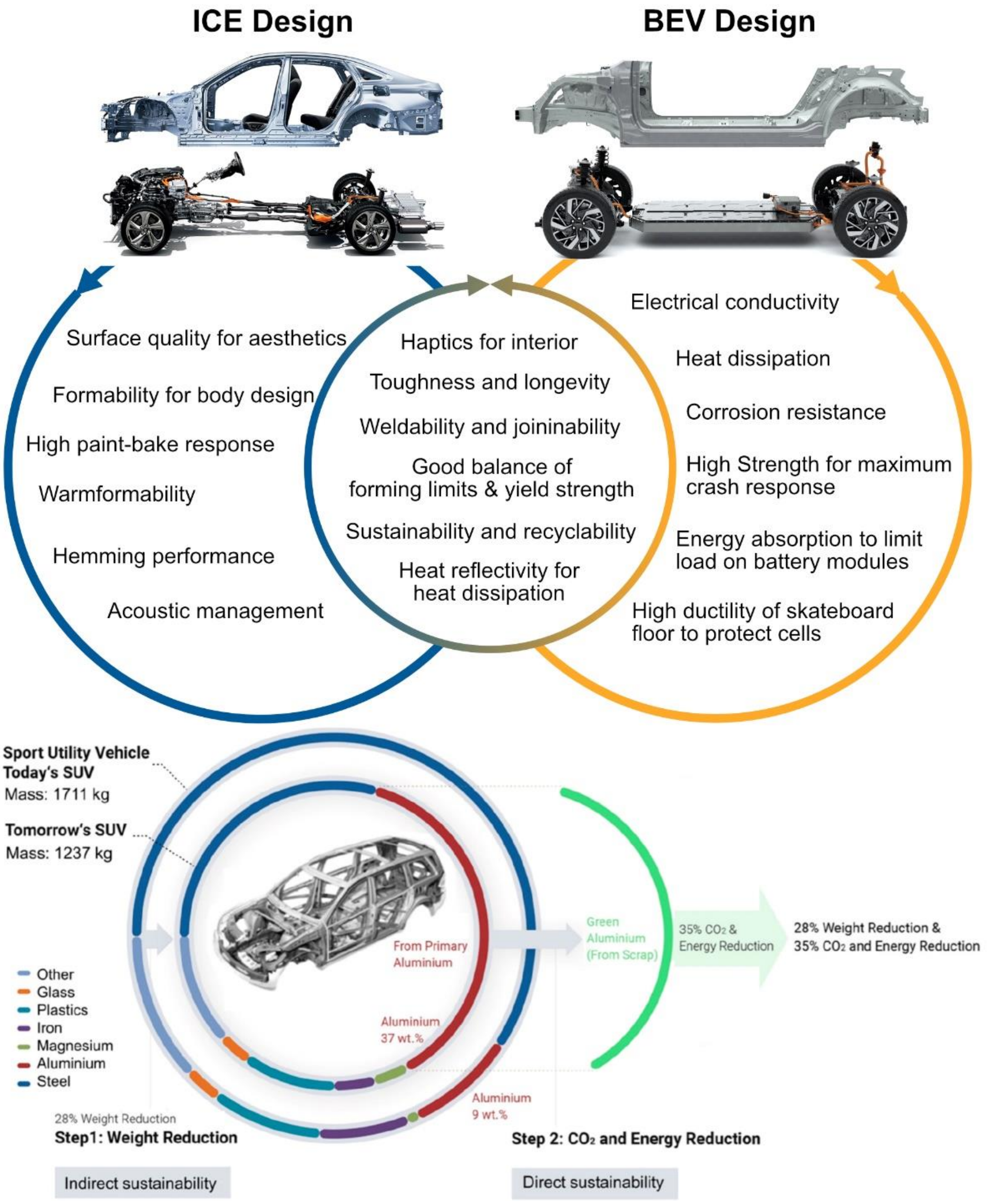

Figure 4-7: Challenges and opportunities for aluminum alloys in the automotive industry redone after [33–35]

4.4 Recycling, Downcycling and Upcycling of Metals and Alloys

The undoubtedly best approach now being established legally in the EU is to reuse and repair parts instead of scrapping according to the European waste Hierarchy Framework Directive [36]. This is, however, not always possible so recycling is the 2nd best option. Recycling drastically increases the availability of metals, as some specific metal supplies become more and more limited on the market, when only taken from mineral resources [32]. Another way now being pursued is to develop re-integrative market elements, also referred to as re-mining, where old, deposited industry waste is retuned back into the recycling stream and used as feedstock. This can be profitable for some materials. In the case of electronic waste a total of 53.6 Mt of E-waste with a value of 57 Billion $ worth in raw materials was generated in 2019 [37]. However, recycling often inherits some loss in material quality called "downcycling".

In conventional recycling, products are re-introduced into the processing cycle from which they once left. In this respect, waste products are reprocessed and transformed into new raw materials, thus acquiring a new use, and re-entering the cycle. However, the material never reaches a full reuse, i.e. the same amount of material. The recycling processes itself can have in part substantial losses and require multiple types of resources to bring the material back into new products. Recycling now is an industry branch of its own, also including aspects of material losses, energy consumption and greenhouse gas emissions.

Since Al_2O_3 has one of the lowest Gibbs energies of all species and Al has a very low electrochemical potential, and a solubility for most elements, as shown in Figure 4-8, it is challenging to remove impurity elements. Since almost all scrap streams inherit impurity elements like Fe, Si, Cu Mn or Mg, feasible and sustainable methods for dealing with scraps streams need to be explored. [38]

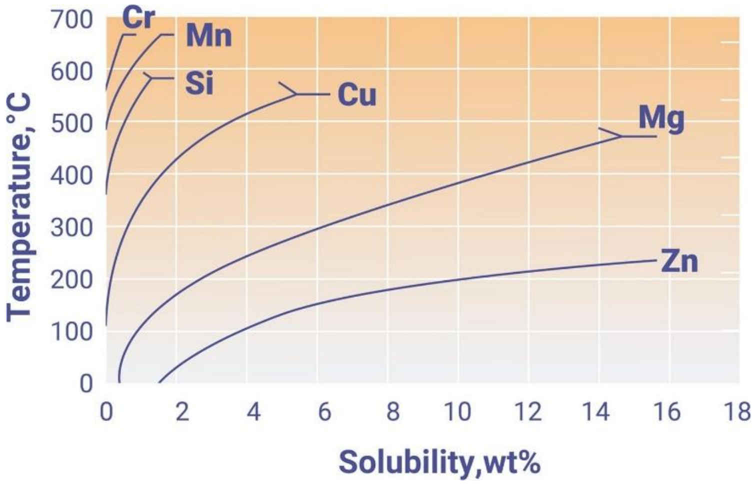

Figure 4-8: Solubility of different elements in aluminum [4]

Due to the fact that the current alloying limits are very tightly bound (especially for wrought Aluminum alloys), innovative concepts are needed to deal with the alloying elements. Taking the automotive sector as the largest source of aluminum scrap and its highest consumer reveals the dramatic need for enhanced alloy processing. While the iron level in applications like cast wheels or nodes used in space frames is limited to a value below 0.2 wt.-%, models predict an iron content from automotive scrap in dependence of the dismantling degree between 0.6 and 0.7 wt.-% [39]. Since the allowed chemical compositions for wrought alloys are narrow most scrap is used for cast alloys. This is leading to a downcycling of alloys, a problem that will become more prominent with the rise of E-mobility. Due to the growing proportion of electric vehicles, the need for ICE-engine blocks is falling and thus also the need for the cast alloy 319

(AlSi6Cu3.5Zn), A380 or A226 (AlSi9Cu3). The alloys represent the largest sink for mixed scrap to date, with a mass of over 80 % of all die-cast alloys [4]. Not only for this a surplus of scrap is predicted in the automotive industry for the years 2025 to 2033, depending on the dismantling degree of car bodies. That event can be further delayed to 2048 by the use of advanced sorting techniques. [39]

First efforts to address this issue are already made by industry. The first step and most effective one is the recycling of aluminum alloys in closed-loop recycling systems for End-of-life (EOL) products. For example: Audi implemented a closed-loop system in 2017 in one of its pressing plants saving 350.000 t CO_2 in three years by using recycled Aluminum [40]. They are also extending this closed loop system currently to other sites [41]. The U.S. car manufactured Ford claims to recycle over 9000 metric tons of using a closed-loop recycling system each month [42]. Nissan even stated a recovery ratio for End-of-life vehicles (ELV) in Japan of 99.4 % in 2021 which contributes to their plan to reduce the amount of virgin material in new vehicles by 30 % [43]. Technology companies like Apple trying to collect the end-of-life products from their costumers and already manufacture the enclosure of all iPads, MacBook's, and apple watches of 100 % recycled Aluminum. They also continue to extend this list [44]. There are also national efforts to combat the scrap surplus. The Japanese NEDO feasibility study program is a framework of industry-academia collaboration addressing the need for new technologies for the fabrication of wrought Aluminum ingots from recycled scrap [45].

With state-of-the-art wrought alloy specifications there are primarily three levers (sorting, pre-casting and post-casting) to deal with the upcoming scrap wave. First, sorting needs to be improved. Simulation of modified dismantling and sorting indicates, that by optimal processing the production of primary Aluminum can be reduced up to 30 % till 2050 [46]. Separation of Iron, Aluminum and plastic scrap can be enhanced through better dismantling, but the separation of different Aluminum alloys with/without coating, surface attachments and especially the separation into wrought and cast alloys is more complicated. Therefore, research is moving towards advanced sorting techniques including Eddy current separators, laser-induced breakdown spectroscopy (LIBS) or X-ray fluorescence (XRF) sorting. By using artificial intelligence during the sorting process, more alloys can be separated at a higher speed. Deep learning algorithms are reported to effectively separate cast and wrought aluminum scrap from RGB and 3D images with an accuracy of up to 98 %. Those algorithms can be integrated into advanced sorting systems in combination with LIBS and XRF. Although these approaches are promising in better dealing with scrap, there are still some issues that need to be addressed in order to employ them completely. Furthermore, for being industrially relevant, the economic gap due to the scrap selling has to be greater than the expenses (OPEX & CAPEX) [45,47,48]

The second possibility to deal with scrap according to state-of-the-art alloy specifications, is pre-casting. There, the impurity content can be reduced by suitable melt treatment. During the melt treatment, the elements Fe, Si and potentially Mn are primarily precipitated as intermetallic compounds (IMC) and removed from the melt. From those elements Fe is considered to be the most precise and detrimental impurity element [49]. Removal of Fe can be, for example, achieved by the addition of a flux containing $Na_2B_4O_7$ and the formation of an Fe_2B-phase. This phase is removable from the melt with sludge formed on the surface leading to a reduction in Fe content from 0.33 to 0.17 wt.-% shown in reference [50]. Also, a removal of elements by fractional crystallization is feasible. In high Mg-melts Fe and Mn show an enhanced primary IMC formation with increasing Mg-content. By cooling the melt close to the liquidus temperature, Fe and Mn intermetallic phases are formed. Those can be removed from the melt by centrifugation, squeezing or filtration [51]. With this procedure a reduction of Fe and Mn down to values of 0.1 and 0.13 wt-% respectively are achieved in an Al-16.8Mg melt at 560 °C [52]. These values can be further decreased to 0.007 wt.-% by increasing the Mg content to 38.5 wt.-% [53,54]. Also, Si is reported to be removable in combination with high Mg-contents through the precipitation of Mg_2Si. According to a patent filed by L. F Mondolfo in 1944 [55] the silicon content can be lowered to values as low as 0.08 wt-.% by the addition of up to 70 wt.-% Mg and cooling of the liquid to a temperature of 500 °C. Another approach for Si removement was conducted by the NEDO study [45]. There, the Si content could be reduced by advanced fractional. They found that the crystallized α-Al fraction was increased by the application of electric stirring. The amount of Silicon could be reduced by pressing and the application of a ceramic filter from 10.7 wt.-% down to 4.9 wt.-% with a Si content of 1.7 wt.-% observed in the primary crystals. These findings suggest the usage of aluminum alloys with high Si content as a component of commercial 6xxx series alloys [45,56]. However, these approaches usually need energy and are therefore cost intensive. Additionally, the issue of the filtered material remains to be solved.

The removal of impurities is also achievable using melting technologies, which work differently from the established methods for scrap melting. Utilizing a solid-state electrolysis process with a liquid salt electrolyte a decrease in impurity concentration from over 10 wt.-% down to 0.1 wt.-% is feasible. Elements like Si, Cu, Fe etc. move to the anode slime, while Al is deposited at the cathode. With this process 99.9 % Al is produced with an estimated energy consumption of 65 MJ/Kg [57]. Here as well the further use of the anode slime needs to be addressed.

Another option for decreasing the impurity level in scrap is dilution with primary Al. This is also referred to as “sweetening” and should not be considered to be a long-term sustainable approach for Aluminum recycling. [4,58]

The shown examples demonstrate that a removal of impurity elements from aluminum is technically possible. Nevertheless, some of the methods mentioned above are not yet industrially mature or are extremely energy-, cost- and time intensive. Therefore, a shift from the stiff state-of-the art alloy classification scheme to a dynamic fit-the-need system is required. By opening the narrow classification scheme for wrought Aluminum alloys, the possibilities for dealing with impurity concentrations might be extended by casting and post-casting technologies, because higher impurity concentrations can be allowed without loss of material quality.

The main objective of those technologies is to maintain the properties of the alloy even with increased impurity levels. There are more than 20 different iron containing intermetallic compounds (IMCs) reported to exist in Al. Common types include β-Al_5FeSi (needle like shape) and α-$Al_{15}(Fe,Mn)_3Si_2$ (compact, Chinese script morphology), Al_3Fe and $Al_6(Mn,Fe)$. The formation and morphology of those phases depend on the elemental composition (Si, Fe, Mn ratios) and cooling rates [59–61]. Iron, in combination with Silicon, often occurs in the form of the brittle the AlFeSi-phase. A needle shaped morphology is extremely harmful for the mechanical performance of the Al alloys, especially for the ductility and fatigue properties. This effect is more pronounced with increasing in size of IMC´s. Hence, research activities try to decrease the size of the intermetallic and modify the morphology towards the less harmful α-AlFeSi modification [61]. During casting, the IMC`s can be broken up and modified by, for example, ultrasonic vibration, electromagnetic stirring or melt shearing [61,62]. The detrimental effect of primary IMC´s is further mitigated by faster cooling, hence smaller precipitates. With direct chill (DC) casting technologies cooling rates are limited around 10 K/s leading to limitation in IMC modification [63–65]. This limitation can be overcome by twin-roll casting technologies where cooling rates of up to 10^3 K/s are reported [66]. Such high cooling rates do not only lead to a finer grain size compared to DC casting but also to finer IMC´s in the finished product [67]. Novel approaches in high-speed vertical twin-roll casting allow conventional 6xxx series alloys with Fe values of up to 1.5 wt.-%. The so produced material exhibits increased strength without major losses in ductility. [45]

Post-casting technologies are focusing on thermal modification and fractioning of IMC´s. By applying a homogenization treatment between 530 °C and 600 °C a transformation from β-phase to α-phase can be achieved. This modification is accompanied by a fragmentation of the phases [68–70]. During hot rolling, the IMC´s can be fragmented as well. This crushing of the particles can happen in different ways depending on the chemical composition and brittleness of the particles and the surrounding matrix material. It was found, that on average the particle size can reduce by more than 10 times during rolling. The reduced particles can further act as nuclei for particle stimulated nucleation [71]. Other post casting techniques for crushing and fragmentation of IMC´s are severe plastic deformation (SPD) techniques like Equal-channel angular pressing (ECAP), High pressure torsion (HPT), Friction stir processing (FSP), Accumulative roll-bonding (ARB) [72], which, however, are not used industrially on a large scale. Also, heavy cold working is leading to fragmentation and alignment of IMC´s in rolling direction. The successful application of post-casting techniques is shown by Trink et. al [73] for an industrial grade 6016 alloy with a high content of impurity elements (1.9 wt.-% Si, 1.4 wt.-% Fe, 1.1 wt.-% Mn). By the application of an optimized homogenization and thermomechanical treatment, the tensile strength could be improved by about 80 MPa without major losses in elongation [73].

Opening alloy classification scheme

Opening the alloy classification scheme is beneficial in many ways. By the introduction of uni-alloys and "crossover alloys" a combination of various desired properties is feasible by simultaneous tolerance of more recycled content in the alloy. By the introduction of 5/7 crossover alloys (combination of 5xxx series alloys and 7xxx series alloys) the longstanding trade-off between the good formability of 5xxx series alloys and the high strength of the 7xxx series alloys could be overcome [74]. This novel research area of crossover alloys already revealed that this alloy class exhibits outstanding hardening and forming potential [75] and good corrosion resistance [76–79]. 5/7 crossover alloys are also reported to be suitable for conventional welding operations [80] and superplastic forming operations [81]. Also space applications seem feasible [82].

The change of the state-of-the-art stiff classification scheme to a fit-the-need dynamic model is gradually making its entrance into the industry. For example, Ford already took actions to support the Ford F150 with a new family of aluminum sheet specifications focused on recyclability. They analysed scrap streams and defined separation ways to produce high and low scrap tolerance alloys [83,84]. The Austrian Aluminum producer AMAG took further action towards the introduction of novel crossover alloys. Recently they reported two crossover alloys named AMAG CrossAlloy.57 [25] and AMAG CrossAlloy.68 [85]. The alloys need to prove themselves on an industrial scale.

Opening the alloy classification scheme also inherits the potential to improve almost any commercial alloy. NanoAl, a company based in Boston [86], has developed a material and processing concept that integrates minor to moderate amounts of alloying elements capable of forming thermally stable nano-scale precipitates that are coherent with the Aluminum matrix [87,88]. Those precipitates allow microstructural designing to further enhance the properties of alloys. An achievable microstructure is shown Figure 4-9 using an 8000 series alloy as an example. By introducing nano-precipitates, a grain size of <1 µm is attainable. Based on this innovative approach, processes with high solidification rates successfully retain ultrafine nano-precipitates. This retention leads to enhanced mechanical properties, electrical and thermal conductivity and thermal stability, expanding the range of alloys suitable for various EV components. Furthermore, this innovative approach contributes to the broader goals of industrial electrification.

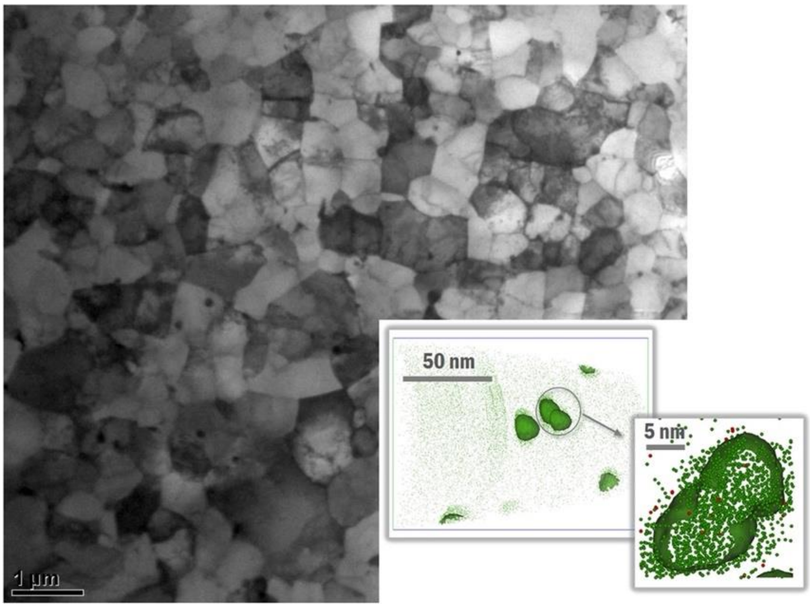

Figure 4-9: Microstructure of an 8000-series Aluminum alloy, processed with NanoAL alloying concept, having a refined grain structure (< 1 um), and a dispersion of thermally stable nano-precipitates (inset atom-probe tomographic pictures) [86]

4.5 Conclusion

The aluminum industry is witnessing a transformation towards sustainable practices and reduced CO_2 emissions, primarily in the primary sector. However, achieving this goal necessitates a significant shift in the electricity mix, and even then, the emissions remain higher than those in secondary production. To embrace a greener future, there is a growing drive towards secondary aluminum, supported by horizontal and upcycling processes. Despite these promising developments, certain challenges, such as the readiness of some technologies, need to be addressed through focused research in the areas of sorting, pre-casting, and post-casting. The successful recycling of aluminum for applications e.g. in EVs demands an expanded of the state-of-the-art alloy classification scheme.

The discussed alloys show considerable benefits from high solidification rates, achievable through innovative processes like Nexcast or Twin roll casting. Especially when dealing with products containing high alloying content, these high solidification rates become crucial to ensure even distribution of alloying elements and other constituents in the cast strip, thus enabling optimal further processing with reduced segregations. Emphasizing these essential steps will significantly advance research in the field, enabling the industry to handle the growing wave of scrap more effectively. To achieve the ambitious goals for CO_2 emissions, a comprehensive approach is required, encompassing efforts at every stage of the aluminum production process, supported by the expansion of the alloy classification scheme and the introduction of Uni-alloys and crossover alloys. By adopting these measures, a surplus of scrap can be avoided, and sustainability objectives in the aluminum industry can be realized.

4.6 References

[1] The Aluminium Institute, Aluminium Recycling FactSheet.

[2] International Aluminium Institute, Global Aluminium Cycle 2020:. alucycle.international-aluminium.org/public-access/public-global-cycle/.

[3] European Aluminium, Environmental Profile Report (2018).

[4] D. Raabe, D. Ponge, P.J. Uggowitzer, M. Roscher, M. Paolantonio, C. Liu, H. Antrekowitsch et al., Making sustainable aluminum by recycling scrap: The science of “dirty” alloys, Progress in Materials Science 128 (2022) 100947.

[5] M. Ashby, Materials and the Environment: Eco-Informed Material Choice, Butterworth-Heinemann, 2021.

[6] Hydro, Annual report 2022. www.hydro.com/globalassets/06-investors/reports-and-presentations/annual-report/jenincharge22/annual-report-2022eng2.pdf.

[7] M. Obaidat, A. Al-Ghandoor, P. Phelan, R. Villalobos, A. Alkhalidi, Energy and Exergy Analyses of Different Aluminum Reduction Technologies, Sustainability 10 (2018) 1216.

[8] B.T. Cremonini, B. Cushman-Roisin, Data, Statistics, and Useful Numbers for Environmental Sustainability: Bringing the Numbers to Life, Elsevier, 2021.

[9] International Aluminium Institute, Primary Aluminium Smelting Power Consumption. international-aluminium.org/statistics/primary-aluminium-smelting-power-consumption/.

[10] Bundesanstalt für Geowissenschaften und Rohstoffe, Aluminium: Sustainability Information. www.bgr.bund.de/EN/Gemeinsames/Produkte/Downloads/Informationen_Nachhaltigkeit/aluminium_en.pdf?__blob=publicationFile&v=4#:~:text=An%20average%20of%20approx.,in%20productive%20use%20%5B9%5D (2024).

[11] J. Hirsch, J. Søreide, T. Payer, Environmental Advantages of Sustainable Aluminum structures, Japan Light Metal Welding Association & Japan Aluminium Association Vol. 58 (2020) 125–130.

[12] CRU International Ltd, Opportunities for aluminium in a post-Covid economy (2022).

[13] S.H. Farjana, N. Huda, M.A.P. Mahmud, Impacts of aluminum production: A cradle to gate investigation using life-cycle assessment, The Science of the total environment 663 (2019) 958–970.

[14] A. Luthin, J.G. Backes, M. Traverso, A framework to identify environmental-economic trade-offs by combining life cycle assessment and life cycle costing – A case study of aluminium production, Journal of Cleaner Production 321 (2021) 128902.

[15] J. Pedneault, G. Majeau-Bettez, V. Krey, M. Margni, What future for primary aluminium production in a decarbonizing economy?, Global Environmental Change 69 (2021) 102316.

[16] P. Sai Krishna, Y. Andrey S., P. Peter V., Progress of Inert Anodes in Aluminium Industry: Review, J. Sib. Fed. Univ. Chem. 11 (2018) 18–30.

[17] International Aluminium Institute, Greenhouse Gas Emissions Intensity - Primary Aluminium. international-aluminium.org/statistics/greenhouse-gas-emissions-intensity-primary-aluminium/.

[18] International Aluminium Institute, 1.5 Degree Scenario: A Model to drive emissions reduction. international-aluminium.org/resource/1-5-degrees-scenario-a-model-to-drive-emissions-reduction/.

[19] G. Fick, O. Jepsen, The next generation aluminum minimill. www.sms-group.com/insights/all-insights/the-next-generation-aluminum-minimill.

[20] William T. Choate, BCS Incorporated John A. S. Green, Ph.D., ITP Aluminum: Energy Requirements for the U.S. Aluminum Industry (2007).

[21] S.K. Das, J.A. Green, J.G. Kaufman, D. Emadi, M. Mahfoud, Aluminum recycling - An integrated, industrywide approach, JOM 62 (2010).

[22] D. Hodgson, T. Vass, Aluminium. www.iea.org/reports/aluminium.

[23] U.S. Geological Survey, Bauxite and alumina, Mineral Commodity Summaries (2023).

[24] J. Hirsch, Aluminium in Innovative Light-Weight Car Design, Materials Transactions 52 (2011) 818–824.

[25] AMAG Austria Metall AG, AluReport 02 2022.

[26] High Power Media Ltd, Skateboard platforms. www.emobility-engineering.com/ev-skateboard-platforms/.

[27] D. Sayan, The role of aluminium in the electric vehicle (EV) Industry, EVreporter Magazine (2023) 34–35.

[28] D. Wang, S. Zhang, S. Zhang, Y. Wang, Analysis and multi-objective optimization design of wheel based on aerodynamic performance, Advances in Mechanical Engineering 11 (2019) 168781401984973.

[29] Y. Liu, H. Chen, J. Gao, Y. Li, K. Dave, J. Chen, M. Federici et al., Comparative analysis of non-exhaust airborne particles from electric and internal combustion engine vehicles, Journal of hazardous materials 420 (2021) 126626.

[30] F. Czerwinski, Current Trends in Automotive Lightweighting Strategies and Materials, Materials (Basel, Switzerland) 14 (2021).

[31] S. Edelstein, Tires and wheels can have a huge effect on electric car range. www.greencarreports.com/news/1128745_tires-and-wheels-can-have-a-huge-effect-on-electric-car-range.

[32] M. Gislev, M. Grohol, F. Mathieux, F. Ardente, S. Bobba, P. Nuss, G.A. Blengini et al., Report on critical raw materials and the circular economy, Publications Office of the European Union, Luxembourg, 2018.

[33] D. Raabe, The Materials Science behind Sustainable Metals and Alloys, Chemical reviews 123 (2023) 2436–2608.

[34] Toyota, Toyota Rolls Out Completely Redesigned Crown: First-generation connected car that continues to innovate and push limits. global.toyota/en/newsroom/toyota/23102775.html.

[35] B. Halvorson, Electric car platform for Hyundai, Kia, Genesis: Bi-directional charging, robotaxi ready. www.greencarreports.com/news/1130487_ev-platform-hyundai-kia-genesis-bi-directional-charging-robotaxi-ready.

[36] European Parliament and Council of the european union, Waste Framework Directive. environment.ec.europa.eu/topics/waste-and-recycling/waste-framework-directive_en.

[37] V. Forti, C.P. Baldé, R. Kuehr, G. Bel, The Global E-waste Monitor 2020. ewastemonitor.info/wp-content/uploads/2020/11/GEM_2020_def_july1_low.pdf.

[38] K. Nakajima, O. Takeda, T. Miki, K. Matsubae, S. Nakamura, T. Nagasaka, Thermodynamic analysis of contamination by alloying elements in aluminum recycling, Environmental science & technology 44 (2010) 5594–5600.

[39] A.N. Løvik, R. Modaresi, D.B. Müller, Long-term strategies for increased recycling of automotive aluminum and its alloying elements, Environmental science & technology 48 (2014) 4257–4265.

[40] Volkswagen Group, Aluminum Closed Loop in the press shop: More than 350,000 metric tons CO2 emissions saved since introduction. www.volkswagenag.com/de/news/2020/06/Aluminium_Closed_Loop.html#.

[41] Audi, Audi Hungaria to introduce Aluminum Closed Loop. www.audi-mediacenter.com/en/press-releases/audi-hungaria-to-introduce-aluminum-closed-loop-13251.

[42] Ford, Integrated Sustainability and Financial Report. corporate.ford.com/content/dam/corporate/us/en-us/documents/reports/2023-integrated-sustainability-and-financial-report.pdf.

[43] Nissan, Sustainability report 2022. www.nissan-global.com/EN/SUSTAINABILITY/LIBRARY/SR/2022/ASSETS/PDF/SR22_E_All.pdf.

[44] Apple, Environmental Progress Report. www.apple.com/environment/pdf/Apple_Environmental_Progress_Report_2022.pdf.

[45] S. Kumai, Role and Potential of Aluminium and Its Alloys for a Zero-Carbon Society, Mater. Trans. 64 (2023) 319–333.

[46] J. Pedneault, G. Majeau-Bettez, M. Margni, How much sorting is required for a circular low carbon aluminum economy?, J of Industrial Ecology (2023).

[47] D. Díaz-Romero, W. Sterkens, S. van den Eynde, T. Goedemé, W. Dewulf, J. Peeters, Deep learning computer vision for the separation of Cast- and Wrought-Aluminum scrap, Resources, Conservation and Recycling 172 (2021) 105685.

[48] S.K. Hussain Shah, J. Iqbal, P. Ahmad, M.U. Khandaker, S. Haq, M. Naeem, Laser induced breakdown spectroscopy methods and applications: A comprehensive review, Radiation Physics and Chemistry 170 (2020) 108666.

[49] M.A. Dewan, M.A. Rhamdhani, J.B. Mitchell, C.J. Davidson, G.A. Brooks, M. Easton, J.F. Grandfield, Control and Removal of Impurities from Al Melts: A Review, MSF 693 (2011) 149–160.

[50] J.W. Gao, D. Shu, J. Wang, B.D. Sun, Effects of Na2B4O7 on the elimination of iron from aluminum melt, Scripta Materialia 57 (2007) 197–200.

[51] G. Gaustad, E. Olivetti, R. Kirchain, Improving aluminum recycling: A survey of sorting and impurity removal technologies, Resources, Conservation and Recycling 58 (2012) 79–87.

[52] Simensen, J., Christian, S. LeBrun, Removal of Iron and Manganese in aluminium alloys by adding magnesium and subsequently centrifuging, Light Metals (2009) 777–781.

[53] K. Kato, Y. Hanai, H. Ono, K. Yamaguchi, K. Komori, Thermodynamics of Formation of Al_6Mn Inter-Metallic Compound for Mn Removal from Molten Al–Mg Alloy, Mater. Trans. 64 (2023) 392–397.

[54] Y. Shinomiya, J. Yamamoto, K. Kato, H. Ono, K. Yamaguchi, K. Komori, Thermodynamics of Formation of Al_3Fe Inter-Metallic Compound for Fe Removal from Molten Al–Mg Alloy, Mater. Trans. 64 (2023) 385–391.

[55] L.F. Mondolfo, Removal of silicone from Aluminium and Aluminium alloys(2,362,147).

[56] Y. Murakami, N. Omura, Reduction of Impurity Elements by Applying Electromagnetic Stirring in Fractional Crystallization, in: L. Perander (Ed.), Light Metals 2021, Springer International Publishing, Cham, 2021, pp. 818–821.

[57] X. Lu, Z. Zhang, T. Hiraki, O. Takeda, H. Zhu, K. Matsubae, T. Nagasaka, A solid-state electrolysis process for upcycling aluminium scrap, Nature 606 (2022) 511–515.

[58] D. Paraskevas, K. Kellens, W. Dewulf, J.R. Duflou, Environmental modelling of aluminium recycling: a Life Cycle Assessment tool for sustainable metal management, Journal of Cleaner Production 105 (2015) 357–370.

[59] J. Grasserbauer, I. Weißensteiner, G. Falkinger, T.M. Kremmer, P.J. Uggowitzer, S. Pogatscher, Influence of Fe and Mn on the Microstructure Formation in 5xxx Alloys-Part I: Evolution of Primary and Secondary Phases, Materials (Basel, Switzerland) 14 (2021).

[60] A. Verma, S. Kumar, P.S. Grant, K. O'Reilly, Influence of cooling rate on the Fe intermetallic formation in an AA6063 Al alloy, Journal of Alloys and Compounds 555 (2013) 274–282.

[61] Z. Que, Y. Wang, C.L. Mendis, C. Fang, J. Xia, X. Zhou, Z. Fan, Understanding Fe-Containing Intermetallic Compounds in Al Alloys: An Overview of Recent Advances from the LiME Research Hub, Metals 12 (2022) 1677.

[62] M. Alizadeh, M. Karamouz, Effect of periodic melt shearing process and cooling rate on structure and hardness of Al–0.7Fe aluminum alloy, Materials & Design 55 (2014) 204–211.

[63] D. Wang, H. Zhang, H. Nagaumi, X. Li, J. Cui, Microstructural Refinement and α-Dispersoid Evolution in Direct-Chill Cast Al–Mg–Si–Fe Alloy, Adv. Eng. Mater. 22 (2020) 2000517.

[64] M.H. Ghoncheh, S.G. Shabestari, M.H. Abbasi, Effect of cooling rate on the microstructure and solidification characteristics of Al2024 alloy using computer-aided thermal analysis technique, J Therm Anal Calorim 117 (2014) 1253–1261.

[65] S. Yin, A. Howells, D.J. Lloyd, M. Gallerneault, V. Fallah, Thin Strip vs Direct Chill Casting: The Effects of Casting Cooling Rate on the As-cast Microstructure of AA6005 Al–Si–Mg Alloy, Metall Mater Trans A 53 (2022) 1928–1933.

[66] R. Song, Y. Harada, S. Kumai, Influence of Cooling Rate on Primary Particle and Solute Distribution in High-Speed Twin-Roll Cast Al-Mn Based Alloy Strip, Mater. Trans. 59 (2018) 110–116.

[67] X. Liu, C. Wang, S.-Y. Zhang, J.-W. Song, X.-L. Zhou, M. Zha, H.-Y. Wang, Fe-bearing phase formation, microstructure evolution, and mechanical properties of Al-Mg-Si-Fe alloy fabricated by the twin-roll casting process, Journal of Alloys and Compounds 886 (2021) 161202.

[68] N. Kuijpers, W.H. Kool, P. Koenis, K.E. Nilsen, I. Todd, S. van der Zwaag, Assessment of different techniques for quantification of α-Al(FeMn)Si and β-AlFeSi intermetallics in AA 6xxx alloys, Materials Characterization 49 (2002) 409–420.

[69] N. Kuijpers, F.J. Vermolen, C. Vuik, P. Koenis, K.E. Nilsen, S. van der Zwaag, The dependence of the β-AlFeSi to α-Al(FeMn)Si transformation kinetics in Al–Mg–Si alloys on the alloying elements, Materials Science and Engineering: A 394 (2005) 9–19.

[70] S. Zajac, B. Hutchinson, A. Johansson, L.-O. Gullman, Microstructure control and extrudability of Al–Mg–Si alloys microalloyed with manganese, Materials Science and Technology (1994) 323–333.

[71] E. Aryshenskii, J. Hirsch, S. Konovalov, Investigation of the Intermetallic Compounds Fragmentation Impact on the Formation of Texture during the as Cast Structure Thermomechanical Treatment of Aluminum Alloys, Metals 11 (2021) 507.

[72] E. Bagherpour, N. Pardis, M. Reihanian, R. Ebrahimi, An overview on severe plastic deformation: research status, techniques classification, microstructure evolution, and applications, Int J Adv Manuf Technol 100 (2019) 1647–1694.

[73] B. Trink, I. Weißensteiner, P.J. Uggowitzer, K. Strobel, S. Pogatscher, High Fe content in Al-Mg-Si wrought alloys facilitates excellent mechanical properties, Scripta Materialia 215 (2022) 114701.

[74] L. Stemper, M.A. Tunes, R. Tosone, P.J. Uggowitzer, S. Pogatscher, On the potential of aluminum crossover alloys, Progress in Materials Science (2021).

[75] L. Stemper, M.A. Tunes, P. Dumitraschkewitz, F. Mendez-Martin, R. Tosone, D. Marchand, W.A. Curtin et al., Giant hardening response in AlMgZn(Cu) alloys, Acta Materialia 206 (2021) 116617.

[76] Y. Pan, Di Zhang, H. Liu, L. Zhuang, J. Zhang, Precipitation hardening and intergranular corrosion behavior of novel Al–Mg–Zn(-Cu) alloys, Journal of Alloys and Compounds 853 (2021) 157199.

[77] C. Cao, Di Zhang, X. Wang, Q. Ma, L. Zhuang, J. Zhang, Effects of Cu addition on the precipitation hardening response and intergranular corrosion of Al-5.2Mg-2.0Zn (wt.%) alloy, Materials Characterization 122 (2016) 177–182.

[78] M.C. Caroll, M.J. Mills, G.S. Daehn, B.R. Dunbar, Effects of Zn additions on the grain boundary precipitation and corrosion of Al-5083, Scripta Materialia 42 (2000) 335–340.

[79] C. Meng, Di Zhang, L. Zhuang, J. Zhang, Correlations between stress corrosion cracking, grain boundary precipitates and Zn content of Al–Mg–Zn alloys, Journal of Alloys and Compounds 655 (2016) 178–187.

[80] Y. Pan, Di Zhang, H. Liu, Z. Zhang, H. Li, L. Zhuang, J. Zhang, Reducing welding hot cracking of high-strength novel Al–Mg–Zn–Cu alloys based on the prediction of the T-shaped device, Science and Technology of Welding and Joining 25 (2020) 483–489.

[81] S. Samberger, I. Weißensteiner, L. Stemper, C. Kainz, P.J. Uggowitzer, S. Pogatscher, Fine-grained aluminium crossover alloy for high-temperature sheet forming, Acta Materialia 253 (2023) 118952.

[82] M.A. Tunes, L. Stemper, G. Greaves, P.J. Uggowitzer, S. Pogatscher, Prototypic Lightweight Alloy Design for Stellar-Radiation Environments, Advanced science (Weinheim, Baden-Wurttemberg, Germany) 7 (2020) 2002397.

[83] L.B. Chappuis, Material specifications & recycling for the 2025 Ford F-150. societyofautomotiveanalysts.wildapricot.org/resources/Documents/Ford_Material_Spec_Recycling_printed.pdf.

[84] Y. Zhu, L.B. Chappuis, R. de Kleine, H.C. Kim, T.J. Wallington, G. Luckey, D.R. Cooper, The coming wave of aluminum sheet scrap from vehicle recycling in the United States, Resources, Conservation and Recycling 164 (2021) 105208.

[85] AMAG Austria Metall AG, AluReport 01 2023.

[86] NanoAl LLC, NanoAl. www.nanoal.com/company.

[87] N.Q. Vo, D.N. Seidman, D.C. Dunand, Aluminum superalloys for use in high temperature applications(US Patent 9,453,272).

[88]S. Siripurapu, C.A. Muojekwu, J.S. Sekunda, R.S. Baker, N.J. Duer, N.Q. Vo, Cables and wires having conductive elements formed from improved aluminum-zirconium alloys(US Patent 10,450,637).

5 SIMULATION OF INDUSTRIAL HEAT TREATMENT PROCESSES

To ensure the successful industrial implementation of 5/7 crossover alloys, enhancing the accuracy of simulating industrial processes is crucial. Since solution annealing followed by water quenching is not always feasible for most forming operations, industrially applicable cooling rates were evaluated. In collaboration with our industrial partner, we designed systems with customized heating and cooling rates to accommodate various feasible industrial scenarios. The response of 5/7 crossover alloys to these changing conditions was then tested, providing valuable insights into the quenching sensitivity and remaining hardening potential of the alloy. These insights are vital for optimizing its industrial applications. The key findings, published in the conference proceedings of EMC 2023, are detailed in the following section.

Effect of Heating/Colling-rates on the aging behavior of Al alloys[2]

Authors' contributions

Sebastian Samberger:	Conceptualization, Methodology, Investigation, Visualization, Writing – Original Draft
Lukas Stemper:	Supervision, Review & Editing.
Florian Schmid:	Supervision, Review & Editing.
Stefan Pogatscher:	Project Administration, Conceptualization, Supervision, Writing – Review & Editing.

Acknowledgements

The financial support by the Christian Doppler Research Association, the Austrian Federal Minis-try for Digital and Economic Affairs and the National Foundation for Research, Technology and Development is gratefully acknowledged. Moreover, the authors wish to express their sincere thanks to AMAG rolling GmbH for the supply of alloy material.

Abstract

Today's design of aluminum alloys requires the material to show an enhanced recyclability and sustainability but still fulfil the requirements for strength and ductility. Higher recycling content results in increased amounts of trace elements which leads to detrimental effects on the material properties. Therefore, more and more sophisticated production routes are required to fit the needs of future alloys. The development of aluminum alloys does not only require an optimization of the elemental composition but also in-depth knowledge about an alloy' behaviour under different heat treatments. As the heating and cooling rates of different processes have a high impact on the materials properties it is – to some extent – possible to tailor the ductility and strength of the material with the applied heat treatment to please the needs of the industry. In this study we investigate material properties of sheet samples manufactures by different lab-scale production routes via tensile testing. Heat treatment in different medias is applied to show the effect of the heating rate on the materials properties. Different cooling rates (quench rates) are applied via multiple lab-scale customized aggregates and media. The effects are demonstrated by observing the aging behaviour of a crossover alloy (Al-Mg-Zn-Cu). Results show the low quench rate sensitivity of the investigated alloy and the possibility for tailoring the mechanical properties by optimized heat treatment, when utilizing advanced laboratory equipment.

---

[2] S. Sambegrer, L. Stemper, F. Schmid, S. Pogatescher, in: GDMB (Ed.), Proceedings of EMC 2023, GDMB Verlag GmbH, 2023.

5.1 Introduction

The development of aluminum alloys toward a more sustainable society has been spurred by rising CO_2 emissions. Therefore, lightweighting approaches are intensified, particularly in the automotive industry [1,2]. However, commonly used alloys are being compromised by a trade-off in strength and formability [3]. This trade-off is addressed by the utilization of various different alloys in current automobiles – the majority of which are age-hardenable aluminum alloys – which results in a limited recyclability at the end of the vehicles life [4,5].

Age-hardenable aluminum alloys are a class of aluminum alloys that are strengthened by a precipitation hardening process, also known as age hardening. This process involves the precipitation of a specific type of particles within the alloy, which leads to an increase in the strength and hardness of the material [6]. One way to overcome the trade-off between good formability and strengthening is the introduction of age-hardenable aluminum crossover alloys. Such alloys are combining the high magnesium content of 5xxx-series alloys (for good formability) with the precipitation hardening capability of 7xxx-series alloys (5/7 crossover) [7]. By keeping the Mg/Zn ratio < 1 hardening is achieved by T-phase ($Mg_{32}(Al,Zn)_{49}$) precipitation [8,9].

The most essential processes in the manufacturing of age-hardenable aluminum alloys are heat treatments, as they enable the manipulation of the microstructure and mechanical properties. The key factors that determine the outcome of the heat treatment process are the heating and cooling rates. In industrial production, heating and cooling rates during warm forming and solution annealing are crucial in terms of i.e. controlling material distortion. The distortion is caused by the internal stress that is generated during the heating and cooling process. The internal stress is a function of both the heating and cooling rates, as well as the temperature at which the material is held during the treatment. In order to minimize distortion, it is essential to control the heating and cooling rates, as well as the temperature, during the warm forming process [10].

In addition to its effect on internal stress both heating and cooling rates also play a crucial role in the age hardening process. The rate at which the alloy is heated and cooled can significantly influence the size, shape, and distribution of the precipitate particles, as well as the kinetics of the precipitate formation and growth. Faster heating and cooling rates tend to result in smaller and more uniformly distributed precipitates resulting in higher strength and hardness of the material. On the other hand, slower heating and cooling rates tend to result in larger and more irregularly distributed particles leading to lower strength and hardness [11–13].

The quench rate sensitivity and its impact in the heat treatment of age-hardenable aluminum crossover alloys is examined in this study. The relationship between heating and cooling rates, as well as the mechanical properties of this good formable and age-hardenable aluminum alloy is demonstrated on laboratory heating and cooling methods. The heat treatments are carried out utilizing different heating media in conjunction with a variety of industrially relevant, lab-scaled cooling processes. The goal is to provide a better knowledge of the significance of heating and cooling rates in the heat treatment of age-hardenable aluminum alloys, as well as how they can be employed to improve these materials' properties for various applications.

5.2 Experimental methods

The investigated alloy is an industrial produced aluminum crossover alloy supplied by AMAG rolling GmbH (AMAG CrossAlloy™.57) with a composition shown in Table 5-1. The 1 mm sheet is produced by hot and cold rolling and was obtained in the T4-FH condition (solution annealed and pre-aged). This condition is most suitable for this study since the sheet does not exhibit excess-dislocations from prior cold rolling, which allows to neglect potential recovery or recrystallization effects.

Table 5-1: Measured chemical composition of the investigated industrially produced sheet

AMAG CrossAlloy™.57	[wt.-%]						
	Mg	Zn	Cu	Si	Fe	Mn	Cr
	4.9	3.5	0.5	0.1	0.2	0.4	0.1

Nine different heat treatment strategies were investigated in this study which are displayed schematically in Figure . They contain two different heating options – air circulating furnace (AF) and a contact press (CP) – followed by four separate cooling methods. A third heating strategy followed by water quenching is done in salt bath (SB) for reference as it contains the most beneficial heating/cooling combination.

The time at temperature for the first two heating methods were chosen to 480 °C/5min. Heat treatment in SB was done at 480 °C for 1 min. The tested holding times represent the time at temperature. Subsequent cooling was done using a water quench (WQ), pressured air quench (PQ), ventilated air quench (VQ) and static air quench (AQ).

After solution annealing (LSG) and cooling the effect on the age-hardenability was measured along a standard heat treatment route. Subsequent to quenching the alloy was pre-aged (PA) at 100 °C for 5h in an oil bath. Pre-aging is followed by seven days of natural aging and final paint-bake (PB) treatment at 185 °C/20 min.

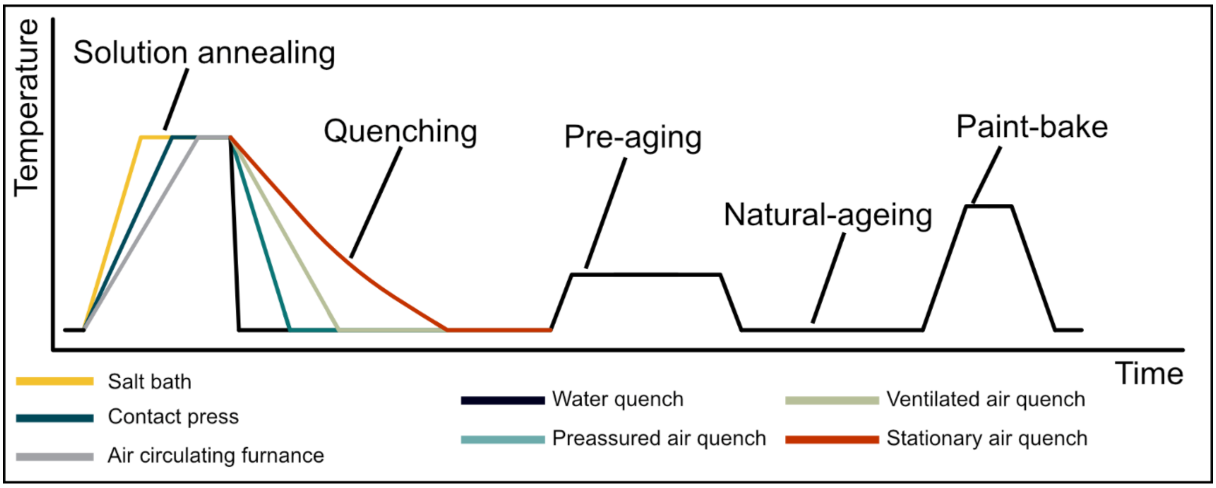

Figure 5-1: Schematic of the applied heat treatment strategies

The effect of the cooling rate on the age-hardenability of the alloy was studied via the mechanical properties in tensile testing. Three samples were tested in each condition for sufficient statistics. Testing was done on a Zwick/Roell BT1-FR100THW.A2K tensile testing machine equipped with a 50 kN load cell. Sample preparation was carried out in accordance with DIN EN ISO 6892-1 [14].

Heating and cooling rates were measured by inserting a 0.5 mm Type-K thermocouple into a 0.55 mm hole drilled into the middle of the 1 mm thick sheet. Data acquisition was conducted using a MC-Measurement Computing USB-2408-2AO data acquisition module. A data acquisition frequency of 50 Hz has shown the lowest noise at highest acquisition rate. Data readout and processing was performed using LabView and OriginPro 2021. To deduce the heating and cooling rate from temperature-time plots, the raw data was first manually adjusted from strongly deviating signals. After smoothing the signal, the first derivative of the temperature was formed. The result represents the heating and cooling rate.

Figure 5-2 shows a selection of aggregates used for heating and cooling. The pressured air-cooling system cooling system utilizes Lechler nozzles on both sides of the sample to ensure that both sides are subjected to the same cooling conditions. The same approach is applied for ventilation air quenching because both sample sides must have the same cooling environment. Contact press heating was performed within a pre-heated steel plate construction (Figure 5-2c). At treatment temperature, the salt shown in the steel container (Figure 5-2b) is liquid.

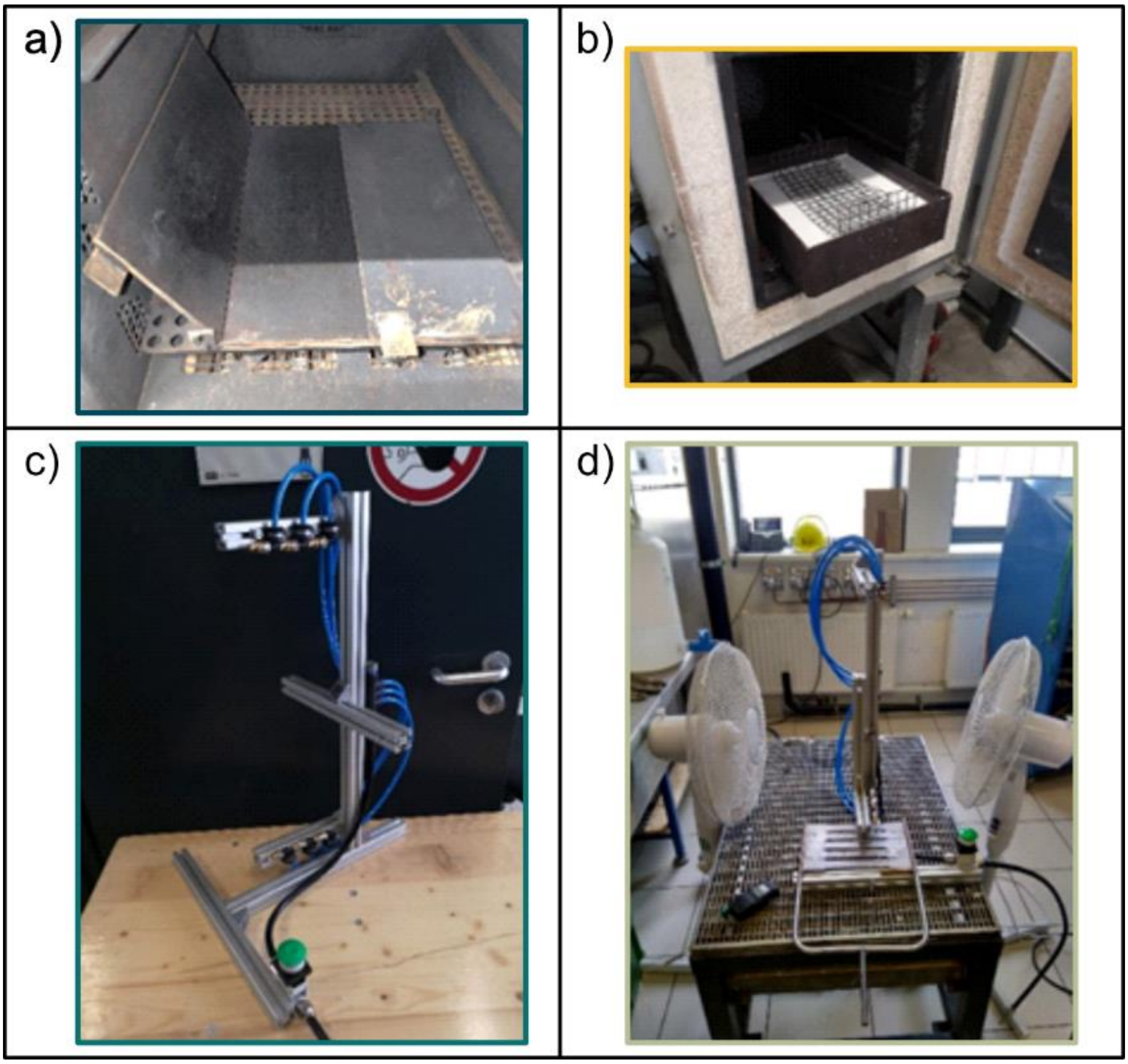

Figure 5-2: Used aggregates for cooling: Pressured air quench (a) and ventilated air quench (b); Aggregates for heating: Contact press (c) and Salt bath with sample holder (in solid form, not heated to temperature) (d)

5.3 Results & Discussion

The obtained heating and cooling rates throughout the conducted experiments can be found in Figure 5-3. The corresponding numeric values are displayed in Table 5-2. It has to be noted, that K-If the temperature variation is not taken into account, incorrect conclusions might be drawn in the case of time-critical processes etype-thermocouples exhibit a drift in the Seebeck coefficient caused by atomic structure fluctuation during temperature changes [15]. As a result, it is necessary to consider the detected temperature value with a standard deviation. According to EN 60854-1:2013 [16] the deviation of class 2 Type-K thermocouples is ± 0.75 %. As this is only valid for unused thermocouples, a value of ± 1 % is chosen in this study. Therefore, the time-at-temperature is considered to start as soon as the measured temperature comes in the range of ± 1 % of the desired temperature, which is 475 °C if 480 °C is the intended holding temperature.

Table 5-2: Heating times and rates of the used aggregates

Aggregate	Time to 475 °C [s]	Time to 480 °C [s]	Maximum heating rate [K/s]
Salt bath	15	21	430
Contact press	74	147	130
Air circulating furnace	164	243	18

As shown in Figure 5-3a, the consideration of temperature deviation results in deviating heating times. This effect is negligible for heating in SB as the time deviation is about 6 s, but more pronounce for slower heating methods. When heating in the contact press, the time to overcome the last 1 % (5 °C) temperature increment is 73 s, which is similar to the time for the first 99 %.

When heated in the air circulation furnace the time to overcome the last 1 % of heating is 79 s. This is about 1/3 of the time to reach 480 °C. If the temperature variation is not taken into account, incorrect conclusions might be drawn in the case of time-critical processes especially if the evaluated features are pronounced at shorter times (e.g., less than 10 min). The heating rate changes during the process as seen from Figure 3b and maxima occur at different temperatures depending on the heating method. This is most probably a result of the media in contact with the aluminum sample. The maximum heating rate for SB is 430 K/s followed by CP with 130 K/s and AF with 18 K/s. Those values are significantly different from each other and can be used to simulate a variety of industrial processes.

The cooling curves and cooling rates are displayed in Figure 5-3c and d, respectively. The corresponding cooling time values and maximum cooling rates are shown in Table 5-3. The cooling rate for WQ is fully displayed in the insert of Figure 5-3d. With a maximum cooling rate of about -800 K/s measured during WQ is approximately 25 times higher than PQ and even 80 times higher than cooling by AQ, which results in cooling times down to 35 °C between 2 s (WQ) and 400 s (AQ).

Table 5-3: Cooling time and maximum cooling rate of the used aggregates

Aggregate	Time to 35 °C [s]	Maximum cooling rate [K/s]
Water quench	2	-800
Preassured air quench	53	-31
Ventilated air quench	203	-13
Stationary air quench	411	-8

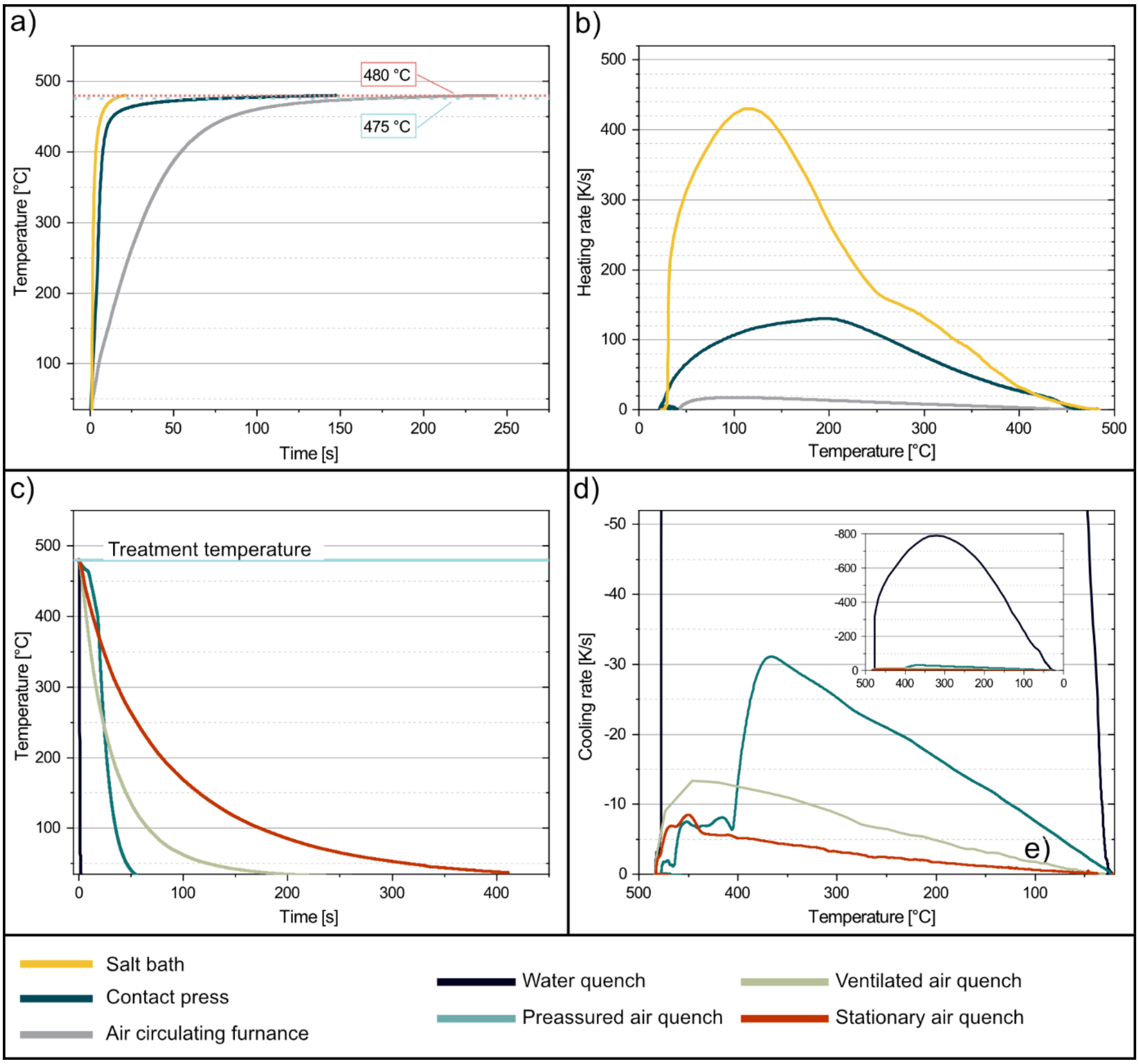

Figure 5-3: Time to temperature (a) and corresponding heating rates (b); Cooling time from treatment temperature (b) and corresponding cooling rates (e) for the used aggregates

5.3.1 Effect of heating rates

The influence of the heating rate on the mechanical properties of the investigated alloy in different heat treatment conditions is shown in Figure 5-4 for the fastest (WQ, Figure 5-4a) and slowest (AQ, Figure 5-4b) cooling rate. In a certain condition the mechanical properties show similar values independently of the heating rate but a strong effect of the cooling rate after quenching.

This behaviour occurs due to the selected initial state of the alloy. Generally, the yield strength of an aluminum alloy is linked to the Hall-Patch relationship and is therefore dependent on the grain size [6]. The initial state of the investigated material (T4-FH) is already recrystallized, and no dislocations are left in the material. Further annealing may result in grain growth and therefore effect mechanical properties. However, this is not the case for the applied solution annealing times, temperatures and heating rates as the mechanical properties are independent of the heating method. Therefore, the initial state can be seen as stable one with respect to the grain structure as no differing recrystallization or growth occurs. [17]

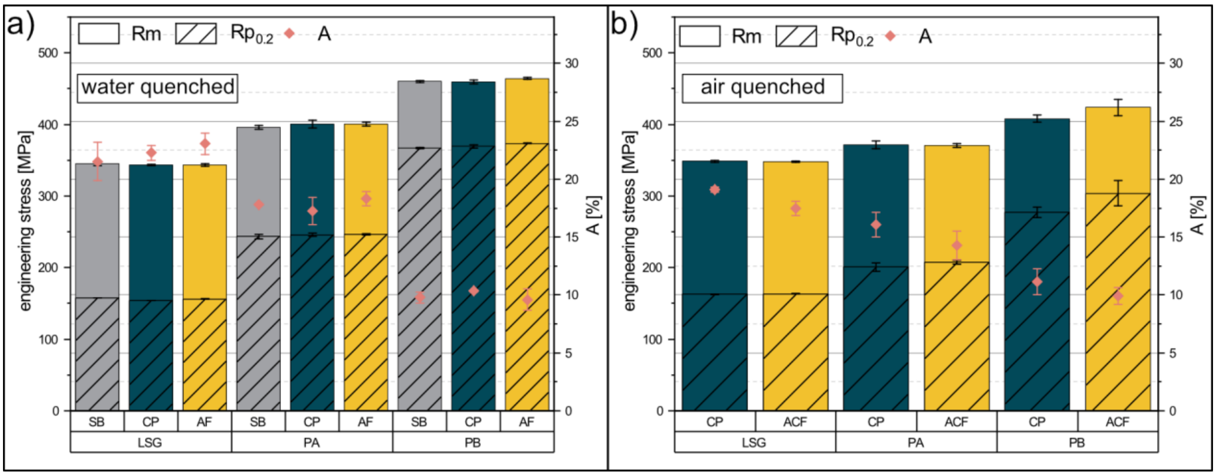

Figure 5-4: Influence of heating rate on the mechanical properties (yield strength YS, ultimate tensile strength UTS and elongation at fracture A) in different aging stages shown by at the example of two the cooling rates extrema quenched in water (a) and quenched in stationary air (b).

5.3.2 Effect of cooling rates

The effect of the cooling rate on the age-hardenability of the alloy is shown by Figure . The mechanical properties YS, UTS and A are displayed after heating in the contact press and quenching in different media. Since the material properties are independent of the heating rate, the data shown in Figure is also valid for the other heating methods. The corresponding yield strength values in the different heat treatment stages are displayed in Table 5-4. The water quenched samples are used as reference since these samples are expected to exhibit the strongest supersaturation of solute elements and excess vacancies and therefore the most beneficial precipitation conditions.

After solution annealing the influence of the quenching condition seems to be neglectable. All samples show the same YS value of about 162 MPa except for WQ, which is about 10 MPa lower, but still within the same range. In contrast, the elongation to fracture shows a pronounced dependence on the cooling rate with a sinking value from WQ (22 ± 0.6 %) to PQ and VA (both 20 ± 0.5 %) and AQ (19 ± 0.6 %). This effect is compensated during pre-aging, where the A values are almost evened out with respect to the standard deviation.

During pre-aging the quench rate sensibility of the alloy becomes more perceptible. While the PQ samples achieve nearly the same YS values as WQ, VQ and AQ show strong declines in strength. Compared to the

WQ sample, the yield strength is lower by 18 MPa and 45 MPa for VA and AQ, respectively. This effect can be explained as follows: During pre-ageing, the elements start to form Guinier-Preston (GP) zones as shown by Stemper et al. [18] and Cao et. al [19]. Since the slow quenched alloy is expected to exhibit more precipitation during the cooling [20], less solutes are available for GP-zone formation during the pre-ageing. Therefore, the YS and UTS is lower compared the WQ sample. This observation is in good agreement with findings by Tang et al. [21] who identifies slower cooling as a reason of reduced GP-zone formation in an Al-Zn-Mg-Cu alloy with a high Zn/Mg-ratio during aging. Additionally, the absence of GP zones limits the hardenability of the alloy, as the GP zones cannot act as nuclei for phase formation.

This effect can be indirectly observed upon comparison of the mechanical properties in PB condition. The strength increases during paint bake (paint-bake response PBR) ranges from 123 MPa for the WQ sample to 76 MPa for the AQ samples. Also notable is the still high PBR of 108 MPa and YS after paint-bake for the samples with intermediate quench rate (PQ and VQ). The deviation in PBR between WQ, PQ and VQ might be minimized by longer natural aging times. As proposed by Strobel et al. [22] the microstructure is dominated by vacancy annihilation and clustering at longer natural aging times.

Compared to other alloys the variation in mechanical properties is quite low for the investigated crossover alloy. Choi et al. [23] investigated the effect of quenching on the mechanic properties in 7xxx series alloys and found a difference in YS of about 40 MPa in as-quenched condition, while the herein investigated crossover alloy shows almost no difference. The findings of this study are in good agreement with observation made by Graf et al. [24]. They compared the precipitation behaviour of a 7xxx series alloy (high Zn/Mg ratio) with a crossover alloy (low Zn/Mg ratio). They found a quench rate, where no precipitation occurs during quenching, of 100 K/s for 7xxx series alloys and 1 K/s for crossover alloys. This demonstrates that the crossover alloy has a very low quench sensitivity and explains the significant decrease in the paint-bake response for the AQ sample.

Table 5-4: Yield strength (Rp0.2) of the different aging stages and sole paint bake response after heating in contact press at 480 °C for 5 min in dependence of the quenching condition

Rp$_{0.2}$ [MPa]	**WQ**	**PQ**	**VQ**	**AQ**
SA	154 ± 2	164 ± 0	162 ± 0	163 ± 0
PA	246 ± 2	238 ± 2	228 ± 2	201 ± 6
PB	369 ± 2	345 ± 11	335 ± 1	277 ± 7
PBR [MPa]	123	108	108	76

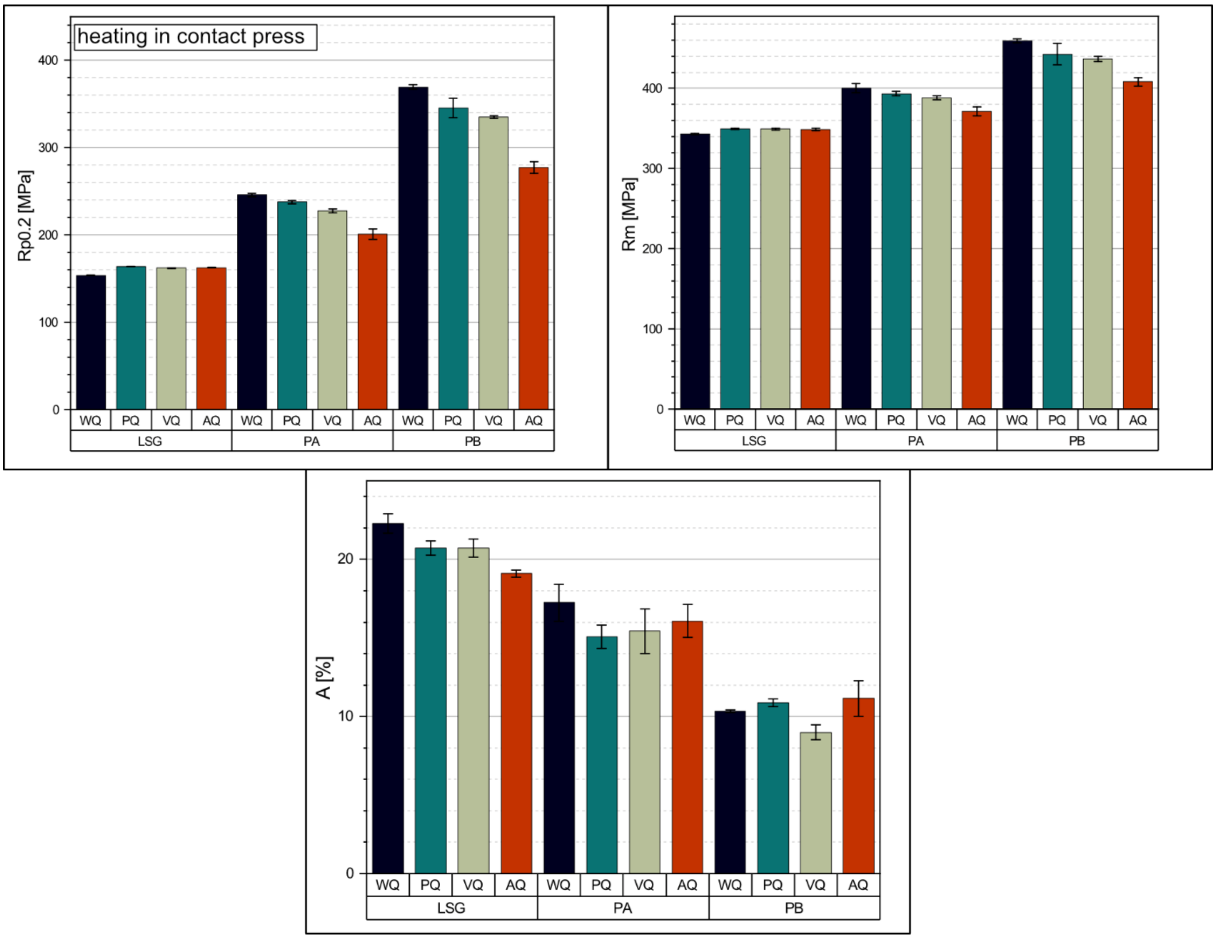

Figure 5-5: Influence of cooling rates (water quench (WQ); pressured air quench (PQ); ventilated air quench (VQ); static air quench (AQ)) on the mechanical properties in different aging stages (solution annealed (LSG); pre-aged (PA); paint-baked (PB)) after heating the samples in contact press at 480 °C for 5 min.

5.4 Conclusion

In this study the heating and cooling rates in different media have been measured and their effect on the age hardenability of a crossover alloy was studied. The main findings can be summarized as followed:

- The temperature needs to be considered as a value with standard deviation. Therefore, the dedicated holding temperature is considered to be reached when measured temperature is within ± 1 %. This deviation is hardly affecting fast heating rates but eventually leads to excessively long holding time at temperature and misinterpretation when the heating rate is lowered.
- Since the starting condition of the herein investigated alloy is T4-FH (solution annealed and pre-aged), the heating rate has no effect on the mechanical properties. This behaviour implies, that the T4-FH condition is stable with respect to the grain structure and no differing recrystallization or growth occurs during the heating.
- In the solution annealed temper, the cooling rate has no influence on the YS and UTS of the alloy. With subsequent aging the effect of the cooling rate is more pronounced resulting in declining yield strength if low cooling rates are applied.

5.5 References

[1] J. Hirsch, Recent development in aluminium for automotive applications, Transactions of Nonferrous Metals Society of China 24 (2014) 1995–2002.

[2] J. Hirsch, Aluminium in Innovative Light-Weight Car Design, Materials Transactions 52 (2011) 818–824.

[3] D. Carle, G. Blount, The suitability of aluminium as an alternative material for car bodies, Materials & Design 20 (1999) 267–272.

[4] A. Poznak, D. Freiberg, P. Sanders, Automotive Wrought Aluminium Alloys, in: Fundamentals of Aluminium Metallurgy, Elsevier, 2018, pp. 333–386.

[5] Jirang Cui, Hans J. Roven, Recycling of automotive aluminum, Transactions of Nonferrous Metals Society of China 20 (2010) 2057–2063.

[6] Freidrich Ostermann, Anwendungstechnologie Aluminium, 2nd ed., Springer, Berlin Heidelberg, 2007.

[7] L. Stemper, M.A. Tunes, R. Tosone, P.J. Uggowitzer, S. Pogatscher, On the potential of aluminum crossover alloys, Progress in Materials Science (2021).

[8] G. Bergman, J. Waugh, L. Pauling, The crystal structure of the metallic phase $Mg_{32}(Al,Zn)_{49}$, Acta Cryst. 10 (1957) 254–259.

[9] A. Bigot, P. Auger, S. Chambreland, D. Blavette, A. Reeves, Atomic Scale Imaging and Analysis of T' Precipitates in Al-Mg-Zn Alloys, Microsc. Microanal. Microstruct. 8 (1997) 103–113.

[10] S. MacKenzie, Quenching Aluminum for Residual Stress and Distortion Control*, HTM Journal of Heat Treatment and Materials 75 (2020) 23–34.

[11] Y. Yin, B. Luo, H. Jing, Z. Bai, Y. Gao, Influences of Quench Cooling Rate on Microstructure and Corrosion Resistance of Al-Cu-Mg Alloy Based on the End-Quenching Test, Metall and Materi Trans B 49 (2018) 2241–2251.

[12] M. Tiryakioglu, "Quench Sensitivity of Aluminum Alloys", Technical papers-society of manufacturing engineers-all series (1999).

[13] B. Liščić, Quenching theory and technology, 2nd ed., CRC Press; International Federation for Heat Treatment and Surface Engineering, Boca Raton, 2010.

[14] DIN EN ISO 6892-1:2017-02, Metallic materials - Tensile testing - Part 1: Method of test at room temperature (ISO 6892-1:2016); German version EN ISO 6892-1:2016, Berlin, Beuth Verlag GmbH, 10.31030/2384831.

[15] E.S. Webster, Drift in Type K Bare-Wire Thermocouples from Different Manufacturers, Int J Thermophys 38 (2017).

[16] DIN EN 60584-1:2014-07, Thermocouples - Part 1: EMF specifications and tolerances (IEC 60584-1:2013); German version EN 60584-1:2013, Berlin, Beuth Verlag GmbH, 10.31030/2153253.

[17] J. Humphreys, Rohrer, S., Gregory, A. Rollett, Recrystallization: and related annealing phenomena, Elsevier, 2017.

[18] L. Stemper, M.A. Tunes, P. Dumitraschkewitz, F. Mendez-Martin, R. Tosone, D. Marchand, W.A. Curtin et al., Giant hardening response in AlMgZn(Cu) alloys, Acta Materialia 206 (2021) 116617.

[19] C. Cao, Di Zhang, L. Zhuang, J. Zhang, Improved age-hardening response and altered precipitation behavior of Al-5.2Mg-0.45Cu-2.0Zn (wt%) alloy with pre-aging treatment, Journal of Alloys and Compounds 691 (2017) 40–43.

[20] A. Deschamps, G. Texier, S. Ringeval, L. Delfaut-Durut, Influence of cooling rate on the precipitation microstructure in a medium strength Al–Zn–Mg alloy, Materials Science and Engineering: A 501 (2009) 133–139.

[21] J.-G. Tang, H. Chen, X.-M. Zhang, S.-D. Liu, W.-J. Liu, H. Ouyang, H.-P. Li, Influence of quench-induced precipitation on aging behavior of Al-Zn-Mg-Cu alloy, Transactions of Nonferrous Metals Society of China 22 (2012) 1255–1263.

[22] K. Strobel, M.D. Lay, M.A. Easton, L. Sweet, S. Zhu, N.C. Parson, A.J. Hill, Effects of quench rate and natural ageing on the age hardening behaviour of aluminium alloy AA6060, Materials Characterization 111 (2016) 43–52.

[23] Y. Choi, C. Moon, M.-G. Lee, Experimental study on the mechanical properties of 7xxx aluminium alloy sheet under different heat treatment conditions, IOP Conf. Ser.: Mater. Sci. Eng. 651 (2019) 12080.

[24] G. Graf, P. Spoerk-Erdely, P. Staron, A. Stark, F. Mendez Martin, H. Clemens, T. Klein, Quench rate sensitivity of age-hardenable Al-Zn-Mg-Cu alloys with respect to the Zn/Mg ratio: An in situ SAXS and HEXRD study, Acta Materialia 227 (2022) 117727.

6 PROPERTY EXPANSION OF 5/7 CROSSOVER ALLOYS

The study of the effect of heating and cooling rates on 5/7 crossover alloys revealed their low quench rate sensitivity, which allows the potential use of hot forming with subsequent age hardening treatment. Additionally, an examination of the grain structure in the cold-rolled state revealed μm-sized T-phase particles. These particles could be used via a particle-stimulated nucleation mechanism to form a fine-grained microstructure suitable for superplastic forming operations. The results of this study were published in the journal Acta Materialia and paved the way for the first prototyping of an industrial Crossalloy.57. The findings of the study are presented in the following section.

Fine-grained aluminum crossover alloy for high-temperature sheet forming[3]

Authors' contributions

Sebastian Samberger:	Conceptualization, Methodology, Investigation, Visualization, Writing – Original Draft
Irmgard Weißensteiner:	Investigation, Visualization, Writing – Review & Editing.
Lukas Stemper:	Writing – Review & Editing.
Christina Kainz:	Investigation, Visualization, Writing – Review & Editing.
Peter J. Uggowitzer:	Conceptualization, Supervision, Writing – Review & Editing.
Stefan Pogatscher:	Project Administration, Conceptualization, Supervision, Writing – Review & Editing.

Acknowledgements

The financial support by the Christian Doppler Research Association, the Austrian Federal Minis-try for Digital and Economic Affairs and the National Foundation for Research, Technology and Development is gratefully acknowledged. Moreover, the authors wish to express their sincere thanks to AMAG rolling GmbH for the supply of alloy material.

Abstract

This study presents age-hardenable, fine-grained AlMgZnCu crossover alloys intended for superplastic and quick plastic forming processes. The study utilizes T-phase ($Mg_{32}(Al,Zn)_{49}$) for both grain refinement and age-hardening. It deploys a uniform distribution of µm-sized T-phase particles, which can be dissolved upon final solution annealing, and which is utilized for heavy particle stimulated nucleation (PSN) during industrial processing of sheets, in order to reach an equiaxed grain size as low as 4 µm. This fine grain size is advantageous for high-temperature forming of aluminum alloys. Elongations above 200% and 400% are achieved when deformed at strain rates of 10^{-2} s^{-1} or $5*10^{-5}$ s^{-1} at 470 °C, and interestingly, the fine grain structure is highly stable even when held at that temperature for one day. Moreover, the material reached yield strength values of more than 380 MPa after a paint-bake heat treatment for quenching in water or compressed air. The study demonstrates the importance of PSN using electron microscopic and texture measurements and describes it by simple modelling of T-phase particle grain refinement. It explores the high stability of the fine grain assembly in terms of the random grain boundary misorientation distribution in combination with high solute content observed, provided via the dissolved T-phase, and Smith-Zener pinning. The simple, commercially available grain refinement strategy demonstrated using the dissolvable T-phase, and the resulting unique property profile, make the crossover alloy in question a promising candidate for high-temperature sheet forming processes.

---

[3] S. Samberger, I. Weißensteiner, L. Stemper, C. Kainz, P.J. Uggowitzer, S. Pogatscher, Fine-grained aluminium crossover alloy for high-temperature sheet forming, Acta Materialia 253 (2023) 118952.

6.1 Introduction

To facilitate further light-weighting and decrease the weight of automobiles, increasing the use of aluminum alloys would be beneficial. However, aluminum alloys' trade-off of good formability and high strength must be addressed if they are to be suitable for advanced applications [1–3]. Crossover alloys [4] can greatly help to solve this problem. They overcome the need for trade-off by combining the high magnesium content of 5xxx-series alloys (for good formability) with the precipitation hardening capability of 7xxx-series alloys (5/7 crossover). By keeping the Mg/Zn ratio < 1 hardening is achieved by T-phase precipitation [5]. The T-phase ($Mg_{32}(Al,Zn)_{49}$) [6] has 162 atoms per unit cell and a wide range of compositions, depending on the alloy composition and the heat treatment applied [7–9]. Precipitation can also be enhanced by adding Ag [10,11] or Cu [11–13] which increase the number density of Guinier-Preston(GP)-zone formation. The precipitation sequence of novel 5/7 crossover alloys has not yet been fully explored. However, it is proposed that while precipitation is not yet fully clear, it proceeds over GP-zones and precursors of T-phase or η-phase, as summarized by Stemper et. al [4].

High strength levels in 5/7 crossover alloys are achieved by using a 2-step heat treatment and adding Cu. Pre-ageing at around 100 °C and paint-baking (or bake-hardening) for 20 minutes at 185 °C results in a paint-bake response (PBR) of more than 150 MPa, to a total yield strength level of over 400 MPa [13–15]. For 5/7 crossover alloys with added Cu, Lüders elongation and the Portevin-Le-Chatelier (PLC)-effect can be prevented or suppressed [16,17], and an enhancement of intergranular corrosion resistance (IGC) due to narrow precipitation-free zones (PFZ) has been reported [18,19]. 5/7 crossover alloys are also reported to exhibit improved stress corrosion cracking (ICC) and exfoliation resistance properties [20,21]. Crossover alloys have been shown to be suitable for friction stir processing (FSP) [22] and conventional welding operations [23]. Even dedicated applications in space seem feasible [24]. Because 5/7 crossover alloys feature a number of promising properties, it is of great interest to explore their potential areas of application. High-temperature forming processes such as superplastic forming (SPF) or quick plastic forming (QPF), for example, would be of commercial interest, as the 5xxx-series alloys most often used, such as EN-AW 5083 [25–27], cannot be age-hardened.

Superplastic forming is a process in which a polycrystalline material can undergo very high elongation without failure. Commercially, such processes are conducted at low strain rates of 10^{-4}–10^{-2} s^{-1} at temperatures in the range of $\geq 0.5T_m$ (melting point) [28]. There are two main requirements if materials are to exhibit superplastic behaviour: first, a high strain rate sensitivity to limit necking; and second, a low rate of damage accumulation (e.g. cavitations) to prevent premature material failure [29]. Because strain rate sensitivity increases with decreasing grain size, it is commonly accepted that a key requirement for commercial superplastic aluminum alloys is a stable grain size of < 10 µm [28,30–33].

The deformation mechanism for superplastic forming is discussed thoroughly in literature. The potential mechanism controlling superplastic forming is grain boundary sliding (GBS) [34]. While it is accepted that GBS is the principal mechanism for superplastic forming at low strain rates and high temperatures, high-temperature forming processes are often accompanied or even fully controlled by solute-drag controlled slip creep (SDC). This is more pronounced at higher strain rates of $\dot{e} \geq 10^{-2}$ s^{-1} and lower temperatures, being more relevant for quick plastic forming [35–37]. While plastic deformation by GBS is characterized by a high strain rate sensitivity exponent (m ≥ 0.5), deformation by SDC is characterized by lower m values of ≈ 0.25–0.33 [29,30,38].

Because a small, stable grain size is essential, various grain refinement techniques have been deployed. Vibration and stirring, rapid solidification and the addition of grain refiner can proceed during the solidification process [39]. Ultra-fine grains can be generated by severe plastic deformation (SPD), i.e. high-pressure torsion [40,41], friction stir processing [42], equal-channel angular pressing [43] or accumulative roll-bonding [44]. However, commercial use of SPD products is still rare due to high costs and small sample sizes [45]. Subsequent grain growth during recrystallization can be supressed by the Zener pinning effect via dispersoids [31,34,46,47].

An interesting refinement technique was reported by Wert et. al [48] for the alloy 7075, where a long overageing treatment is applied to precipitate coarse η-phase prior to rolling. After heavy medium temperature rolling at 200 °C with a thickness reduction of 90 % they achieved a grain size after recrystallization at 482 °C/30 min of about 10 µm in rolling and transverse direction and of 6 µm in the normal direction. However, this requires a complex and unconventional manufacturing route. In the usual case the particle stimulated nucleation (PSN) applied above is found at µm-sized constituent particles [49].

This study presents a 5/7 crossover alloy with an equiaxed fine-grained microstructure (≤ 5 µm grain size) which is perfectly suitable for SPF and QPF operations and is produced with no additional manufacturing steps or chemical modifications. Grain refinement during processing is achieved by a unique distribution of µm-sized T-phase particles, which are dissolved in a final solution annealing. The study shows that the fine grained microstructure obtained by T-phase-induced PSN during recrystallization is very stable even at temperatures of 470 °C for 24 h, with no additional elements such as Zr or Sc to form dispersoids. It also demonstrates that the alloy possesses the usual high age-hardening potential even when cooling with air is performed after hot forming.

6.2 Experimental

The study is based on an industrially produced sheet material with the chemical composition shown in Table 6-1, measured by optical emission spectroscopy (Spectromaxx spark spectrometer). The rolling process involved hot and cold rolling stages. The final steps of hot rolling were carried out at temperatures below 400 °C. The finished 1 mm sheet was delivered in the cold-rolled state with a cold-rolling degree (CRD) of 58 %. For investigations with 85 % CRD the 1 mm sheet was processed further in a lab-scale mini rolling mill.

Table 6-1: Measured chemical composition of the industrially produced 5/7 crossover alloy sheet investigated

		Mg	Zn	Cu	Si	Fe	Mn	Cr	Ti
5/7 crossover alloy	[wt.-%]	4.91	3.46	0.46	0.10	0.13	0.33	0.06	0.01
	[at.-%]	5.56	1.46	0.20	0.10	0.07	0.17	0.03	0.01

Heat treatment strategies for microstructure evolution investigations are shown in Table 6-2. While Route 1 (R1) represents recrystallization where no dissolution of T-phase occurs, Route 2 (R2) is a solution annealing treatment. By comparing R1 and R2, an idea of the interplay between recrystallisation and phase dissolution is obtained. To limit recovery prior to recrystallization, the heat treatment was best performed in a salt bath (Route 1-3) to enable a high heating rate (approx. 400 K/s). For reference, the heat treatment of Route 4 (R4) was carried out using an air circulation furnace with a lower heating rate (approx. 18 K/s). Route 3 and Route 5 simulate a hot forming process after recrystallization (R3) and solution annealing (R5), with long exposure times at high temperatures to evaluate the stability of the grain assembly. A second recrystallization heat treatment step was conducted in a plate press during R3 to simulate a slower heating rate, comparable to industrial hot forming processes. The second stage in R5 simulates the thermal load applied during slow high-temperature forming. Quenching of all samples during the first heat treatment step was performed in water to suppress any cooling effects on the microstructure. Quenching after the second heat treatment stage was carried out in air.

Table 6-2: Parameters for the recrystallization heat treatment procedures applied to samples with 58% and 85% CRD

Route	1st step heat treatment	2nd step heat treatment	CRD [%]
Route 1 (R1)	380°C/5min + WQ	-	58/85
Route 2 (R2)	480°C/1min + WQ	-	58/85
Route 3 (R3)	380°C/5min + WQ	480°C/10min + AQ	58/85
Route 4 (R4)	480°C/35min + WQ	-	58/85
Route 5 (R5)	480°C/1min + WQ	470°C/≈24h + AQ	58

WQ: Water quenching; AQ: Air quenching

To finally test age hardenability, recrystallized alloys were solution annealed (480°C/1min) in a salt bath and subsequently pre-aged at 100°C for 5h. Natural aging at RT for 14 days followed, after which the alloys were subjected to a paint-baking treatment at 185°C for 20 min. After solution annealing the samples were quenched using both water and compressed air; this was because water quenching after hot forming is not always feasible, particularly due to distortion issues [50].

Microstructure and texture investigations were conducted with a scanning electron microscope (SEM) (JEOL 7200F FEG-SEM, Tokyo, Japan) equipped with a Symmetry S2 electron backscatter diffraction (EBSD) detector and an energy dispersive X-ray (EDX) detector (XMax-80, Oxford Instruments, Abingdon, UK). This included the option of automatic particle ("feature") analysis of backscattered electron images using threshold limits.

The parameters for EBSD measurement were chosen as 20 kV with a 16 mm working distance (WD). Measuring was performed using a 70° pre-tilt specimen holder. For grain reconstruction, a misorientation tolerance of 5° was chosen in accordance with ASTM E2627-13 [51]. The EBSD data was smoothed using the auto smoothing option of Oxford Instruments "AZtec" software [52]. This software removes pixels that are significantly different from surrounding ones (wild spikes) and performs an iterative removal of zero solutions. The grain size was estimated from EBSD data using the average equivalent circle diameter (ECD) [53,54]. Grain size measurement was carried out on ground and oxide polished or electropolished samples using EBSD techniques. The grain boundary misorientation distribution was calculated using "AZtecCrystal" software by considering the disorientations between neighbouring datapoints with a threshold limit of 5° [55]. All EBSD measurements for grain size determination were performed at the same magnification to produce non-normalized comparable data sets.

For more detailed data evaluation of partially recrystallized structures and for texture analysis, the Matlab-based toolbox mtex was deployed [56]. For the maps showing local misorientations, a grain tolerance angle of 5°, a step size of 10 nm and an average of 5th-order misorientations were applied. For texture analysis, at least 2 mm^2 over the complete sheet thickness were analysed, and the orientation distribution functions (ODF) were calculated via a kernel density estimation as explained in [57].

Automated SEM/EDX feature analyses were used to determine the density of coarse particles. The threshold limits for particle detection were set to select particles brighter (heavier) than the surrounding matrix. The size limit for particle detection was set at > 9px and an ECD of > 0.5 μm. Parameters for these measurements were chosen as 15 kV, 10 mm WD and 3 s measuring time [58–60]. The area fraction of coarse particles was calculated by dividing the area covered by particles (obtained by automated feature analysis) by the area covered by total structure. The area fraction of particles was assumed to be the same as per unit volume, which is considered a valid estimation for coarse particles [61]. The volume fraction and size of particles of < 0.5 μm in diameter were characterized using the method of J. Österreicher et. al. [62].

For the X-ray diffraction (XRD) measurement, a Bruker-AXS D8 Advance diffractometer, which operates with CuK_α radiation, was used. The measurement was performed in Bragg-Brentano geometry, where a θ range of 20-85° was probed. Using the software package Topas 6 by Bruker, Rietveld refinement allowed to quantify the phase fraction of the T-phase [63].

High angle annular dark field (HAADF) and EDX scanning transmission electron microscope (STEM) measurements were carried out using a Thermo Fisher Scientific™ Talos F200X instrument. Samples were prepared for STEM by grinding the alloys to a thickness of approx. 100 μm. Punched-out 3 mm discs were processed further by twin jet electro-polishing using a solution of 25 % nitric acid in methanol in a temperature range of -16 °C to -20 °C and a voltage range of 10 V to 20 V.

Tensile testing at room temperature (RT) was performed on a Zwick/Roell BT1-FR100THW.A2K tensile testing machine equipped with a 50 kN load cell. Sample preparation was carried out in accordance with DIN EN ISO 6892-1 [64]. High-temperature tensile tests were conducted in accordance with DIN EN ISO 6892-2 [65] at strain rates ($\dot{\varepsilon}$) of $1*10^{-2}$, $5*10^{-4}$ and $5*10^{-5}$ s^{-1} respectively. The temperature of high-temperature tensile testing was chosen as 470 °C. Three samples were tested in each condition.

6.3 Results

6.3.1 Microstructure development

Figure 6-1 displays the microstructure of the cold rolled sheet with 58 % CRD. The SEM-BSE micrographs and the corresponding EDX maps of the coarse particles (Figure 6-1b) refer to T-phase, as the particles mainly consist of Mg, Zn, Cu and Al. This assumption is supported by XRD-analysis (Figure 6-1c). In addition to face-centered cubic Al [66], also reflections stemming from the T-phase ($Mg_{32}(Al,Zn)_{49}$) [67] can be identified. A quantitative Rietveld refinement of the recorded diffractogram reveals around 5 wt.-% T-phase in the cold rolled sheet. The high amount of small angle grain boundaries as a result of cold rolling is shown by the grain boundary misorientation distribution displayed in Figure 6-1d. The high number density of μm-sized particles and their homogenous distribution in the matrix, in combination with the high dislocation density due to cold working, offers the advantage of particle stimulated nucleation (PSN) during subsequent recrystallisation heat treatment [68].

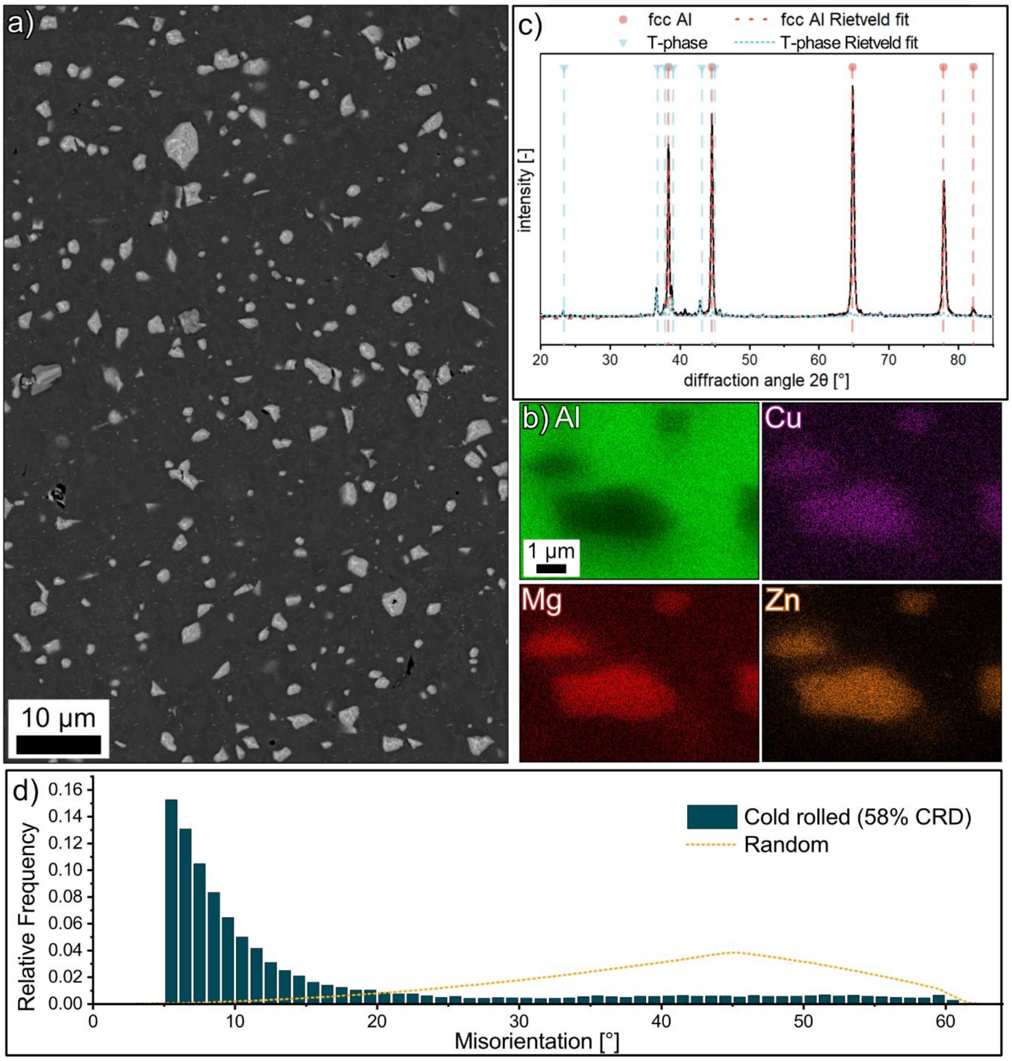

Figure 6-1: SEM-BSE micrograph of cold-rolled 5/7 crossover alloy (a); EDX mapping of found particles indicating T-phase (b), which can be verified by the XRD-analysis diffractogram (c); distribution of grain boundary misorientation compared to random after Mackenzie (d) [69]

Figure 6-2 demonstrates that in addition to the T-phase, dispersoids are also present in the alloy. The measurement was made after R2 (480°C/1min/WQ) to dissolve T-phase and to avoid overlapping effects with T-phase particles. This approach is suitable because the dispersoids are unaffected by the relatively low temperatures during the heat treatment. The element composition of the dispersoids present and thermodynamic calculations [70] indicate a mixture of E-Phase $Al_{18}Mg_3Cr_2$ (with incorporated Zn, Cu and Mn), $Al_{11}(Cr,Mn)_2$, $Al_6(Mn,Fe)$, Al_9Mn_2Si and $Al_7(Mn,Fe,Cu)$. No further investigation of the exact nature of the dispersoids was conducted as this is beyond the scope of this study. The volume fraction and size distribution were calculated from SEM/BSE micrographs according to the method of Österreicher et. al [62], with the average composition of the dispersoids obtained from STEM/EDX measurements. Because a high fraction of the STEM/EDX measurements show an element composition close to E-Phase, this phase is considered the main dispersoid phase in all further investigations. The average radius of the dispersoids was measured as 58 nm, deduced from SEM/BSE images with a calculated volume fraction of 0.6 %.

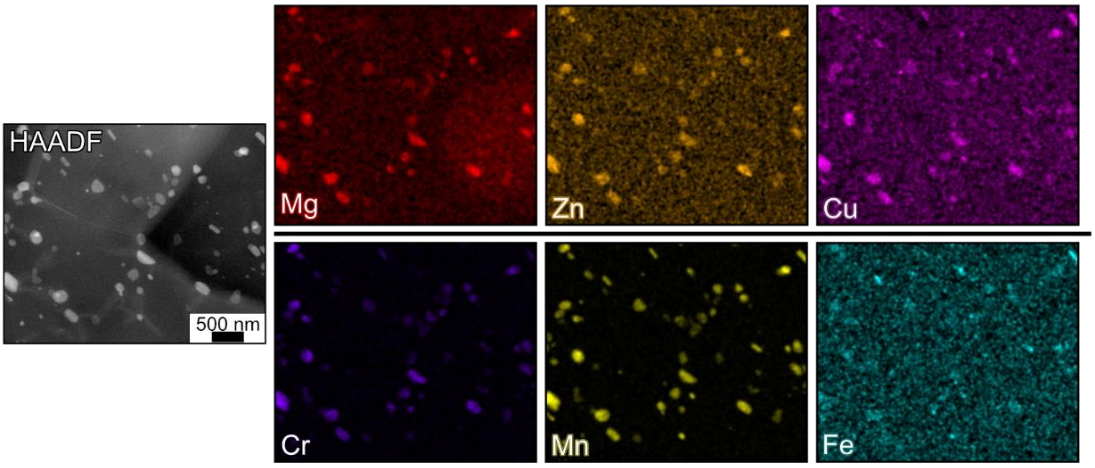

Figure 6-2: STEM/EDX mapping of dispersoid in the alloy after R2; the scale bar of the HAADF image also applies for the EDX images

Figure 6-3 shows the effect of the heat treatments on the T-phase. After R1 (380°C/5min/WQ) the BSE micrograph (see Figure 6-3a) displays the particles remaining. These particles are comparable in size to those found in the cold rolled sheet. Feature analysis of the material after R1 reveals that the particle density is somewhat lower than in the cold rolled state (see Table 6-3) (note that thermodynamic calculations revealed the solvus temperature of the T-phase to be about 415 °C [70]). Table 6-3 summarizes the results of automated feature analysis of particles in the cold rolled state and after R1 and R2. The area fraction of particles was assumed to be the same as per unit volume, which is considered a valid estimation for coarse particles [61]. The calculated volume fraction of 6.55 % is in good agreement with the weight fraction determined by Rietveld refinement as the theoretical density of the T-phase is reported to be 2.736 g/cm^3 [67]. The mean roundness was calculated by dividing the perimeter of a circle with the same area by the measured perimeter of the particle.

While the number of constituent particles containing Fe, Si, Mn, and Cr (primary phases or large dispersoids) is at the same level as in the cold rolled state after all conducted heat treatments, the number of particles without those elements is somewhat lower. After the R2 solution treatment (480°C/1min/WQ), which is above the solvus temperature of the T-phase (Figure 6-3b), the number of particles drops drastically. In the solution annealed condition, some porosity is perceptible (Figure 6-3b). This can either have been caused by the thermomechanical treatment or be an artifact of the polishing process.

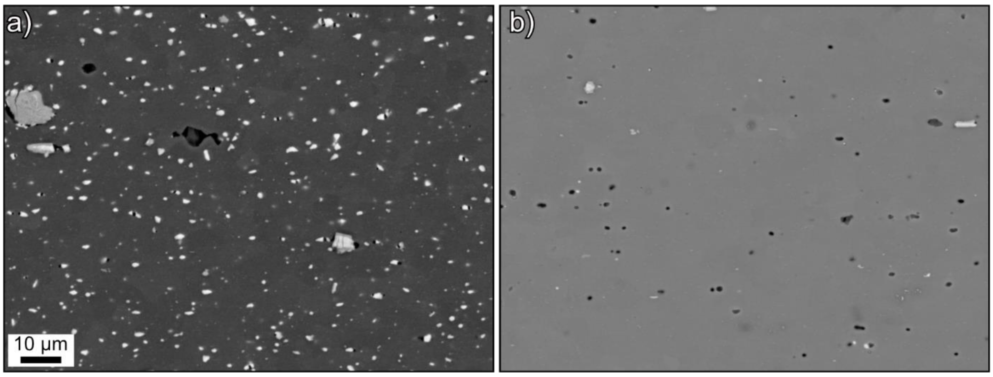

Figure 6-3: SEM/BSE microstructure images of the sheet after recrystallization annealing (380°C/5min/WQ) (a) and solution annealing (480°C/1min/WQ) (b)

Table 6-3: Particle properties from feature analysis after different heat treatments of sheets with 58% CRD

Condition	**Measured particles [particle/mm2]**	**Mean ECD [µm]**	**Mean roundness**	**Volume fraction [%]**	**Particles with Fe, Si, Mn, Cr [%]**	**Particles without Fe, Si, Mn, Cr [%]**
Cold-rolled 58% CRD	38348	1.4	0.84 ± 0.1	6.55	13	87
R1	28071	1.4	0.85 ± 0.2	5.31	15	85
R2	3567	1.3	0.77 ± 0.22	0.75	100	0

6.3.2 Grain size evolution

Figure 6-4 displays the grain size of samples after heat treatment routes R1–R4 in the 58 % CRD sheet investigated. Table 6-4 presents the corresponding grain analysis values for ECD and grain roundness.

Figure 6-4a illustrates the homogeneously fine grain size after recrystallization and solution annealing, respectively, using inverse pole figure (IPF) colour maps. Figure 6-4c displays the normalized distribution of grain size classes for divisions starting from 0.5 µm with a class range of 1 µm. Heat treatment at 380 °C, i.e. below the solvus temperature of the T-phase (R1), results in a large number of small grains with a sharp peak at around 3.5 µm. A subsequent heat treatment at 480 °C in a plate press (R3) does not shift the peak but lowers its height due to slight coarsening. While grains after R1 have a size of 4.7 ± 2.4 µm, the peak increases with subsequent heating by 0.44 µm to a grain size of 5.1 ± 2.6 µm (R5). As this coarsening is within the standard deviation of the whole assembly, it is considered stable. When the first heat treatment step is performed at 480 °C, i.e., above the solvus temperature of the T-phase, a slight peak shift from 3.5 µm (R1) to 4.5 µm (R2) is observed and the average grain size increases from 4.7 ± 2.4 µm to 5.0 ± 2.3 µm. Besides the stability of the grain assembly for longer holding times, even at higher temperatures, it is worth noting that the roundness of the grains (0.8 ± 0.1) is independent of the heat treatment route.

The effect of the low heating rate in the air circulation furnace can be seen in Figure 6-4b and the line for R4 in Figure 6-4c. Compared to a high heating rate in a salt bath (Figure 6-4a), the grain distribution is not as uniform at a lower heating rate (Figure 6-4b): coarser grains are occasionally visible. While almost no grains are observed for classes >11.5 µm for routes conducted in a salt bath, R4 shows a significant number of grains up to 14.5 µm. The deviation is probably due to recovery effects prior to recrystallisation, meaning that particles have been less successful in serving as nucleation sites for new grains.

Figure 6-4d displays the grain boundary misorientation distribution after the various heat treatment routes. (Note that Humphreys et al. [71] links the effect of solutes on the grain boundary mobility to the randomness of the grain boundary misorientation distribution. For this reason all EBSD datasets were evaluated for the grain boundary misorientation distribution with respect to the random distribution after Mackenzie [69], which is indicated as blue dotted lines).

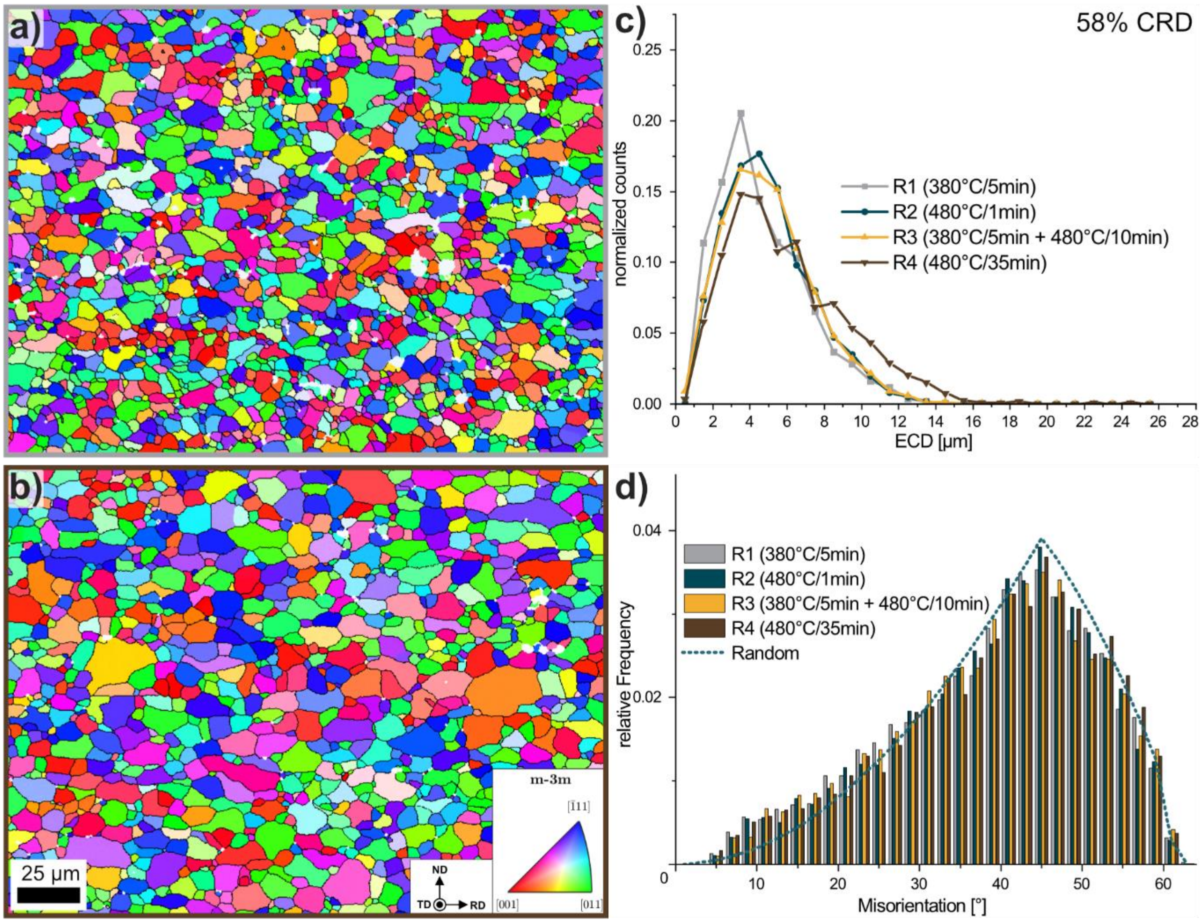

Figure 6-4: SEM-EBSD IPF mapping and >5° grain boundaries of material with 58 % CRD after heat treatment: recrystallization annealing in a salt bath R1 (380/5min) (a); solution annealing in air furnace R4 (480°C/35min) (b); points not indexed as fcc aluminum phase displayed in white; histogram of normalized grain size distribution (c); distribution of grain boundary misorientation compared to random after Mackenzie (d) [69]

Table 6-4: EBSD measurements showing morphological parameters of grains after different heat treatment routes, for samples with 58 % CRD

Condition	ECD [µm]	Roundness
R1	4.7 ± 2.4	0.8 ± 0.1
R2	5.0 ± 2.3	0.8 ± 0.1
R3	5.1 ± 2.6	0.8 ± 0.1
R4	6.0 ± 3.2	0.8 ± 0.1
R5	5.2 ± 2.5	0.8 ± 0.1

Figure 6-5 shows the EBSD micrographs, grain size distribution and grain boundary misorientation plots for samples with 85 % CRD. Table 6-5 displays the corresponding average ECD and roundness values. The trends correspond to the findings for the sample with 58 % CRD. As expected, the grain size decreased with increased cold working and thus higher dislocation density. This effect is more pronounced for R1 and R2 than for R3 and R4. This can probably be attributed to grain growth due to high-temperature heating in R3 and the reduction of dislocation density through recovery in R4. The grain boundary misorientation distribution is close to random, which – as in samples with 58 % CRD – is also stable for long holding times at higher temperatures. The overall grain assemblies for all heat treatment routes also exhibit a high degree of roundness.

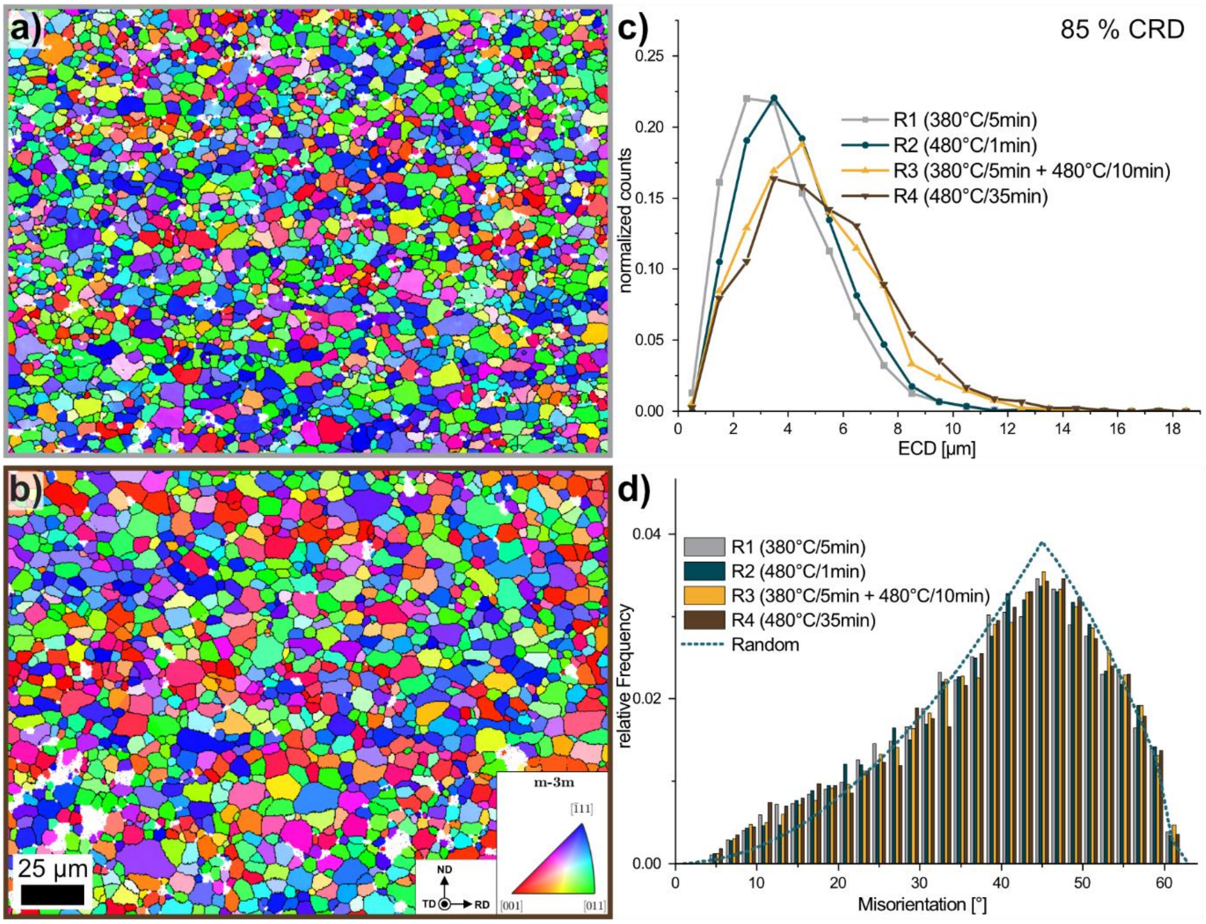

Figure 6-5: SEM-EBSD IPF mapping and >5° grain boundaries of material with 85 % CRD after heat treatment: recrystallization annealing in a salt bath (380/5min) (a); solution annealing in an air furnace (480°C/35min) (b); points not indexed as fcc aluminum phase displayed in white; histogram of normalized grain size distribution (c); distribution of grain boundary misorientation compared to random after Mackenzie (d) [69]

Table 6-5: EBSD measurements showing morphological parameters of grains after different heat treatment routes, for samples with 85 % CRD

Condition	ECD [µm]	Roundness
R1	3.7 ± 1.7	0.8 ± 0.1
R2	4.2 ± 1.8	0.9 ± 0.1
R3	4.8 ± 2.2	0.9 ± 0.1
R4	5.2 ± 2.4	± 0.1

6.3.3 Texture development

The processing routes described (R1–R5) generate very weak textures (mtex texture index <1.17 with a kernel halfwidth of 5° for the ODF calculation), as shown in Figure 6-11 of the appendix. Nevertheless, differences in characteristics can be observed. Material that is directly heated above the solvus temperature of the T-phase (R2) tends to develop an increased fraction of grains with rotated cube orientations (10°–

25° in normal direction), with slightly higher intensities after greater cold rolling reductions. Keeping the samples at 470 °C for 24 h (R5) weakens the rotated cube orientations, and S and Bs orientations emerge. In contrast, samples that recrystallize while T-phase is present (R1) still tend to form new grains in rotated cube orientation closer to CubeND45 ({001}<110>). After cold rolling to 85 %, CubeND45 dominates and spreads towards Q {013}<231>.

6.3.4 Behaviour at elevated temperatures

To determine the superplastic forming potential of the material, high-temperature tensile testing was carried out.

Figure 6-6a displays the true stress-strain diagram of a 1 mm thick sheet with 58% CRD after solution annealing (R2). Testing was performed at three different strain rates of $1*10^{-2}$, $5*10^{-4}$ and $5*10^{-5}$ s^{-1}, after reheating the samples to 470 °C and holding the temperature for 10 min prior to testing. The strain rate of $1*10^{-2}$ s^{-1} represents the QPF regime [36], while the others are typical of SPF processes [72]. In the QPF strain rate regime a true elongation to fracture of 1.21 ± 0.04 was achieved, corresponding to a technical elongation to fracture of 235 ± 17 %, while elongations to fracture of 1.69 ± 0.02 (445 ± 10 %) and 1.64 ± 0.05 (417 ± 25 %) were measured in the SPF regime at strain rates of $5*10^{-4}$ and $5*10^{-5}$ s^{-1}, respectively. Figure 6-6b displays a sample before and after testing at a strain rate of $5*10^{-5}$ s^{-1}, where an elongation to fracture of 1.64 (417 %) was achieved.

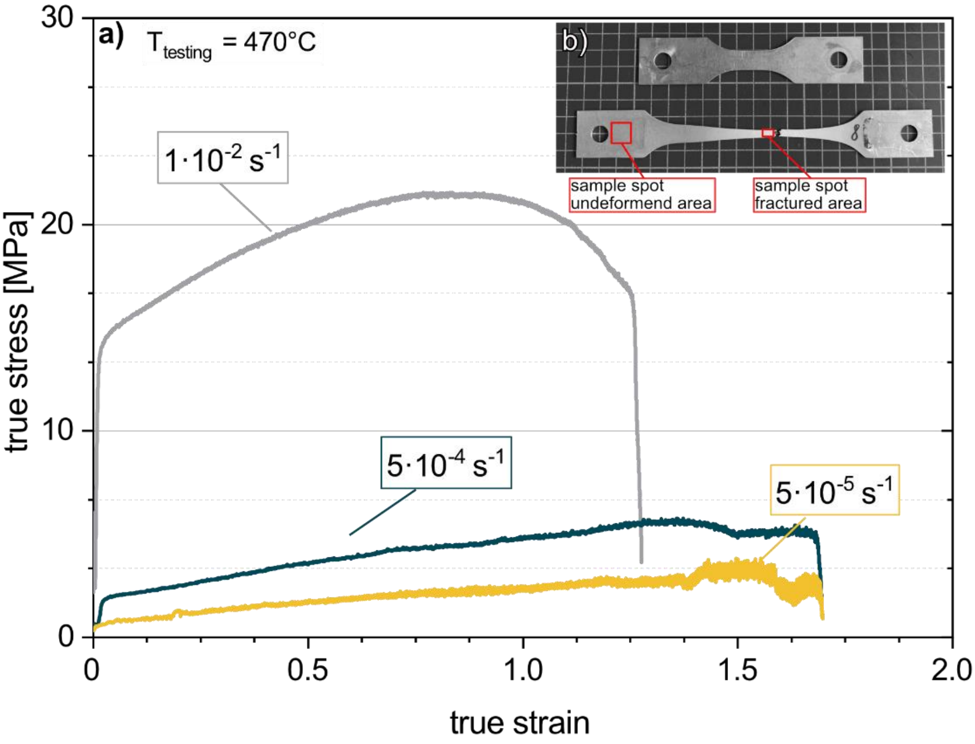

Figure 6-6: True stress-true strain curves of sheets with 58% CRD after solution annealing in a salt bath (480°C/1min). Test conducted at a temperature of 470 °C and constant strain rates of $1\cdot10^{-2}$ s^{-1} (gray), $5\cdot10^{-4}$ s^{-1} (blue) and $5\cdot10^{-5}$ s^{-1} (yellow) (a). Sample before and after tensile testing at a strain rate of $1\cdot10^{-5}$ s^{-1} with locations for sampling shown in red. The grid cell size is 1 cm (b)

Figure 6-7 presents the undeformed and deformed zones of the samples after high-temperature testing (see areas marked in red in Figure 6-6b). The IPF colour map in Figure 6-7a displays the undeformed zone of a sample drawn with $5*10^{-5}$ s^{-1}. After 24 h at 470 °C (R5) the average grain size is 5.2 ± 2.5 µm, with a roundness of 0.8 ± 0.1. The average misorientation of the grain bond has remained nearly unchanged at 39.8 ° (Figure 6-7b) and is still close to random. This indicates the enormous stability of the grain structure even for long periods at high temperatures. Figure 6-7c-e shows the band contrast in the strongest deformed area close to the fracture surface. No grain elongation or coarsening can be observed in the specimen drawn at a high strain rate (see Figure 6-7c): the average grain size is measured as 5.6 ± 3.9 µm. At lower strain rates the grains start to elongate slightly and to coarsen. The grain sizes observed are 6.1 ± 5.3 µm and 9.7 ± 7.2 µm for strain rates $5*10^{-4}$ and $5*10^{-5}$ s^{-1} respectively. The grain elongation can be displayed as the mean grain roundness, which decreases from 0.8 ± 0.1 to 0.7 ± 0.1 with increasing strain rate. All specimens display voids that are sparse at high strain rates and become coarser and more frequent at lower strain rates.

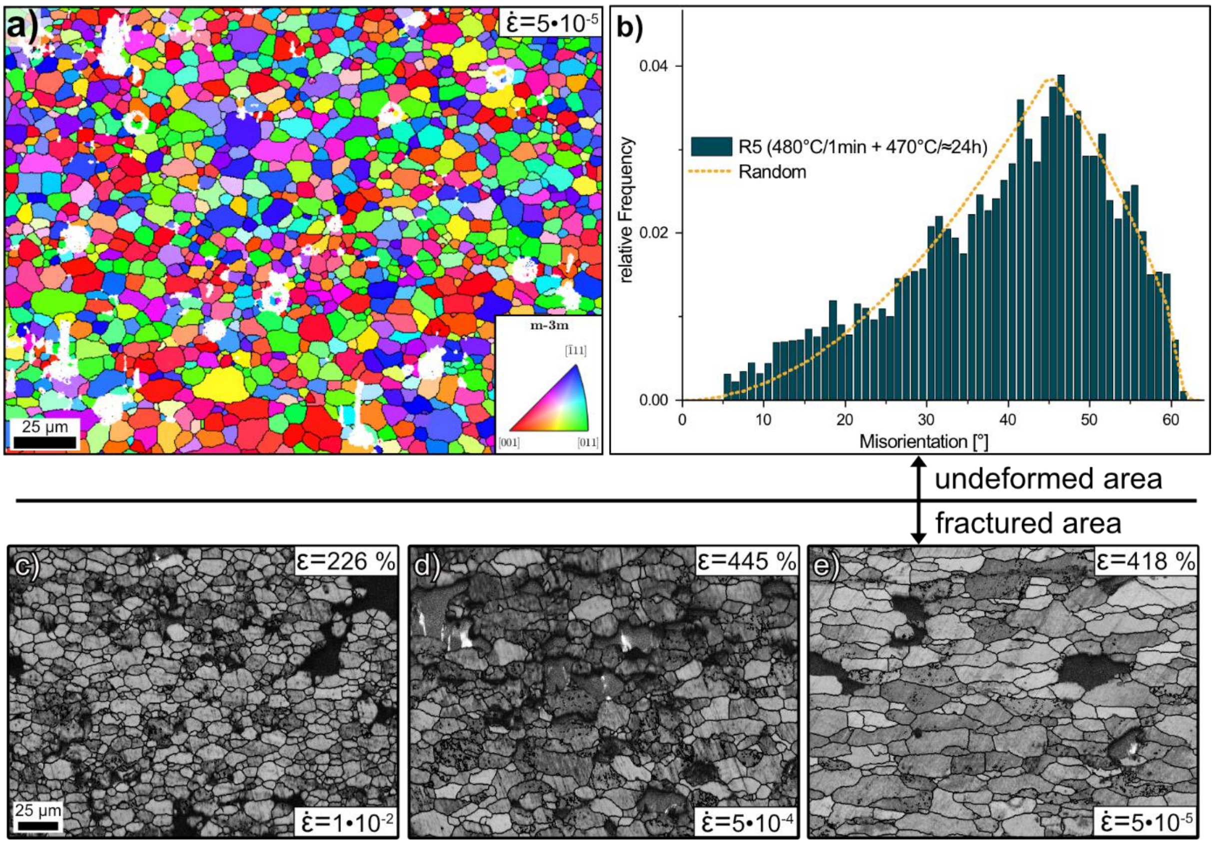

Figure 6-7: SEM-EBSD IPF mapping and >5° grain boundaries of material with 58 % CRD after heat treatment: solution annealing in a salt bath and (480°C/1min) and subsequent HT-tensile testing (470°C/24h) (a); points not indexed as fcc aluminum phase displayed in white; distribution of grain boundary misorientation compared to random after Mackenzie (b) [69]; EBSD Band contrast micrograph of the deformed area close to fracture surface; test temperature 470°C with strain rates of 10^{-2} s^{-1} (c), $5*10^{-4}$ s^{-1} (d) and $5*10^{-5}$ s^{-1} (e); load direction is horizontal

6.3.5 Ageing behaviour

Figure 6-8 shows the yield strength (YS), ultimate tensile strength (UTS) and elongation to fracture (A) of samples after solution annealing and after paint-bake treatment. The colours distinguish between samples quenched in water (WQ) and compressed air (CAQ) after solution annealing. As the purpose of this treatment is to evaluate hardening potential after forming, it must again be pointed out that solution annealing corresponds to the hot forming step because both take place at the same temperature level. In the following, the term Δ is used to describe the difference between WQ and CAQ samples in the same condition.

After solution annealing the YS and UTS are mostly unaffected by the cooling conditions (ΔYS=2.9 MPa, ΔUTS=9.2 MPa), while A is 4.9 % lower for CAQ than WQ. The elongation at fracture after the PB is about 5 % higher for the WQ sample than for the CAQ sample, with absolute values of 12 % and 7 % respectively. At about 113 MPa, the paint-bake response (PBR) is independent of the cooling rate, resulting in a YS of 398 MPa for the WQ sample and 371 MPa for the CAQ sample.

The variations in mechanical properties are quite minimal compared to other alloys. Liu Q. et al [73] shows the effect of quenching on mechanical properties in 7xxx series alloys (with high Zn/Mg-ratios), indicating the comparably low quench rate sensitivity of the crossover alloy with a low Zn/Mg-ratio used here.

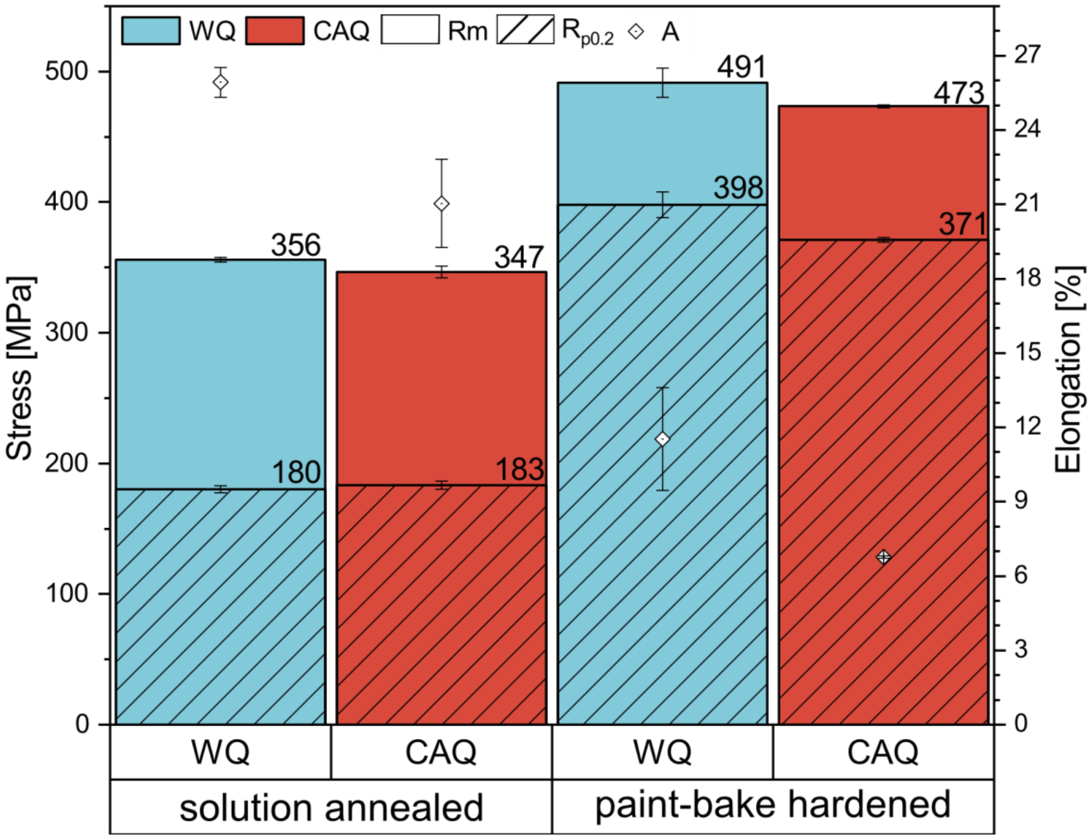

Figure 6-8: Mechanical properties of 1 mm 5/7 crossover sheet after solute annealing (SA) in a salt bath (480°C/1min) with water quenching (WQ) and compressed air quenching after SA and paint-bake (PB) (180°C/20min); pre ageing (PA) (100°C/5h) was conducted after SA and 14 days of natural ageing (NA) at 25 °C were deployed between PA and PB

6.4 Discussion

This study reports on the process of obtaining a fine-grained crossover alloy and its suitability for superplastic and quick plastic forming. Its main results can be summarized as follows:

- In the as-delivered cold rolled state, the alloy consists of a high fraction of coarse T-phase ($Mg_{32}(Al,Zn)_{49}$) precipitates and primarily fine E-Phase ($Al_{18}Mg_3Cr_2$) dispersoids. The T-phase particles may act as nuclei for new grains during recrystallization, generating a fine grain size far below 10 μm and a randomization of the grain boundary misorientation distribution. By increasing the dislocation density through higher CRD, the grain size can be reduced further.
- The grain size is exceptionally stable. It does not change even if the material is reheated to temperatures of 470°C (R5) and 480°C (R3), which are significantly higher than the recrystallization temperature of 380°C (R1) and lie above the solvus temperature of the T-phase. Nor does the average grain boundary misorientation change if held at high temperatures, but always remains close to random.
- Tensile testing at elevated temperatures of 470 °C demonstrates the suitability of the fine-grained crossover alloy for SPD and QPF processes. In the regime of QPF at a strain rate of $1*10^{-2}\ s^{-1}$ the alloy achieves an average elongation to fracture of 235 %. The highest elongation to fracture, 445 %, is seen at a strain rate of $5*10^{-4}\ s^{-1}$.
- The hardenability potential of the crossover alloy is maintained after simulated high-temperature forming. The alloy also exhibits low quench sensitivity. The YS value after a paint bake process deviates by only 18 MPa between air cooling and water quenching and nearly approaches 400 MPa.

These results are discussed in detail in the following.

6.4.1 Mechanism of grain refinement during recrystallization

The presence of coarse T-phase particles after recrystallization treatment (R1) (see Figure 6-3a) is the first indication that particle stimulated nucleation (PSN) is the main grain refinement mechanism during recrystallization. This is supported by observations made in Figure 6-9. After a short heat impulse, the recrystallization tends to start near the T-phase particles. The high resolution EBSD analysis (in the RD-TD plane) in Figure 6-9 shows this intermediate state after heating for 3 s to 380 °C. Figure 6-9a displays a common IPF map, showing the absence of preferred orientations in the RX grains. Figure 6-9b visualizes the local misorientations (indicative of a high density of geometrically necessary dislocations), which are significantly more numerous in the non-recrystallized areas which still exhibit deformation structures. The recrystallized grains show an even and low degree of local deformation. A comparison with Figure 6-9c also makes it apparent that the main deformed areas are near Brass {011}<112> and S{123}<624> orientations, which are typical orientations for cold rolled Al alloys. The newly formed grains often have a random orientation, with a slight tendency to C, rotated C (ND22°, ND45°), P{011}<566> and Q. The appearance of recrystallisation around the T-phase particles (yellow) and the orientation of the new grains are clear indications of PSN. The flower-like recrystallization shape is also considered to indicate PSN in the literature [49,74,75].

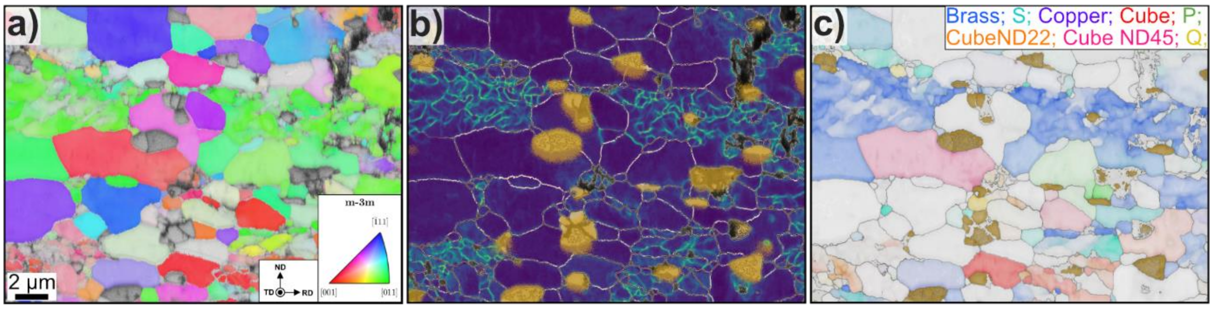

Figure 6-9: EBSD micrographs of a cold rolled sheet after 3s at 380°C in a salt bath; map in RD-ND plane with IPF colouring of the Al-matrix T-phase (a); KAM map (5th order), with an overlay of Zn-rich datapoints (indicator of T-phase) in yellow (b); relevant texture components with a tolerance angle of 10°; Zn-rich datapoints are again yellow (c)

By assuming at least one successful grain nucleation per particle, the resulting grain size after recrystallization (D_{rxx}) can be calculated using equation (6-1). It is directly related to the volume fraction N_v of particles with average diameter d_{PSN} [76]:

$$D_{rxx} = \overline{d_{PSN}} * N_v^{-\frac{1}{3}} \tag{6-1}$$

As described by Nes [77], the cold worked microstructure of the alloy consists of three main structural elements: the bimodal particle distribution of coarse particles (see Figure 6-1) and fine dispersoids (see Figure 6-2), and the subgrain structure from cold working. The fine dispersoids stabilize the subgrain structure by Smith-Zener pinning [78] and exhibit a drag force on the migrating subgrain boundaries (P_{SZ}). This retarding pressure counteracts the driving pressure for growth exerted by the dislocation density (P_D). Therefore, the number of nucleation events shrinks with increasing dispersoid content. The minimum size of a particle to successfully act as a nucleation site during recrystallization also increases. Its required minimum diameter (d_{min}) is described in relation to the driving and retarding pressure by the Gibbs-Thompson equation as [71,79]:

$$d_{min} = \frac{4\gamma_B}{P_D - P_{SZ}} = \frac{4\gamma_B}{\frac{\rho * G * b^2}{2} - \frac{3F_v * \gamma_{IF}}{2r}} \tag{6-2}$$

Table 6-6 lists the values for equation (6-2) relevant to the alloy. The interfacial energy of E-Phase particle was chosen as 500 mJ/m² as it is reported to be semi-coherent or incoherent with relation to the matrix [80–82].

Table 6-6: Factors, their values and origin for equation (6-2)

Factor	Value	Origin
Grain boundary energy (γ_{GB})	324 mJ/m^2	[83]
Dislocation density (ϱ)	58 % CRD: $8.97*10^{14}$ m^{-2} 85 % CRD: $11.6*10^{14}$ m^{-2}	Interpolated from [84]
Shear modulus (G)	$26*10^9$ Pa	[71]
Burgers vector (b)	$2.86*10^{-10}$ m	[71]
Volume fraction of small particles (F_v)	0.6 %	Calculated after [62]
Radius of small particles (r)	$5.8*10^{-8}$ m	Measured after [62]
Interfacial energy (γ_{IF})	500 mJ/m^2	-

By taking the particle parameters of the as-delivered material as constant, d_{min} is reduced to a function of the dislocation density. After calculating d_{min}, a new average d_{PSN} and N_v is calculated in which only particles larger than d_{min} are considered. Therefore, D_{rxx} can then also be calculated as a function of the dislocation density. The calculation provides d_{min} values of 1.48 µm and 1.13 µm for 58 % and 85 % CRD respectively. This raises the average particle diameter usable for PSN $(\overline{d_{PSN}})$ to 2.07 µm and 1.81 µm, resulting in a volume fraction N_v of 6.24 % and 7.40 % for 58 % and 85 % CRD, respectively. Thus, a grain size of 5.2 µm can be calculated for CRD of 58 % and 4.3 µm for CRD of 85 %. These figures agree well with the experimental results, where the grain size after heat treatment was measured to be 4.7–5.2 µm and 3.7–4.8 µm for 58 % and 85 % CRD, respectively. The grain sizes measured for R4 are not considered in the comparison because the calculation does not take into account the significant recovery effects upon slow heating prior to recrystallization. The effect of heating rate on recovery prior to recrystallization is addressed in various other publications [85–87].

6.4.2 Microstructure stability

Comparing the grain sizes of R2 (5.0 µm) and R5 (5.2 µm) makes the extraordinary stability of the grain structure obvious. The following factors may be involved in reducing grain boundary mobility:

- Solute drag at grain boundaries caused by the sizable content of main alloying elements, which tend to form grain boundary solute segregations
- Increased stability caused by the high average misorientation degree of the grain assembly, which serves as a preferential site for solute segregations
- Dragging force of the finely dispersed dispersoids

The recrystallization and heat treatments above the solvus temperature of the T-phase increase the content of dissolved alloying elements in the Al matrix, which tend to segregate [88,89] and thus affect the dragging force acting on the grain boundaries [90,91]. According to Humphreys et al. [71] the effect of decreasing grain boundary mobility with increasing solute segregation is particularly pronounced for random grain boundaries. This applies to the microstructure in this study. The almost perfect random misorientation observed in our samples is usually only observed in Al-Mg SPF alloys produced by SPD techniques [92–94]. The effect of solutes on the grain boundary migration energy in Al was investigated by Gordon and Vandermeer [95]. The alloy investigated in their study, like ours, had a high solute content and a nearly random distribution of grain boundary misorientation after recrystallization. The authors concluded that the activation energy for grain boundary migration is greatly increased by the solute content, and that therefore the grain arrangement will remain unchanged even after long annealing times at high temperatures.

A small grain size after primary recrystallization implies increased grain boundary energy, which is equivalent to a greater driving force for normal grain growth. However, the finely dispersed dispersoids present in the structure act as a retarding obstacle. This generates a balance equivalent to the Zener equation [96], which states that normal grain growth will be inhibited if the grain size reaches a critical value R_c:

$$R_c = K\frac{r}{f^m} \tag{6-3}$$

According to Manohar et al. [96,97], good agreement with experimental values is obtained if a value of 0.17 is used for the constant K and a value of 1 for the exponent m of the volume fraction. This generates a grain size value of approx. 3.2 μm. From this it can be deduced that the critical grain size has already been exceeded after primary recrystallization and no normal grain growth can be envisaged. Therefore, the grain assembly can be considered stable. If the porosity shown in Figure 6-3b is caused by processing, it may also contribute to the stability of the microstructure.

6.4.3 Hot forming

It is generally accepted that grain boundary segregation of alloying elements affects GBS and thus superplastic properties [98–100]. A particularly interesting effect is generated by Zn. Experimental findings [99] and ab initio calculations [100] indicate that an increased Zn content in Al-Mg alloys causes the formation of Zn grain boundary segregations and thus generates a noticeable decrease in the barrier to grain boundary sliding and an increase in SRS. Recent findings [101] also link the formation of Zn layers at grain boundaries in the alloy Al-15 Zn (at.%) to enhanced room temperature GBS. In the 5/7 crossover alloy in this study we addressed the ideal case of high Zn content in Al-Mg, with the resulting increased Zn segregation level and positive effect on superplasticity. The initial grain boundary misorientation distribution, with its large amount of high angle grain boundaries (see Figure 6-4d), is also very beneficial for GBS [30].

Because the requirements for GBS have been fulfilled, one would expect grain elongation at fast strain rates due to solute drag creep and grain rotation, accompanied by grain growth at slow strain rates as reported by Pérez-Prado et. al. [102]. However, Figure 6-7c shows that the 5/7 crossover alloy behaves quite differently. The grains remain almost the same size (5.6 ± 3.9 μm) and shape as initially observed at high strain rates, and start to elongate at slower strain rates.

Mukhopadhyay et. al [103] demonstrate for an Al-Zn-Mg-Cu-Zr alloy tested at 475 °C at a strain rate of 10^{-2} s^{-1} that the grains do not elongate as expected in the QPF region [35,104,105], but instead recrystallize and coarsen. They also link the decrease in stress over the experimental duration to the higher degree of recrystallization and the formation of voids. The same behaviour was observed in this study for a sheet tested at 470 °C and 10^{-2} s^{-1} (see Figure 6-6a, grey curve; and Figure 6-7c). Mikhalovskaya et. al [106] even see a decrease in grain size during tensile testing of an Al–(3.5–4.5)Zn–(3.5–4.5)Mg–(0.7–0.9)Cu–(1.0–3.0)Ni–(0.25–0.30)Zr (wt.%) alloy. They observe a reduction in grain size with increasing recrystallization from 2.4 μm to 1.8 μm at a temperature of 440 °C and an SR of $3x10^{-3}$ s^{-1}. These observations are quite consistent with those of this study.

Ma et al. [107] describe the superplastic deformation behaviour of friction stir welded alloy 7075. They see evidence of GBS at a forming temperature of 490 °C with a strain rate of $3*10^{-3}$ s^{-1} and an m-value of 0.5. With increasing strain the evidence for GBS increases, as does the grain elongation. According to Li et al. [108] GBS is accompanied by intragranular dislocation creep and therefore by grain elongation. This is caused by grain rotation and grain growth due to grain coalescence. With growing grains, the amount of dislocation creep and grain elongation also increases. These observations are consistent with those made in this study for the low strain rates $5*10^{-4}$ s^{-1} and $5*10^{-5}$ s^{-1} (see Figure 6-7c and d). Because grains have more time to rotate and grow, the effect is more pronounced at lower strain rates. The latter consideration is even more evident if testing times are considered. At a strain rate of $5*10^{-4}$ s^{-1} the time required to reach an elongation of 400 % is 2 h, while it takes 22 h at a strain rate of $5*10^{-5}$ s^{-1} to achieve the same.

6.4.4 Age hardenability

The Al-Mg alloys of the 5xxx family often used for SPF processes are not age-hardenable and retain their modest yield strength after SPF forming. The situation is completely different for the 5/7 crossover alloy presented here. Figure 6-8 demonstrates the good age hardenability of the alloy, even at low quenching rates. Graf et. al [109] investigated the difference in precipitation behavior between a 7xxx series alloy (high Zn/Mg-ratio) and a crossover alloy (low Zn/Mg ratio). They found a critical quench rate where no precipitation during quenching occurs, of 100 K/s for 7xxx series alloys and 1 K/s for crossover alloys. This indicates the crossover alloy's low quench sensitivity. It is a good explanation for the equal age-hardening response observed at both cooling rates applied in this study, as the quench rate for the CAQ cooled sample is well above 1 K/s.

6.5 Conclusion

This study presents an industrially viable way to produce fine-grained crossover alloys with grain sizes of far below 10 μm for sheet forming operations. The study identifies the main grain refinement mechanism in the process as particle stimulated nucleation. Using coarse T-phase particles, Figure 6-10 displays a schematic illustration of the PSN grain refinement process in these crossover alloys. Because the phase is dissolved into the matrix during and after recrystallization it can no longer exert the same detrimental effect on mechanical properties as would non-dissolvable phases of the same size (and leading to age-hardening at a later processing stage).

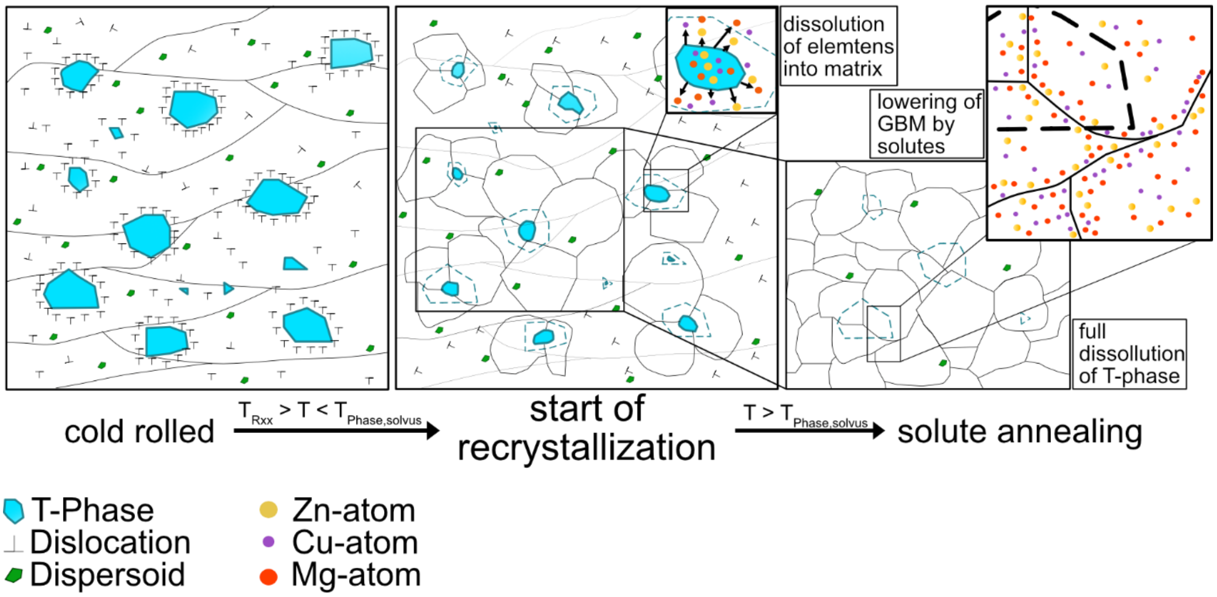

Figure 6-10: Schematic illustration of the grain refinement process by PSN in 5/7 crossover alloys with subsequential stabilization by solute atoms

The structure exhibits outstanding stability, showing minimal grain growth even after holding at 470 °C for 24 h after solute annealing. The high stability of the grain assembly is due firstly to the increased effect of the solute content on grain boundary mobility caused by the close-to-random grain boundary misorientation distribution. Secondly, it can be clearly shown that the dispersoids present exhibit a Zener size limit of approx. 3.2 µm, meaning that after primary recrystallization the grain assembly has already exceeded the critical grain size and no normal grain growth can be envisaged.

High-temperature tensile testing demonstrated the alloys' suitability for superplastic and quick plastic forming processes. The alloys achieve elongation values of up to 445 % and 235 % respectively in these regimes, figures which are comparable to those featured by industrially established alloys.

The study illustrates the alloys' high preserved age hardening potential based on two different quench rates. Independent of either, the alloys showed an age-hardening response after a paint-bake cycle of close to 400 MPa yield strength, and 500 MPa tensile strength.

The properties demonstrated above, together with their potential for simple production and large-scale commercial use, make fine-grained 5/7 aluminum crossover alloys very promising for high-temperature sheet forming operations.

6.6 Appendix

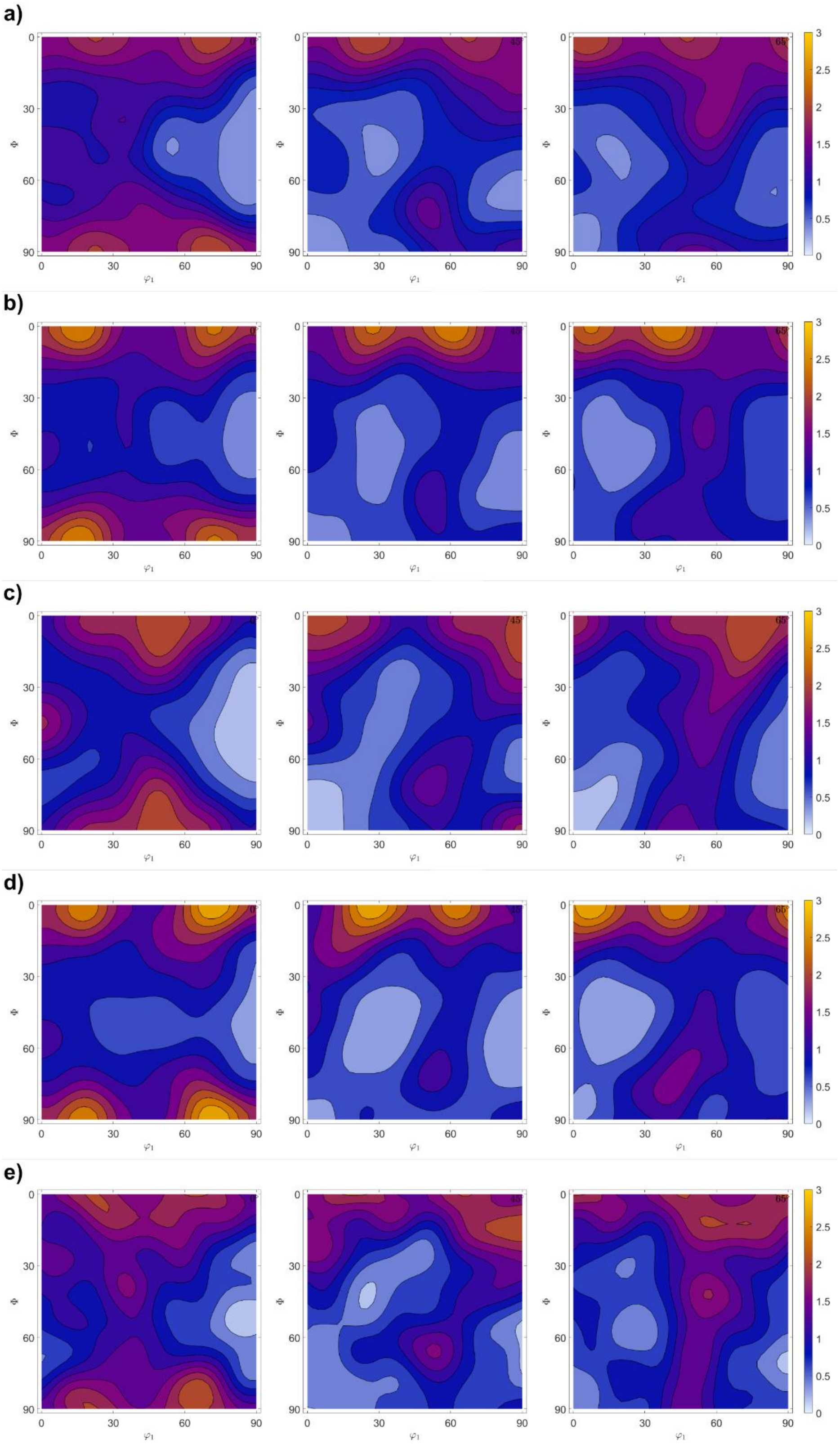

Figure 6-11: Sections of orientation distribution functions at phi2 = 0°, 45° and 65° for conditions after R1 for samples with 58 %(a) and 85 % (c) CRD; after R2 for samples with 58 %(b) and 85 % (d) CRD; and after R5 for samples with 58 % CRD (e)

6.7 References

[1] D. Carle, G. Blount, The suitability of aluminium as an alternative material for car bodies, Materials & Design 20 (1999) 267–272.

[2] A. Poznak, D. Freiberg, P. Sanders, Automotive Wrought Aluminium Alloys, in: Fundamentals of Aluminium Metallurgy, Elsevier, 2018, pp. 333–386.

[3] J. Hirsch, Aluminium in Innovative Light-Weight Car Design, Materials Transactions 52 (2011) 818–824.

[4] L. Stemper, M.A. Tunes, R. Tosone, P.J. Uggowitzer, S. Pogatscher, On the potential of aluminum crossover alloys, Progress in Materials Science (2021).

[5] A. Bigot, P. Auger, S. Chambreland, D. Blavette, A. Reeves, Atomic Scale Imaging and Analysis of T' Precipitates in Al-Mg-Zn Alloys, Microsc. Microanal. Microstruct. 8 (1997) 103–113.

[6] G. Bergman, J. Waugh, L. Pauling, The crystal structure of the metallic phase Mg32(Al,Zn)49, Acta Cryst. 10 (1957) 254–259.

[7] J.H. Auld, B.E. Williams, X-ray powder data of T phases composed of aluminium and magnesium with silver, copper or zinc, Acta Cryst. 21 (1966) 830–831.

[8] Y. Song, S. Zhan, B. Nie, H. Qi, F. Liu, T. Fan, D. Chen, First-Principles Investigations on Structural Stability, Elastic Properties and Electronic Structure of Mg32(Al,Zn)49 Phase and MgZn2 Phase, Crystals 12 (2022) 683.

[9] Y. Zou, X. Wu, S. Tang, Q. Zhu, H. Song, M. Guo, L. Cao, Correlation between bulk and precipitate composition in Al-Zn-Mg-Cu alloys, Philosophical Magazine Letters (2021) 1–12.

[10] H. Liu, Z. Zhang, Di Zhang, J. Zhang, The effect of Ag on the tensile strength and fracture toughness of novel Al-Mg-Zn alloys, Journal of Alloys and Compounds 908 (2022) 164640.

[11] L. Stemper, M.A. Tunes, P. Oberhauser, P.J. Uggowitzer, S. Pogatscher, Age-hardening response of AlMgZn alloys with Cu and Ag additions, Acta Materialia 195 (2020) 541–554.

[12] Y. Geng, Q. Song, Z. Zhang, Y. Pan, H. Li, Y. Wu, H. Zhu et al., Quantifying early-stage precipitation strengthening of Al–Mg–Zn(-Cu) alloy by using particle size distribution, Materials Science and Engineering: A 839 (2022) 142851.

[13] L. Stemper, M.A. Tunes, P. Dumitraschkewitz, F. Mendez-Martin, R. Tosone, D. Marchand, W.A. Curtin et al., Giant hardening response in AlMgZn(Cu) alloys, Acta Materialia 206 (2021) 116617.

[14] C. Cao, Di Zhang, L. Zhuang, J. Zhang, Improved age-hardening response and altered precipitation behavior of Al-5.2Mg-0.45Cu-2.0Zn (wt%) alloy with pre-aging treatment, Journal of Alloys and Compounds 691 (2017) 40–43.

[15] L. Stemper, B. Mitas, T. Kremmer, S. Otterbach, P.J. Uggowitzer, S. Pogatscher, Age-hardening of high pressure die casting AlMg alloys with Zn and combined Zn and Cu additions, Materials & Design 181 (2019) 107927.

[16] Y. Geng, Di Zhang, J. Zhang, L. Zhuang, On the suppression of Lüders elongation in high-strength Cu/Zn modified 5xxx series aluminum alloy, Journal of Alloys and Compounds 834 (2020) 155138.

[17] Y. Geng, Di Zhang, J. Zhang, L. Zhuang, Zn/Cu regulated critical strain and serrated flow behavior in Al–Mg alloys, Materials Science and Engineering: A 795 (2020) 139991.

[18] Y. Pan, Di Zhang, H. Liu, L. Zhuang, J. Zhang, Precipitation hardening and intergranular corrosion behavior of novel Al–Mg–Zn(-Cu) alloys, Journal of Alloys and Compounds 853 (2021) 157199.

[19] C. Cao, Di Zhang, X. Wang, Q. Ma, L. Zhuang, J. Zhang, Effects of Cu addition on the precipitation hardening response and intergranular corrosion of Al-5.2Mg-2.0Zn (wt.%) alloy, Materials Characterization 122 (2016) 177–182.

[20] M.C. Caroll, M.J. Mills, G.S. Daehn, B.R. Dunbar, Effects of Zn additions on the grain boundary precipitation and corrosion of Al-5083, Scripta Materialia 42 (2000) 335–340.

[21] C. Meng, Di Zhang, L. Zhuang, J. Zhang, Correlations between stress corrosion cracking, grain boundary precipitates and Zn content of Al–Mg–Zn alloys, Journal of Alloys and Compounds 655 (2016) 178–187.

[22] Di Zhang, X. Wang, Y. Pan, S. Hou, J. Zhang, L. Zhuang, L. Zhou, Friction stir welding of novel T-phase strengthened Zn-modified Al–Mg alloy, J Mater Sci (2020).

[23] Y. Pan, Di Zhang, H. Liu, Z. Zhang, H. Li, L. Zhuang, J. Zhang, Reducing welding hot cracking of high-strength novel Al–Mg–Zn–Cu alloys based on the prediction of the T-shaped device, Science and Technology of Welding and Joining 25 (2020) 483–489.

[24] M.A. Tunes, L. Stemper, G. Greaves, Uggowitzer, Peter, J., S. Pogatscher, Metal Alloy Space Materials: Prototypic Lightweight Alloy Design for Stellar‐Radiation Environments (Adv. Sci. 22/2020), Advanced Science (2020) 2070126.

[25] J.S. Vetrano, C.A. Lavender, C.H. Hamilton, M.T. Smith, S.M. Bruemmer, Superplastic behavior in a commercial 5083 aluminum alloy, Scripta Metallurgica et Materialia 30 (1994) 565–570.

[26] I. Vysotskiy, K. Kim, S. Malopheyev, S. Mironov, R. Kaibyshev, Superplastic behavior of friction-stir welded Al–Mg–Sc–Zr alloy in ultrafine-grained condition, Transactions of Nonferrous Metals Society of China 32 (2022) 1083–1095.

[27] R. Verma, A.K. Ghosh, S. Kim, C. Kim, Grain refinement and superplasticity in 5083 Al, Material Science and Engineering A191 (1995) 143–150.

[28] N. Ridley, Metals for superplastic forming, in: Superplastic Forming of Advanced Metallic Materials, Elsevier, 2011, pp. 3–33.

[29] M.-A. Kulas, W.P. Green, E.M. Taleff, P.E. Krajewski, T.R. Mcnelley, Deformation mechanisms in superplastic AA5083 materials, Metall and Mat Trans A 36 (2005) 1249–1261.

[30] O. D. Sherby, J. Wadsworth, Superplasticity and superplastic forming processes.

[31] L. Bhatta, A. Pesin, A.P. Zhilyaev, P. Tandon, C. Kong, H. Yu, Recent Development of Superplasticity in Aluminum Alloys: A Review, Metals 10 (2020) 77.

[32] R.B. Figueiredo, T.G. Langdon, Effect of grain size on strength and strain rate sensitivity in metals, J Mater Sci 57 (2022) 5210–5229.

[33] J.W. Edington, K.N. Melton, C.P. Cutler, Superplasticity, Progress in Materials Science 21 (1976) 61–170.

[34] X. Wang, Q. Li, R. Wu, X. Zhang, L. Ma, A Review on Superplastic Formation Behavior of Al Alloys, Advances in Materials Science and Engineering 2018 (2018) 1–17.

[35] T.R. Mcnelley, K. Oh-ishi, A.P. Zhilyaev, S. Swaminathan, P.E. Krajewski, E.M. Taleff, Characteristics of the Transition from Grain-Boundary Sliding to Solute Drag Creep in Superplastic AA5083, Metall and Mat Trans A 39 (2008) 50–64.

[36] P.E. Krajewski, J.G. Schroth, Overview of Quick Plastic Forming Technology, MSF 551-552 (2007) 3–12.

[37] R. Boissiere, S. Terzi, J.J. Blandin, L. Salvo, Quick-plastic forming: Similarities and differences with super-pastic forming, EuroSPF08 Sep 2008 Carcassonne, France. hal-00359715.

[38] E.M. Taleff, G.A. Henshall, T.G. Nieh, D.R. Lesuer, J. Wadsworth, Warm-temperature tensile ductility in Al−Mg alloys, Metall Mater Trans A 29 (1998) 1081–1091.

[39] R.-G. Guan, Di Tie, A Review on Grain Refinement of Aluminum Alloys: Progresses, Challenges and Prospects, Acta Metall. Sin. (Engl. Lett.) 30 (2017) 409–432.

[40] S.V. Dobatkin, E.N. Bastarache, G. Sakai, T. Fujita, Z. Horita, T.G. Langdon, Grain refinement and superplastic flow in an aluminum alloy processed by high-pressure torsion, Materials Science and Engineering: A 408 (2005) 141–146.

[41] A.P. Zhilyaev, T.G. Langdon, Using high-pressure torsion for metal processing: Fundamentals and applications, Progress in Materials Science 53 (2008) 893–979.

[42] R.S. Mishra, Z.Y. Ma, Friction stir welding and processing, Materials Science and Engineering: R: Reports 50 (2005) 1–78.

[43] C. Xu, M. Furukawa, Z. Horita, T.G. Langdon, Developing High Strain Rate Superplasticity in Aluminum Alloys, MSF 475-479 (2005) 2949–2954.

[44] Y. Saito, N. Tsuji, H. Utsunomiya, T. Sakai, R.G. Hong, Ultra-fine grained bulk aluminum produced by accumulative roll-bonding (ARB) process, Scripta Materialia 39 (1998) 1221–1227.

[45] E. Bagherpour, N. Pardis, M. Reihanian, R. Ebrahimi, An overview on severe plastic deformation: research status, techniques classification, microstructure evolution, and applications, Int J Adv Manuf Technol 100 (2019) 1647–1694.

[46] L. Ye, X. Zhang, D. Zheng, S. Liu, J. Tang, Superplastic behavior of an Al–Mg–Li alloy, Journal of Alloys and Compounds 487 (2009) 109–115.

[47] S. Lee, A. Utsunomiya, H. Akamatsu, K. Neishi, M. Furukawa, Z. Horita, T. Langdon, Influence of scandium and zirconium on grain stability and superplastic ductilities in ultrafine-grained Al–Mg alloys, Acta Materialia 50 (2002) 553–564.

[48] J.A. Wert, N.E. Paton, C.H. Hamilton, M.W. Mahoney, Grain refinement in 7075 aluminum by thermomechanical processing, MTA 12 (1981) 1267–1276.

[49] F.J. Humphreys, The nucleation of recrystallization at second phase particles in deformed aluminium, Acta Metallurgica 25 (1977) 1323–1344.

[50] S. MacKenzie, Quenching Aluminum for Residual Stress and Distortion Control*, HTM Journal of Heat Treatment and Materials 75 (2020) 23–34.

[51] ASTM International, Standard Practice for Determining Average Grain Size Using Electron Backscatter Diffraction (EBSD) in Fully Recrystallized Polycrystalline Materials(E2627-13), West Conshohocken, PA, ASTM International, 10.1520/E2627-13R19.

[52] Oxford Instuments, AZtec EBSD Data Analysis User Guide.

[53] F.J. Humphreys, Grain and subgrain characterisation by electron backscatter diffraction, Journal of material science (2001) 3833–3854.

[54] R.L. Fullman, Measurement of Particle Sizes in Opaque Bodies, JOM 5 (1953) 447–452.

[55] Oxford Instuments, AztecCrystal User Guide.

[56] F. Bachmann, R. Hielscher, H. Schaeben, Texture Analysis with MTEX – Free and Open Source Software Toolbox, SSP 160 (2010) 63–68.

[57] J. Grasserbauer, I. Weißensteiner, G. Falkinger, S. Mitsche, P.J. Uggowitzer, S. Pogatscher, Evolution of Microstructure and Texture in Laboratory- and Industrial-Scaled Production of Automotive Al-Sheets, Materials (Basel, Switzerland) 13 (2020).

[58] B.G. Bartosiaki, J.A.M. Pereira, W.V. Bielefeldt, A.C.F. Vilela, Assessment of inclusion analysis via manual and automated SEM and total oxygen content of steel, Journal of Materials Research and Technology 4 (2015) 235–240.

[59] M. Nuspl, W. Wegscheider, J. Angeli, W. Posch, M. Mayr, Qualitative and quantitative determination of micro-inclusions by automated SEM/EDX analysis, Analytical and bioanalytical chemistry 379 (2004) 640–645.

[60] O. Walusinski, Doctoral Thesis, in: O. Walusinski (Ed.), Georges Gilles de la Tourette, Oxford University Press, 2018, pp. 129–144.

[61] C.W. Corti, P. Cotterill, G.A. Fitzpatrick, The Evaluation of the Interparticle Spacing in Dispersion Alloys, International Metallurgical Reviews 19 (1974) 77–88.

[62] J.A. Österreicher, F. Grabner, A. Schiffl, S. Schwarz, G.R. Bourret, Information depth in backscattered electron microscopy of nanoparticles within a solid matrix, Materials Characterization 138 (2018) 145–153.

[63] R.A. Young, Rietveld method, The, Oxford Univ. Press, 1996.

[64] DIN EN ISO 6892-1:2017-02, Metallic materials - Tensile testing - Part 1: Method of test at room temperature (ISO 6892-1:2016); German version EN ISO 6892-1:2016, Berlin, Beuth Verlag GmbH, 10.31030/2384831.

[65] DIN EN ISO 6892-2:2018-09, Metallic materials - Tensile testing - Part 2: Method of test at elevated temperature (ISO 6892-2:2018); German version EN ISO 6892-2:2018, Berlin, Beuth Verlag GmbH, 10.31030/2864330.

[66] International Centre for Diffraction Data, PDF-2 Release, Card Number 01-074-5237, (2018).

[67] International Centre for Diffraction Data, PDF-2 Release, Card Number 00-019-0029, (2018).

[68] J.R. Porter, F.J. Humphreys, Nucleation of recrystallization at second-phase particles in deformed copper alloys, Metal Science 13 (1979) 83–88.

[69] J.K. Mackenzie, second paper on statstics with the random disorientation of cubes, Biometrika 45 (1958) 229–240.

[70] C.W. Bale, P. Chartrand, S.A. Degterov, G. Eriksson, K. Hack, R. Ben Mahfoud, J. Melançon et al., FactSage thermochemical software and databases, Calphad 26 (2002) 189–228.

[71] J. Humphreys, Rohrer, S., Gregory, A. Rollett, Recrystallization: and related annealing phenomena, Elsevier, 2017.

[72] R. Grimes, Superplastic forming of aluminium alloys, in: Superplastic Forming of Advanced Metallic Materials, Elsevier, 2011, pp. 247–271.

[73] Q. Liu, S. Chen, R. Gu, W. Wang, X. Wei, Effect of Heat Treatment Conditions on Mechanical Properties and Precipitates in Sheet Metal Hot Stamping of 7075 Aluminum Alloy, J. of Materi Eng and Perform 27 (2018) 4423–4436.

[74] S. Heimann, M. Knyazeva, M. Pohl, EBSD-Gefügeuntersuchungen an Aluminiummatrix-Verbundwerkstoffen, Practical Metallography 47 (2010) 640–653.

[75] E. Damavandi, S. Nourouzi, S.M. Rabiee, R. Jamaati, J.A. Szpunar, EBSD study of the microstructure and texture evolution in an Al–Si–Cu alloy processed by route A ECAP, Journal of Alloys and Compounds 858 (2021) 157651.

[76] F.J. Humphreys, W.S. Miller, M.R. Djazeb, Microstructural development during thermomechanical processing of particulate metal-matrix composites, Materials Science and Technology 6 (1990) 1157–1166.

[77] E. Nes, The effect of a fine particle dispersion on heterogeneous recrystallization, Acta Metallurgica 24 (1976) 391–398.

[78] C.S. Smith, "Introduction to Grains, Phases, and Interfaces—an Interpretation of Microstructure," Trans. AIME, 1948, vol. 175, pp. 15–51, by C.S. Smith, Metals Technology 41 (1948) 15–51.

[79] N. Wang, K. Huang, Y. Li, K. Marthinsen, The Influence of Processing Conditions on Microchemistry and the Softening Behavior of Cold Rolled Al-Mn-Fe-Si Alloys, Metals 6 (2016) 61.

[80] M.E. Fine, Precipitation hardening of aluminum alloys, Metallurgical Transactions A (1975) 625–630.

[81] S. Chayong, H.V. Atkinson, P. Kapranos, Multistep induction heating regimes for thixoforming 7075 aluminium alloy, Materials Science and Technology 20 (2004) 490–496.

[82] L. Ding, L. Zhao, Y. Weng, D. Schryvers, Q. Liu, H. Idrissi, Atomic-scale investigation of the heterogeneous precipitation in the E ($Al_{18}Mg_3Cr_2$) dispersoid of 7075 aluminum alloy, Journal of Alloys and Compounds 851 (2021) 156890.

[83] J.M. Howe, Interfaces in materials: Atomic structure, thermodynamics and kinetics of solid-vapor, solid-liquid and solid-solid interfaces, John Wiley & Sons, New York, 1997.

[84] S.C. Wang, Z. Zhu, M.J. Starink, Estimation of dislocation densities in cold rolled Al-Mg-Cu-Mn alloys by combination of yield strength data, EBSD and strength models, Journal of microscopy 217 (2005) 174–178.

[85] E.A. Simielli, R. Lesley Plaut, A. Fernando Padilha, Influence of Heating Time on the Recrystallization of Two Aluminium Alloys, International Journal of Materials Research 78 (1987) 770–776.

[86] Y. Zhao, L. Li, Z. Lu, G. Teng, S. Liu, Z. Hu, A. He, The effect of annealing temperature on the recrystallization and mechanical properties of severe plastic deformed commercial pure aluminium during ultra-fast annealing, Mater. Res. Express 8 (2021) 46515.

[87] W.J. Poole, M. Militzer, M.A. Wells, Modelling recovery and recrystallisation during annealing of AA 5754 aluminium alloy, Materials Science and Technology 19 (2003) 1361–1368.

[88] H. Zhao, F. de Geuser, A. Da Kwiatkowski Silva, A. Szczepaniak, B. Gault, D. Ponge, D. Raabe, Segregation assisted grain boundary precipitation in a model Al-Zn-Mg-Cu alloy, Acta Materialia 156 (2018) 318–329.

[89] G. Sha, L. Yao, X. Liao, S.P. Ringer, Z. Chao Duan, T.G. Langdon, Segregation of solute elements at grain boundaries in an ultrafine grained Al-Zn-Mg-Cu alloy, Ultramicroscopy 111 (2011) 500–505.

[90] K.T. Aust, u.J. Rutter, Grain boundary migration in high-purity lead and dilute lead-tin alloys., Transaction of the American Institute of Mining and Metallurgical Engineers (1959) 119–127.

[91] J.W. Cahn, The impurity-drag effect in grain boundary motion, Acta Metallurgica 10 (1962) 789–798.

[92] F.C. Liu, Z.Y. Ma, F.C. Zhang, High Strain Rate Superplasticity in a Micro-grained Al–Mg–Sc Alloy with Predominant High Angle Grain Boundaries, Journal of Materials Science & Technology 28 (2012) 1025–1030.

[93] F.C. Liu, Z.Y. Ma, L.Q. Chen, Low-temperature superplasticity of Al–Mg–Sc alloy produced by friction stir processing, Scripta Materialia 60 (2009) 968–971.

[94] N. Kumar, R.S. Mishra, Ultrafine-Grained Al-Mg-Sc Alloy via Friction-Stir Processing, Metall and Mat Trans A 44 (2013) 934–945.

[95] P. Gordon, R. Vandermeer, Mechanism of grain boundary migration in recrystallization, Transaction of Metallurgical Society of AIME 224 (1962) 917-&.

[96] P.A. Manohar, M. Ferry, T. Chandra, Five Decades of the Zener Equation, ISIJ International 38 (1998) 913–924.

[97] P.A. Manohar, D.P. Dunne, T. Chandra, C.R. Killmore, Grain Growth Predictions in Microalloyed Steels, ISIJ International 36 (1996) 194–200.

[98] K. Edalati, Z. Horita, R.Z. Valiev, Transition from poor ductility to room-temperature superplasticity in a nanostructured aluminum alloy, Scientific reports 8 (2018) 6740.

[99] A.V. Mikhaylovskaya, O.A. Yakovtseva, A.G. Mochugovskiy, J. Cifre, I.S. Golovin, Influence of minor Zn additions on grain boundary anelasticity, grain boundary sliding, and superplasticity of Al-Mg-based alloys, Journal of Alloys and Compounds 926 (2022) 166785.

[100] A. Kuznetsov, L. Karkina, Y. Gornostyrev, P. Korzhavyi, Effects of Zn and Mg Segregations on the Grain Boundary Sliding and Cohesion in Al: Ab Initio Modeling, Metals 11 (2021) 631.

[101] Z. Song, R. Niu, X. Cui, E.V. Bobruk, M.Y. Murashkin, N.A. Enikeev, J. Gu et al., Mechanism of room-temperature superplasticity in ultrafine-grained Al–Zn alloys, Acta Materialia 246 (2023) 118671.

[102] M.T. Pérez-Prado, G. González-Doncel, O.A. Ruano, T.R. McNelley, Texture analysis of the transition from slip to grain boundary sliding in a discontinuously recrystallized superplastic aluminum alloy, Acta Materialia 49 (2001) 2259–2268.

[103] A.K. Mukhopadhyay, A. Kumar, S. Raveendra, I. Samajdar, Development of grain structure during superplastic deformation of an Al–Zn–Mg–Cu–Zr alloy containing Sc, Scripta Materialia 64 (2011) 386–389.

[104] J.-K. Chang, K. Takata, K. Ichitani, E.M. Taleff, Abnormal grain growth and recrystallization in Al-Mg Alloy AA5182 Following Hot Deformation, Metallurgical and materials transacations A (2010) 1942–1953.

[105] A.V. Mikhaylovskaya, O.A. Yakovtseva, M.N. Sitkina, A.D. Kotov, A.V. Irzhak, S.V. Krymskiy, V.K. Portnoy, Comparison between superplastic deformation mechanisms at primary and steady stages of the fine grain AA7475 aluminium alloy, Materials Science and Engineering: A 718 (2018) 277–286.

[106] A.V. Mikhaylovskaya, A.D. Kotov, A.V. Pozdniakov, V.K. Portnoy, A high-strength aluminium-based alloy with advanced superplasticity, Journal of Alloys and Compounds 599 (2014) 139–144.

[107] Z. Ma, R. Mishra, M. Mahoney, Superplastic deformation behaviour of friction stir processed 7075Al alloy, Acta Materialia 50 (2002) 4419–4430.

[108] F. Li, D.H. Bae, A.K. Ghosh, Grain elongation and anisotropic grain growth during superplastic deformation in an Al-Mg-Mn-Cu alloy, Acta Materialia 45 (1997) 3887–3895.

[109] G. Graf, P. Spoerk-Erdely, P. Staron, A. Stark, F. Mendez Martin, H. Clemens, T. Klein, Quench rate sensitivity of age-hardenable Al-Zn-Mg-Cu alloys with respect to the Zn/Mg ratio: An in situ SAXS and HEXRD study, Acta Materialia 227 (2022) 117727.

7 ACCELERATION OF QUALITY CONTROL MEASUREMENTS

The fine grain size of industrial 5/7 crossover alloys presents a significant challenge for microscopic etching in the solution annealed or pre-aged condition. Electron backscattered diffraction (EBSD) methods represent an alternative for grain size investigations, but they require trained personnel and are not practical for industrial quality control due to high costs and time consumption. Various etchants were tested without success until a pivotal advancement was made by modifying the grain boundary chemistry. This modification enhanced the potential differences between the matrix and the grain boundary, enabling etchability without changing the grain size. The relationships between etchability and grain boundary chemistry, as well as the accelerated manufacturing process, represent a significant advancement in quality control for these alloys. These findings were published in the journal Advanced Engineering Materials and are detailed in the following section.

Metallographic etching of Al-Mg-Zn-(Cu) crossover alloys[4]

Authors' contributions

Sebastian Samberger:	Conceptualization, Methodology, Investigation, Visualization, Writing – Original Draft
Thomas Kremmer:	TEM investigations
Lukas Stemper:	Review & Editing.
Serena Tourey:	Etching experiments.
Peter J. Uggowitzer:	Conceptualization, Supervision, Writing – Review & Editing.
Stefan Pogatscher:	Project Administration, Conceptualization, Supervision, Writing – Review & Editing.

Acknowledgements

This work was funded by the Christian Doppler Research Association within the framework of the Christian Doppler Laboratory for Advanced Aluminum Alloys. Financial support from the Austrian Federal Ministry for Digital and Economic Affairs, the National Foundation for Research, Technology and Development and the Christian Doppler Research Association is gratefully acknowledged. The authors wish to express their sincere thanks to AMAG Rolling for the valuable discussions. The transmission electron microscopy facility used in this work received funding from the Austrian Research Promotion Agency (FFG), project known as "3DnanoAnalytics" under contract number FFG-No. 858040.

Abstract

Various alloys demand customized etchants due to their diverse chemical compositions, particularly in the realm of aluminum alloys. Consequently, this study proposes a technique for metallographic visualization of small grain structures within Al-Mg-Zn-(Cu) crossover alloys. The method relies on a thermal pre-treatment combined with an etching process. The study primarily seeks to comprehend how grain boundary precipitation affects etchability, addressing the complexities of characterizing these alloys. The demonstrated approach facilitates the swift assessment of grain sizes <10 µm using light optical microscopy. Exploring the etchability of Al-Mg-Zn-(Cu) crossover alloys across a standard heat treatment pathway identifies the optimal treatment and suitable etchant for grain visualization. Through process refinement, a reduction in processing time is achieved by employing a single-step preheat treatment lasting 20 minutes at 180 °C post solution annealing. Transmission electron microscope analysis reveals continuous occupancy of the grain boundary with T-phase as the key factor influencing the alloy's etchability. Grain size assessment involves line intercept counting and equivalent circle diameter (ECD) measurement for precise characterization.

---

[4] Samberger, S., Kremmer, T., Stemper, L., Tourey, S., Uggowitzer, P.J. and Pogatscher, S. (2024), Metallographic Etching of Al–Mg–Zn–(Cu) Crossover Alloys. Adv. Eng. Mater. 2400576.

7.1 Introduction

Light optical microscopy is a fast, reliable and cost-effective technique for the visualisation of many microstructural features and plays a central role in the characterisation of industrially produced alloys. As aluminum alloys have a wide range of chemical composition and mechanical properties, the metallographic preparation varies greatly depending on the alloy. For each commercial aluminum alloy, several polishing and etching methods with adjusted parameters are known to reveal different features such as phases or grain structures. [1,2]

Visualisation of the grain structure is not straightforward for all alloys. At minor alloying content, relief effects resulting in "steps" at the grain boundaries dominate. In these cases, it is necessary to apply an anodic layer and observe the microstructure with polarised light using an analyser. The anodic layer is usually applied by electrochemical etching utilizing, for example, Barker's reagent [2]. However, structures with very fine grains (< 10 μm) require high magnification and the colour or grey value contrast provided by anodising becomes so low that measuring grain structures is almost impossible [3]. In systems with high alloying content, grain boundaries precipitates can be utilized by chemical etching to contrast the grain boundary and reveal the grain size of the alloy [1,3]. As there is a wide range of etchants and parameters that are tailored to each alloy system, suitable parameters need to be determined for novel alloy systems such the Al-Mg-Zn-(Cu) crossover alloys or sometimes 5/7 crossover alloys (combination of 5xxx and 7xxx series alloys) to enable rapid light optical microscopy investigation.

Al-Mg-Zn(-Cu) crossover alloys are a new class of alloys that overcome the strength/ductility trade-off, for example for the automotive industry [4], by exhibiting good formability after pre-aging, combined with improved hardening responses up to yield strength levels in excess of 400 MPa [5]. In addition, these alloys exhibit a low quench rate sensitivity [6], good weldability [7] and improved resistance to intergranular corrosion [8,9], exfoliation corrosion [10] and stress corrosion cracking [11]. Age hardening is achieved by precipitation of T-phase ($Mg_{32}(Al,Zn)_{49}$) or its precursors [12], where Zn can be replaced by Ag [13,14] or Cu [5,14,15], which additionally increases the hardening potential. These promising properties are driving the alloy´s development towards industrialization and commercialization [16]. The precipitation sequence for age hardening in this system is proposed by Hou et al. [17] as: supersaturated solid solution (SSSS) → GPI zone → GPII zone (intermediate phase T'') → intermediate phase T' → equilibrium phase T-($Mg_{32}(Al,Zn)_{49}$). The first step in the age hardening process is solution annealing (SA), where elements dissolve into solid solution. Since the temperature of SA is higher than the recrystallization temperature, the matrix also tends to recrystallize in this process step. Previous studies [18] have shown that at this stage dislocations – which have been previously introduced by cold working – in combination with coarse precipitates can be utilised to produce a fine grained crossover alloy suitable for quickplastic and superplastic forming operations. Once the coarse precipitates have dissolved into the matrix and sufficient supersaturation is established by quenching, T-phase precursors begin to form within the grains upon subsequent heat treatment. Additionally, precipitate forming elements also diffuse towards the grain boundary leading to grain boundary segregation and precipitation. Increased solute concentration at the grain boundary reduces its mobility and shifts the grain growth temperature to higher values, leading to an increased stability of the grain size. [19]

In the solution annealed state, the supersaturated matrix, the absence of precipitates, and the fine-grained structure create a condition that is extremely unfavourable for light optical microscopic grain structure studies in these new materials. Therefore, this study investigates the suitability of thermal pre-treatment strategies and various etchants to improve grain visibility in Al-Mg-Zn-(Cu) crossover alloys. A prerequisite for the use of a suitable pre-treatment is the assurance that the annealing treatment will not result in a change in grain size, which is also invested in the study. Moreover, the basic mechanisms behind the contrast formation in the metallography of Al-Mg-Zn-(Cu) crossover alloys are discussed.

7.2 Experimental

The Al-Mg-Zn-(Cu) crossover alloy used in this study is a sheet material industrially produced by the company AMAG rolling GmbH with the composition shown in Table 6-1. The composition of the 1 mm sheet material is measured by optical emission spark spectroscopy (Spectromaxx spark spectrometer).

Table 7-1: Measured chemical composition of the industrially produced Al-Mg-Zn-(Cu) crossover alloy sheet investigated

		Mg	**Zn**	**Cu**	**Si**	**Fe**	**Mn**	**Cr**	**Ti**
5/7 crossover alloy	[wt.-%]	4.91	3.46	0.46	0.10	0.13	0.33	0.06	0.01
	[at.-%]	5.56	1.46	0.20	0.10	0.07	0.17	0.03	0.01

Optical visualisation tests are carried out along a heat treatment route as shown in Figure 7-1a., which is suitable for precipitate formation. As known from previous studies [18], the solution annealing (SA) process is also the recrystallization step. After recrystallization at 480 °C/1min the alloy has a grain size of 5.0 ± 2.5 μm measured by electron backscatter diffraction (EBSD). The grain size is given as the mean of the equivalent circle diameter (ECD) measured. Since the study shows that the grain size does not change during subsequent heat treatment at elevated temperatures [18], it can be assumed that no grain growth will occur during heat treatment procedures in the temperature range of precipitate formation. Thermal pre-treatments can therefore be used perfectly for modifying the grain boundary composition to enable metallographic grain size measurements.

For grain visualisation, samples were tested in the SA condition, in the pre-aged (PA) condition after soaking for 5 h at 100 °C, and after paint baking (PB), which brings the alloy close to peak hardness at 180 °C for 20 min.

Given that a heat treatment exceeding 5 hours is impractical for industrial analysis, an optimised heat treatment was employed to streamline the process. This optimisation, outlined in Figure 7-1b, involves subjecting the recrystallised sheet material to a single-stage heat treatment at 180 °C after the solution annealing (SA) step. Grain visualisation tests are then performed after 5, 20 and 40 min of heat treatment to identify the most efficient treatment duration.

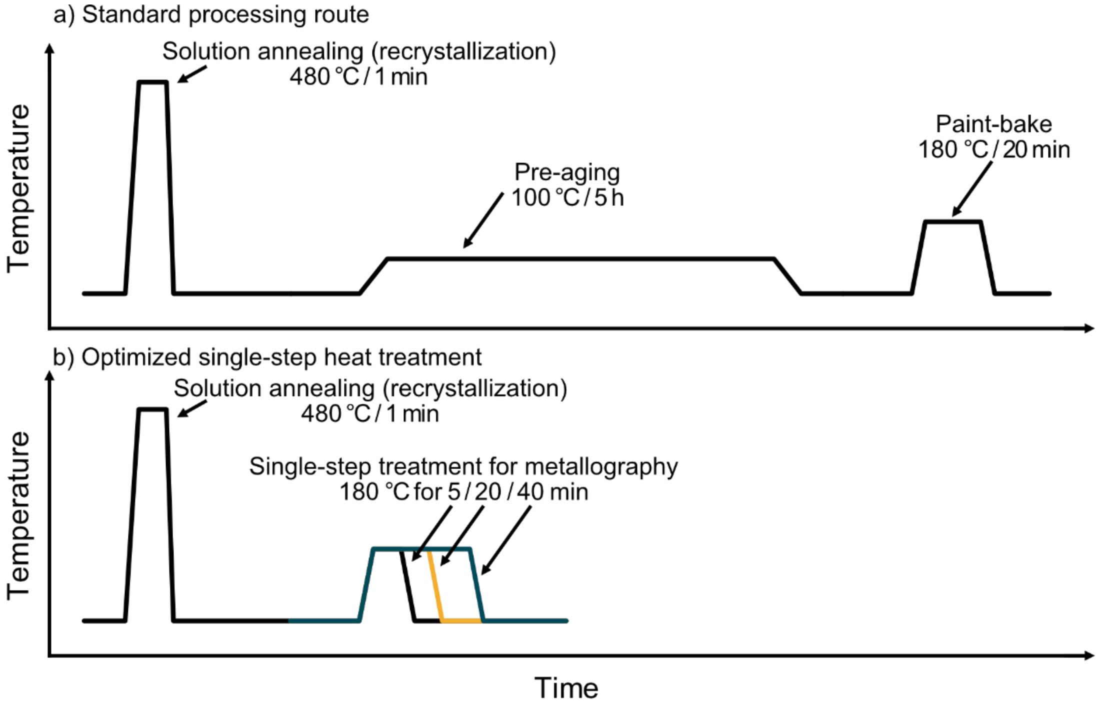

Figure 7-1: Heat treatment strategies applied for grain visualization in Al-Mg-Zn-(Cu) crossover alloys. The heat treatment strategies applied are a standard heat treatment route including pre-aging and paint bake (a) and an single step treatment for shorter analysis times (b).

The samples underwent grinding with a maximum grit size of 4000 and were then polished with a diamond suspension to a minimum of 1 µm. Prior to etching, the final surface preparation involved polishing with an oxide polishing suspension (OP-S) for 45 seconds. This step ensured a good surface finish, minimizing the presence of scratches for optimal etching results.

Etchants were selected based on the etching process for 5xxx series alloys and age-hardenable alloys, especially 7xxx series alloys. The composition of the etchants and the application parameters of the etching methods are given in Table 7-2. Keller, Dix-Keller and Weck are non-electrolytic etching methods which were used at room temperature with immersion times between 30 and 120 s, except for Weck, which was applied at 40°C. Barker is an electrolytic etching method applied using the Struers Lectropol 5 electrolytic polishing and etching machine. The parameters here are voltage and treatment time.

Table 7-2: Etching methods, etchant composition and treatment parameters used to visualize grain structures in Al-Mg-Zn-(Cu) crossover alloys from [20,21]

Method	Reagents	Parameters
Keller	18.2 ml H_2ODeion. 20 ml HCl (32%) 20 ml HNO_3(65%) 6.8 ml HF (48%)	room temperature 30–120 s soaking time
Dix-Keller	95 ml H_2ODeion 1.5 ml HCl (32%) 2.5 ml HNO_3 (65%) 1 ml HF (40%)	room temperature 30–120 s soaking time
Weck	100 ml H_2ODeion 4 g $KMnO_4$ 1 g NaOH	40 °C 30–120 s soaking time
Barker	HBF_4 (10%) in H_2ODeion.	20–40 V 5–10 s soaking time

Grain size investigations of the alloys were carried out using a digital microscope (Keyence VHX-7000) equipped with a polarisation filter. The microscope is capable of semi-automated grain size measurements in accordance with ASTM E112-10 [22]. Grain size was determined either by line intercept counting, giving ASTM grain size (G) values, or by measuring the equivalent circle diameter (ECD) of individual grains. Distinction between grains for single ECD measurements was made by grey value thresholds, where the grain boundary must show a strong contrast deviation from the grain interior.

Since grain boundary precipitates were pinpointed as the primary factor influencing the alloy's etchability variation across different heat treatment stages, we conducted a detailed examination of the grain boundaries using transmission electron microscopy (TEM). High angle annular dark field (HAADF) and energy dispersive X-ray (EDX) scanning transmission electron microscopy (STEM) measurements were performed using a Thermo Fisher Scientific™ Talos F200X instrument. Samples were prepared for STEM by grinding the alloys to a thickness of approximately 100 µm. Punched 3 mm discs were further processed by twin-jet electropolishing using a solution of 25% nitric acid in methanol at a temperature range of -16°C to -20°C and a voltage range of 10 V to 20 V.

7.3 Results & Discussion

7.3.1 Standard processing route

Micrographs of etching tests along a standard heat treatment route (Figure 7-1a) in each condition with different etching reagents are shown in Figure 7-2. The micrographs represent the most representative etching parameters. A detailed analysis of the full range of parameters can be found elsewhere [23]. Shorter or longer soaking times lead to under- or over-etching or show no change in the etchability of the sample. In the solution annealed condition (Figure 7-2a–d) none of the etching methods used were able to visualise the grain size of the Al-Mg-Zn-(Cu) crossover alloy. Due to the small grain size, the Barker etching method does not allow the formation of a grain dependent anodization layer on the sample. When a polarisation filter is used, the entire surface of the sample has the same colour. This is the reason for the slight yellow colour seen in Figure 7-2a. Adjusting the angle of the polarisation filter will change the colour but will not improve the visibility of the grains. Immersion etching techniques such as Weck, Keller or Dix-Keller are also unable to reveal the grain structure of this fine-grained alloy.

The same tests are carried out on the samples after pre-ageing for 5 h at 100 °C. The micrographs of the etched samples are shown in Figure 7-2e–h. As for the solution annealed condition, the etchability in the pre-aged condition is clearly insufficient.

The visibility of the grains is drastically changed after a paint bake treatment at 180 °C for 20 min. The final stage of an industrial heat treatment process is suitable to reveal the grain structure of the fine grain Al-Mg-Zn-(Cu) crossover alloys. The micrographs associated with this heat treatment stage are shown in Figure 7-2i-l. Etching with Barker's reagent still does not deposit an anodization layer related to grain orientation. Therefore, when a polarisation filter is applied, the grains have the same colour as in the solution annealed and pre-aged condition. However, by etching with Barker´s reagent, grains are visible as the electrochemical process dissolves the grain boundary visualising the grain interior. This can be seen by the yellowish colour with dark grain boundaries in Figure 7-2i. The same behaviour is observed for samples etched with Weck's and Dix-Keller etchants (Figure 7-2k and l). However, it can be stated that immersion etching with Keller's reagent is not suitable for visualising the grains in Al-Mg-Zn-(Cu) crossover alloys as there are still no visible grains in the paint bake condition.

The grain size was measured by line intercept counting for each etching method to be 5.8 ± 0.5 μm, 4.7 ± 0.5 μm and 5.7 ± 0.5 μm for the Barker, Weck and Dix-Keller etched samples, respectively. According to ASTM 112-10 [22], the grain size measured by line intercept counting can be converted to ECD by its G-number. This gives an ECD of approximately 6.6 μm, 5.3 μm and 6.6 μm for the Barker, Weck and Dix-Keller etched samples, respectively, which is in good agreement with the grain size of 5.0 ± 2.5 μm determined by EBSD in previous studies. [18]

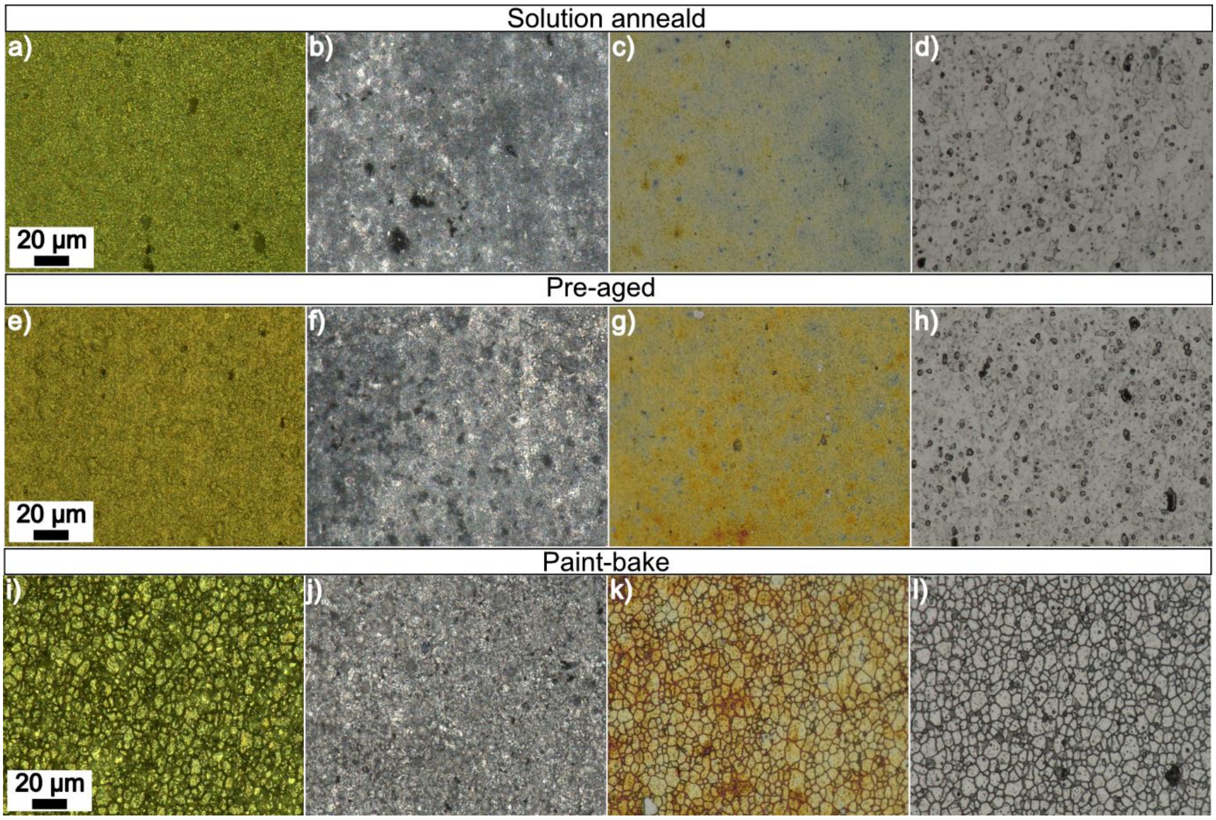

Figure 7-2: Samples in the solution-annealed condition (480 °C/1 min) after treatment with different etchants: Barker (20 V/2 min) (a); Keller (75 s) (b); Weck (25 s) (c) and Dix-Keller (90 s) (d); in pre-aged condition (100 °C/5 h) after treatment with different etchants: Barker (20 V/2 min) (e); Keller (75 s) (f); Weck (25 s) (g) and Dix-Keller (90 s) (h) and after baking (180 °C/20 min) with different etchants: Barker (25 V/2 min) (i); Keller (75 s) (j); Weck (25 s) (k) and Dix-Keller (90 s) (l).

The investigation into the variability in etchability across different heat treatment conditions is elucidated by scrutinizing the grain boundaries during the actual processing steps. High-angle annular dark field micrographs portraying the grain boundaries of the crossover alloy in states of solution annealing (SA), pre-aging (PA), and paint baking (PB) along the processing pathway are depicted in Figure 7-3a-c. Furthermore, EDX mappings illustrating the distribution of Mg and Zn serve as representatives of T-phase precipitation. According to literature [5,14] $Mg_{32}(Al,Zn)_{49}$ constitutes are the dominant phase in this system and the applied heat treatment regime. Hence, Mg and Zn serve as reliable indicators of T-phase precipitation.

In the solution annealed condition, all elements are dissolved in the matrix to form a supersaturated solid solution. As expected, there is no precipitation in this state. The alloy's etchability is diminished due to the absence of notable elemental variance, resulting in a lack of potential difference between the grain interior and the grain boundary. Solutes tend to segregate at the grain boundary, driven by the system's endeavor to minimize its Gibbs energy [24]. In 7xxx series alloys, this segregation becomes apparent already after solution annealing and quenching [25], a phenomenon not observed in crossover alloys, as depicted in Figure 7-3a. The difference in the occurrence of grain boundary segregation is also evident in the difference in quench rate sensitivity of these two alloy classes [6]. The thermal activated grain boundary segregation accelerates the precipitation of phases, as evidenced in Figure 7-3b where a slight discontinuous occupancy of the grain boundary is visible. Furthermore, elemental diffusion towards the grain boundary, along with the presence of precipitated phases, serves to stabilize the grain size by reducing grain boundary mobility [19]. Consequently, the grain size observed after age-hardening treatment remains consistent with that after recrystallization. The discontinuous occupation of the grain boundary in the pre-aged condition does not alter the potential difference between the grain boundary and the grain interior significantly enough to cause preferential etching, thus preserving the invisibility of the grain structure.

In the paint-bake condition, hardness close to peak hardness is achieved by further precipitation and evolution of the T-phase particles. The coarsening and further precipitation of the particles within the matrix and along the grain boundary results in a precipitation free zone (PFZ) and the occupation of the grain boundary becomes nearly continuous. In this state, a notable potential difference exists between the grain boundary and the grain interior, enabling potent etchants like Barker, Weck, or Dix-Keller to dissolve the grain boundary and unveil the grain structure. Nonetheless, the alloy maintains a significant chemical stability, as evidenced by its resistance to Keller's reagent. With pre-aging treatment alone, the precipitation-free zone formed is very narrow, with low potential differences between the matrix and grain boundaries and therefore preserved good intergranular corrosion resistance. [8,9].

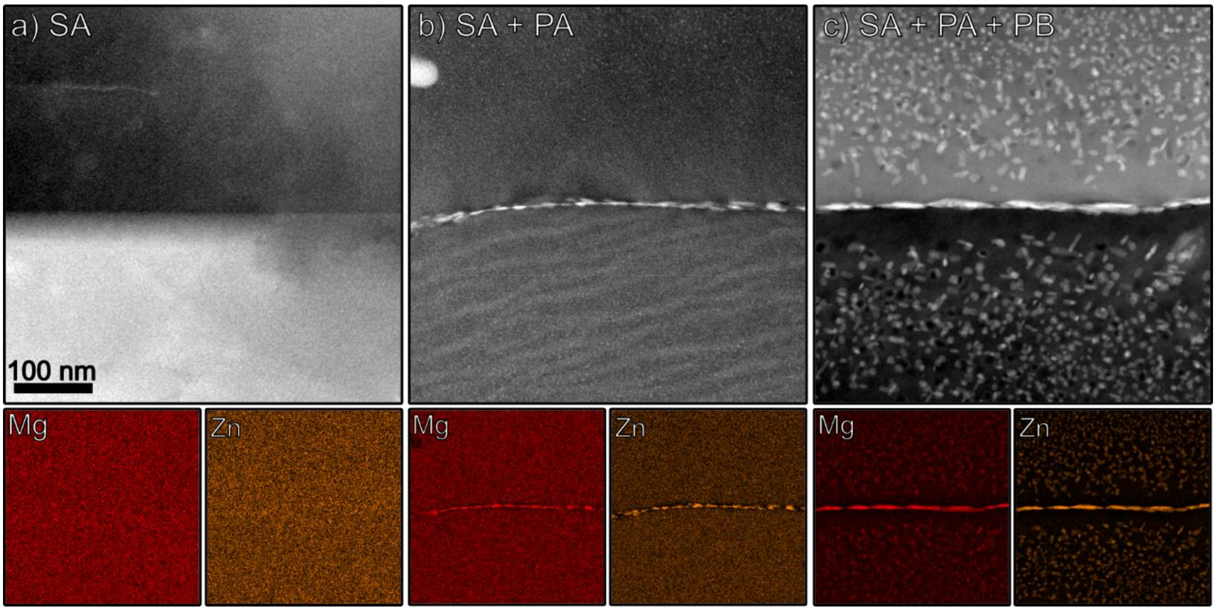

Figure 7-3: HAADF micrographs of grain boundaries at different states along the standard heat treatment route showing increased grain boundary precipitation with no precipitation in SA condition (a); PA condition (b) and PB (c); EDX maps of Mg and Zn in each condition are shown as representative of T-phase precipitates.

7.3.2 Treatment optimization

As grain boundary precipitates dictate the etchability of the Al-Mg-Zn-(Cu) crossover alloys, treatment optimization was pursued to expedite grain boundary precipitation for shorter analysis durations. Given the superior contrast achieved with the Dix-Keller immersion etching method, only this technique was employed in subsequent experiments. Figure 7-4a-c depicts the Dix-Keller etched samples after varying durations at 180 °C following solution annealing. The process optimization experiments reveal that a heat treatment of 180 °C for 5 minutes is inadequate for grain visualization. While initial chemical reactions with the grain boundary precipitates are discernible, they are insufficient to clearly visualize the grain size (see Figure 7-4a). However, after 20 min the grain size becomes distinctly visible, as shown in Figure 7-4b, due to the dissolution of the grain boundary by the etchant. This effect intensifies with an extension of the time to 40 min, where the grain boundaries become even more visible as the attacked zone expands.

The grain size is determined through linear intercept counting, yielding measurements of 5.5 ± 0.6 μm for the 20 min heat treated sample and 6.7 ± 0.9 μm for the 40 min heat treated sample, which can be converted by their ASTM grain size numbers to ECD values of 6.1 μm and 7.5 μm, respectively. Remarkably, these values align closely with those obtained using the standard heat treatment route. Implementing this optimized route reduces processing time by roughly 5 h and requires fewer aggregates and temperature stages.

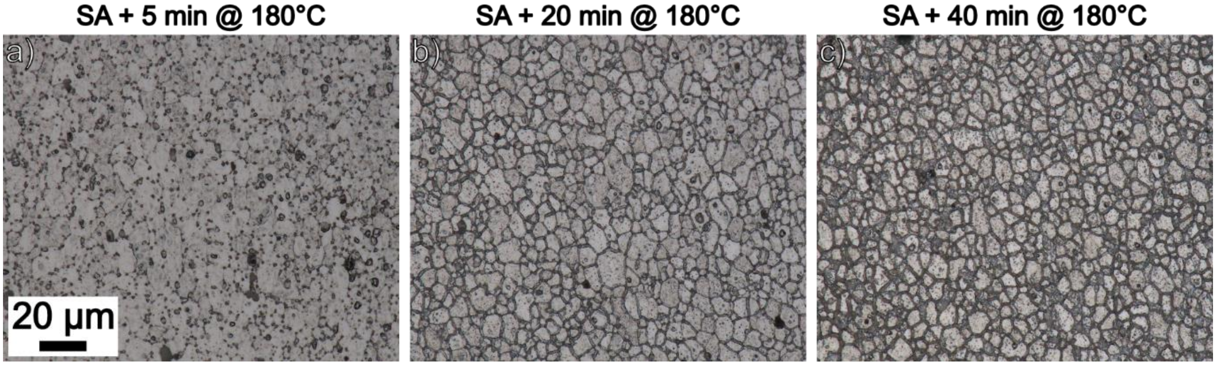

Figure 7-4: Samples after solution annealing (recrystallization) and ageing at 180 °C for 5 min (a), 20 min (b) and 40 min (c); etching with Dix-Keller an immersion time of 90 s.

The Dix-Keller etching method not only provides good etchability of the sample, but also results in clearly distinguishable grey values between the grain interior and grain boundary. Hence, it becomes feasible to measure individual grains using grey value thresholds through the software provided with the Keyence VHX-7000 digital microscope. Comparable to the methodology applied in evaluating EBSD measurements, the software calculates the area of each individual grain, enabling the derivation of an average ECD value. The grain size determined by this method yields a mean ECD value of 4.3 ± 2.0 μm for the standard heat treatment route after paint baking (PB). Through treatment optimization mean ECD values of 5.1 ± 2.8 μm and 4.4 ± 2.0 μm are obtained for 20 and 40 min, respectively. It should be noted that ECD measurements should only be conducted on samples with equiaxial grains, as elongated grains will lead to incorrect grain size interpretation with this method.

Mean ECD measurements can be depicted as a normalized distribution of grain size classes, as shown in Figure 7-5. The grain sizes (starting from 0.5 μm with a class width of 1 μm) is presented for samples in the PB condition of the standard heat treatment route, and for samples after treatment optimization (20 and 40 min at 180 °C). Additionally, the normalized grain size distribution from EBSD measurements is shown as dotted lines for comparison. The curve peak of the PB sample, as well as after 20 min of accelerated precipitation, align well with the position identified in the EBSD measurement. Nonetheless, the peak heights are marginally lower for these methods due to a higher amount of smaller grains detected in the PB sample and an increased share of coarse grains found in the 20 min sample.

Extended soak times beyond 40 min shift the peak of the grain size distribution from 3.5 µm (20 min annealing) to 2.5 µm, resulting in a smaller detected mean grain size. Additionally, the proportion of grains > 8 µm is reduced compared to shorter treatment times. This is due to the widening of the attacked zone in samples treated for 40 minutes. Consequently, prolonged ageing times may yield a distorted representation of grain size. To optimize the process, it is imperative to select soak times that ensure clear visibility of the grains while preventing widening of the etched zone.

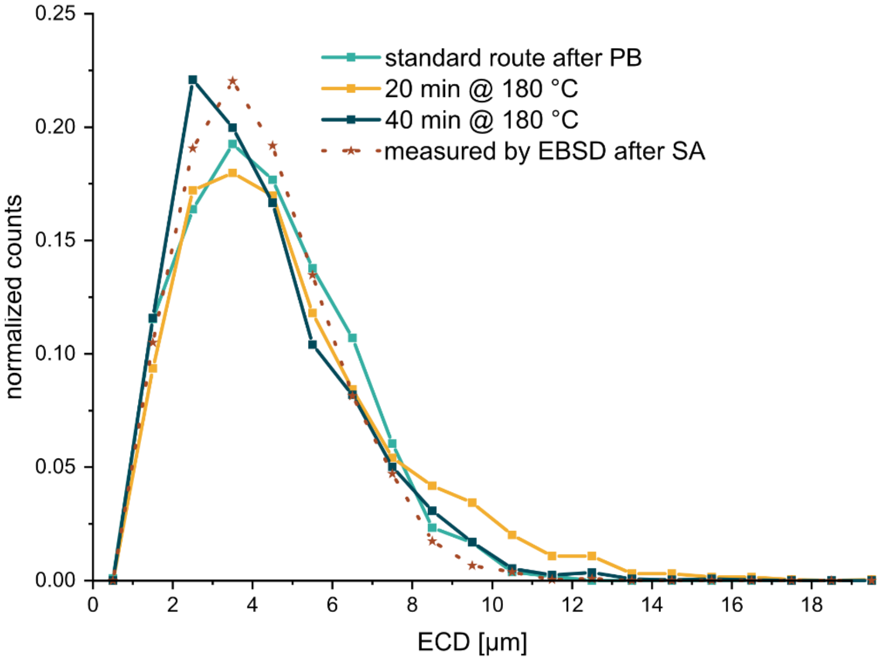

Figure 7-5: Normalized grain size distribution of grains detected by light optical microscopy for samples etched with Dix-Keller etchant for 90 s after standard heat treatment route in PB condition (turquoise) and process optimization with preheat treatment for 20 min (yellow) and 40 min (blue) at 180 °C; data of EBSD measurements from previous studies (red) are given for comparison [18]

TEM-HAADF micrographs and EDX analysis of the grain boundaries were carried out to gain a better understanding of the process optimization and etchability after different soaking times. The corresponding grain boundary micrographs and EDX mappings of Mg and Zn are shown in Figure 7-6.

After a 5-minute soak following solution annealing, coarse grain boundary precipitates start to emerge. They are identified as T-phase particles based on their EDX mappings. Similar to the pre-aged condition, the precipitation is not continuous. Consequently, the etchability is not guaranteed after 5 min of soaking. However, owing to the size of the precipitates in this condition, the grains are vaguely visible, as depicted in Figure 7-4a, but not in a quantifiable manner.

With the extension of the treatment duration at 180°C, the grain boundary precipitates gradually evolve into a connected band after 20 minutes. At this point the grain boundary becomes susceptible to chemical attack. Interestingly, the $Mg_{32}(Al,Zn)_{49}$ particles at the grain boundary do not increase in size with longer treatment times. However, it is to be expected that a higher concentration gradient and potential difference will develop between the inside of the grain and the grain boundary when the phase reaches a more stable state. This will result in a widening of the attacked zone and therefore falsely smaller grain sizes.

It is noteworthy that the area around the grain boundary is quite different in samples with pre-aging prior to the 20 min at 180 °C treatment. When pre-aging is applied, the grain interior is enriched with precipitates, resulting in a narrow PFZ (see Figure 7-3c). Conversely, in samples without pre-aging, no precipitates are evident within the grains (Figure 7-6c).

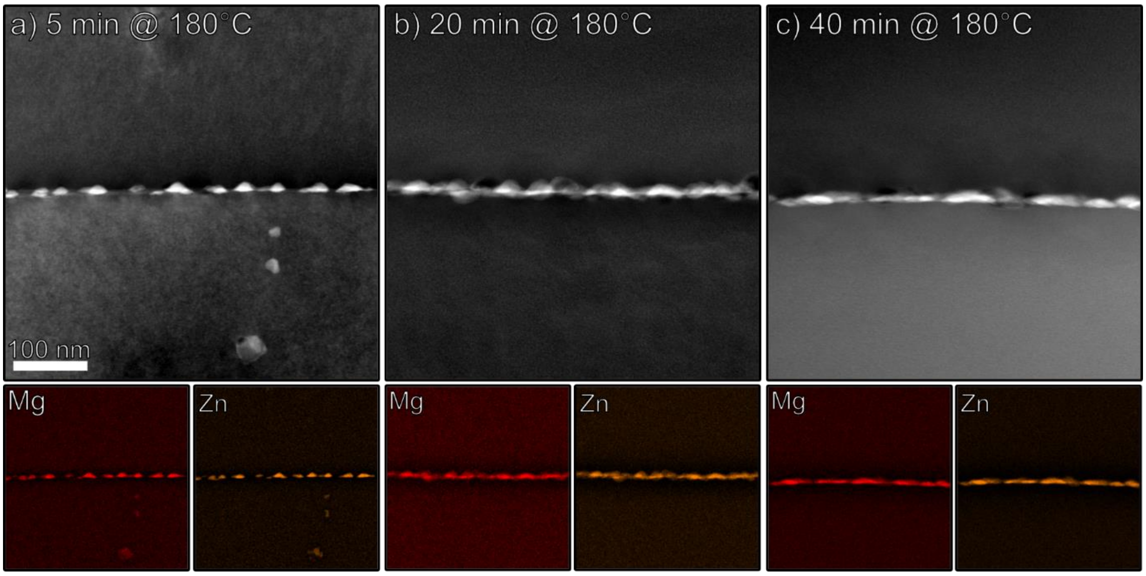

Figure 7-6: HAADF micrographs of grain boundaries at different times at 180 °C during the treatment optimization showing the evolution of grain boundary precipitates after 5 minutes (a) 20 minutes (b) and 40 minutes (c) soaking time; EDX maps of Mg and Zn in each condition are shown as representative of T-phase precipitates.

7.4 Conclusion

In this study, we explored various metallographic etching techniques to visualize fine grains in novel Al-Mg-Zn-(Cu) crossover alloys. The key findings can be summarized as follows:

- Grain boundary precipitation, and hence the potential difference between the matrix and the grain boundary, emerges as the primary factor driving for successful etchability of the alloy.
- Etchability is not observed in either the solution annealed or pre-aged condition due to the lack of continuous grain boundary precipitates or solute enrichment. However, in the paint-bake condition (100 °C / 5 h + 180 °C / 20 min), etchability is given for the Barker, Weck and Dix Keller etching methods, as they effectively chemically attack the continuously decorated grain boundary.
- The procedure to visualize the grain boundaries can be optimized by using a short single temperature treatment at 180 °C subsequent to solution annealing. In this way, grain boundary precipitation is favoured, resulting in better etchability.
- The Dix-Keller etchant with a treatment time of 90 seconds was found to be the most suitable for etching Al-Mg-Zn-(Cu) crossover alloys, as the grey level threshold allows grain area measurements to be made, leading to the possibility of mean ECD measurements as a representative value of grain size.
- The duration of the pre-heat treatment must be carefully selected, as a treatment time that is too short will not guarantee etchability, while an excessively long treatment time will result in widening of the etched zone. A widening of the attacked zone will result in lower detected ECD values.

7.5 References

[1] ASM handbook volume 9 metallography and microstructures, 10th ed., ASM International, Materials Park, Ohio, 2004.

[2] J. Davis, ASM specialty handbook aluminum and aluminum alloys, 1st ed., American Society For Metals, Ohio, 1993.

[3] M. Mohammadtaheri, A New Metallographic Technique for Revealing Grain Boundaries in Aluminum Alloys, Metallogr. Microstruct. Anal. 1 (2012) 224–226.

[4] L. Stemper, M.A. Tunes, R. Tosone, P.J. Uggowitzer, S. Pogatscher, On the potential of aluminum crossover alloys, Progress in Materials Science (2021).

[5] L. Stemper, M.A. Tunes, P. Dumitraschkewitz, F. Mendez-Martin, R. Tosone, D. Marchand, W.A. Curtin et al., Giant hardening response in AlMgZn(Cu) alloys, Acta Materialia 206 (2021) 116617.

[6] G. Graf, P. Spoerk-Erdely, P. Staron, A. Stark, F. Mendez Martin, H. Clemens, T. Klein, Quench rate sensitivity of age-hardenable Al-Zn-Mg-Cu alloys with respect to the Zn/Mg ratio: An in situ SAXS and HEXRD study, Acta Materialia 227 (2022) 117727.

[7] Y. Pan, Di Zhang, H. Liu, Z. Zhang, H. Li, L. Zhuang, J. Zhang, Reducing welding hot cracking of high-strength novel Al–Mg–Zn–Cu alloys based on the prediction of the T-shaped device, Science and Technology of Welding and Joining 25 (2020) 483–489.

[8] Y. Pan, Di Zhang, H. Liu, L. Zhuang, J. Zhang, Precipitation hardening and intergranular corrosion behavior of novel Al–Mg–Zn(-Cu) alloys, Journal of Alloys and Compounds 853 (2021) 157199.

[9] C. Cao, Di Zhang, X. Wang, Q. Ma, L. Zhuang, J. Zhang, Effects of Cu addition on the precipitation hardening response and intergranular corrosion of Al-5.2Mg-2.0Zn (wt.%) alloy, Materials Characterization 122 (2016) 177–182.

[10] M.C. Caroll, M.J. Mills, G.S. Daehn, B.R. Dunbar, Effects of Zn additions on the grain boundary precipitation and corrosion of Al-5083, Scripta Materialia 42 (2000) 335–340.

[11] C. Meng, Di Zhang, L. Zhuang, J. Zhang, Correlations between stress corrosion cracking, grain boundary precipitates and Zn content of Al–Mg–Zn alloys, Journal of Alloys and Compounds 655 (2016) 178–187.

[12] G. Bergman, J. Waugh, L. Pauling, The crystal structure of the metallic phase Mg32(Al,Zn)49, Acta Cryst. 10 (1957) 254–259.

[13] H. Liu, Z. Zhang, Di Zhang, J. Zhang, The effect of Ag on the tensile strength and fracture toughness of novel Al-Mg-Zn alloys, Journal of Alloys and Compounds 908 (2022) 164640.

[14] L. Stemper, M.A. Tunes, P. Oberhauser, P.J. Uggowitzer, S. Pogatscher, Age-hardening response of AlMgZn alloys with Cu and Ag additions, Acta Materialia 195 (2020) 541–554.

[15] Y. Geng, Q. Song, Z. Zhang, Y. Pan, H. Li, Y. Wu, H. Zhu et al., Quantifying early-stage precipitation strengthening of Al–Mg–Zn(-Cu) alloy by using particle size distribution, Materials Science and Engineering: A 839 (2022) 142851.

[16] L. Stemper, F. Schmid, R. Tosone, AMAG CrossAlloy®—Lightweighting the Future by Unconstraint Alloy Design: A Case Study, in: S. Wagstaff (Ed.), Light Metals 2024, Springer Nature Switzerland, Cham, 2024, pp. 241–247.

[17] S. Hou, P. Liu, Di Zhang, J. Zhang, L. Zhuang, Precipitation hardening behavior and microstructure evolution of Al–5.1 Mg–0.15Cu alloy with 3.0Zn (wt%) addition, J Mater Sci 53 (2018) 3846–3861.

[18] S. Samberger, I. Weißensteiner, L. Stemper, C. Kainz, P.J. Uggowitzer, S. Pogatscher, Fine-grained aluminium crossover alloy for high-temperature sheet forming, Acta Materialia 253 (2023) 118952.

[19] J. Humphreys, Rohrer, S., Gregory, A. Rollett, Recrystallization: and related annealing phenomena, Elsevier, 2017.

[20] E. Weck, E. Leistner, Metallographic instructions for colour etching by immersion, Dt. Verl. für Schweisstechnik, DVS-Verl., Düsseldorf, 1986.

[21] G. Petzow, Metallographisches, keramographisches, plastographisches Ätzen, 7th ed., Gebrüder Borntraeger, Stuttgart, 2015.

[22] E04 Committee, Test Methods for Determining Average Grain Size, West Conshohocken, PA, ASTM International, 10.1520/E0112-10.

[23] S. Tourey, Evaluierung von Präparationsmethoden zur Gefügeuntersuchung von Aluminium crossover-Legierungen. Master Thesis, Montanuniversität Leoben, 2024.

[24] P. Lejcek, Grain Boundary Segregation in Metals, Springer Berlin Heidelberg, Berlin, Heidelberg, 2010.

[25] H. Zhao, F. de Geuser, A. Da Kwiatkowski Silva, A. Szczepaniak, B. Gault, D. Ponge, D. Raabe, Segregation assisted grain boundary precipitation in a model Al-Zn-Mg-Cu alloy, Acta Materialia 156 (2018) 318–329.

8 SUSTAINABILITY ASPECTS OF CROSSOVER ALLOYS

Sustainability in connection with aluminum always involves an increase in Fe and Si content of the material. To account for an increased impurity content in the alloy due to a approached increase in recycled material in production, the effect of Fe and Si on the mechanical behaviour of 5/7 crossover alloys was investigated. Fe and Si form primary phases with potential detrimental impact, which from during the cooling process during casting. As industrial and laboratory alloy production involve different cooling conditions, multiple trails with different solidification rates were conduction.

8.1 Effect of recycling content on lab scale

The findings of the effect of elevated Fe- and Si content on the processability of the alloys at the laboratory scale were presented and published in the conference proceedings of TMS 2024. The study is shown in the following.

Influence of solidification rate and impurity content on 5/7 crossover alloys[5]

Authors' contributions

Sebastian Samberger:	Conceptualization, Methodology, Investigation, Visualization, Writing – Original Draft
Lukas Stemper:	Review & Editing.
Peter J. Uggowitzer:	Conceptualization, Supervision, Writing – Review & Editing.
Ramona Tosone:	Review & Editing.
Stefan Pogatscher:	Project Administration, Conceptualization, Supervision, Writing – Review & Editing.

Acknowledgements

The financial support by the Christian Doppler Research Association, the Austrian Federal Minis-try for Digital and Economic Affairs and the National Foundation for Research, Technology and Development is gratefully acknowledged. Moreover, the authors wish to express their sincere thanks to AMAG rolling GmbH for the supply of alloy material.

Abstract

In view of an upcoming scrap wave and the need for products with lower carbon footprint, there is an urgent need to increase the recycled fraction in wrought aluminum alloys. However, due to the narrow compositional limits of conventional aluminum wrought alloys and the higher impurity levels in scrap material, the applicable recycling content is limited. Therefore, new approaches need to be identified to increase the recycled content. The introduction of the AlMgZn(Cu) crossover alloy concept may prove to be a step forward in escaping the corset of conventional alloying systems. The 5/7 crossover alloy not only overcomes the long-standing trade-off between the excellent formability of 5xxx-series alloys and the outstanding strength of 7xxx-series alloys by combining both properties, but may also tolerate a higher content of impurity elements. The scope of this study is to properly address the 5/7 crossover alloy's sustainability in terms of its ability to be manufactured from secondary raw materials. AlMgZn(Cu) alloys with different tramp element concentrations were investigated.

---

[5] Samberger, S., Stemper, L., Uggowitzer, P.J., Tosone, R., Pogatscher, S. (2024). Influence of Solidification Rate and Impurity Content on 5/7 crossover Alloys. In: Wagstaff, S. (eds) Light Metals 2024. TMS 2024. The Minerals, Metals & Materials Series. Springer, Cham. https://doi.org/10.1007/978-3-031-50308-5_28

8.1.1 Introduction

The escalating concerns over fuel consumption and greenhouse gas emissions have compelled the automotive industry to prioritize lightweighting as a pivotal strategy for achieving sustainability goals. In this context, utilizing aluminum as an exceptional lightweight material has gained prominence due to its potential to enable efficient manufacturing processes and achieve remarkable weight reductions of up to 50 % compared to traditional steel, all while maintaining safety standards. [1, 2]

Although low density materials such as aluminum are well established in the automotive industry, many different aluminum alloys must be implemented to meet all manufacturing and product requirements. This, on the other hand, has a negative impact on automotive recyclability as the different alloys cannot be readily mixed together. [3, 4]

Overcoming the limitations of current lightweighting concepts necessitates the development of new alloy design strategies capable of delivering an extended property portfolio that includes both good formability during processing and high strength in use. Industry efforts are already addressing these needs. The company AMAG reported two Crossover alloys named AMAG CrossAlloy.57 [5] and AMAG CrossAlloy.68 [6]. The Crossover alloying concept works beyond the current state-of-the-art alloy classification scheme in a more fit-the-need classification scheme. By the introduction of 5/7 crossover alloys (combination of 5xxx series alloys and 7xxx series alloys), the longstanding trade-off between the good formability of 5xxx series alloys and the high strength of the 7xxx series alloys could be overcome [7]. Furthermore, the 5/7 crossover alloy are not only reported to exhibit outstanding hardening potential with up to 400 MPa Yield strength values [8] by T-phase ($Mg_{32}(Al,Zn)_{49}$) hardening, but also a good corrosion resistance [9–12] and the ability to prevent or suppress the Lüders elongation and the Portevin-Le-Chatelier (PLC)-effect [13, 14]. Thus, this alloy can be considered a very interesting candidate for automotive applications.

Since the current alloying limits are narrow (especially for wrought aluminum alloys), new approaches regarding alloying strategies are required. Considering the automotive industry as the largest source of aluminum scrap and the largest consumer reveals the urgent need for enhanced alloy design. While the iron content in applications such as cast wheels or nodes used in space frames is limited to less than 0.2 wt. %, estimate calculations, however, predict an iron content in automotive scrap ranging between 0.6 and 0.7 wt. % depending on the degree of dismantling [15]. Mainly due to such Fe limitations, a scrap surplus in the automotive industry is predicted for the years 2025 to 2033, depending on the degree of dismantling of car bodies. That event might be further delayed to 2048 by the use of advanced sorting techniques, but nevertheless metallurgical actions are urgently required. [15]

Fe is considered as one of the most detrimental elements in aluminum with over 20 different Fe-containing intermetallics reported in the past few decades [16]. The phase appearance can change depending on the elements present in the matrix [17] and they are able to transform during homogenization treatment [18, 19]. Therefore, it is of major importance to know which phases are forming and how they appear in dependence of main alloying elements, casting conditions and heat treatment strategies. In this study, the effect of enhanced Fe and Si content on the phase formation and appearance in novel 5/7 crossover alloys will be illustrated.

8.1.2 Experimental

To evaluate the effect of increased impurity content on the phase development in 5/7 crossover alloys, the Si and Fe content was raised from a low (***L***) to a high content (***H***). The ***L*** options represent the Si and Fe content present in industrial grade EN-AW 5182 alloy, which serves as the base alloy in the production of those 5/7 crossover alloys.

The composition of the produced alloys are shown in Table 8-1. The elemental composition was measured by optical emission spectroscopy (Spectromaxx spark spectrometer). The concentration of the main alloying elements is given as a mean value from all alloy variants.

Table 8-1: composition of casted 5/7 crossover alloys with different Si and Fe content [wt. %]

Alloy	**[wt.-%]**						
	Si	**Fe**	**Mn**	**Mg**	**Zn**	**Cu**	**Cr**
SiL-FeL	0.09 ± 0.00	0.15 ± 0.01	0.38 ±0.01	4.33 ±0.06	3.54 ±0.05	0.48 ±0.02	0.06 ±0.00
SiL-FeH	0.11 ± 0.01	0.48 ± 0.06					
SiH-FeH	0.53 ± 0.04	0.46 ± 0.03					

Production of alloys was done using an inductively heated lab scale vacuum furnace (Indutherm MC 100V) with a sample weight of about 100 g. Casting was performed in accordance with Schmid et. al [20] using a copper mould, leading to a maximum cooling rate of about 60 K/s.

As cast microstructure investigations were conducted using a scanning electron microscope (SEM) (JEOL 7200F FEG-SEM, Tokyo, Japan) equipped with an energy dispersive X-ray (EDX) detector (XMax-80, Oxford Instruments, Abingdon, UK).

Automated SEM/EDX particle ("feature") analysis of backscattered electron images using threshold limits were used to determine the density of primary matrix features. The threshold limits for feature detection were set to select particles brighter (heavier) and darker (lighter) than the surrounding matrix. The size limit for particle detection was set to an Equivalent Circle Diameter (ECD) of > 0.5 μm. Parameters for these measurements were chosen as 15 kV, 10 mm WD and 5 s measuring time [21–23]. The area fraction of coarse particles was calculated by dividing the area covered by particles (obtained by automated feature analysis) by the area covered by total structure. The area fraction of particles was assumed to be the same as per unit volume, which is considered a valid estimation for coarse particles [24].

Thermodynamic calculations were done using the software FactSage 8.2 [25] utilizing the FactPS (2022) and FTLite (2022) Database.

8.1.3 Results and Discussion

The FactSage simulation data displayed in Figure 8-1 represents a Scheil solidification simulation for the samples Si***L***-Fe***L*****,** Si***L***-Fe***H*** and Si***H***-Fe***H***. Within the solidification interval, the formation of four phases is predicted. These are two Fe-containing phases Al_3Fe and Al_6(Fe,Mn), as well as Mg_2Si and T-phase. The T-phase forms eutectically as a result of solidification segregation. For Si***L***-Fe***H*** and Si***H***-Fe***H***, the phase fraction of Al_3Fe and Al_6(Fe,Mn) is about 1 wt. %, the higher Si content of Si***H***-Fe***H*** is reflected in a higher Mg_2Si fraction. For Si***L***-Fe***L***, the prediction for Al_3Fe and Al_6(Fe,Mn) yields the values of about 0.5 wt. %. It should be noted that all samples exhibit approximately the same amount of eutectically solidified residual melt 5–6 wt. % T-phase and a solidus temperature of ≈ 400 °C. The lowered amount of T-phase in the Si***H***-Fe***H*** samples is caused by the consumption of Mg by Mg_2Si formation.

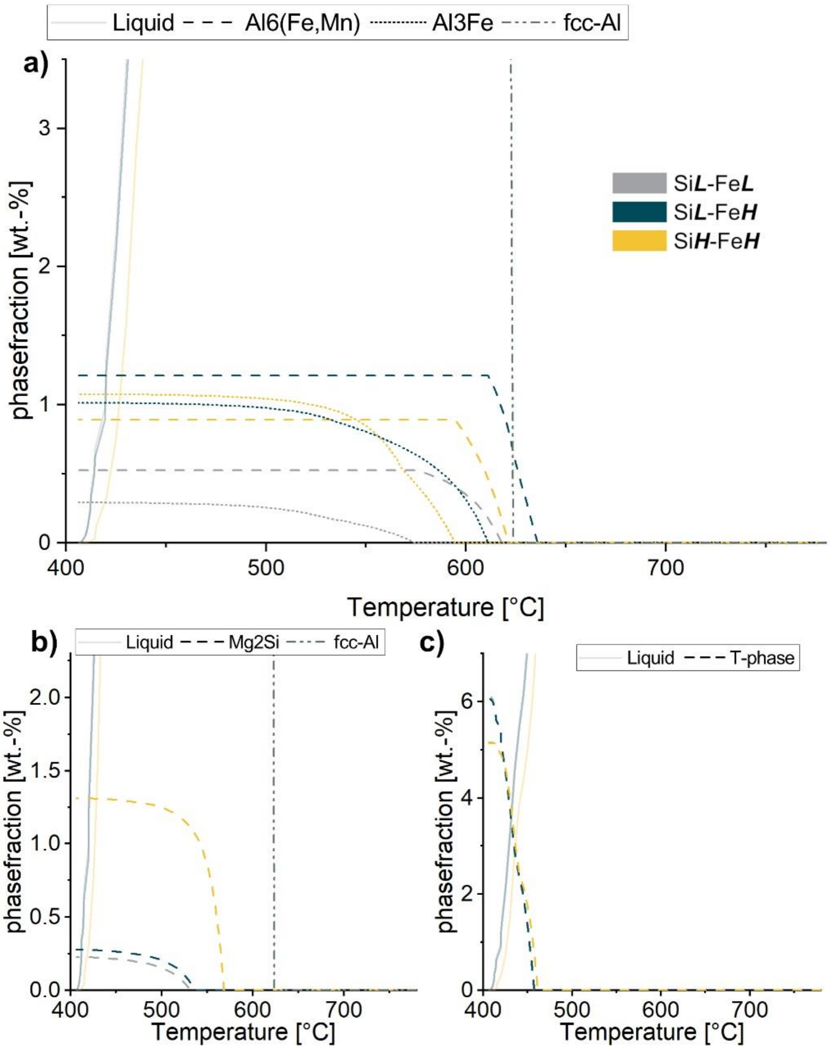

Figure 8-1: Scheil solidification simulation of the crossover alloys with different Si and Fe content showing Fe-bearing phases (a), Mg_2Si formation (b); T-Phase formation (c);

The results of thermodynamic equilibrium calculations are shown in Figure 8-2. Here, the Fe-bearing intermetallics (Figure 8-2a) are found to be Al_3Fe, Al_6(Fe,Mn) and Al(Fe,Mn)Si phases. At the solidus temperature the following amounts are present: ≈1.45 % Al_6(Fe,Mn) and ≈0.25 % Al(Fe,Mn)Si in Si***L***-Fe***L;***

≈1.7 % Al$_6$(Fe,Mn) and ≈0.9 % Al$_3$Fe in Si***L***-Fe***H***; ≈1.7 % Al$_6$(Fe,Mn) and ≈0.95 % Al$_3$Fe in Si***H***-Fe***H***. For Si***H***-Fe***H*** the Al(Fe,Mn)Si-phase exhibits a narrow stability region at about 570 °C (displayed in the insert of Figure 8-2a).

The formation of Mg$_2$Si is shown in Figure 8-2b. The difference in Mg$_2$Si content from Si***L***-Fe***L*** to Si***L***-Fe***H*** derives from the absence of Al(Fe,Mn)Si in the Si***L***-Fe***H*** sample as there is consequently more Si available to form Mg$_2$Si. At high Si levels, the Mg$_2$Si equilibrium content is calculated to ≈ 1.5 wt. %.

As shown in Figure 8-2c, the fraction of the hardening T-phase decreases by about 1.5 wt. % with the increase of Si content, because Mg is consumed to form Mg$_2$Si instead of T-phase (note that for Si***L*** the variants Fe***L*** and Fe***H*** are congruent). Furthermore, the onset of T-phase formation is reduced by 14 °C from 408 °C to 394 °C, leading to a possible opening of the solution heat treatment window.

The thermodynamic calculation show that Mg$_2$Si can´t be used as hardening phase in 5/7 crossover alloys as it is used in 6xxx series alloys [26], because it's solvus temperature is beyond the solidus temperature of the alloy. Therefore, it has to be considered as a primary phase with possible detrimental effects on the alloy's properties.

A comparison of the Scheil and equilibrium simulations shows that the predictions for the Fe-containing phases Al$_6$(Fe,Mn) and Al$_3$Fe match quite well (both Si***L***-Fe***H*** and Si***H***-Fe***H*** in sum approx. 2.6 wt. %, corresponding ≈1.9 Vol. % [27]). In contrast to the equilibrium, however, the Si-containing Fe phase Al(Fe,Mn)Si does not appear in the Scheil simulation for Si***L***-Fe***L***.

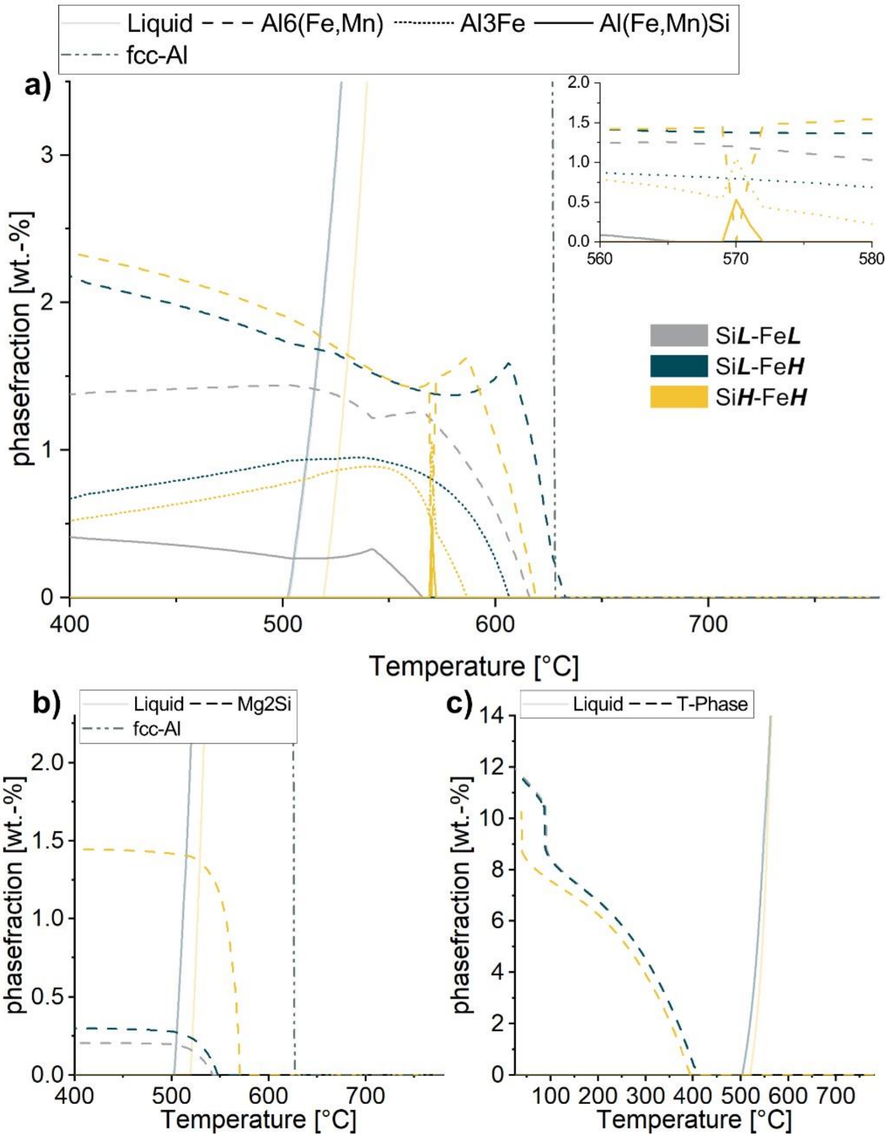

Figure 8-2: FactSage calculations of equilibrium phase formation in the processed alloys; Fe-bearing phases with cut-out section between 560 and 580 °C (a); development of Mg_2Si (b) and T-phase (c)

Microstructural investigations of the produced alloys are shown in Figure 8-3. All alloys produced contain voids that can be interpreted as shrinkage porosity (Label 1). Their size increases as the Fe and Si content increases. All alloys possess about the same amount of segregation zones (Label 2). Those segregation zones are eutectically solidified residual melt, with the intermetallic phase identified as T-phase. The segregation zones are well represented by the Zn-mappings in Figure 8-3, their measured composition is displayed in Table 8-3.

The dark appearing phases in BED micrographs (Label 3) are identified as Mg_2Si particles, as shown by the Si-mappings. There are very few Mg_2Si constituents in the Si***L*** samples, which appear as stretched phase at the cell boundaries. The appearance of the Mg_2Si particles transforms to a net-like structure as the Si content (Si***H*** samples) increases.

In BED micrographs, Fe bearing phases (Label 4) have a bright appearance with about the same contrast as the segregation zones. Mn is present in all Fe-bearing phases of all alloys produced. Fe-phases in Fe***L*** samples, like Si-phases, are barely evident and needle-shaped. When the Fe-content (Si***L***-Fe***H***) is increased, Fe-phases grow, and form plated fishbone structures. When the Si content is increased to match the iron content (Si***H***-Fe***H***), the appearance of the Fe-bearing phases remains nearly the same, with some needle-like phases found in the matrix as well as plated fishbone structures.

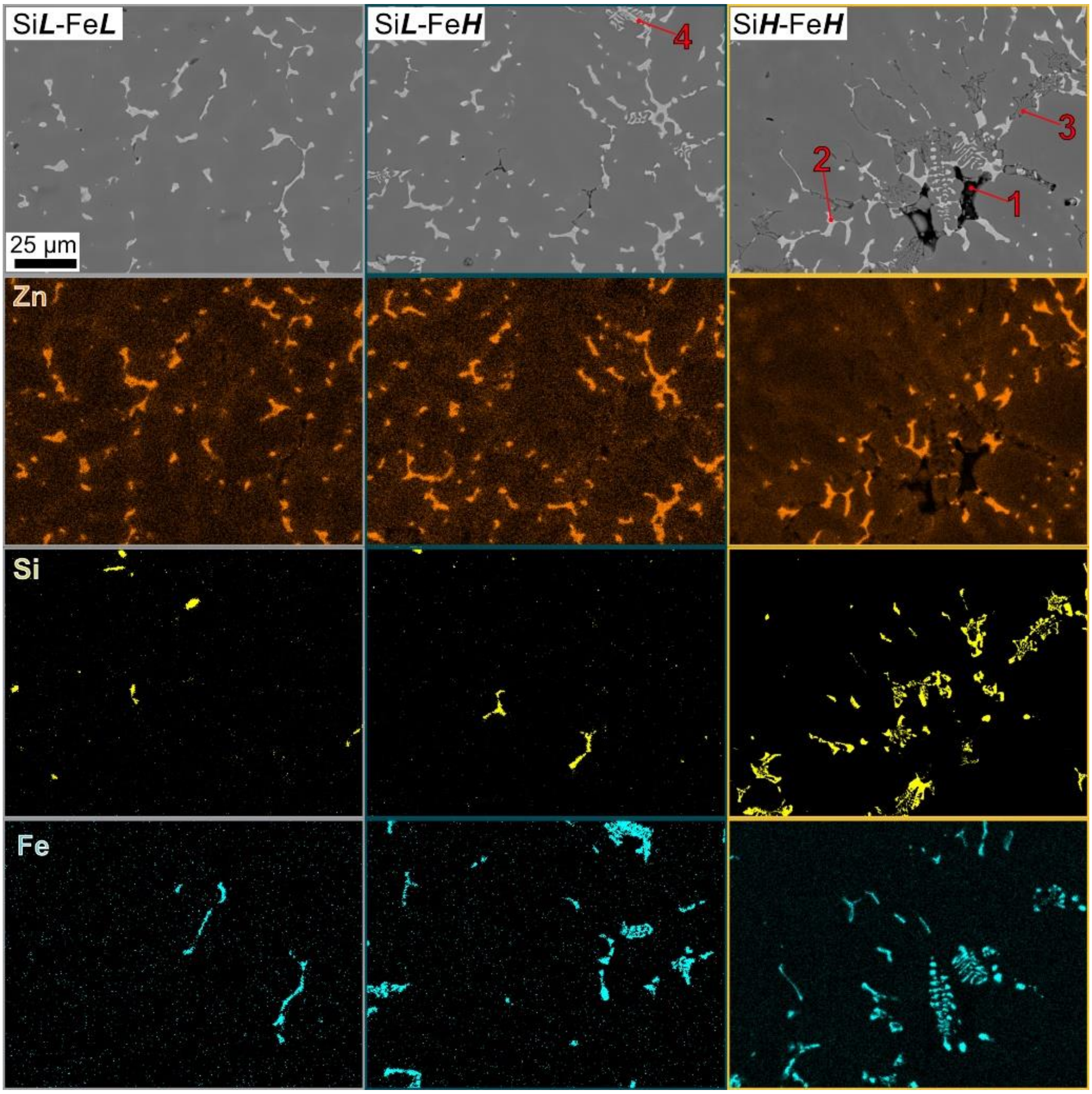

Figure 8-3: SEM-BED micrographs (x700) of produced alloys with mappings of Zn, Fe and Si representing the different phases showing voids (1); segregation zones (2); Mg_2Si-particles (3) and Fe-bearing phases (4)

There is no overlap of Si and Fe-mappings visible at lower magnification (Figure 8-3). Higher magnifications, however, reveal an overlap of Fe and Si, as shown in Figure 8-4. Those phases can be assumed to be of the type Al(Fe,Mn)Si. It should be noted that the majority of Fe-bearing phases visually identified in Si***H***-Fe***H*** are of the type Al(Fe,Mn)Si, with only little Al_6(Fe,Mn).

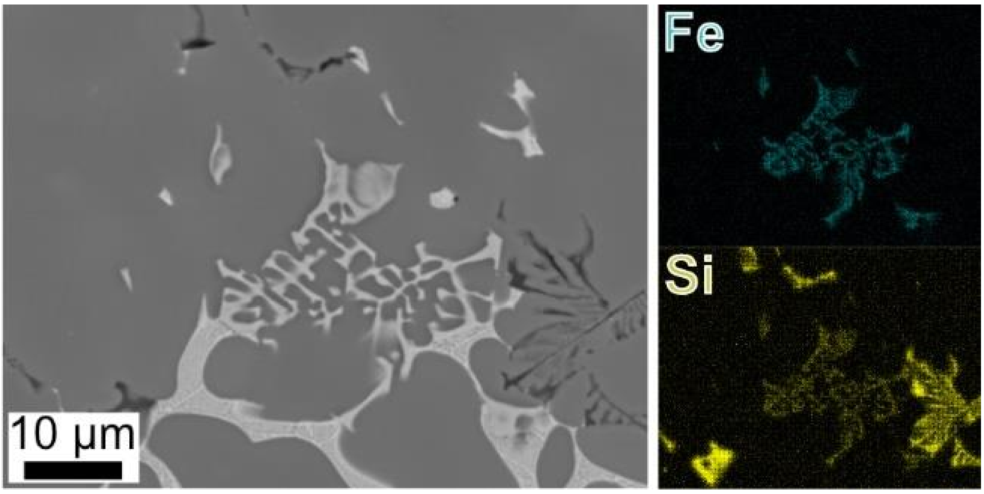

Figure 8-4: SEM-BED micrograph (x1500) of Fe-bearing phases in Si**H**-Fe**H** alloy with corresponding Si and Fe mappings indicating Al(Fe,Mn)Si phase

The as-cast alloys were subjected to quantitative SEM automated feature analysis to determine the content of the different phases formed during casting. The data displayed in Table 8-3 show the fraction of each feature detected for the single alloys. Phases are distinguished first by their greyscale and afterwards according to their iron and silicon content.

From Si***L*** to Si***H*** the Mg_2Si content is rising from 0.2 Vol. % to a value of 0.9 Vol. %. With the density of Mg_2Si being 1.99 gcm^{-3}, a weight fraction of 0.66 wt. % is calculated, which is below the simulated weight fraction of ≈1.5 wt. % for the Si***H***-Fe***H*** sample. It can be assumed that the Si content remains partially supersaturated in the matrix, at least to small amounts, as the cooling rate is quite fast with a maximum of about 60 K/s [20]. This enables to control the Mg_2Si phase, which cannot be dissolved in this alloy system, in size and distribution during homogenization treatment.

The content of Fe-bearing phases containing Si is rising while the number of Fe-bearing phases without Si is decreasing from about 0.9 % to 0.4 %. It is worth noting that also in the Si***L*** samples, Fe-bearing phases with Si-content are found. The Fe-bearing intermetallics without Si are identified to be Al_6(Fe,Mn) while Fe-bearing intermetallics with Si are identified to be of the form Al(Fe,Mn)Si. It is interesting to note, that Scheil simulations did not reveal any formation of Al(Fe,Mn)Si as it is found in equilibrium calculations. This is most likely, because Scheil solidification is only allowing diffusion in liquid and the fact that elements once precipitated are removed from the mass balance. [25]

When investigating the Si***H***-Fe***H*** sample, other than expected by thermodynamic calculations, the amount of Al_6(Fe,Mn) is lowered in comparison to the Si***L*** samples while the Al(Fe,Mn)Si content is raised. Obviously, the high cooling rate during solidification causes the formation of Al(Fe,Mn)Si rather than Al_6(Fe,Mn). This is consistent with the findings of Liu et al. [28] who report transformation in phase formation from Al_6(Fe,Mn) to $Al_{15}(Fe,Mn)_3Si_2$ with increasing cooling rate.

The porosities found in the samples are widely spread and inhomogeneous. The number of pores is slightly decreasing with increasing intermetallic content, but the porosity size is increasing. The increment of porosity size in Si***H***-Fe***H*** samples shown in Figure 8-3 appears due to more intermetallic particles blocking the interdendritic feeding channels like reported by Závodská et. al. [29].

Table 8-2: Calculated fraction of features found by automated feature analysis in [Vol.-%]

Features	**Fraction [Vol.-%]**			
	Pores	**Mg_2Si**	**Fe-containing**	
			Without Si	**With Si**
Si**L**-Fe**L**	0.3	0.2	0.7	0.1
Si**L**-Fe**H**	0.2	0.2	0.9	0.03
Si**H**-Fe**H**	0.1	0.9	0.4	0.6

The chemical composition of the phase in as-cast structures is displayed in Table 8-3. Since the phase composition does not differ significantly across the samples, the values and standard deviations shown in Table 8-3 are representative for all samples.

SEM EDX measurements reveal an elevated Cu and Cr content in the Fe bearing phases, indicating that those elements are incorporated in the intermetallic phases. It should also be noted that the data in Table 8-3 take into account matrix excitation effects for Zn and Mg in Fe-bearing phases and Al in Mg_2Si.

Table 8-3: Measured composition of phases detected by SEM EDX measurements in [at.-%]

Phase	**[at.-%]**							
	Mn	**Fe**	**Si**	**Mg**	**Cu**	**Cr**	**Al**	**Zn**
Al_6(Fe,Mn)	3.1 ±0.9	11.1 ±1.9	-	-	1.1 ±0.3	0.1 ±0.1	84.5 ±2.1	-
Al(Fe,Mn)Si	3.0 ±0.7	11.3 ±2.1	3.4 ±1.1	-	0.8 ±0.5	0.2 ±0.1	81.1 ±2.8	-
Mg_2Si	-	-	35.5 ±4.5	64.5 ±4.5	-	-	-	-
T-phase $Mg_{32}(Al,Zn)_{49}$	-	-	-	24.9 ±1.4	4.5 ±0.7	-	59.3 ±3.1	11.4 ±1.2

8.1.4 Conclusion

In this study, 5/7 crossover alloys with varying levels of Fe and Si were cast with a maximum cooling rate of about 60 K/s and characterized in the as-cast condition using automated feature analysis and EDX measurements. The results were also compared with thermodynamic calculations. The following conclusions can be drawn from these investigations:

- Structures found in the alloy can be identified to be Al_6(Fe,Mn), Al(Fe,Mn)Si, Mg_2Si and T-phase in segregation zones.
- Cu and Cr are incorporated in the Fe-bearing phases.
- At high Si and Fe levels (0.5 wt. %) and high cooling rates, the phase composition changes from Al_6(Fe,Mn) to Al(Fe,Mn)Si.

- The low melting point of 435 °C of the T-phase segregation zones must be taken into account for subsequent homogenization treatment.
- At high Si levels, the Mg_2Si precipitation is partially suppressed by the high cooling rate and the precipitation might be controlled by subsequent homogenization treatment.

This knowledge allows for a better adaption of the crossover alloys to customers needs.

8.1.5 References

[1] J. Hirsch, Aluminium in Innovative Light-Weight Car Design, Materials Transactions 52 (2011) 818–824.

[2] J. Hirsch, J. Søreide, T. Payer, Cr, Japan Light Metal Welding Association & Japan Aluminium Association Vol. 58 (2020) 125–130.

[3] D. Carle, G. Blount, The suitability of aluminium as an alternative material for car bodies, Materials & Design 20 (1999) 267–272.

[4] S.K. Das, J.A. Green, J.G. Kaufman, The development of recycle-friendly automotive aluminum alloys, JOM 57 (2007) 47–51.

[5] AMAG Austria Metall AG, AluReport 02 2022.

[6] AMAG Austria Metall AG, AluReport 01 2023.

[7] L. Stemper, M.A. Tunes, R. Tosone, P.J. Uggowitzer, S. Pogatscher, On the potential of aluminum crossover alloys, Progress in Materials Science (2021).

[8] L. Stemper, M.A. Tunes, P. Dumitraschkewitz, F. Mendez-Martin, R. Tosone, D. Marchand, W.A. Curtin et al., Giant hardening response in AlMgZn(Cu) alloys, Acta Materialia 206 (2021) 116617.

[9] Y. Pan, Di Zhang, H. Liu, L. Zhuang, J. Zhang, Precipitation hardening and intergranular corrosion behavior of novel Al–Mg–Zn(-Cu) alloys, Journal of Alloys and Compounds 853 (2021) 157199.

[10] C. Cao, Di Zhang, X. Wang, Q. Ma, L. Zhuang, J. Zhang, Effects of Cu addition on the precipitation hardening response and intergranular corrosion of Al-5.2Mg-2.0Zn (wt.%) alloy, Materials Characterization 122 (2016) 177–182.

[11] M.C. Caroll, M.J. Mills, G.S. Daehn, B.R. Dunbar, Effects of Zn additions on the grain boundary precipitation and corrosion of Al-5083, Scripta Materialia 42 (2000) 335–340.

[12] C. Meng, Di Zhang, L. Zhuang, J. Zhang, Correlations between stress corrosion cracking, grain boundary precipitates and Zn content of Al–Mg–Zn alloys, Journal of Alloys and Compounds 655 (2016) 178–187.

[13] Y. Geng, Di Zhang, J. Zhang, L. Zhuang, On the suppression of Lüders elongation in high-strength Cu/Zn modified 5xxx series aluminum alloy, Journal of Alloys and Compounds 834 (2020) 155138.

[14] Y. Geng, Di Zhang, J. Zhang, L. Zhuang, Zn/Cu regulated critical strain and serrated flow behavior in Al–Mg alloys, Materials Science and Engineering: A 795 (2020) 139991.

[15] A.N. Løvik, R. Modaresi, D.B. Müller, Long-term strategies for increased recycling of automotive aluminum and its alloying elements, Environmental science & technology 48 (2014) 4257–4265.

[16] Z. Que, Y. Wang, C.L. Mendis, C. Fang, J. Xia, X. Zhou, Z. Fan, Understanding Fe-Containing Intermetallic Compounds in Al Alloys: An Overview of Recent Advances from the LiME Research Hub, Metals 12 (2022) 1677.

[17] Z. Que, Y. Zhou, Y. Wang, C.L. Mendis, Z. Fan, Effects of Mg addition on the Al_6(Fe,Mn) intermetallic compounds and the grain refinement of α-Al in Al-Fe-Mn alloys, Materials Characterization 171 (2021) 110758.

[18] B. Trink, I. Weißensteiner, P.J. Uggowitzer, K. Strobel, A. Hofer-Roblyek, S. Pogatscher, Processing and microstructure–property relations of Al-Mg-Si-Fe crossover alloys, Acta Materialia 257 (2023) 119160.

[19] O. Engler, K. Kuhnke, J. Hasenclever, Development of intermetallic particles during solidification and homogenization of two AA 5xxx series Al-Mg alloys with different Mg contents, Journal of Alloys and Compounds 728 (2017) 669–681.

[20] F. Schmid, L. Stemper, T. Ebner, W. Leitner, S. Pogatscher, Industry-oriented sample preparation of 6xxx and 5xxx aluminium alloys in laboratory, Proceedings of EMC 2019 (2019).

[21] B.G. Bartosiaki, J.A.M. Pereira, W.V. Bielefeldt, A.C.F. Vilela, Assessment of inclusion analysis via manual and automated SEM and total oxygen content of steel, Journal of Materials Research and Technology 4 (2015) 235–240.

[22] M. Nuspl, W. Wegscheider, J. Angeli, W. Posch, M. Mayr, Qualitative and quantitative determination of micro-inclusions by automated SEM/EDX analysis, Analytical and bioanalytical chemistry 379 (2004) 640–645.

[23] O. Walusinski, Doctoral Thesis, in: O. Walusinski (Ed.), Georges Gilles de la Tourette, Oxford University Press, 2018, pp. 129–144.

[24] C.W. Corti, P. Cotterill, G.A. Fitzpatrick, The Evaluation of the Interparticle Spacing in Dispersion Alloys, International Metallurgical Reviews 19 (1974) 77–88.

[25] C.W. Bale, P. Chartrand, S.A. Degterov, G. Eriksson, K. Hack, R. Ben Mahfoud, J. Melançon et al., FactSage thermochemical software and databases, Calphad 26 (2002) 189–228.

[26] F. Ostermann, Anwendungstechnologie Aluminium, 2nd ed., Springer, Berlin Heidelberg, 2007.

[27] N.A. Belov, A.A. Aksenov, D.G. Eskin, Iron in Aluminium Alloys, CRC Press, London, 2002.

[28] Y. Liu, L. Luo, C. Han, L. Ou, J. Wang, C. Liu, Effect of Fe, Si and Cooling Rate on the Formation of Fe- and Mn-rich Intermetallics in Al–5Mg–0.8Mn Alloy, Journal of Materials Science & Technology 32 (2016) 305–312.

[29] D. Závodská, E. Tillová, I. Švecová, M. Chalupová, L. Kuchariková, J. Belan, The Effect of Iron Content on Microstructure and Porosity of Secondary AlSi7Mg0.3 Cast Alloy, Period. Polytech. Transp. Eng. 47 (2019) 283–289.

8.2 Effect of recycling content on an industrial simulation scale

The objective of this study is to estimate the effect of increased recycling content on the properties of alloys produced under near-industrial conditions. Casting trials with higher sample volume and lower cooling rates were conducted. The study found that the size and type of formed intermetallic phases are significantly influenced by cooling conditions during casting and the Fe/Si ratio. Processing of the alloys revealed the causes for the adverse effects of raised impurity content on the mechanical properties and identified potential mitigation strategies. The findings of this study, which reveal the impact of raised impurity content on mechanical properties and potential mitigation strategies, are presented in the following section and were submitted to the journal *Nature Sustainability*.

Bridging sustainable scrap metallurgy and aluminum crossover alloys[6]

Authors' contributions

Sebastian Samberger: Conceptualization, Methodology, Investigation, Visualization, Writing – Original Draft
Irmgard Weißensteiner: Visualization, Writing – Review & Editing.
Matheurs A. Tunes: Visualization, Writing – Review & Editing.
Lukas Stemper: Review & Editing.
Christina Kainz: *XRD*-Investigation, Visualization, Writing – Review & Editing.
Roland Morak: Pandat calculations, Review & Editing
Peter J. Uggowitzer: Conceptualization, Supervision, Writing – Review & Editing.
Stefan Pogatscher: Project Administration, Conceptualization, Supervision, Writing – Review & Editing.

Acknowledgements

The financial support by the Christian Doppler Research Association, the Austrian Federal Ministry for Digital and Economic Affairs and the National Foundation for Research, Technology and Development is gratefully acknowledged. Moreover, the authors wish to express their sincere thanks to AMAG rolling GmbH for the supply of alloy material.

Abstract

Attempts to increase the recyclability of metal alloy products at the end of their lifetime have recently given rise to the science of "dirty" alloys, resulting in international efforts to enable sustainable metallurgy within the circular economy. In this context, aluminum crossover alloys have been developed to provide a wide range of properties within a single alloy composition, an approach that by design facilitates the recyclability of aluminum-based end products. Despite the crossover alloy initiative, nowadays, the major challenge in the recyclability of aluminum is to cope with multi-material mixtures and undesired metal impurities. Herein we demonstrate that both the elemental impurity ratio between Fe and Si and processing parameters such as the cooling rate during casting can be manipulated and optimized to facilitate the production of AlMgZn(Cu) crossover alloys from today's scrap mix. We report on the occurrence of a 6-to-3 transformation –$Al_6(Fe,Mn) \rightarrow Al_{13}(Fe,Mn)_4$ – and a 6-to-alpha transformation – $Al_6(Fe,Mn) \rightarrow Al(Fe,Mn)Si$ – in these AlMgZn(Cu) crossover alloys when with high content of Fe and Si impurities as a major underlying phenomena to be understood amid improving their recyclability. The transformations occurred during the homogenization treatment and both the Fe/Si ratio and the cooling rate upon casting correlate directly with the processability of the alloys. The 6-to-3 transformation can effectively decrease the size of intermetallic particles, facilitating rolling of a recycled alloy in relevant industrial conditions. Higher cooling rates always resulted in smaller and more spheroidized intermetallic phases, facilitating rolling. Slower cooling rates resulted in larger and more stable intermetallic phases, complicating rolling. By shedding light on the key role of phase transformation during

---

[6] Current status: submitted to Nature *Sustainability*

homogenization treatments, our study is bridging for the first time the science of dirty alloys with the emerging field of aluminum crossover alloys, providing valuable findings for future alloy design studies with a focus on metal recycling..

8.2.1 Introduction

The demand for aluminum, particularly in its recycled form, is steadily increasing. Predictions suggest that between 2040 and 2050, the quantity of recycled aluminum may surpass that of aluminum produced from primary sources [1]. This demand is driven by aluminum's significant role in reducing vehicle weight by over 30%, leading to substantial reductions in CO_2 emissions [2,3].

Nevertheless, the great success story of aluminum is somewhat overshadowed by its energy-intensive energy-driven primary production, which involves high CO_2 emissions [4,5]. Moreover, the use of secondary aluminum, especially post-consumer scrap, in the automotive industry is limited due to tramp element limitations. For example, the iron content in space frames is limited to values below 0.2 wt.-%, while models predict iron levels of 0.6 to 0.7 wt.-% in automotive scrap, depending on the dismantling process [6]. The industry is facing an upcoming scrap wave arising from the automotive industry and a potential loss of scrap sinks for aluminum alloys containing high levels of silicon [7]. The limited and cost-intensive removability of tramp elements from aluminum [8–11] and the stringent composition requirements for wrought alloys is generating a need for new approaches in alloy design.

One of those approaches is the aluminum crossover alloying concept. State-of-the-art aluminum alloys suffer from a strength-ductility trade-off which limits their usability in automotive applications. With 5/7 aluminum crossover alloys, a combination between 5xxx and 7xxx series alloys, this trade-off could be overcome [12]. These wrought alloys not only achieve high elongations of about 20% after a pre-aging process, but also show hardening responses of over 180 MPa after thermo-mechanical treatment. This leads to an alloy with yield strength values of over 400 MPa [13]. Additionally, these alloys exhibit a low quench rate sensitivity [14], good weldability [15] and enhanced resistance to intergranular corrosion [16,17], exfoliation corrosion [18] and stress corrosion cracking [19]. 5/7 crossover alloys have also shown potential in superplastic and quick plastic forming processes, making them attractive candidates for automotive applications [20].

The hardening mechanism in the 5/7 crossover system occurs primarily through T-phase ($Mg_{32}(Al,Zn)_{49}$) [21] precipitation, where Zn can be replaceable by Ag [22,23] and/or Cu [13,23,24], enhancing the hardening potential. Interestingly, the T-phase is known to withstand high irradiation rates, also making applications in extreme environments possible [25,26].

The crossover alloying concept is not limited to the 5/7 combination. Trink et al. [27] developed a 6xxx series with increased amounts of Fe, representing a 6/8 aluminum crossover alloy [28]. 2/7 aluminum crossovers are also feasible [29,30].

With their broad property profile crossover alloys address the need to increase recyclability of complex products (e.g. cars) through design that is reducing the multitude of the materials used by putting different properties into one material. Although crossover alloys have by their definition the potential to expand the mix of today's alloys that can be used for recycling (e.g. 5xxx and 7xxx series alloys in 5/7 crossover alloys), we will have to cope with complex scrap mixtures in their manufacture and expand research into the area of science of dirty alloys [7] until the desired transition to future product designs with reduced chemical complexity is reached.

Iron is one of the most studied tramp elements in Al wrought alloys, because intermetallic particles (IMPs) containing iron are known to exhibit a major detrimental effect on material properties [31]. More than 20 different IMPs containing iron are reported to exist in Al. Common types include β-Al_5FeSi (needle-like shape), a'-Al_8FeSi or α-$Al_{15}(Fe,Mn)_3Si_2$ (compact or Chinese script morphology), $Al_{13}Fe_4$ and $Al_6(Mn,Fe)$. The formation and morphology of these phases depend on the elemental composition (Si, Fe, Mn-ratio) and the cooling rates [32–34]. The type of phase which forms during solidification depends strongly on the cooling rate. An increased cooling rate can generate α'-Al_8FeSi instead of β-Al_5FeSi. The formation of α-$Al_{15}(Fe,Mn)_3Si_2$ or α'-Al_8FeSi is desirable due to their compactness, with fewer detrimental effects on material properties [34].

$Al_{13}Fe_4$, also written as Al_3Fe, is the Al-richest stable structure in the Al-Fe system. Due to non-equilibrium solidification the $Al_{13}Fe_4$ phase is suppressed in favor of metastable phases such as Al_mFe, Al_xFe or Al_6Fe phase [35,36]. This suppression is influenced by the cooling rate and by other elements present in the Al matrix. Alloying elements influence the formation, composition and morphology of the Fe-bearing phases. The metastable $Al_6(Fe,Mn)$ phase shows a solubility for alloying elements such as Cu [37,38] and Cr [39]. It has also been reported that the morphology of the $Al_6(Fe,Mn)$ phase changes from needle-like to plate-like when the Mg content in the matrix is increased, while no Mg is dissolved in the phase [40]. As metastable phases strive towards a state of equilibrium, both $Al_m(Fe,Mn)$ and $Al_6(Fe,Mn)$ transform into $Al_{13}Fe_4$ (or $Al_{13}(Fe,Mn)_4$) during heat treatment [35,41–43].

Thermomechanical treatment also has a significant effect on phase structure and morphology. Trink et al. [44] and Krall et. al. [45] were able to transform the morphology of potentially detrimental intermetallics using a combination of heat treatment and hot rolling. Here they not only mitigated the detrimental effect of high Fe and Si content on formability, but further improved the mechanical properties of the alloy. Another phenomenon related to Fe-bearing IMP mainly observed in 3xxx series alloys is the so-called 6-to-alpha transformation [46–48]. During casting, the main primary phase observed is $Al_6(Fe,Mn)$. During the course of subsequent heat treatment Si, which originates from the partial dissolution of Mg_2Si particles or from supersaturated solid solution, diffuses into the phases. The Si is then incorporated into the lattice, gradually transforming the $Al_6(Fe,Mn)$ phase into α-$Al(Fe,Mn)Si$ instead of $Al_{13}Fe_4$. The $Al(Fe,Mn)Si$ phase has been reported to have a variety of composition and crystal structures, ranging from simple cubic, bcc to hcp depending on the Mn/Fe ratio of the alloy [49–51].

It has already been shown that 5/7 crossover alloys are good candidates for use in the automotive industry [52]. However, little is known about the effects of increased Fe and Si content on their mechanical performance and processability, which would affect how much recycling content is usable in production. Because several elements are known to interact with the Fe-bearing IMPs, it is of vital interest to understand the nature of the phases that precipitate in this crossover alloy system. This study therefore aims to fill the knowledge gap by exploring the effect of different industrially relevant Fe and Si contents and ratios on the processability of 5/7 crossover alloys. An insight into the effect of Fe and Si on the processability and mechanical properties of alloys is crucial to addressing the challenges of deploying aluminum with a higher recycled content in automotive manufacturing, where tramp element management is key to sustainability and performance.

8.2.2 Experimental

The study is based on a 5/7 crossover material with fixed Mg, Zn and Cu contents of 4.5, 3.5 and 0.5 wt.-%, respectively. An industrial-grade EN-AW 5182 alloy was used as the base material for producing the alloys. The effect of increased tramp element concentration was evaluated by varying the Fe and Si content. Increasing the tolerance limits of the tramp elements can make it possible to use more scrap and different types of scrap. These limits were adjusted to range from a low content (↓) representing the tramp element content of the base alloy 5182 to a high content (↑) of 0.5 wt.-% of both Fe and Si. The Mn content was not adjusted for this study and represents the content of the base alloy. Table 8-4 shows the elemental averages and standard deviation (four points per measurement) of the alloys produced as measured by optical emission spectroscopy (OES) (Spectromaxx spark spectrometer).

Table 8-4: Mean values of the alloys produced, measured by OES [wt.-%]

Alloy	[wt.-%]						
	Fe	Si	Mn	Cu	Mg	Zn	Cr
Fe↓ - Si↓ (Ref.)	$0.09_{\pm 0.00}$	$0.15_{\pm 0.01}$	$0.38_{\pm 0.01}$	$0.48_{\pm 0.02}$	$4.33_{\pm 0.06}$	$3.54_{\pm 0.05}$	$0.06_{\pm 0.00}$
Fe↑ - Si↓	$0.48_{\pm 0.06}$	$0.11_{\pm 0.01}$					
Fe↑ - Si↑	$0.53_{\pm 0.04}$	$0.46_{\pm 0.03}$					

Alloy production was performed in accordance with the production routes described by Schmid et al [53]. Three different cooling rates were utilized for each of the three 5/7 crossover samples. A schematic illustration of the production routes used is displayed in Figure 8-5. Fast-cooled samples were produced using an inductively heated furnace with a sample size of approximately 100 g. By casting into a copper mold, a cooling rate of up to 60 K/s was achieved. Medium and slow cooling rate samples were produced using a resistively heated furnace with a sample size of approximately 7 kg. The medium cooling rate was achieved using a mold heated and cooled by an ionic liquid [54]. The result was a medium cooling rate of approximately 3 K/s. It is important to note that this rate is comparable to that of industrial continuous casting systems. The slow cooling condition is obtained by cooling the mold in ambient air, giving a cooling rate of ≤ 1 K/s.

After casting, the samples were homogenized at a temperature of 480 °C with a holding stage at 425 °C for 1 h during heating. To examine the homogenized condition, the samples investigated in this condition were quenched in water. This ensures suppression of T-phase precipitation, as the finely dispersed T-phase particles interfere with the automated particle ("feature") analysis of the primary phases. Samples for subsequent processing were slowly cooled to room temperature in the furnace to simulate industrial practice.

Hot rolling was performed at a temperature above 400 °C, followed by cold rolling. Intermediate annealing at 370 °C was carried out between the cold rolling steps to set the cold rolling degree (CRD) of the finished 1.2 mm material at 60%.

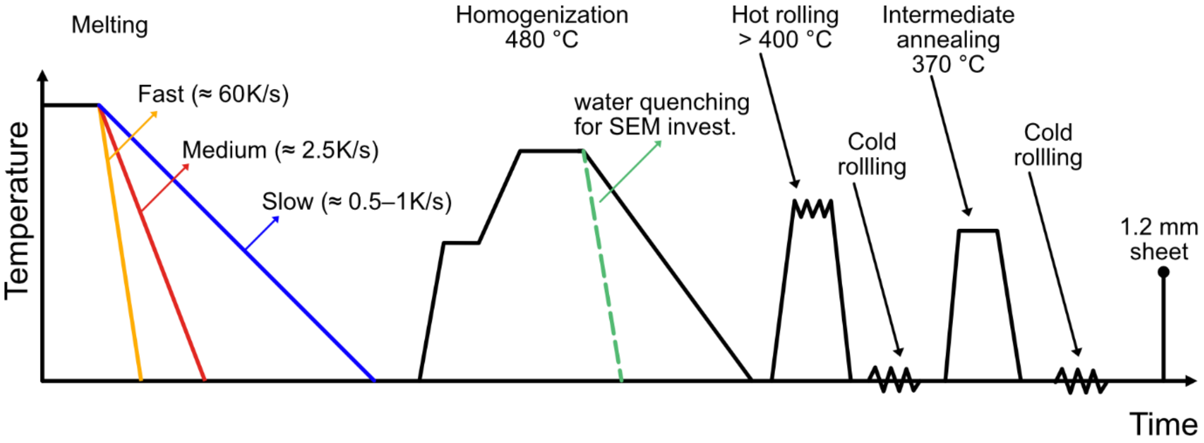

Figure 8-5: Schematic of the process routes used in this study

Microstructure and texture investigations were conducted with a scanning electron microscope (SEM) (JEOL 7200F FEG-SEM, Tokyo, Japan) equipped with an energy dispersive X-ray (EDX) detector (XMax-80, Oxford Instruments, Abingdon, UK). The device includes the option of automatic feature analysis of backscattered electron images using threshold limits.

Automated SEM/EDX feature analyses were applied to determine the area density of coarse particles. The threshold limits for particle detection were set to select particles brighter (heavier) and darker (lighter) than the surrounding matrix. The size limit for particle detection was adjusted to the size of primary features in the samples with respect to the measurement time. Because as-cast features in rapidly cooled samples are small, higher magnification and a size limit of an equivalent circle diameter (ECD) of > 0.5 µm were deployed. In slow- and medium-cooled samples the primary features are coarser, and to account for the samples' inhomogeneity large areas of up 75 mm^2 were scanned. In order to conduct such large area scans in a feasible time, the feature detection limit was set to an ECD of > 3.15 µm. This limitation to coarse features was necessary because the T-phase segregation zones, with their sponge-like structure in as-cast samples, would otherwise be split into numerous small features, making the measurement time unrealistically long. For the re-analysis of selected medium-cooled samples a smaller size limit of > 0.7 µm was chosen in order to increase accuracy and detect transformed small phases.

The parameters for these measurements were chosen as 15 kV, 10 mm working distance (WD) and > 20.000 counts per feature [55–57]. The particles were measured at in central point to mitigate co-excitation of the surrounding particles. The features detected were categorized according to their brightness level and elemental composition. As it was not possible to fully supress co-excitation and matrix effects, the categorization of the particles was based on elemental threshold limits. The area fraction of coarse particles was calculated by dividing the area covered by particles (obtained by automated feature analysis) by the area covered by the total structure. The area fraction of particles was assumed to be equivalent to volume fraction, which is considered a valid estimation for coarse particles [58].

To validate and re-assess the change in the area fraction of primary particles through heat treatment procedures, re-analysis of EDX micrographs from feature analysis was performed using Fiji software [59]. As image based analysis only allowed the detection of pixels brighter than the matrix, the T-phase (also brighter than the matrix) had to be eliminated from the as-cast dataset to allow comparison of IMPs. The spatially resolved chemical information from the feature analysis data allowed then for separation and comparison of T-phase and IMPs.

For a more accurate analysis of the phase composition, high-magnification EDX measurements were performed on representative points of several features in the matrix. Data from each point was collected for 10 s to ensure sufficient data for meaningful analysis. The settings for the high-magnification EDX measurements were again 15 kV and 10 mm WD.

X-ray diffraction (XRD) measurements were carried out with a Bruker-AXS D8 Advance diffractometer, operating with CuK_α radiation. The measurement was performed in Bragg-Brentano geometry, where a 2θ range of 30–85° was probed. A more detailed XRD analysis was carried out on selected samples using a Bruker D8-Discover-II diffractometer, operating with CuK_α radiation. For the latter a 2θ range of 15–36° was probed.

Thermodynamic calculations were performed to estimate the nature and evolution of the phases occurring during processing. Equilibrium and Scheil calculations were carried out using FactSage [60] and Pandat [61] software, with a temperature step size of 1 °C. This also allowed a comparative analysis between FactSage (FactPS and FTlight databases) and Pandat calculations (PanAl2021 database).

8.2.3 Results and Discussion

8.2.3.1 Casting and Homogenization

Figure 8-6 shows the Fe-bearing intermetallic phases predicted by FactSage (Figure 8-6 a, c, d) and Pandat (Figure 8-6 b, d, e). Both procedures calculate the Fe-bearing phases occurring in equilibrium as $Al_{13}Fe_4$, $Al_6(Fe,Mn)$ and Al(Fe,Mn)Si.

According to FactSage calculations, $Al_{13}Fe_4$ is expected for all Fe↑ alloys with a shift in appearance temperature from about 610°C to 580°C at higher Si levels in the alloy. No $Al_{13}Fe_4$ phase is predicted for low Fe content. This is inconsistent with the Pandat calculation. Here $Al_{13}Fe_4$ is predicted for all alloys with a shift in appearance temperature with increasing Fe content from 640°C to 690°C, which is clearly above the liquidus temperature of fcc-Al. According to FactSage and Pandat, $Al_6(Fe,Mn)$ is present in all elemental compositions with an increasing fraction at higher Fe levels. While FactSage predicts the formation of $Al_6(Fe,Mn)$ from the melt at around 620 °C, which is close to the liquidus temperature of the fcc-Al matrix, Pandat states that the $Al_6(Fe,Mn)$ formation is generated by a phase transformation of Al(Fe,Mn)Si. This is best seen at high Fe content when comparing Figure 8-6d and f at around 480 °C, where the amount of Al(Fe,Mn)Si decreases while the amount of $Al_6(Fe,Mn)$ increases steadily. However, such behaviour is not predicted by the FactSage calculations. Here the Al(Fe,Mn)Si has only a small stability region at 570 °C (see inset in Fig. 1a) at high Fe and high Si content. This small stability region forms at the expense of $Al_6(Fe,Mn)$.

For Fe↓-Si↓, the existence of Al(Fe,Mn)Si is predicted independently of other phases with a phase fraction below 0.5 wt %.

The non-Fe-bearing phases predicted, which turn out to be T-phase and Mg_2Si, are shown in Figure 8-18 of the appendix. For these phases the Pandat and FactSage calculations are almost identical at the onset of phase formation. The onset and amount of T-phase shifts from around 410 °C to 390 °C as the Si content in the alloy increases. This is due to the consumption of Mg by the formation of Mg_2Si. As with the T-phase, the prediction for Mg_2Si formation is almost identical for both equilibrium calculations. While the amount of Mg_2Si formed is about 0.3 wt % at low Si content, it increases to about 1.5 wt % at an Si content of 0.5 wt %. As the Si content increases, the precipitation onset temperature also increases from about 550 °C to 570 °C. The formation of Mg_2Si always occurs in the presence of a liquid phase. This effectively means that once formed, Mg_2Si cannot be dissolved back into solid solution without the presence of a liquid phase. Therefore Mg_2Si must be considered as a potentially harmful primary phase in this alloy system.

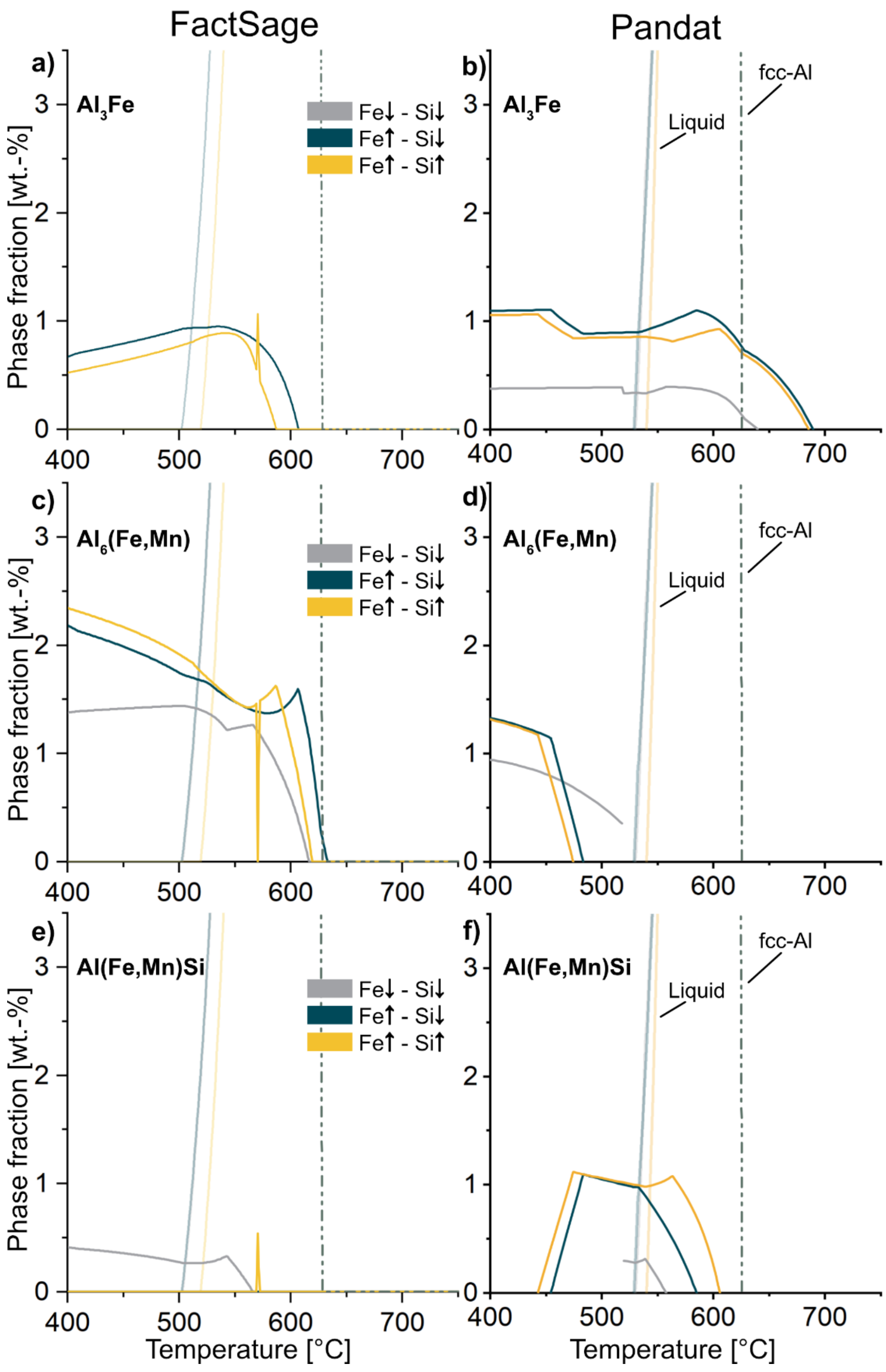

Figure 8-6: Thermodynamic equilibrium calculations of Fe-containing phases for samples with different Si and Fe content. Comparison of the results after FactSage and Pandat for $Al_{13}(Fe,Mn)_4$ (written as Al_3Fe) (a) and (b); $Al_6(Fe,Mn)$ (c) and (d) and Al(Fe,Mn)Si (e) and (f)

In addition to equilibrium calculations, Scheil cooling simulation was simulated with both FactSage and Pandat to determine phases occurring during the solidification procedure (displayed in Figure 8-19 of the appendix). Both calculations predict eutectic T-phase formation. Other phases predicted by FactSage after solidification are $Al_{13}Fe_4$ and Al_6Fe and Mg_2Si as shown in a previous studies [62]. According to Pandat, the only phases appearing besides eutectic T-phase are Mg_2Si and Fe- and Si-bearing IMPs, called Al(FeMn)Si in the following. The composition of the alloy used has no influence on the types of phase predicted, but it does influence their quantity and the start of their occurrence.

After casting under the various cooling conditions, the microstructure of the slabs was investigated by SEM-EDX measurements. Because the microstructure in the as-cast state is inhomogeneous, large areas of up to 75 mm^2 were studied. The micrographs in Figure 8-7 show representative areas of the samples; overview area scan images can be found in the supplementary materials section (SI). The features identified in the alloys were: shrinkage pores from solidification (1); eutectic T-phase segregation zones (2); Fe-bearing IMPs (3); Si-bearing IMPs (4); and Fe- and Si-bearing IMPs (5). For better visibility, EDX mappings of Fe (magenta) and Si (red) are shown as an overlay to the backscattered electron (BSE) micrographs. Si-bearing IMPs also contain Mg and are therefore identified as Mg_2Si. IMPs containing Fe and Si are named Al(Fe,Mn)Si phases in accordance with the phases predicted by equilibrium calculations.

The eutectically solidified T-phase segregations have the same composition for all alloys produced, which is measured multiple times by EDX to: $24.9{\pm}1.4$ at. % Mg, $4.5{\pm}0.7$ at. % Cu, $11.4{\pm}1.2$ at. % Zn and $59.3{\pm}3.1$ at. % Al. The composition of the T-phase segregation zones is of paramount importance as these zones may form an unexpected liquid phase during homogenization, which means the heating rate must be chosen such that the segregation zone is able to dissolve back into the matrix before melting phenomena occur [63]. According to FactSage equilibrium calculations, the observed segregation zone is predicted to melt at a temperature of 435 °C. Therefore a low heating rate was selected for the subsequent homogenization treatment, in order to dissolve the segregation zone into the matrix and suppress melting phenomena.

Mg_2Si is present in all alloys. While samples with low Si content have small scattered and spherical precipitates, the size and number of Mg_2Si particles increases with increasing Si content. The morphology of the Mg_2Si particles is unaffected by the cooling rate and shows a branched arm-like structure. The impact of the cooling rate is, however, evident in that the slower the cooling condition is, the greater is the increase in phase size.

In samples with low Fe content, the Fe-bearing phases exhibit almost the same morphological appearance as Mg_2Si. The spherical Fe-containing phases increase in size with a decreasing cooling rate but do not change significantly in appearance. Where there is higher iron content, however, the morphology of the phases appearing changes drastically in dependence on the cooling condition. At high cooling rates the Fe-bearing phases are very small, and have a spherical, skeletal structure. In BSE micrographs they are difficult to distinguish from segregation zones, as they show almost identical contrast levels. The Fe-phase appearance does not change with the variation of Si, they are present as long shaped plates and Chinese script structures. The only difference is the more frequent occurrence of Fe/Si overlaps (Al(Fe,Mn)Si-phases) in Fe↑-Si↑ samples. These overlaps are more pronounced at intermediate cooling rates than in the slowly cooled samples. It is noteworthy that the morphology of the Fe-bearing phase does not correlate to the presence of Si. At slow cooling rates the primary phases often have a block-like appearance with sharp edges, indicating very stable structures.

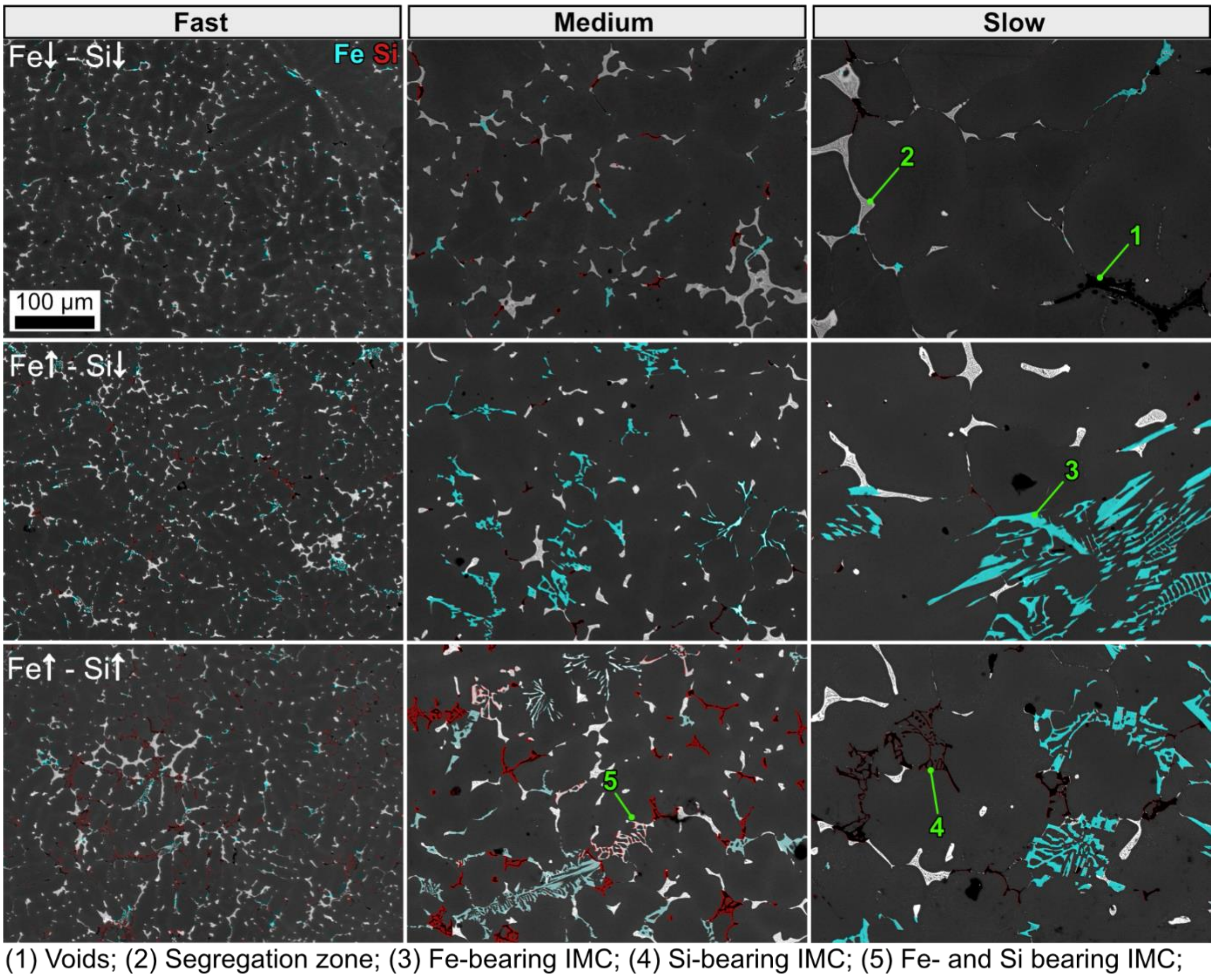

Figure 8-7: SEM-BSE micrographs of the alloys produced, in the as-cast state with Fe- and Si-mapping as overlays. The features found are shrinkage voids in black (1), segregations zones in light grey (2), bright Fe-bearing phases colored cyan (3), black Si-bearing phases in black colored red (4) and Fe/Si-bearing phases in light grey with blue and red overlay (5)

After casting, homogenization was performed at 480 °C at a slow heating rate sufficient to dissolve T-phase segregation prior to melting. To not compromise evaluation of Fe-bearing IMPs by T-phase precipitation, the samples were quenched after homogenization to suppress the re-formation of T-phases. Again, representative micrographs of the samples after homogenization are shown in Figure 8-8 (large-scale images can be found in the SI). For better visibility of the Fe- and Si-bearing phases, the BSE micrographs are again overlaid with Fe (cyan) and Si (red) EDX mappings. Apart from the dissolution of T-phase back into the matrix, all other phases of the as-cast state were also present in the homogenized case.

In samples subjected to fast cooling conditions, the IMPs start to spheroidize during homogenization. The spheroidization of IMPs during the homogenization of rapidly cooled samples is very recognizable in Figure 8-9a and b.

Under slow cooling conditions slight phase spheroidization is still observable in the Fe↓-Si↓ sample, but when the Fe and Si levels are raised the spheroidization of phases does not take place.

Under medium cooling conditions and in samples with Si↓, a significant morphology transformation of the Fe-bearing IMPs is observed. During homogenization the Fe-bearing IMPs in the Fe↑-Si↓ sample obviously disintegrate into small fragments. This is probably due to a phase transformation from $Al_6(Fe,Mn)$ to the thermodynamically stable state $Al_{13}(Fe,Mn)_4$, which can be called a 6-to-3 transformation. When the Si level is adjusted to the Fe level, this transformation into fragments is no longer observed. The phases retain approximately the same size and morphology as in the as-cast state, and a higher frequency of Fe- and Si overlaps is detected, indicating an $Al_6(Fe,Mn)$ to Al(Fe,Mn)Si or 6-to-alpha transformation.

At high Si levels, the spheroidization of Mg_2Si is only achieved in samples subjected to fast cooling rates during solidification. In medium- and slow-cooled samples, the Mg_2Si particles retain the same morphology and size as they had in the as-cast state, while an additional precipitation on the Fe-bearing IMPs is observed.

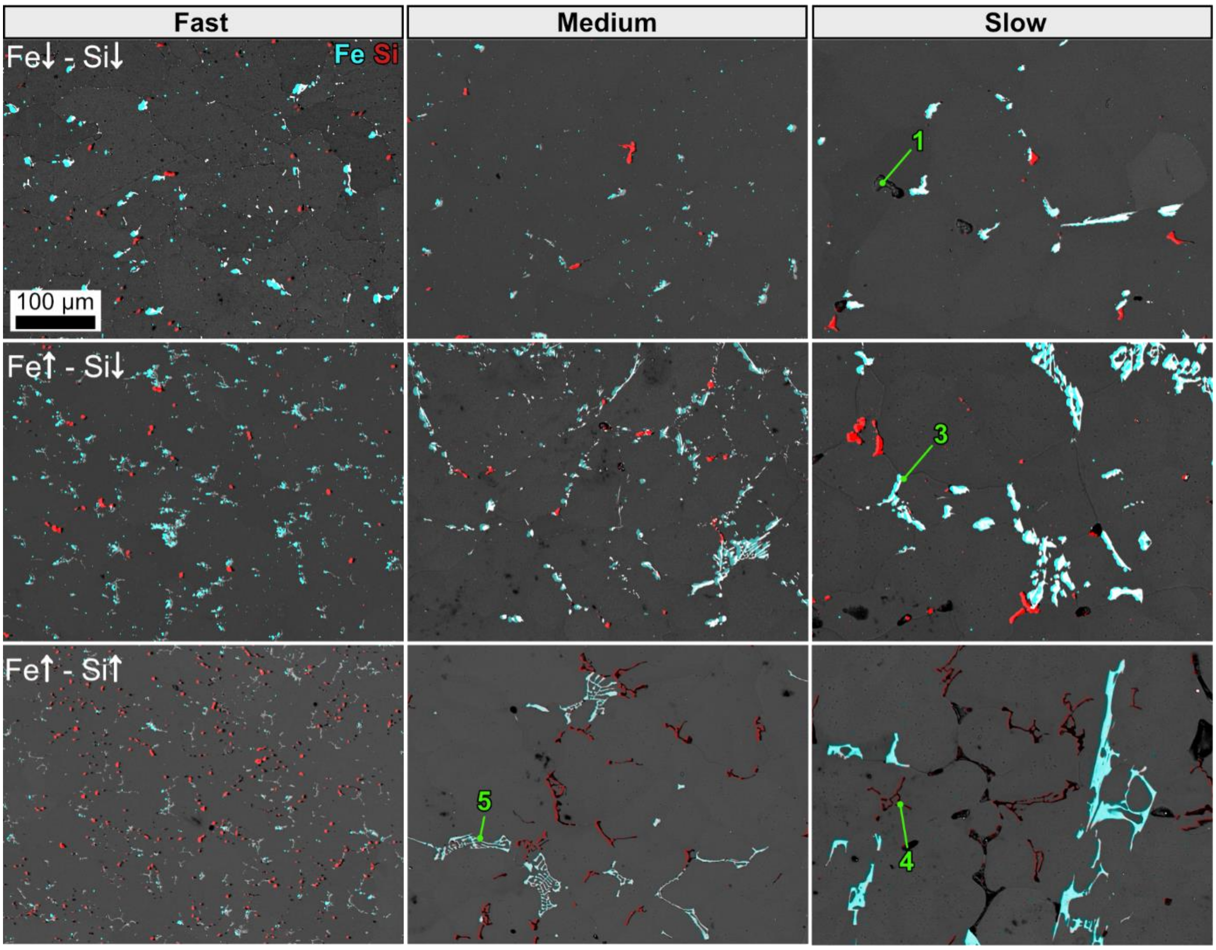

(1) Voids; (3) Fe-bearing IMC; (4) Si-bearing IMC; (5) Fe- and Si bearing IMC;

Figure 8-8: SEM-BSE micrographs of the alloys produced in the homogenized state with Fe and Si mapping as overlays. The features observed are shrinkage voids in black (1), Fe-bearing phases colored cyan (3), Si-bearing phases in black and red (4) and Fe/Si-bearing phases in light grey with cyan and red overlay (5)

In samples with raised Si levels additional precipitation of Mg_2Si particles at the surface of coarse particles is observed, as shown in Figure 8-9. This effect is not limited to Al(Fe,Mn)Si phases, but can also be seen at the surface of any type of Fe-bearing IMPs.

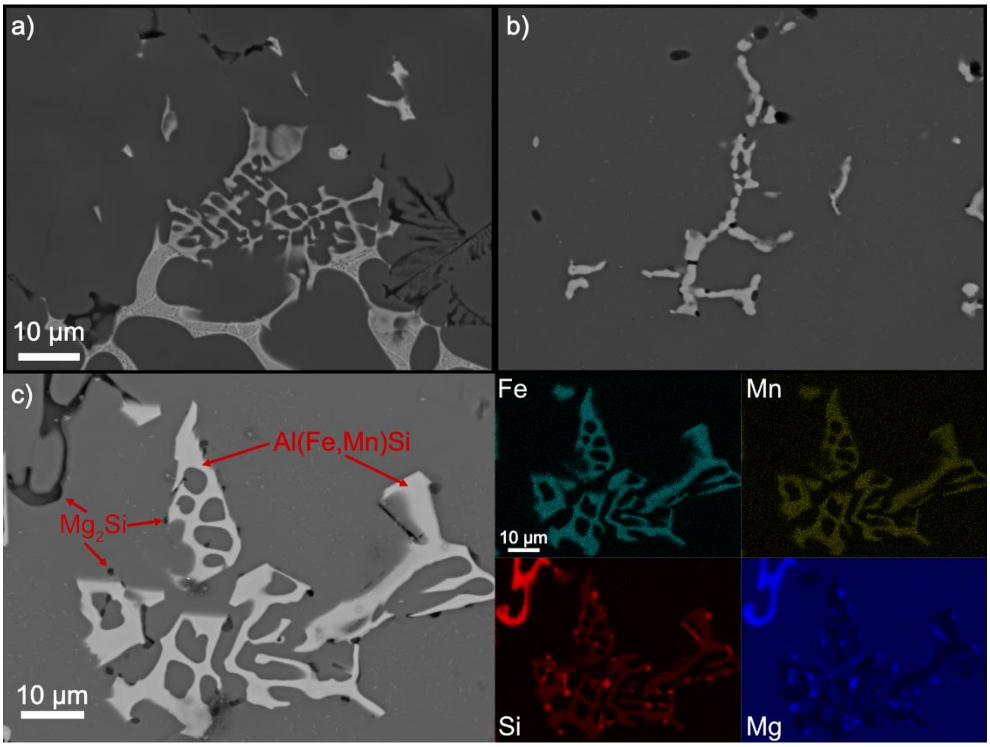

Figure 8-9: SEM-BSE micrograph of sample Fe↑ - Si↑ subjected to fast cooling conditions after casting (a) and homogenization (b) showing the spheroidization of the small IMPs; SEM-BSE micrograph of sample Fe↑ - Si↑ subjected to medium cooling conditions after homogenization (c) with EDX mappings of Fe, Mn, Si and Mg displaying the precipitation of Mg_2Si particles on the surface of the Fe-bearing IMPs

8.2.3.2 Feature identification

As the microstructure is very inhomogeneous across the samples, in particular in the occurrence of voids, automated feature analysis was carried out to gain a better insight into the phase evolution. Large areas of up to 75 mm^2 per sample were analyzed to ensure uniformity, and EDX measurements were conducted on the features identified; see the SI for the images. Feature types were, based on the grey value and the elemental content thresholds, assigned to Mg_2Si, voids, T-phase, Fe-bearing IMPs and Fe- and Si-bearing IMPs. A categorization of the phases as $Al_6(Fe,Mn)$ and $Al_{13}(Fe,Mn)_4$ was not feasible, because the range of elemental compositions precludes clear subcategorization.

The data in Figure 8-10 and Figure 8-11 represent the phase fraction of the identified features together with standard error of the mean. The data must be regarded with some uncertainty because some of the particles may be misinterpreted as others due to co-excitation effects caused by both particle and beam size. This is of particular interest because there are several areas where Fe-phases are integrated into T-phase segregation zones and vice versa (they exhibit approximately the same grey value), and Mg_2Si particles have precipitated on the surface of coarse Fe-bearing phases. The phase fraction of T-phase segregation zones is not shown in the graphs; its value is 2.0 ± 0.6% for all samples in the as-cast condition and it fully dissolves into the matrix during homogenization.

The phase fraction of Mg_2Si particles for all the samples produced is shown in Figure 8-10a. At low Si levels the phase fraction is approximately the same for all samples at 0.2–0.3%, while no change is observed during homogenization. When the Si content of the alloy is increased, the phase fraction of Mg_2Si increases continuously from 0.9% after rapid cooling to 1.3% after slow cooling. During homogenization, the Mg_2Si fraction increases further, by about 0.3% in rapidly cooled Fe↑-Si↑ samples and 0.2% in medium- and slow-cooled samples. This means that supersaturation of Si can be achieved in all samples, with higher efficiency at increased cooling conditions. This suggests the possibility of phase modification during subsequent heat treatment, and could mitigate the potentially negative impact of primary Mg_2Si.

As seen in the BSE micrographs in Figure 8-7 and Figure 8-8, voids are present in all samples and are inhomogeneously distributed in the matrix. The proportion of voids present in the alloys as a function of cooling condition is shown in Figure 8-10b. Decreasing colling rates during solidification lead to an increase in number and size of voids, their fraction does not change significantly during the homogenization treatment. The variations in numbers seen in Figure 8-10b represent the inhomogeneous distribution of voids in the matrix. Although large areas were analyzed, the inhomogeneous distribution of voids within the matrix only allows a qualitative comparison between cooling rates within the scope of the experiments.

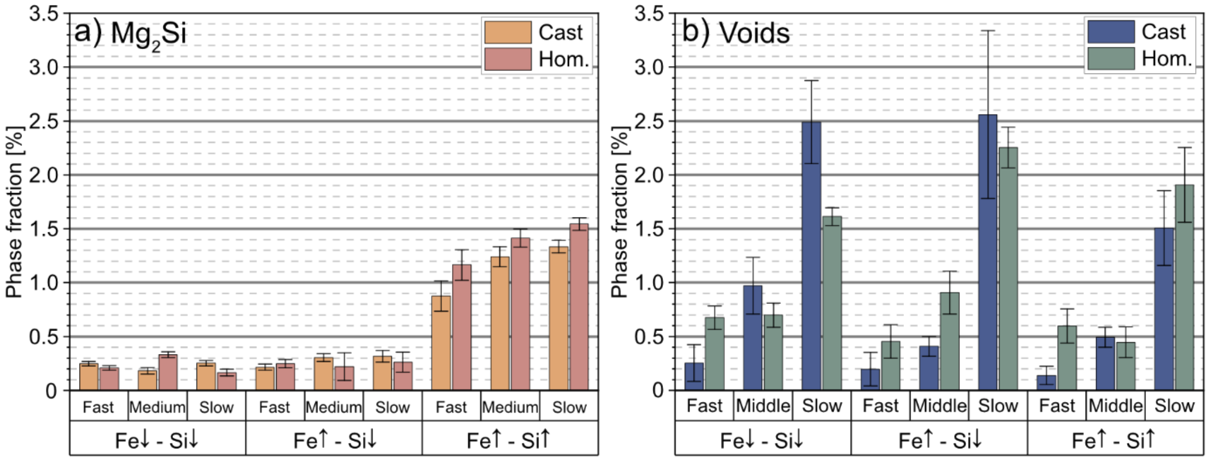

Figure 8-10: Feature analysis with phase fraction and standard deviation of the mean for Mg_2Si and voids in the as-cast and homogenized condition with different levels of tramp element content and different cooling rates

Figure 8-11a relates the evolution of the Fe-bearing phases to the cooling conditions during casting. In samples with low Fe content, this fraction is around 0.7% and below. These values do not depend on the cooling rate. During homogenization treatment the fraction decreases slightly, which can be linked to phase transformation towards the stable $Al_{13}Fe_4$ condition.

The amount of Fe-bearing phase increases significantly with an increase in Fe content. In rapidly cooled Fe↑-Si↓ samples the precipitation of coarse particles is, with a fraction of about 0.9%, suppressed in contrast to medium and slow cooled samples where the fraction of Fe-bearing phases increases to a value of about 2%. During homogenization the fraction of Fe-bearing phases does not change in rapidly cooled samples, but seem to decreas in medium- and slow-cooled samples. As can be seen in Figure 8-7 and Figure 8-8, the Fe-bearing phases in the medium-cooled Fe↑-Si↓ sample transform into small fragments during homogenization. Therefore a considerable proportion is too small for the 3 µm ECD detection limit applied for medium- and slow-cooled samples. A repeated measurement of the medium-cooled Fe↑-Si↓ sample in the homogenized condition (marked with an *) generates a higher particle detection rate. Nevertheless, a significant decrease the detected in phase fraction is observed when the $Al_6(Fe,Mn)$ phase transforms into $Al_{13}(Fe,Mn)_4$.

Another type of phase transformation during the homogenization treatment is observed in Fe↑-Si↑ samples. In the as-cast condition, the Fe-bearing phase fraction increases from below 0.5% in rapidly cooled samples to > 2.5% in medium- and slow-cooled samples. The amount of Fe-bearing phase in the medium-cooled sample then decreases during the homogenization treatment to approximately the same level as that observed in the rapidly cooled sample (around 0.5%). At the same time, the fraction of Al(Fe,Mn)Si phase increases during the heat treatment, as shown in Figure 8-10b. This is obviously caused by a transformation of the $Al_6(Fe,Mn)$ phase into an Al(Fe,Mn)Si phase, which is associated with a slight decrease in volume fraction. Such a phase transformation is also observed in the slow-cooled sample, but to a much lesser extent due to the coarser phases.

The amount of Al(Fe,Mn)Si in the as-cast condition in samples with Si↑ after fast cooling, compared to other cooling conditions, is high and then decreases with subsequent heat treatment. Even though the content of $Al_6(Fe,Mn)$ in these samples increases during the homogenization step, no clear statement can be made about an reverse effect to that seen in samples subjected to other cooling rates (with respect to the standard error of the mean). When the Si content is low Al(Fe,Mn)Si is still present in all alloys, but in negligible amounts, as Figure 8-10b shows.

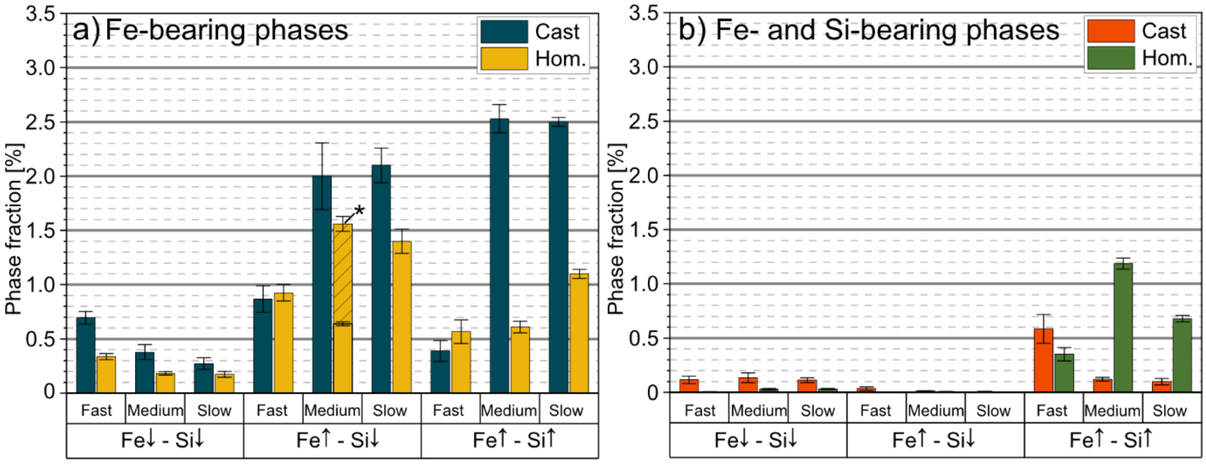

Figure 8-11: Results of the feature analysis of phase fraction, with standard deviation of the mean, of the Fe-bearing intermetallics $Al_6(Fe,Mn)$ and $Al_{13}Fe_4$ (a) and Fe- and Si bearing intermetallics (Al(Fe,Mn)Si) (b) after the subjection to different cooling conditions of cast samples in the as-cast and homogenized conditions. The bar marked with an (*) represents a re-measurement with a smaller feature size threshold than the other measurements, to increase the detection rate of smaller particles after the 6-to-3 transformation

Automated feature analysis allows phase identification based on grey values based on BSE images and elemental threshold limits. The magnification for these measurements is low and the exact point of measurement highly influenced by the shape of the feature. Therefore the elemental content detected should be taken as a rough estimate that does not reflect the exact composition. To gain a better understanding of the exact phase type, several manual spot measurements of Fe-bearing IMPs were conducted at high magnification in all alloys produced. The elemental compositions of the phases obtained and the assigned phase are listed in Table 8-5. Because the variation in elemental composition does not differ significantly between samples and is not essentially affected by cooling conditions, the values given represent the mean values over all samples. The standard deviation given represents the deviation over all measurements made on all samples.

All observed Fe-bearing phases show a solubility for Cr, Cu and Zn. Zn has to be treated with respect to the surrounding matrix. There the Zn content is about 3.5 wt.-%, which is much higher than the values found in the phases. Note that the high Al content detected is due to co-excitation of the surrounding matrix. Thus the Zn content in the IMPs may be slightly lower than indicated by the measurement. The majority of phases observed in the as-cast condition are assigned to $Al_6(Fe,Mn)$, with only a few $Al_{13}(Fe,Mn)_4$ phases. As mentioned above, the content of the latter increases during homogenization, especially in the Fe↑ - Si↓ sample subjected to medium cooling.

During homogenization, more Cu from the surrounding matrix is consumed by all Fe-bearing IMPs. This leads to an increase of 1 at.-% Cu in $Al_6(Fe,Mn)$ and 0.5 at.-% Cu in the Al(Fe,Mn)Si phase.

Table 8-5: EDX point measurements of Fe-containing phases for all alloys. Standard deviations correspond to the mean values of the phases in each alloy produced [at.-%]; per value at least five measurements were done.

Assigned phase	Condition	[at.-%]						
		Al	Si	Cr	Mn	Fe	Cu	Zn
$Al_6(Fe,Mn)$	As cast	$84.0_{\pm0.6}$	-	$0.2_{\pm0}$	$4.2_{\pm0.4}$	$9.8_{\pm0.6}$	$0.5_{\pm0.1}$	$1.1_{\pm0.1}$
	Homogenized	$83.2_{\pm0.3}$	-	$0.2_{\pm0}$	$3.9_{\pm0.5}$	$10.2_{\pm0.5}$	$1.5_{\pm0.2}$	$1.0_{\pm0.1}$
$Al_{13}Fe_4$	As cast	$77.4_{\pm1.4}$	-	$0.2_{\pm0.1}$	$2.9_{\pm0.4}$	$17.6_{\pm1.3}$	$1.6_{\pm0.22}$	$0.39_{\pm0.4}$
	Homogenized	$77.2_{\pm0.9}$	-	$0.2_{\pm0.1}$	$3.9_{\pm0.4}$	$16.7_{\pm0.9}$	$1.8_{\pm0.3}$	$0.3_{\pm0.1}$
$Al_{16}(Fe,Mn)_4Si_3$	As cast	$75.7_{\pm0.9}$	$3.5_{\pm2.0}$	$0.7_{\pm0.2}$	$4.8_{\pm0.7}$	$13.4_{\pm3.0}$	$0.6_{\pm0.3}$	$0.3_{\pm0}$
	Homogenized	$77.2_{\pm0.9}$	$3.3_{\pm1.0}$	$0.4_{\pm0.1}$	$5.8_{\pm0.6}$	$11.5_{\pm1.5}$	$1.1_{\pm0.3}$	$0.5_{\pm0.2}$

XRD measurements were conducted to additionally quantify the phases, phase transformations and precipitation occurrences identified by automated feature analysis and EDX point measurements. XRD analysis was carried out on selected samples in the 2θ range of 15–36°, with special effort to detect peaks with very low intensities (see Figure 8-12 and Figure 8-13). A full XRD investigation was performed in the 2θ range of 30–85° on all samples produced in this study, in both the as-cast and homogenized conditions (all diffractograms are shown in Figure 8-20 of the appendix). However, the detection limit of XRD methods is usually about 2% by volume [64], and the small amounts of intermetallic phases makes it difficult to distinguish their diffraction peal from the background noise.

The samples Fe↑-Si↓ and Fe↑-Si↑ subjected to medium cooling rates were selected, because the cooling rate is of industrial relevance and the phase transformations observed are most pronounced in these two alloys. The diffractogram of the Fe↑-Si↓ sample subjected to a medium cooling rate in the as-cast condition and after homogenization is displayed in Figure 8-12. The phases identified are Mg_2Si [65], T-phase ($Mg_{32}(Al,Zn)_{49}$) [66], Al_6Fe [67], $Al_6(Fe,Mn)$ [68] and $Al_{13}Fe_4$ [69]. Mn and Fe in Al_6Fe are isostructural [70], but a change in composition leads to a slight shift in the peak position of this phase. This is most evident in the plateau forming at about 34°, which indicates the presence of several metastable phases. During homogenization the peaks become sharpened as the phases transform into a more stable condition with a more uniform composition. The XRD measurements also provide an indication of the occurrence of the 6-to-3 phase transformation from Al_6Fe to $Al_{13}Fe_4$. While the overall height of the peaks of Al_6(Fe,Mn) decreases during homogenization, the peaks of $Al_{13}Fe_4$ increase. It should be noted that due to the crystal structure of the phases, the theoretical peak intensity of $Al_{13}Fe_4$ is very low compared to that of more complex phases such as Al_6Fe or T-phase. Therefore the minor changes in intensity need to be seen with respect to the very low intensity of the phase overall. In addition, peaks for T-phase particles disappear during homogenization treatment because the phase is dissolved back into the matrix and not reprecipitated due to water quenching.

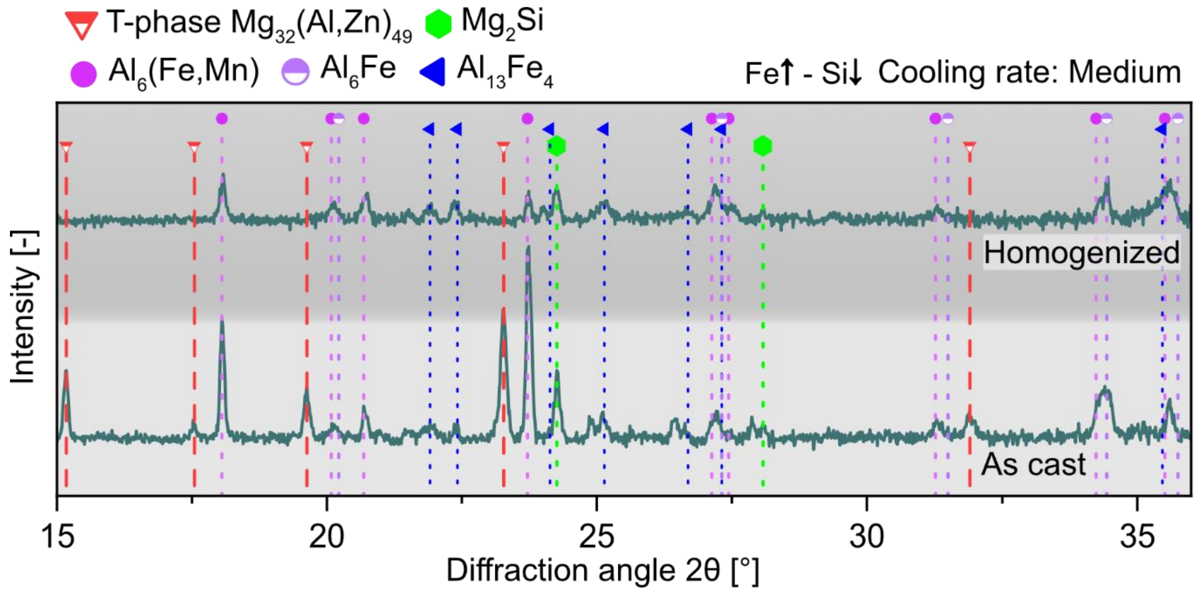

Figure 8-12: XRD diffractogram of the Fe↑-Si↓ sample subjected to a medium cooling rate in the as-cast and homogenized condition. During homogenization the peak of Al_6(Fe,Mn)/Al_6Fe decreases, while the peak of $Al_{13}Fe_4$ increases

The diffractograms shown in Figure 8-13 displays the change in phase type during homogenization of the Fe↑-Si↑ sample subjected to a medium cooling rate during casting. The phases identified are of the same type as found in the Fe↑-Si↓, except that instead of $Al_{13}Fe_4$ a cubic $Al_{16}Mn_4Si_3$ phase [71] is seen. The latter has a solubility for Fe [72], and can be written as α-$Al_{16}(Mn,Fe)_4Si_3$. In the as-cast condition this α-phase has a minor appearance, but it increases significantly upon the homogenized condition, as also indicated by feature analysis (see Figure 8-11). The 6-to-alpha transformation from Al_6(Fe,Mn) to the alpha phase is thus confirmed by the XRD measurements.

The intensity of Mg_2Si peaks increases during homogenization treatment as more phase is precipitated, especially at the surface of coarse IMPs.

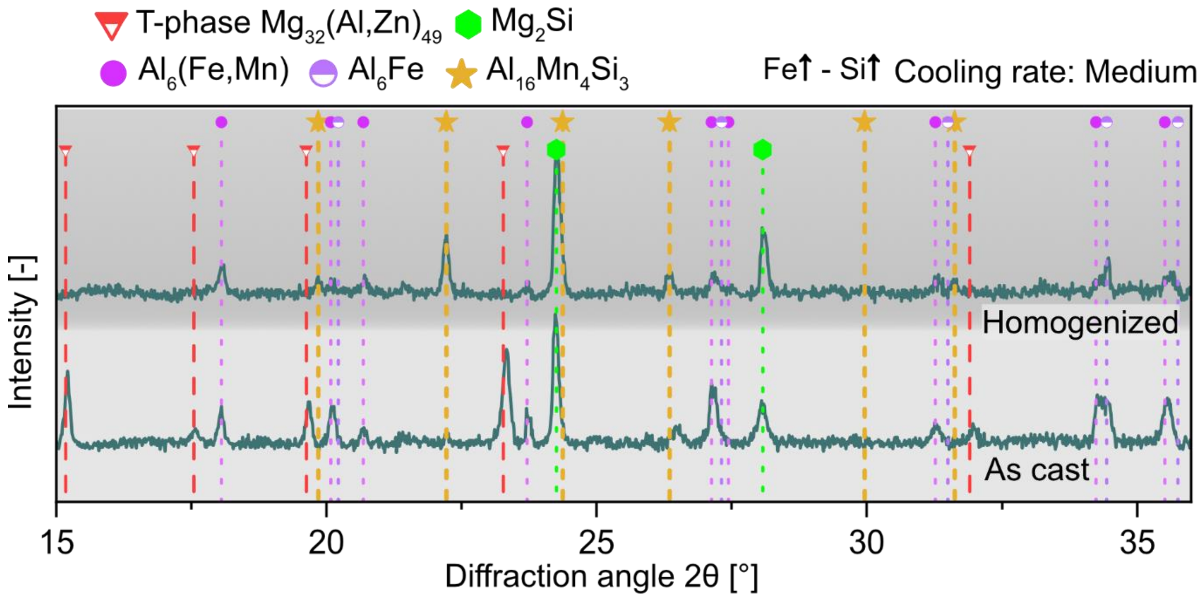

Figure 8-13: XRD diffractogram of the Fe↑-Si↑ sample subjected to a medium cooling rate in the as-cast and homogenized condition. During homogenization the peak of $Al_6(Fe,Mn)/Al_6Fe$ decreases, while the peak of $Al_{16}Mn_4Si_3$ increases

8.2.3.3 Processing

Hot rolling was performed after homogenization and for these alloys commonly done at a temperature of about 400 °C. Microstructural examination of the alloy after hot rolling reveals the behavior of the primary phases during this process. The fact that the phase fraction and size of IMPs in Fe↓-Si↓ samples are negligibly small ensures good workability. The small size of IMPs in all rapidly cooled samples facilitates good processability, while the coarse particles and higher number of voids in slow-cooled samples make for insufficient processability. Therefore only samples with high iron content and industrially relevant medium cooling conditions were investigated.

The micrographs in Figure 8-14 show the two cases observed. In the first (Fe↑-Si↓, medium cooling rate; Figure 8-14a), the size of the primary particles is successfully reduced by the 6-to-3 transformation, despite the high Fe content. The small particles are predominantly oriented in the rolling direction and do not affect the integrity of the material during rolling. When the Si level is increased to the high Fe level, the occurring 6-to-alpha transformation does not result in a major change in morphology of IMPs. The effect of this on rolling is shown in Figure 8-14b using the example of Fe↑-Si↑ under medium cooling conditions. Here the coarse primary phases become the starting points for crack formation: cracks typically form at a 45 ° angle to the rolling direction and progress along the coarse primary phases.

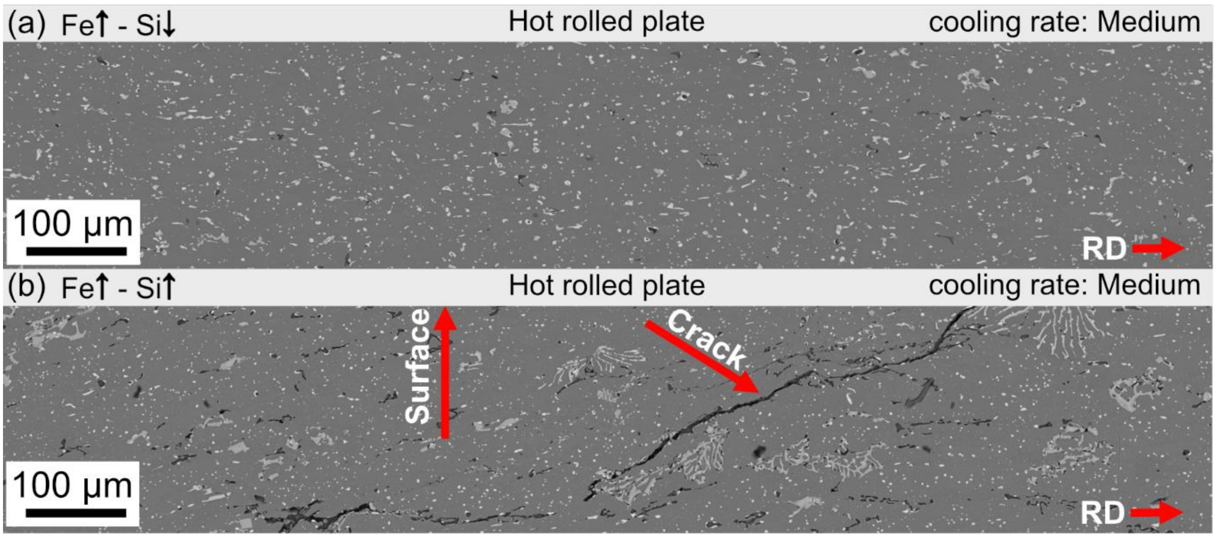

Figure 8-14: SEM-BSE micrographs of crossover material with Fe↑-Si↓ (a) and Fe↑-Si↑ (b) under medium cooling conditions after hot rolling at ≈ 400 °C

It should be noted that not all the particles seen in Figure 8-14 represent Fe- and Si-bearing IMPs. Automated feature analysis of the samples reveal a fraction of 2.7 ± 0.5% T-phase after hot rolling, which increases further to 4.8 ± 0.5% T-phase in the finished cold-rolled product. The mean values given represent characteristic measurements of the Fe↑-Si↓ and Fe↑-Si↑ samples at medium conditions. These measurements are in good agreement with each other, as the amounts of Mg, Zn and Cu are the same in both alloys.

All the alloys produced were processed into finished cold-rolled 1.2 mm sheets, regardless of the surface defects introduced during the rolling process. In order to achieve the desired cold rolling degree (CRD), rolling was combined with intermediate annealing at 370 °C for 1 h. Overview images of the finished sheet material are shown in Figure 8-15. The images are displayed together with representative images of the phases present in the alloys after casting and homogenization. This is because the phase morphology in the homogenized condition was found to be vital for the processability of the alloy.

The surface quality and rolling capability change dramatically according to the cooling rate and the Fe/Si ratio. The processability of samples with high Fe/Si ratios or overall low tramp element content is satisfactory at fast and medium cooling rates. Samples with simultaneously high Fe and Si content can only be successfully rolled in the rapidly solidified condition. Two different phase morphologies are visible in each case. Samples showing successful processability inherit small, dispersed Fe-containing IMPs after the homogenization treatment. Samples showing poor processability and delamination, as seen in medium- and slow-cooled Fe↑-Si↑ samples, contain large blocky phases after heat treatment.

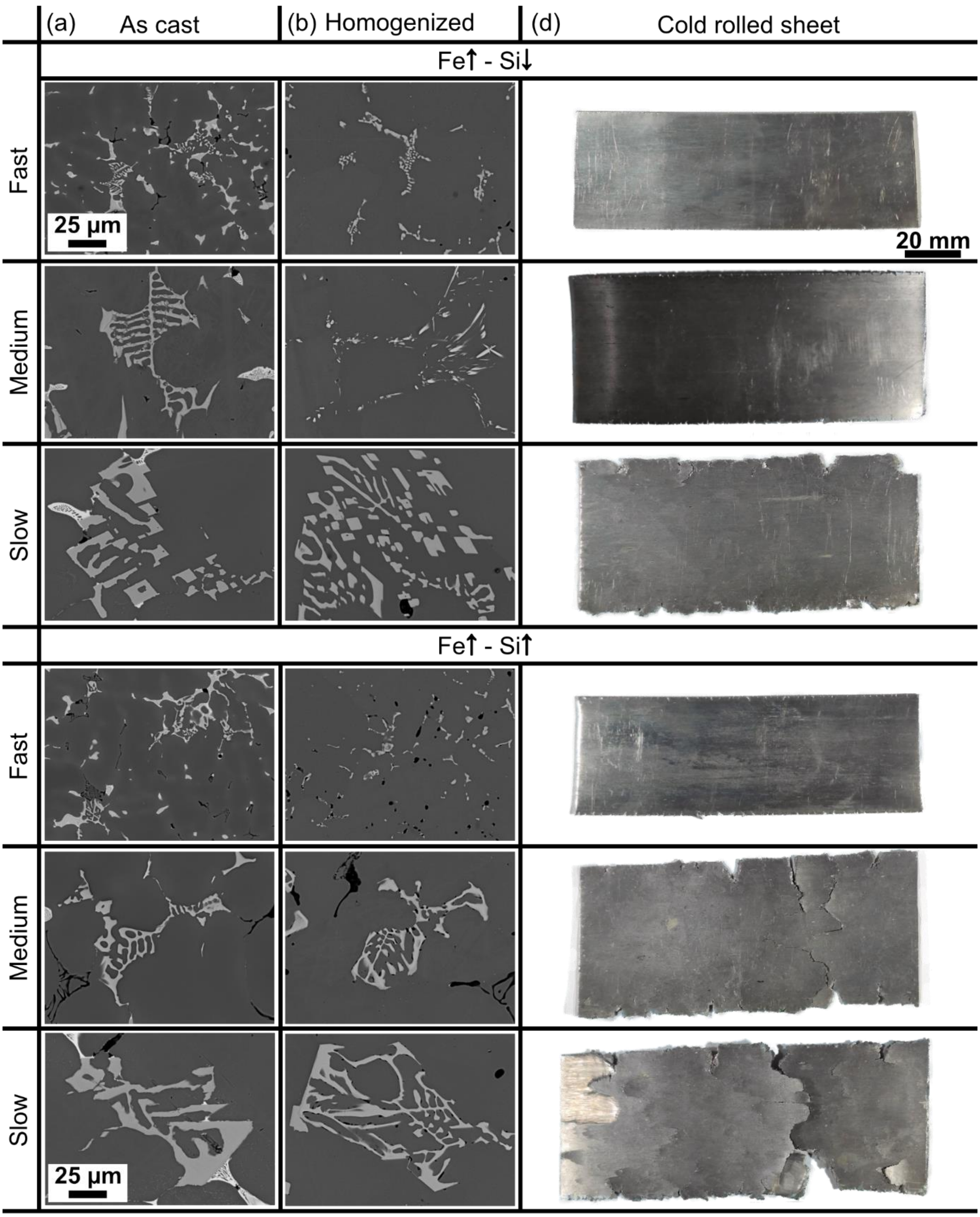

Figure 8-15: Tramp element phases found in the alloys produced under both the as-cast (a) and homogenized (b) conditions with different cooling rates applied during casting. Where the phases are not spheroidized and reduced in size during homogenization the processability of the alloy is negatively affected, as shown in the 1.2 mm cold-rolled sheet material photographs (c)

This study reports on the effect increased Fe and Si content has on the microstructure evolution and processability of novel 5/7 crossover alloys. Its main findings can be summarized as follows:

- Thermodynamic calculations after Scheil using FactSage and Pandat software both predict T-phase segregations, but disagree in terms of the IMPs predicted. While FactSage predicts $Al_{13}Fe_4$, Al_6Fe and Mg_2Si, Pandat calculations predict an Al(Fe,Mn)Si phase.
- The thermodynamic equilibrium calculations of FactSage and Pandat are inconsistent with one other. According to Pandat the 6-to-alpha transformation and the 6-to-3 transformation can be achieved at a homogenization temperature of 480 °C, while FactSage predicts the co-existence of $Al_{13}Fe_4$ and Al_6Fe.
- The IMP phase morphology depends strongly on the cooling condition during casting. Fast cooling leads to small phases whose size increases with decreasing cooling rate.
- Homogenization after fast cooling results in spheroidization, while phases after slow cooling are stable and do not significantly change their shape. IMP phase transformation is dependent on both the Fe/Si ratio and the cooling condition. This is particularly noticeable at medium cooling rates. In Fe↑-Si↓ a 6-to-3 transformation is observed with a simultaneous decrease in IMP size and fraction, while in Fe↑-Si↑ a 6-to-alpha transformation takes place, with a decrease in quantity but no pronounced change in morphology.
- The processability of the 5/7 crossover alloy depends strongly on the size of the IMPs in the alloy. Small IMPs generate good rollability, and coarse IMPs lead to crack formation during hot rolling.

Solidification rate has a major influence on the occurrence of spheroidization. At higher cooling rates, the IMPs are rather small and show slightly rounded corners due to an increased nucleation rate and limited growth time. During the subsequent homogenization treatment the phases do not grow significantly. They remain approximately the same size but spheroidize. The tendency to spheroidize is caused by instabilities at the interface between the IMP and the matrix, i.e. the increased interface energy [73,74]. At slower cooling rates, the phases grow and form more stable surfaces because the atoms have more time to arrange themselves into a more stable, ordered state closer to equilibrium. Higher cooling rates can also result in phases with more defects and fewer stable phases. [75,76]

According to feature analysis, EDX point measurements and XRD analysis, two IMP transformations occur during homogenization treatment in the 5/7 crossover system with high Fe content. These transformations depend on the Si level of the alloy. The 6-to-3 transformation and the 6-to-alpha transformation observed are both in good agreement with Pandat equilibrium calculations. These phase transformations are most visible in alloys subjected to industrially relevant medium cooling rates during direct chill casting. They are shown in Figure 8-16.

The transformation process from the metastable $Al_6(Fe,Mn)$ phase to the stable $Al_{13}(Fe,Mn)_4$ condition is illustrated in Figure 8-16a for the Fe↑-Si↓ sample after medium cooling conditions. This 6-to-3 transformation is reported as a decomposition process where the metastable phase decomposes to $Al_{13}Fe_4$ and Al [77], or a nucleation process where the $Al_{13}Fe_4$ phase nucleates at the surface of the nearest area around the $Al_6(Fe,Mn)$ particles. The nucleation process involves a simultaneous dissolution/precipitation event. In this case the transformation of 6-to-3 is controlled by the diffusion rate of Fe in the matrix [41] and may already occur at temperatures of 400 °C [78]. As seen in Figure 8-16a the $Al_6(Fe,Mn)$ phase (dark grey) decomposes into $Al_{13}(Fe,Mn)_4$ (light grey), but the round shaped surface of the phase may be interpreted as evidence of dissolution. As seen in the overview images provided in the supplementary section, a homogeneous distribution of $Al_{13}(Fe,Mn)_4$ needles is found preferentially in the region of grain boundaries. This is to be expected, because grain boundaries act as favoured diffusion paths for the Fe atoms. The 6-to-3 transformation follows the equation $4Al_6(Fe,Mn) \rightarrow Al_{13}(Fe,Mn)_4 + 11Al$. Taking into account the molecular weight of the composites and a density of $Al_6(Fe,Mn)$ with 3.35 g/cm^3 and $Al_{13}(Fe,Mn)_4$ with 3.99 g/cm^3, a reduction in volume of IMPs of about 45% is to be expected. Comparing the feature analysis values for the Fe↑-Si↓ sample subjected to a medium cooling rate in the as-cast and re-measured homogenized condition generates a decrease in volume of ≈ 23 %. Note that a re-assessment of all microphases was performed using ImageJ software. According to this procedure, the Fe↑-Si↓ sample contains a fraction of 4.6% and 1.4% of particles brighter than the matrix in the as-cast and homogenized conditions, respectively. Considering the 2% of T-phase, as measured by automated feature analysis in the as cast condition (also brighter than the matrix), and that only Fe-bearing IMPs are brighter than the matrix after homogenization, the decrease in volume is calculated as 46%. In view of the measurement uncertainties and the fact that not all of the $Al_6(Fe,Mn)$ was transformed, the metallographic values confirm the decrease in volume surprisingly well.

In Fe↑-Si↑ samples subjected to medium cooling conditions, a greatly increased quantity of Al(Fe,Mn)Si phases is observed after homogenization, while the fraction of $Al_6(Fe,Mn)$ particles is significantly reduced. This is assumed to be the result of a 6-to-alpha transformation, which is validated by XRD measurements (see Figure 8-13). However, in this process the IMPs do not significantly change in size and morphology. The course and evolution of the 6-to-alpha transformation can be understood well by comparing the phase fractions of the different cooling rates. The sample subjected to the fast cooling rate contains Al(Fe,Mn)Si as the main Fe-bearing IMP, with a fraction of about 0.6%, while the fraction of $Al_6(Fe,Mn)$ is comparatively low, with a value of 0.4%. The preferential formation of Al(Fe,Mn)Si by accelerated cooling is also reported by Liu et al [79]; they found a metastable Al(Fe,Mn)Si phase as the main Fe-bearing phase. According to Liu et al [79] the solidification front is enriched with Si during rapid cooling and reaches the threshold for the formation of the quaternary Al(Fe,Mn)Si phase. During the homogenization treatment, part of the Al(Fe,Mn)Si phase transforms into $Al_6(Fe,Mn)$. This is caused by the slow heating process in a temperature region where $Al_6(Fe,Mn)$ is the more stable phase. As Si is already consumed by the Al(Fe,Mn)Si phase during casting and the formation of Mg_2Si, the 6-to-alpha transformation is no longer feasible at the homogenization temperature due to the lack of free Si in the alloy. Therefore, the Al(Fe,Mn)Si phase fraction decreases during heat treatment while the $Al_6(Fe,Mn)$ fraction increases in the fast cooled Fe↑-Si↑ sample.

This phenomenon is reversed in samples subjected to slower cooling rates during casting. Here the cooling rate is suitable for the formation of $Al_6(Fe,Mn)$. This is reflected by the low Al(Fe,Mn)Si fraction of < 0.1% in medium- and slow-cooled samples compared to > 1.5% $Al_6(Fe,Mn)$ in the as-cast condition (see Figure

8-11). During subsequent heat treatment Si diffuses into the Al_6(Fe,Mn) phases, resulting in the 6-to-alpha transformation. This has been extensively studied by Alexander and Greer in the 3xxx alloy system [46,47,80]. They found that no detectable Si enrichment was present in the areas around the Al_6(Fe,Mn) particles after casting. However, during subsequent heat treatment most of the phases transform to the alpha phase, which is controlled by the diffusion of Si in the matrix [80].

Our XRD analysis identified the alpha-Al(Fe,Mn)Si by the $Al_{15}MnSi_3$ phase [81]. In this phase Mn can be replaced by Fe to a large extent. The Si content in the phase is also variable, with the lowest values found when Fe replaces more than 80% of Mn [82,83]. The phase transformation occurs on the Al_6(Fe,Mn)/Al-matrix interface. Subsequently the Al(Fe,Mn)Si phase covers the Al_6(Fe,Mn) phase like a shell and slows down the diffusion and further phase transformation [84], as seen in Figure 8-16b. In diffusion-controlled transformations like that discussed here [48,80] the rearrangement of atoms within the phase is gradual and controlled, meaning that the crystal structure changes slowly from one configuration to another [85]. This effectively means that the change in crystal structure does not necessarily involve a change in morphology. The Al(Fe,Mn)Si phase is harder than the Al_6(Fe,Mn) phase, generating a hard-shell / soft-core structure [48]. While in 3xxx series alloys this is deployed as an advantage for cleaning the die during drawing, the high hardness of the phase causes massive negative effects in the system discussed here as it is more prone to cracking. [86]

The 6-to-alpha transformation follows the reaction $4Al_6(Fe,Mn) \rightarrow Al_{16}(Fe,Mn)_4Si_3 + 8Al$. With a density of the $Al_{16}Mn_4Si_3$ phase of 3.63 g/cm^3 and the composition, a reduction in volume of 21% is expected. By analysing all SEM/BSE images taken using ImageJ and considering a 2% T-phase in the as cast condition, a decrease in volume of 25.5% is calculated, which agrees with the expected volume decrease.

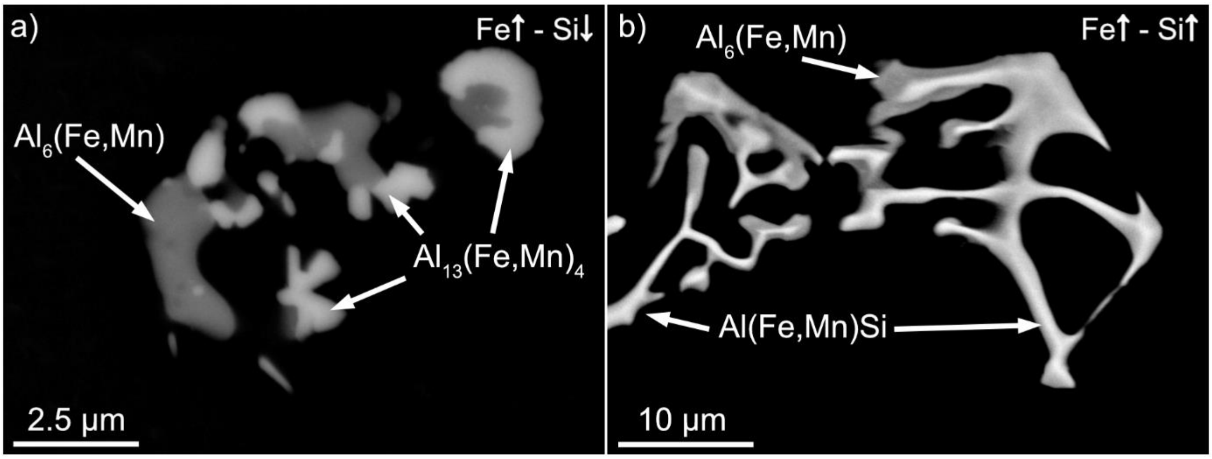

Figure 8-16: SEM/BSE micrographs of phases after homogenization treatment at 480 °C. In Fe↑ - Si↓ samples (a) the transformation of Al_6(Fe,Mn) (dark grey) to Al_{13}(Fe,Mn)$_4$ (light grey) is visible. In the Fe↑ - Si↑ (b) alloy the transformation of Al_6(Fe,Mn) (dark grey) into an Al(Fe,Mn)Si phase (light grey) is visible

Apart from the core/shell phase transformation, another possible cause of phase stabilization during processing in the Fe↑-Si↑ sample at intermediate cooling rates is the formation of Mg_2Si at the surface of the Fe-bearing IMPs. It is well known that stable and coarse equilibrium Mg_2Si particles nucleate on coarse primary phases which contain elements such as Fe, Mn and Si [87,88] (see Figure 8-9c). According to simulations applying the ClagN precipitation model this precipitation occurs simultaneously with the 6-to-alpha transformation [89]. For 5xxx-series alloys homogenization at temperatures > 500 °C is reported to dissolve this phase back into the matrix [42,89,90]. This is not feasible in our alloy system because melting starts at temperatures of about 500 °C.

At high Fe content, the Si level is identified as the major decisive factor for the processability of the alloy. This is shown schematically in Figure 8-17.

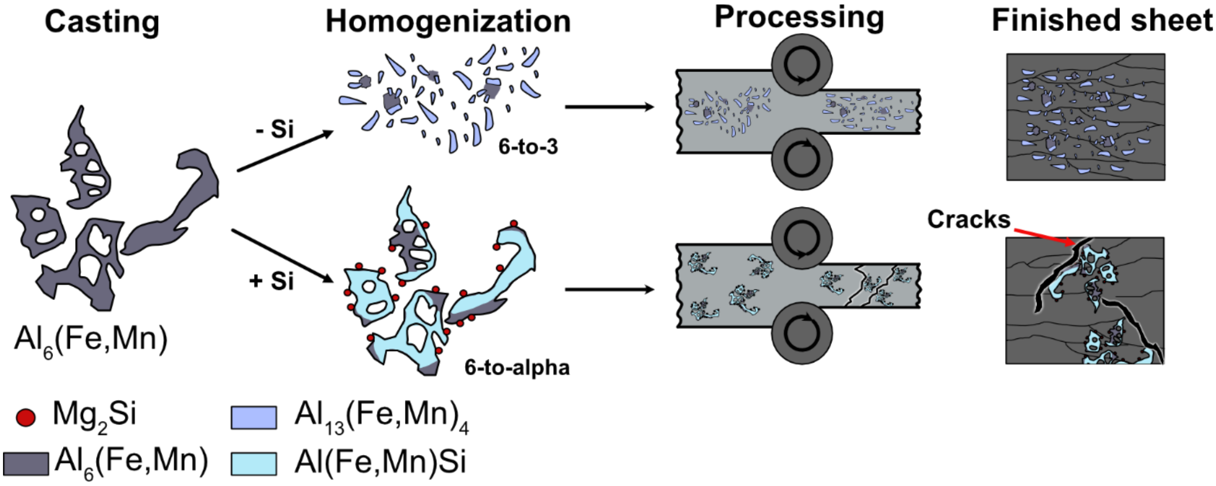

Figure 8-17: Schematic of the possible phase transformation paths and their outcomes in Al-Mg-Zn-Cu alloys. At raised Fe content and medium cooling rates the phase transformation path during homogenization is dependent on the Si content in the alloy

An increased Fe content combined with a high Si content leads to the primary precipitation of both Fe-containing intermetallic phases and Mg_2Si.

However, at slow and moderate solidification combined with a simultaneously high Fe and Si content, no microstructure formation can be achieved that ensures satisfactory rollability. The 6-to-alpha phase transformation ($Al_6(Fe,Mn) \rightarrow Al(Fe,Mn)Si$) controlled by Si diffusion observed during homogenization does not lead to any favorable morphological change in the IMPs. Consequently, in order to avoid the simultaneous presence of a high Fe content and a high Si content during large-scale processing of 5/7 crossover alloys, it is necessary to consider the composition of the recycling materials used to produce novel 5/7 crossover alloys.

8.2.4 Conclusion

This study provides a comprehensive investigation of the microstructural evolution and processability of 5/7 crossover aluminum alloys containing various amounts of Fe and Si and subjected to various cooling rates upon casting. At low tramp element content, processability is always a given because the IMPs which form are small and few in number. At raised tramp element content, processability depends strongly on the Fe/Si ratio and the cooling condition, as follows:

- Fast cooling (approx. 60 K/s) during processes such as thin strip casting enables good processability, independent of the amount of tramp element content. This is due to small phases formed during the casting process which spheroidize further during the homogenization procedure, as seen in Fe↑-Si↓ samples.
- Medium cooling (approx. 3 K/s) during direct chill casting mainly results in coarse, Chinese-script-like $Al_6(Fe,Mn)$ phases which transform further during homogenization treatment in dependence on the Fe/Si ratio. In Fe↑-Si↓ samples, the 6-to-3 transformation observed ($Al_6(Fe,Mn) \rightarrow Al_{13}(Fe,Mn)_4$) is accompanied by a decrease in particle size, leading to good rollability of the alloy. In contrast, in Fe↑-Si↑ samples a 6-to-alpha transformation ($Al_6(Fe,Mn) \rightarrow Al(Fe,Mn)Si$) generated a hard-shell / soft-core structure in the Chinese-script phase, with a highly detrimental impact on the rollability of the alloy.
- Slower cooling rates (< 1 K/s) allow the primary phases to grow to into stable, coarse and block-like structures. Phase transformation during homogenization is partly suppressed, with a major detrimental impact on rollability.

In the commercial processing of AlMgZn(Cu) crossover alloys via continuous casting, the above study indicates that homogenization combined with a controlled Fe/Si ratio contributes significantly to the successful processing of these alloys in rolling processes.

8.2.5 Appendix

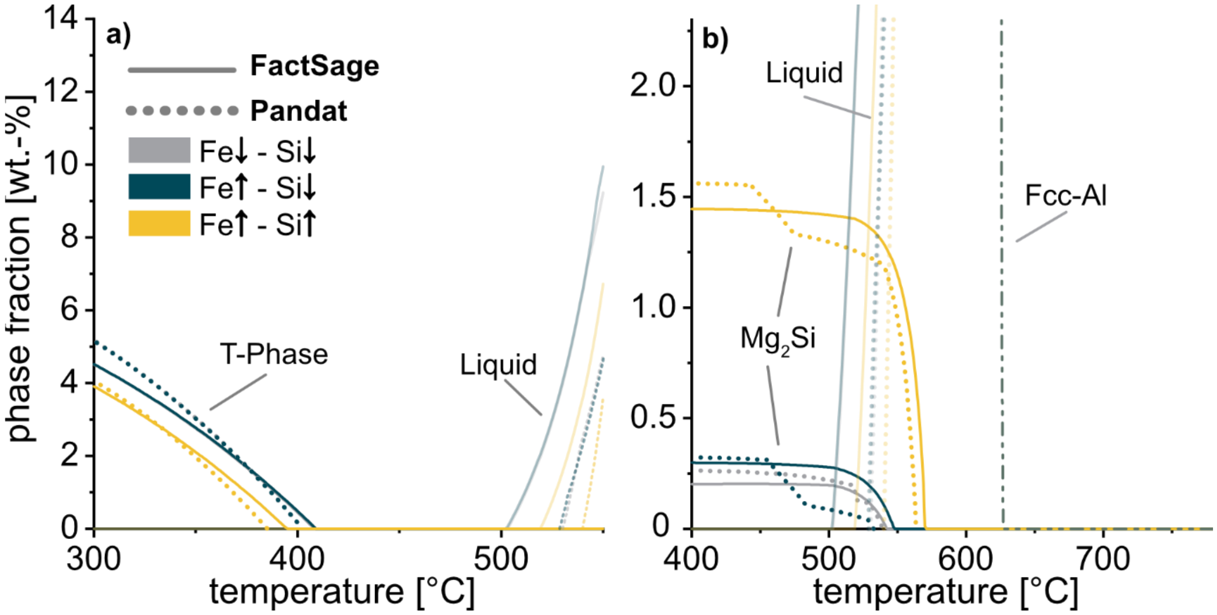

Figure 8-18: Thermodynamic equilibrium calculations for T-phase (a) and Mg_2Si (b) formation according to FactSage and Pandat

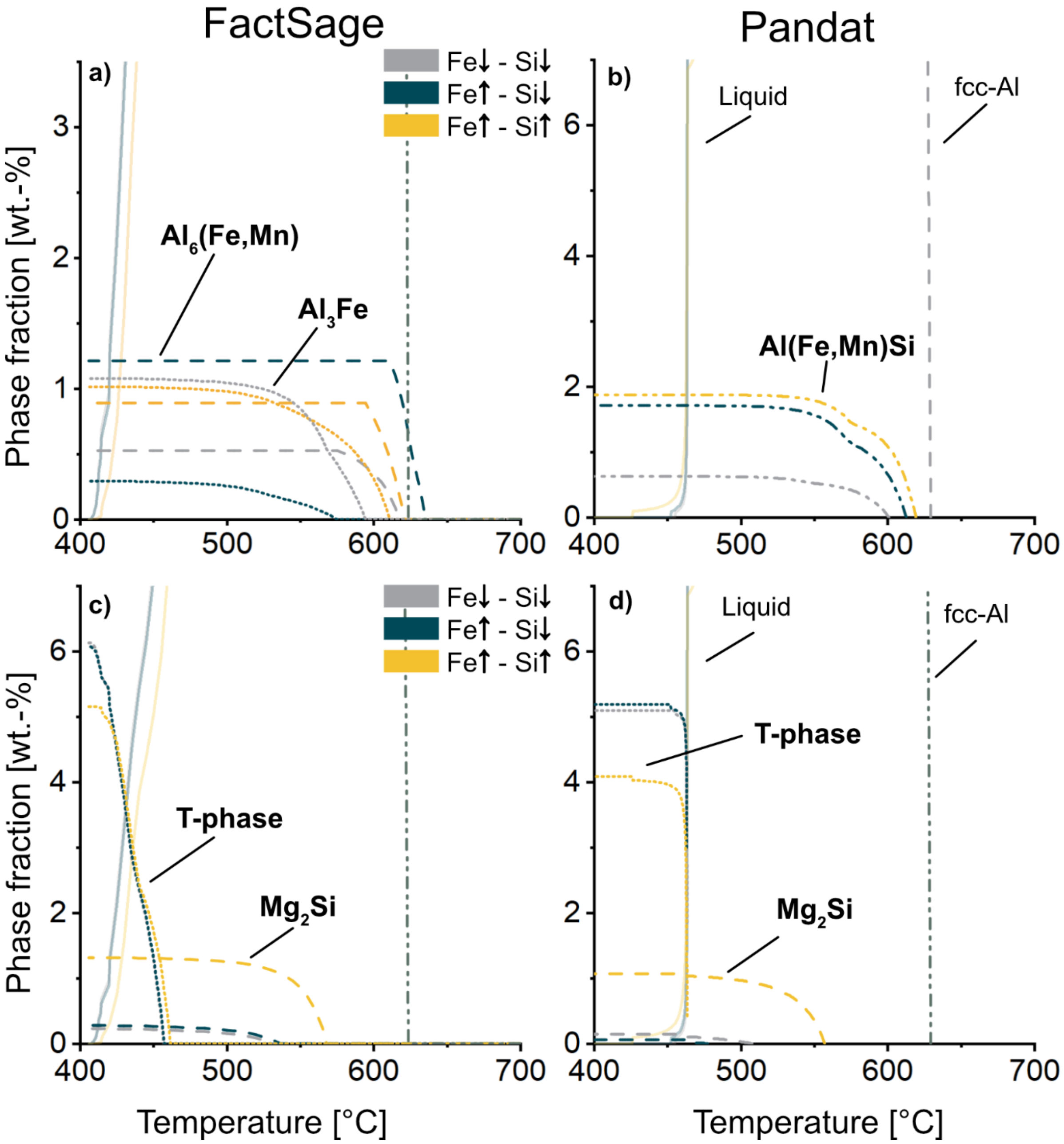

Figure 8-19: Thermodynamic calculations after Scheil of Fe-containing phases, T-phase and Mg$_2$Si for samples containing various amounts of Si and Fe. Comparison of the results for Fe-bearing IMPs according to FactSage (a) and Pandat (b). Comparison of T-phase and Mg$_2$Si according to Factsage (c) and Pandat (d)

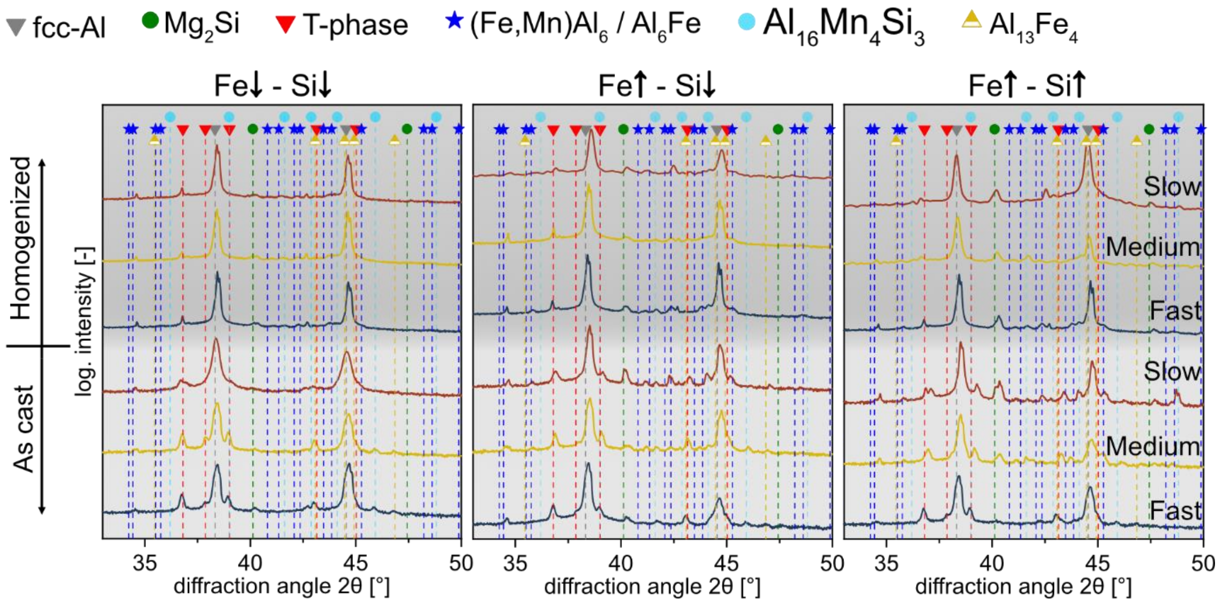

Figure 8-20: XRD-diffraction pattern of all samples in the as-cast and homogenized states. The different colors of the lines correspond to the different cooling conditions from casting

8.2.6 References

[1] International Aluminium Institute, Global Aluminium Cycle 2020:. alucycle.international-aluminium.org/public-access/public-global-cycle/.

[2] J. Hirsch, Aluminium in Innovative Light-Weight Car Design, Materials Transactions 52 (2011) 818–824.

[3] J. Hirsch, Recent development in aluminium for automotive applications, Transactions of Nonferrous Metals Society of China 24 (2014) 1995–2002.

[4] A. Luthin, J.G. Backes, M. Traverso, A framework to identify environmental-economic trade-offs by combining life cycle assessment and life cycle costing – A case study of aluminium production, Journal of Cleaner Production 321 (2021) 128902.

[5] J. Pedneault, G. Majeau-Bettez, V. Krey, M. Margni, What future for primary aluminium production in a decarbonizing economy?, Global Environmental Change 69 (2021) 102316.

[6] A.N. Løvik, R. Modaresi, D.B. Müller, Long-term strategies for increased recycling of automotive aluminum and its alloying elements, Environmental science & technology 48 (2014) 4257–4265.

[7] D. Raabe, D. Ponge, P.J. Uggowitzer, M. Roscher, M. Paolantonio, C. Liu, H. Antrekowitsch et al., Making sustainable aluminum by recycling scrap: The science of “dirty” alloys, Progress in Materials Science 128 (2022) 100947.

[8] L. Zhang, J. Gao, L.N.W. Damoah, D.G. Robertson, Removal of Iron From Aluminum: A Review, Mineral Processing and Extractive Metallurgy Review 33 (2012) 99–157.

[9] Simensen, J., Christian, S. LeBrun, Removal of Iron and Manganese in aluminium alloys by adding magnesium and subsequently centrifuging, Light Metals (2009) 777–781.

[10] K. Nakajima, O. Takeda, T. Miki, K. Matsubae, S. Nakamura, T. Nagasaka, Thermodynamic analysis of contamination by alloying elements in aluminum recycling, Environmental science & technology 44 (2010) 5594–5600.

[11] L.F. Mondolfo, Removal of silicone from Aluminium and Aluminium alloys(2,362,147).

[12] L. Stemper, M.A. Tunes, R. Tosone, P.J. Uggowitzer, S. Pogatscher, On the potential of aluminum crossover alloys, Progress in Materials Science (2021).

[13] L. Stemper, M.A. Tunes, P. Dumitraschkewitz, F. Mendez-Martin, R. Tosone, D. Marchand, W.A. Curtin et al., Giant hardening response in AlMgZn(Cu) alloys, Acta Materialia 206 (2021) 116617.

[14] G. Graf, P. Spoerk-Erdely, P. Staron, A. Stark, F. Mendez Martin, H. Clemens, T. Klein, Quench rate sensitivity of age-hardenable Al-Zn-Mg-Cu alloys with respect to the Zn/Mg ratio: An in situ SAXS and HEXRD study, Acta Materialia 227 (2022) 117727.

[15] Y. Pan, Di Zhang, H. Liu, Z. Zhang, H. Li, L. Zhuang, J. Zhang, Reducing welding hot cracking of high-strength novel Al–Mg–Zn–Cu alloys based on the prediction of the T-shaped device, Science and Technology of Welding and Joining 25 (2020) 483–489.

[16] Y. Pan, Di Zhang, H. Liu, L. Zhuang, J. Zhang, Precipitation hardening and intergranular corrosion behavior of novel Al–Mg–Zn(-Cu) alloys, Journal of Alloys and Compounds 853 (2021) 157199.

[17] C. Cao, Di Zhang, X. Wang, Q. Ma, L. Zhuang, J. Zhang, Effects of Cu addition on the precipitation hardening response and intergranular corrosion of Al-5.2Mg-2.0Zn (wt.%) alloy, Materials Characterization 122 (2016) 177–182.

[18] M.C. Caroll, M.J. Mills, G.S. Daehn, B.R. Dunbar, Effects of Zn additions on the grain boundary precipitation and corrosion of Al-5083, Scripta Materialia 42 (2000) 335–340.

[19] C. Meng, Di Zhang, L. Zhuang, J. Zhang, Correlations between stress corrosion cracking, grain boundary precipitates and Zn content of Al–Mg–Zn alloys, Journal of Alloys and Compounds 655 (2016) 178–187.

[20] S. Samberger, I. Weißensteiner, L. Stemper, C. Kainz, P.J. Uggowitzer, S. Pogatscher, Fine-grained aluminium crossover alloy for high-temperature sheet forming, Acta Materialia 253 (2023) 118952.

[21] G. Bergman, J. Waugh, L. Pauling, The crystal structure of the metallic phase $Mg_{32}(Al,Zn)_{49}$, Acta Cryst. 10 (1957) 254–259.

[22] H. Liu, Z. Zhang, Di Zhang, J. Zhang, The effect of Ag on the tensile strength and fracture toughness of novel Al-Mg-Zn alloys, Journal of Alloys and Compounds 908 (2022) 164640.

[23] L. Stemper, M.A. Tunes, P. Oberhauser, P.J. Uggowitzer, S. Pogatscher, Age-hardening response of AlMgZn alloys with Cu and Ag additions, Acta Materialia 195 (2020) 541–554.

[24] Y. Geng, Q. Song, Z. Zhang, Y. Pan, H. Li, Y. Wu, H. Zhu et al., Quantifying early-stage precipitation strengthening of Al–Mg–Zn(-Cu) alloy by using particle size distribution, Materials Science and Engineering: A 839 (2022) 142851.

[25] P.D. Willenshofer, M.A. Tunes, H.T. Vo, L. Stemper, O. Renk, G. Greaves, P.J. Uggowitzer et al., Radiation-resistant aluminium alloy for space missions in the extreme environment of the solar system, arXiv, 2022.

[26] M.A. Tunes, L. Stemper, G. Greaves, P.J. Uggowitzer, S. Pogatscher, Prototypic Lightweight Alloy Design for Stellar-Radiation Environments, Advanced science (Weinheim, Baden-Wurttemberg, Germany) 7 (2020) 2002397.

[27] B. Trink, I. Weißensteiner, P.J. Uggowitzer, K. Strobel, S. Pogatscher, High Fe content in Al-Mg-Si wrought alloys facilitates excellent mechanical properties, Scripta Materialia 215 (2022) 114701.

[28] AMAG Austria Metall AG, AluReport 01 2023.

[29] P. Tan, Z. Liu, J. Qin, Q. Wei, B. Wang, D. Yi, Enhanced corrosion performance by controlling grain boundary precipitates in a novel crossover Al-Cu-Zn-Mg alloy by optimizing Zn content, Materials Characterization 208 (2024) 113615.

[30] S. Wenner, J. Friis, C.D. Marioara, R. Holmestad, Precipitation in a mixed Al–Cu–Mg/Al–Zn–Mg alloy system, Journal of Alloys and Compounds 684 (2016) 195–200.

[31] N.A. Belov, A.A. Aksenov, D.G. Eskin, Iron in Aluminium Alloys, CRC Press, London, 2002.

[32] J. Grasserbauer, I. Weißensteiner, G. Falkinger, T.M. Kremmer, P.J. Uggowitzer, S. Pogatscher, Influence of Fe and Mn on the Microstructure Formation in 5xxx Alloys-Part I: Evolution of Primary and Secondary Phases, Materials (Basel, Switzerland) 14 (2021).

[33] A. Verma, S. Kumar, P.S. Grant, K. O'Reilly, Influence of cooling rate on the Fe intermetallic formation in an AA6063 Al alloy, Journal of Alloys and Compounds 555 (2013) 274–282.

[34] Z. Que, Y. Wang, C.L. Mendis, C. Fang, J. Xia, X. Zhou, Z. Fan, Understanding Fe-Containing Intermetallic Compounds in Al Alloys: An Overview of Recent Advances from the LiME Research Hub, Metals 12 (2022) 1677.

[35] Q. Li, J. Wang, C. Xue, S. Wang, X. Yang, G. Tian, H. Su et al., Transforming detrimental intermetallics by accumulative thermal and strain energies in the Al–Fe–Si alloy, J Mater Sci 59 (2024) 1699–1720.

[36] C.M. Allen, K. O'Reilly, B. Cantor, P.V. Evans, Intermetallic phase selection in 1XXX Al alloys, Progress in Materials Science 43 (1998) 89–170.

[37] K. Liu, X. Cao, X.-G. Chen, Effect of Mn, Si, and Cooling Rate on the Formation of Iron-Rich Intermetallics in 206 Al-Cu Cast Alloys, Metall Mater Trans B 43 (2012) 1231–1240.

[38] N.A. Belov, T.K. Akopyan, N.O. Korotkova, S.O. Cherkasov, A.O. Yakovleva, Effect of Fe and Si on the Phase Composition and Microstructure Evolution in Al-2 wt.% Cu-2 wt.% Mn Alloy During Solidification, Cold Rolling and Annealing, JOM 73 (2021) 3827–3837.

[39] Min Sang Kim, Dae Young Kim, Young Do Kim, Hyun Joo Choi, Se Hoon Kim, Effect of Fe-Mn Solid Solution Precursor Addition on Modified AA 7075, Archives of Metallurgy and Materials (2023).

[40] Z. Que, Y. Zhou, Y. Wang, C.L. Mendis, Z. Fan, Effects of Mg addition on the Al_6(Fe,Mn) intermetallic compounds and the grain refinement of α-Al in Al-Fe-Mn alloys, Materials Characterization 171 (2021) 110758.

[41] J. Arbeiter, M. Vončina, B. Šetina Batič, J. Medved, Transformation of the Metastable Al6Fe Intermetallic Phase during Homogenization of a Binary Al-Fe Alloy, Materials (Basel, Switzerland) 14 (2021).

[42] A. Halap, T. Radetić, M. Popović, E. Romhanji, Study of Homogenization Treatments of Cast 5xxx Series Al-Mg-Mn Alloy Modified with Zn, in: C.E. Suarez (Ed.), Light Metals 2012, Springer International Publishing, Cham, 2016, pp. 387–392.

[43] M. Shakiba, N. Parson, X.-G. Chen, Effect of homogenization treatment and silicon content on the microstructure and hot workability of dilute Al–Fe–Si alloys, Materials Science and Engineering: A 619 (2014) 180–189.

[44] B. Trink, I. Weißensteiner, P.J. Uggowitzer, K. Strobel, A. Hofer-Roblyek, S. Pogatscher, Processing and microstructure–property relations of Al-Mg-Si-Fe crossover alloys, Acta Materialia 257 (2023) 119160.

[45] P. Krall, I. Weißensteiner, S. Pogatscher, Recycling aluminum alloys for the automotive industry: Breaking the source-sink paradigm, Resources, Conservation and Recycling 202 (2024) 107370.

[46] D.T.L. Alexander, A.L. Greer, Nucleation of the Al_6(Fe, Mn)-to-α-Al–(Fe, Mn)–Si transformation in 3XXX aluminium alloys. I. Roll-bonded diffusion couples, Philosophical Magazine 84 (2004) 3051–3070.

[47] D. Alexander, A.L. Greer, Solid-state intermetallic phase tranformations in 3XXX aluminium alloys, Acta Materialia 50 (2002) 2571–2583.

[48] Y.J. Li, A. Håkonsen, D. Mortensen, T. Pettersen, T. Furu, Modelling the Phase Transformation from Al_6(Mn,Fe) to α-Al(Mn,Fe)Si Phase during Homogenization of AA3xxx Alloys, MSF 519-521 (2006) 297–302.

[49] J.E. Yoo, A. Shan, I.G. Moon, S.J. Maeng, A study on composition and crystal structure of dispersoids in AlMgSi alloys, J Mater Sci 34 (1999) 2679–2683.

[50] P. Orozco-González, M. Castro-Román, J. López-Cuevas, A. Hernández-Rodríguez, R. Muñiz-Valdez, S. Luna-Álvarez, C. Ortiz-Cuellar, Effect of iron addition on the crystal structure of the α-AlFeMnSi phase formed in the quaternary Al-Fe-Mn-Si system, Revmetal 47 (2011) 453–461.

[51] P. Donnadieu, G. Lapasset, T.H. Sanders, Manganese-induced ordering in the α-(Al-Mn-Fe-Si) approximant phase, Philosophical Magazine Letters 70 (1994) 319–326.

[52] L. Stemper, F. Schmid, R. Tosone, AMAG CrossAlloy®—Lightweighting the Future by Unconstraint Alloy Design: A Case Study, in: S. Wagstaff (Ed.), Light Metals 2024, Springer Nature Switzerland, Cham, 2024, pp. 241–247.

[53] F. Schmid, L. Stemper, T. Ebner, W. Leitner, S. Pogatscher, Industry-oriented sample preparation of 6xxx and 5xxx aluminium alloys in laboratory, Proceedings of EMC 2019 (2019).

[54] Mettop, ILTEC Technology. mettop.com/api/cdn/uploads/1682401237_mchujnsf.pdf.

[55] B.G. Bartosiaki, J.A.M. Pereira, W.V. Bielefeldt, A.C.F. Vilela, Assessment of inclusion analysis via manual and automated SEM and total oxygen content of steel, Journal of Materials Research and Technology 4 (2015) 235–240.

[56] M. Nuspl, W. Wegscheider, J. Angeli, W. Posch, M. Mayr, Qualitative and quantitative determination of micro-inclusions by automated SEM/EDX analysis, Analytical and bioanalytical chemistry 379 (2004) 640–645.

[57] O. Walusinski, Doctoral Thesis, in: O. Walusinski (Ed.), Georges Gilles de la Tourette, Oxford University Press, 2018, pp. 129–144.

[58] C.W. Corti, P. Cotterill, G.A. Fitzpatrick, The Evaluation of the Interparticle Spacing in Dispersion Alloys, International Metallurgical Reviews 19 (1974) 77–88.

[59] J. Schindelin, I. Arganda-Carreras, E. Frise, V. Kaynig, M. Longair, T. Pietzsch, S. Preibisch et al., Fiji: an open-source platform for biological-image analysis, Nature methods 9 (2012) 676–682.

[60] C.W. Bale, P. Chartrand, S.A. Degterov, G. Eriksson, K. Hack, R. Ben Mahfoud, J. Melançon et al., FactSage thermochemical software and databases, Calphad 26 (2002) 189–228.

[61] S.-L. Chen, S. Daniel, F. Zhang, Y.A. Chang, X.-Y. Yan, F.-Y. Xie, R. Schmid-Fetzer et al., The PANDAT software package and its applications, Calphad 26 (2002) 175–188.

[62] S. Samberger, L. Stemper, P.J. Uggowitzer, R. Tosone, S. Pogatscher, Influence of Solidification Rate and Impurity Content on 5/7 crossover Alloys, in: S. Wagstaff (Ed.), Light Metals 2024, Springer Nature Switzerland, Cham, 2024, pp. 226–233.

[63] P.-E. Droenen, N. Ryum, Local melting in Al-Mg-Zn-alloys, Metall and Mat Trans A 25 (1994) 521–530.

[64] B.D. Cullity, S.R. Stock, Elements of X-ray diffraction, 3rd ed., Pearson education Limited, Harlow, 2014, 2014.

[65] International Centre for Diffraction Data, PDF-4+ Release, Card Number 01-074-6835, (2023).

[66] International Centre for Diffraction Data, PDF-4+ Release, Card Number 04-010-7478, (2023).

[67] International Centre for Diffraction Data, PDF-4+ Release, Card Number 47-1433, (2023).

[68] International Centre for Diffraction Data, PDF-4+ Release, Card Number 04-001-6010, (2023).

[69] International Centre for Diffraction Data, PDF-4+ Release, Card Number 00-050-0797, (2023).

[70] L.K. Walford, The structure of the intermetallic phase $FeAl_6$, Acta Cryst 18 (1965) 287–291.

[71] International Centre for Diffraction Data, PDF-4+ Release, Card Number 04-024-5380, (2023).

[72] J.G. Barlock, L.F. Mondolfo, Structure of Some Aluminium-Iron-Magnesium-Manganese- Silicon Alloys, International Journal of Materials Research 66 (1975) 605–611.

[73] A.M.A. Mohamed, E. Samuel, Y. Zedan, A.M. Samuel, H.W. Doty, F.H. Samuel, Intermetallics Formation during Solidification of Al-Si-Cu-Mg Cast Alloys, Materials (Basel, Switzerland) 15 (2022).

[74] P.Y. Zhu, Q.Y. Liu, Kinetics of granulation of discontinuous phase in eutectic structures, Materials Science and Technology 2 (1986) 500–507.

[75] K. Wang, S. Lv, H. Wu, G. Wu, S. Wang, J. Gao, J. Zhu et al., Recent research progress on the phase-field model of microstructural evolution during metal solidification, Int J Miner Metall Mater 30 (2023) 2095–2111.

[76] Y. Zhao, M.J. Powell-Palm, G. Ukpai, C. Bilbao-Sainz, L. Chen, J. Wang, B. Rubinsky, Phase change interface stability during isochoric solidification of an aqueous solution, Applied Physics Letters 117 (2020).

[77] Y. Li, L. Arnberg, A eutectoid phase transformation for the primary intermetallic particle from Al_m(Fe,Mn) to Al_3(Fe,Mn) in AA5182 alloy, Acta Materialia 52 (2004) 2945–2952.

[78] A. Tonejc, X-ray study of the decomposition of metastable Al-rich Al-Fe solid solutions, Metall Trans 2 (1971) 437–440.

[79] Y. Liu, L. Luo, C. Han, L. Ou, J. Wang, C. Liu, Effect of Fe, Si and Cooling Rate on the Formation of Fe- and Mn-rich Intermetallics in Al–5Mg–0.8Mn Alloy, Journal of Materials Science & Technology 32 (2016) 305–312.

[80] D.T.L. Alexander, A.L. Greer, Nucleation of the Al_6(Fe, Mn)-to-α-Al–(Fe, Mn)–Si transformation in 3XXX aluminium alloys. II. Transformation in cast aluminium alloys, Philosophical Magazine 84 (2004) 3071–3083.

[81] K. Sugiyama, N. Kaji, K. Hiraga, Re-Refinement of α-(AlMnSi), Acta Crystallogr C Cryst Struct Commun 54 (1998) 445–447.

[82] J.E. Tibballs, R.L. Davis, B.A. Parker, Al−Si substitution in α-phase AIMnSi, J Mater Sci 24 (1989) 2177–2182.

[83] M. Armand, On the Phases in the Ternary System Aluminium-Iron-Silicon, CR Seances Acad. Sci (1952) 1506–1508.

[84] M. Warmuzek, G. Mrówka, J. Sieniawski, Influence of the heat treatment on the precipitation of the intermetallic phases in commercial $AlMn_1FeSi$ alloy, Journal of Materials Processing Technology 157-158 (2004) 624–632.

[85] X. Liu, H. Li, M. Zhan, A review on the modeling and simulations of solid-state diffusional phase transformations in metals and alloys, Manufacturing Rev. 5 (2018) 10.

[86] Y.J. Li, L. Arnberg, Evolution of eutectic intermetallic particles in DC-cast AA3003 alloy during heating and homogenization.

[87] R. Kahlenberg, T. Wojcik, G. Falkinger, A.L. Krejci, B. Milkereit, E. Kozeschnik, On the precipitation mechanisms of β-Mg_2Si during continuous heating of AA6061, Acta Materialia 261 (2023) 119345.

[88] B. Milkereit, M.J. Starink, P.A. Rometsch, C. Schick, O. Kessler, Review of the Quench Sensitivity of Aluminium Alloys: Analysis of the Kinetics and Nature of Quench-Induced Precipitation, Materials (Basel, Switzerland) 12 (2019).

[89] O. Engler, Z. Liu, K. Kuhnke, Impact of homogenization on particles in the Al–Mg–Mn alloy AA 5454 – Experiment and simulation, Journal of Alloys and Compounds 560 (2013) 111–122.

[90] O. Engler, S. Miller-Jupp, Control of second-phase particles in the Al-Mg-Mn alloy AA 5083, Journal of Alloys and Compounds 689 (2016) 998–1010.

9 SUMMARY AND OUTLOOK

The pursuit of carbon neutrality has necessitated the adoption of more sustainable practices and materials in various industries, with aluminum being a key focus due to its lightweight properties and widespread use in the transportation sector. However, primary aluminum production is highly energy-intensive, contributing significantly to global CO_2 emissions. Recycling offers a more sustainable alternative, consuming substantially less energy. Nonetheless, the integration of recycled aluminum presents challenges, particularly with the increase in impurities such as iron and silicon, which can adversely affect the material's quality and performance.

The thesis is supporting an accelerated industrial establishment of 5/7 crossover alloys by exploring several critical aspects of these novel alloys: (i) the effect of heating and cooling rates by simulation of industrial heat treatment processes, (ii) identification of unique properties of 5/7 crossover alloys, (iii) accelerated quality measurements and (iiii) the impact of higher recycling content with a comparison of lab-scale and industrial scale.

The study on heating and cooling rates revealed that these alloys exhibit low quench rate sensitivity, enabling the potential use of hot forming followed by age hardening treatments. This insight is crucial for industrial applications where uniform cooling conditions are challenging to maintain. Examination of the grain structure in the cold-rolled state revealed micron-sized T-phase particles, which could be utilized via particle-stimulated nucleation to form a fine-grained microstructure suitable for superplastic forming operations. These findings paved the way for the first prototyping of industrial Crossalloy.57.

Traditional microscopic etching methods were found to be inadequate due to the fine grain size of the alloys. An innovative approach involving the modification of grain boundary chemistry was developed, enhancing the etchability of the alloys without altering the grain size. This advancement significantly improves the feasibility of quality control in an industrial setting. The sustainability aspects of 5/7 crossover alloys were also investigated, focusing on the effect of increased Fe and Si content on the mechanical behavior of the alloys, both at the laboratory scale and in near-industrial simulations. The study highlighted the importance of understanding the phase formation and nature of these impurities to develop strategies for their management. The results demonstrated that with appropriate alloy design and processing techniques, the detrimental impacts of increased impurity concentrations could be mitigated, even at industrial feasible cooling conditions.

The development of 5/7 crossover alloys mark a significant advancement in aluminum metallurgy, offering a sustainable solution to the strength-ductility trade-off. This innovation can not only reduce the environmental impact associated with aluminum production but also supports the circular economy by potentially maximizing the use of end-of-life scrap. Future research and development should focus on optimizing industrial processes, advanced alloy design, sustainability assessments, industrial prototyping and applications, quality control innovations, and policy and industry collaboration. Continued refinement of industrial heat treatment processes is essential to fully exploit the potential of 5/7 crossover alloys. This includes optimizing cooling rates and heat treatment schedules to enhance mechanical properties and ensure consistency across large-scale production. Further exploration of alloying elements and their interactions with Fe and Si impurities can lead to the development of broader alloy compositions with even better performance characteristics. Understanding the fundamental mechanisms of impurity management can enable the design of alloys that can tolerate higher levels of recycled content.

Furthermore, a comprehensive life cycle assessments (LCAs) of 5/7 crossover alloys should be conducted to quantify their environmental benefits compared to traditional alloys. This includes evaluating the entire production chain, from raw material extraction to end-of-life recycling.

10 APPENDIX

Table 10-1: Usage of AI

Object	Share of AI (in %)	Tools/ Version	Remarks	prompting
Improving linguistic legibility	30	ChatGPT 4o DeepL write	Texts were created in-house and revised with AI to improve readability	https://oc.unileoben.ac.at/index.php/s/Yyb7MCnxcF8gOh9
Preparation of the abstracts and a summary	80	ChatGPT 4o	To improve productivity, the AI was trained with all the information from the thesis.	